Functional and structural biomarkers to optimize vagus nerve stimulation therapy in drug-resistant epilepsy

Alexandre Berger

Secteur des Sciences de la Santé - SSS
Institute Of NeuroSciences – IoNS

Thesis submitted in fulfillment of the requirement for the degree of Doctorate in Biomedical and Pharmaceutical Sciences

Thèse présentée en vue de l'obtention du grade de Docteur en Science Biomédicales et Pharmaceutiques

September 2024

Cover image: *Soothing Vigilance,* Alexandre Berger, *2023*. Scientific image exhibited at the Micro-Art Exhibition, Arte-Fac, Brussels.

Supervisor

Prof. El Tahry Riëm
Université Catholique de Louvain
Institute of NeuroScience (IoNS)

Co-supervisor

Prof. Vandewalle Gilles
Université de Liège
GIGA – CRC – Human Imaging

Examination Board

President
Prof. Hanseeuw Bernard
Catholic University of Louvain

Secretary
Prof. Mouraux André
Catholic University of Louvain

Prof. Delbeke Jean
Catholic University of Louvain

Prof. Dricot Laurence
Catholic University of Louvain

Prof. Phillips Christophe
University of Liège

Prof. Ibrahim George
University of Toronto

Prof. Levy Robert
Marcus Neuroscience Institute
Boca Raton – FL

Prof. Lundell Henrik
University of Copenhagen

This research was supported by Synergia Medial SA and the Walloon Region (Industrial Doctorate Program n°8193).

With just one polka dot, nothing can be achieved. In the universe, there is the sun, the moon, the earth, and hundreds of millions of stars. All of us live in the unfathomable mystery and infinitude of the universe. Pursuing 'philosophy of the universe' through art under such circumstances has led me to what I call 'stereotypical repetition'.

Yayoi Kusama

TABLE OF CONTENTS

ABBREVIATIONS

Abbreviation	Definition
AD	Axial diffusivity
AIMD	Active implantable medical device
ASM	Antiseizure medication
AUC	Area under the curve
BAI	Beck anxiety inventory
BDI	Beck depression inventory
BMI	Body mass index
BOLD	Blood oxygenation level-dependent
CA	Cornu ammonis
CI	Confidence interval
CSD	Contrained spherical deconvolution
CSF	Cerebrospinal fluid
DBS	Deep brain stimulation
DRE	Drug-resistant epilepsy
DRN	Dorsal raphe nucleus
DSC	Sørensen-Dice similarity coefficient
DTI	Diffusion tensor imaging
EEG	Electroencephalogram
EPI	Echo-planar imaging
FA	Fractional anisotropy
FDA	Food and Drug Administration
FDG	Fluorodeoxyglucose
FDR	False discovery rate
FLASH	Fast low angle shot
FMRI	Functional magnetic resonance imaging
FN	False negative
FOD	Fiber orientation distribution
FP	False positive
FSE	Fast spin echo
FVF	Fiber volume fraction
FWE	Family-wise error

GAT	Gaba transporter
GFAP	Glial fibrillary acidic protein
GLM	General linear model
GRAPPA	Generalized autocalibrating partial parallel acquisition
GRE	Gradient-recalled echo
HF	High frequency
HLE	Hindlimb extension
HRF	Hemodynamic response function
HRV	Heart rate variability
ICA	Independent component analysis
ILAE	International league against epilepsy
IPG	Implanted pulse generator
IQR	Interquartile range
IR	Inversion recovery
LC	Locus coeruleus
LED	Light emitting diode
LGI	Leucine-rich glioma inactivated
LM	Linear model
LMEP	Laryngeal motor evoked potential
LOO	Leave-one-out
MB	Multi-band
MD	Mean diffusivity
MES	Maximal electroshock seizure
MF	Microstructure fingerprinting
MNI	Montreal neurological institute
MPRAGE	Magnetization-prepared - rapid gradient echo
MP2RAGE	Magnetization-prepared with two rapid gradient echoes
MR	Magnetic resonance
MRI	Magnetic resonance imaging
MSMT	Multi-shell multi-tissue
MT	Magnetization transfer
MTC	Magnetization transfer contrast
NDI	Neurite Density Index
NE	Norepinephrine
NIR	Near-infrared
NMDA	N-methyl-D-aspartate
NODDI	Neurite orientation dispersion and density imaging

NPG	Nucleus paragigantocellularis
NPH	Nucleus prepositus hypoglossi
NR	Non-responder
NTS	Nucleus tractus solitarius
OCD	Optical communication device
ODI	Orientation dispersion index
OL	Optical lead
P2P	Peak-to-peak
PCB	Printed circuit board
PD	Photodiode
PDF	Probability density function
PET	Positron emission tomography
PGSE	Pulsed gradient spin echo
PR	Partial responder
PSQI	Pittsburgh sleep quality index
PTSD	Posttraumatic stress disorder
QSI	Q-sampling imaging
R	Responder
RBF	Radial basis function
RD	Radial diffusivity
RF	Radiofrequency
RFE	Recursive feature elimination
RhF	Rhomboid fossa
ROI	Region-of-interest
REM	Rapid eye movement
RF	Radiofrequency
RFE	Recursive feature elimination
RNS	Responsive neurostimulation
ROC	Receiver operating curve
SC	Smart charger
SD	Standard deviation
SE	Spin echo
SMA	Supplementary motor area
SPGR	Spoiled gradient
SVM	Support vector machine
TA	Acquisition time
TE	Time-to-echo

TFL	Turbo-flash
TI	Inversion time
TN	True negative
TP	True positive
TR	Repetition time
TSE	Turbo spin echo
tVNS	Transcutaneous vagus nerve stimulation
UHF	Ultra-high field
VCSEL	Vertical-cavity surface-emitting laser
VIF	Variance inflation factor
VNS	Vagus nerve stimulation

SYMBOLS

Symbol	Description	Units
A_{ec}	Normalized signal of the extracellular compartment	-
A_{ic}	Normalized signal of the intracellular compartment	-
A_{iso}	Normalized signal of the isotropic compartment	-
b	b-value	$s \cdot mm^{-2}$
B_0	External magnetic field strength	T
C	Regularization parameter	-
C_5	Charge threshold for LMEP induction	nC
C_{50}	Charge leading to 50% LMEP saturation	nC
C_{98}	Charge leading to 98% LMEP saturation	nC
C_s	Clinical charge of the patient treatment	nC
D	Diffusion tensor	-
$d_{e,\parallel}$	Axial diffusivity in the extra-neurite space	$mm^2 \cdot s$
$d_{e,\perp}$	Radial diffusivity in the extra-neurite space	$mm^2 \cdot s$
$d_{i,\parallel}$	Axial diffusivity in the intra-neurite space ($1.7 * 10^{-3}$)	$mm^2 \cdot s$
d_{iso}	Diffusivity in the isotropic compartment ($3 * 10^{-3}$)	$mm^2 \cdot s$
e	Basis of the natural logarithm (~ 2.7183)	-
f(n)	Watson orientation distribution	-
g	Gradient profile of diffusion sequence	-
G	Gradient intensity	$mT \cdot m^{-1}$
I	Stimulation current	mA
I_{sat}	Stimulation current for LMEP saturation	mA
I_{stim}	Clinically applied stimulation current	mA
k	Slope of the dose-response curve	$\mu V \cdot nC^{-1}$
L_c	Latency of the LMEP	ms
M	Confluent hypergeometric function	-

	(Kummer's function)	
M_0	Macroscopic magnetization	$N \cdot T^{-1} \cdot m^{-2}$
n	Number of samples	-
p	Statistical p-value	-
p_{FDR}	FDR-corrected p-value	-
r	Radius of the axons	m
s	Spacing between the axons	m
T	Student's T-value	-
T1	Longitudinal relaxation time	s
T2	Transverse relaxation time	s
T2*	Effective transverse relaxation time	s
u_k	Orientation of the kth fascicle	°
Y_{sat}	Maximal LMEP amplitude	µV
Z	Impedance	Ω
α	Flip angle	°
γ	Gyromagnetic ratio	$MHz \cdot T^{-1}$
δ	Diffusion gradient duration	ms
Δ	Diffusion time	ms
κ	Concentration parameters of the Watson distribution	-
Λ	Diagonalized diffusion tensor	-
$\lambda_{1,2,3}$	Eigenvalues of the diffusion tensor	$mm^2 \cdot s$
v_{ec}	Volume fraction of the extracellular compartment	-
v_i	Volume fraction of compartment i	-
v_{ic}	Volume fraction of the intracellular compartment	-
v_{iso}	The volume fraction of the isotropic compartment	-
π	Pi contant (~ 3.1416)	-
Ω_i	Diffusion compartment i	-

ACKNOWLEDGMENTS

I am truly appreciating the remarkable opportunity that has allowed me to embark on a PhD journey at the Epilepsy and Neuromodulation Lab (ENL) following the completion of my Master's degree at the Ecole Polytechnique de Louvain (EPL). This transformative experience would have taken a distinct course without the invaluable encounters with individuals who offered me intellectual support and significantly contributed to my personal development.

First, I would like to thank Prof. **Riëm El Tahry**, my supervisor, who not only granted me the opportunity to embark on this academic journey but has steadfastly supported me throughout these 4 years. Starting a PhD amidst a pandemic, where human contacts and communication were limited is not easy, but Riëm proved to be easily accessible and ever-present, offering me a valuable guidance. I am also truly grateful to Prof. **Gilles Vandewalle**, my co-supervisor, for allowing me to be part of the Sleep and Chronobiology lab and becoming a locus coeruleus expert. Gilles has always been supporting my research with unwavering enthusiasm, always ready to address my questions and concerns.

I also would like to express my appreciation to Prof. **Laurence Dricot**, who has been by my side since the realization of my Master's thesis. Laurence directly contacted me when the ENL had a vacant PhD position. I cannot thank Laurence, the *'MRI-guru'*, enough for her invaluable contribution to my work and her well-known expression *'look at the data'*.

I am deeply grateful to **Pascal Doguet**, my first contact in Synergia Medical, who allowed me to discover the industrial realm. Pascal has always helped me for any technical difficulty and inspired me with his passion of

advancing medicine through technology. I also would like to thank **Attila Borbath** and the Walloon Region, who allowed me to pursue my thesis as part of an Industrial Doctorate Program.

My sincere appreciation extends to the Jury members of my thesis, Prof. **Bernard Hanseeuw**, Prof. **André Mouraux**, Prof. **Jean Delbeke** and Prof. **Christophe Phillips**, for accepting to read and evaluate my work and give me valuable input during the different steering committees. I truly thank the three external members of my Jury, including Prof. **George Ibrahim**, Prof. **Robert Levy** and Prof. **Henrik Lundell** for agreeing to read and evaluate my thesis.

All the research projects would not have been possible without the help of the patients who willingly participated in my studies. Their kindness, patience and genuine interest in the study results have been crucial to their realization.

And now, the members of the ENL lab. **Vénéthia**, it is obvious that we shared a strong and evolving connection over the years. Thank you for the wonderful moments we have experienced both at the lab and outside of the lab. Your presence has been integral, and my PhD journey would have been critically different without you. Véronique, many IoNS members and friends were right. **Elena**, my Krusty, you have been such a great colleague and friend, always bringing laughter into any situation. For both of you, I have to say that I am so grateful for the delightful moments we experienced during the road trip in Florida. These memories will forever be etched in my mind.

Thank you, **Simone**, for your guidance from the beginning of my thesis until your public PhD defense and for making me discover one of the finest pizza places in Brussels. Thank you for the great moments of laughter we shared in Geneva. Thank you also to the other ENL members, including **Inci** (I will remember the coffee breaks on the balcony), **Roberto** (especially for the hilarious moments in Dublin pubs), **Manon**, **Elise**, **Auriane**, **Javier** (I am

delighted we introduced you to the taste of Carrousels that you will – or not – remember), **Enrique**, **Andres** and **Ayse**. Thank you also, **Nicolas**, for the great collaboration since the realization of our Master's thesis until the transition to the role of jointly supervising a thesis, for which your insight was fundamental. To all NEUR members, thank you for the great moments spent together (and the memorable Christmas raclettes). Thank you to **Marc-Henri**, **Solenn**, **Amélie,** and **Vlad** - "les gens bien"- for the funny dinners and drinks.

Thank you to the CRC members, in particular **Katya** for the great teamwork for the ASLEEP project and the mutual psychological support when delineating the locus coeruleus of dozens of participants manually, that was worth it. Thank you to my other locus coeruleus buddy, **Elise**, for the great collaboration and help in our respective projects. Thank you to the entire ASLEEP and HILIGHT teams, including **Roya**, **Ilenia**, **Islay**, **Puneet**, **Nasrin**, and **Fermin** for the great cooperation and teamwork. Thank you to **Gaëtan** and **Siya**, for providing me a physicist input and help me in the different MRI projects.

Thank you to the Synergia Medical team for warmly welcoming me into the team. In particular, thank you **Simon** and **Jérôme** for your help in the sheep project and the long-lasting hours spent in the MRI room and the optical laboratory, **Yohan** and **Aurore** for the great moments spent in Washington, and **Catherine** for your great help and support. I would also like to thank **Soizic** for her valuable help and follow-up of the sheep at the CER.

I would like to extend my gratitude to other UCLouvain members who assisted me in various ways during my thesis, including **Leila**, **Cathy**, **Véronique**, **Sonia,** and **Loreta**.

Of course, I would like to thank all the people outside of the research environment who supported me during these four years. The support of my mom, dad, and sister in my life decisions was critical for me to pursue this academic journey. I would not thank you enough for the love and

belief in my abilities, that have been a constant source of inspiration. Sharing with you the joy of this achievement means a lot to me.

I will conclude with a huge thanks to all my friends (and specifically my Marinus friends & Co) with whom I shared incredible and indescribable moments and laugher throughout my PhD. You easily changed my mind off things during the hectic – and often restless - weekends.

SUMMARY

Vagus Nerve Stimulation (VNS) has been used for three decades as an adjunctive treatment for patients with drug-resistant epilepsy. Despite its established use, the precise mechanisms underlying its therapeutic efficacy remain a subject of ongoing investigation. Moreover, a comprehensive understanding of the biological prerequisites for responding to the treatment is yet to be achieved. In the context of optimizing VNS therapy, a novel approach for the titration of the stimulation parameters is proposed in this thesis and relies on the recording of VNS-induced Laryngeal Motor Evoked Potentials (LMEPs).

Another key aspect of this research involves the exploration of response biomarkers to deepen our current knowledge about the biological prerequisites linked to the therapeutic response. In this context, electrophysiological recordings of LMEPs and multimodal Magnetic Resonance Imaging (MRI) – including structural and functional analyses – were used to develop response biomarkers. In particular, the research delved into the structural and functional characteristics of the locus coeruleus, a small brainstem nucleus involved in the antiseizure effects of VNS, as well as the structural attributes of thalamocortical tracts in patients with drug-resistant epilepsy who were implanted with a VNS device.

Finally, an industrial part of this thesis aimed at developing a system, the Optical Communication Device (OCD), to communicate remotely (from the command room) with the fully MRI-compatible Synergia Medical optoelectronic neurostimulator in an MRI environment. The use of the OCD will ultimately help in the realization of functional MRI studies, aiming at better understanding the acute effects of VNS administration and optimizing this therapy by tuning the stimulation

parameters to maximize the recruitment of structures involved in the antiseizure effects.

RÉSUMÉ

La stimulation du nerf vague (VNS) est une thérapie utilisée depuis plus de trois décennies chez les patients atteints d'épilepsie réfractaire. Malgré sa longue utilisation, les mécanismes d'action de la VNS liés à son efficacité thérapeutique sont toujours en cours d'investigation. De plus, les fondements biologiques nécessaires pour répondre favorablement à ce traitement demeurent partiellement compris. Afin d'optimiser ce traitement, une nouvelle approche de titration des paramètres de stimulation est proposée dans cette thèse, et se base sur l'enregistrement des potentiels évoqués moteurs laryngés (LMEPs) induits par la VNS.

Un autre volet essentiel de cette étude réside dans le développement de biomarqueurs de réponse, visant à approfondir la compréhension des prérequis biologiques associés à l'efficacité thérapeutique de la VNS. Dans ce contexte, des techniques d'enregistrement électrophysiologique des LMEPs ont été utilisées, ainsi qu'une approche multimodale basée sur l'imagerie par résonance magnétique (incluant des analyses structurelles et fonctionnelles) pour l'élaboration de biomarqueur de réponse. En particulier, les caractéristiques structurelles et fonctionnelles du locus coeruleus, un noyau du tronc cérébral impliqué dans les effets antiépileptiques de la VNS, ainsi que les propriétés structurelles des voies thalamo-corticales sont étudiées dans le cadre de ces investigations et corrélées à l'efficacité thérapeutique chez des patients épileptiques implantés d'un neurostimulateur.

Enfin, une composante industrielle de cette thèse se consacre au développement d'un system, l'Optical Communication Device (OCD), permettant de communiquer dans un environnement IRM et à distance - depuis la salle de commande - avec le neurostimulateur optoélectronique

IRM-compatible conçu par Synergia Medical. L'utilisation de l'OCD permettra la réalisation d'études exploitant l'IRM fonctionnelle dans le dessein d'approfondir la compréhension des effets aigus de la VNS au niveau central. Ces études pourraient également contribuer à optimiser la thérapie par VNS en aidant à sélectionner les paramètres de stimulation maximisant le recrutement des structures impliquées dans les effets antiépileptiques de la VNS.

CHAPITRE 1. INTRODUCTION

1. HISTORY AND DEFINITION OF EPILEPSY

Historically, during antiquity, epilepsy was seen as a mystic intervention of gods or demonic possessions. Evidence that seizures originated from a cortical disruption was first described by the Egyptians in 1700 BC in the Edwin Smith Surgical Papyrus (1). Nonetheless, it was not until the 5th Century BC, when the School of Hippocrates emerged in Greece, that the idea of the brain being the primary source of the disease challenged the prevailing divine explanation of the illness (1). However, this medical belief gained popularity in Europe only at the beginning of the 17th Century (2). Later, with the discovery of the human electroencephalogram (EEG) in 1929, Hans Berger demonstrated that seizures were due to an abnormal electrical activity in the brain (2). Based on these findings, William Lennox showed in 1935 that an increased electrical activity occurred in the brain before the seizure and was further elevated during the seizure, suggesting a new etiology for epilepsy (1).

Epilepsy is a common disease with a prevalence of 7.60 per 1000 persons (3), with around 34-76 per 100,000 people developing this condition every year (4). Epilepsy is associated with stigma, which can result in an impaired quality of life and sometimes psychological difficulties for patients affected by this condition.

Since 2014, the operational and practical clinical definition of **epilepsy** has been established by the International League Against Epilepsy (ILAE) as one of the following conditions: (i) at least two unprovoked (or reflex) seizures occurring >24h apart, (ii) one unprovoked (or reflex) seizure and a probability of further seizures similar to the general recurrence risk (at

least 60%) after two unprovoked seizures, occurring over the next 10 years, or (iii) diagnosis of an epilepsy syndrome (5). The ILAE also added the definition of individuals with **resolved epilepsy** as (i) patients who had an age-dependent epilepsy syndrome but who are now past the applicable age or (ii) individuals who have remained seizure-free for at least 10 years without using antiseizure medications for at least 5 years.

2. DEFINITION OF A SEIZURE AND CLASSIFICATION

The definition of an epileptic seizure was proposed by the ILAE and has not changed since 2005. In their report, the ILAE defines a seizure as a transient occurrence of signs and/or symptoms due to an abnormal excessive or synchronous neuronal activity in the brain (6) due to an imbalance between excitation and inhibition of cortical areas (7).

Classification of seizures has been established to better characterize the underlying pathology and facilitate the customization of treatment options based on individual needs. This classification is also critical in research to better stratify patients and refine the current knowledge about this disorder. The 2017-ILAE classification divides seizures into three types based on their onset zone: focal, generalized, or unknown (6). For the three types of epilepsies, observable symptoms can encompass both motor and non-motor manifestations, playing a critical role in the classification of the seizures. A complete diagram for the classification of seizure types can be found in **Figure 1.1**.

- **Focal** seizures, also called “partial seizures” or “localized seizures”, present an onset zone in a specific area located in one hemisphere of the brain. These types of seizures are the most common ones in adults with epilepsy. According to the 2017-ILAE classification, approximately 61.9% of epileptic patients present focal seizures (8).

A seizure with a focal onset zone can be classified as “aware” (or “simple”) - when the patient is conscious and aware of the environment, or with “impaired awareness” (or “complex”), when consciousness is significantly altered, and the patient may not remember the seizure afterward. In seizures with a focal onset zone, motor onsets can be atonic, clonic, hyperkinetic, myoclonic, tonic, or with automatisms or epileptic spasms. Non-motor onsets can be autonomic, cognitive, emotional, sensory, or with behavior arrest. Focal seizures can also generalize, resulting in bilateral tonic-clonic seizures.

- In **generalized** seizures, the two hemispheres are involved in the generation of a seizure. Approximately 32.5% of patients with epilepsy experience generalized seizures (8). In such cases, motor onsets may manifest as tonic-clonic, clonic, tonic, myoclonic, myoclonic-tonic-clonic, myoclonic-atonic, atonic, or even include epileptic spasms. For these types of seizures, non-motor (or “absence”) onsets can be typical (when the seizure exhibits defined features of a well-defined seizure type), atypical (when the seizure does not conform to a well-known seizure type), myoclonic or present eyelid myoclonia.

- When the onset of the seizure is not known, but manifestations can be classified, the seizure's onset is defined as “**unknown**” (found in approximately 5.6% of patients with epilepsy). For this type of seizure, the motor onset can be tonic-clonic or show epileptic spasms, while non-motor onsets present behavioral arrest.

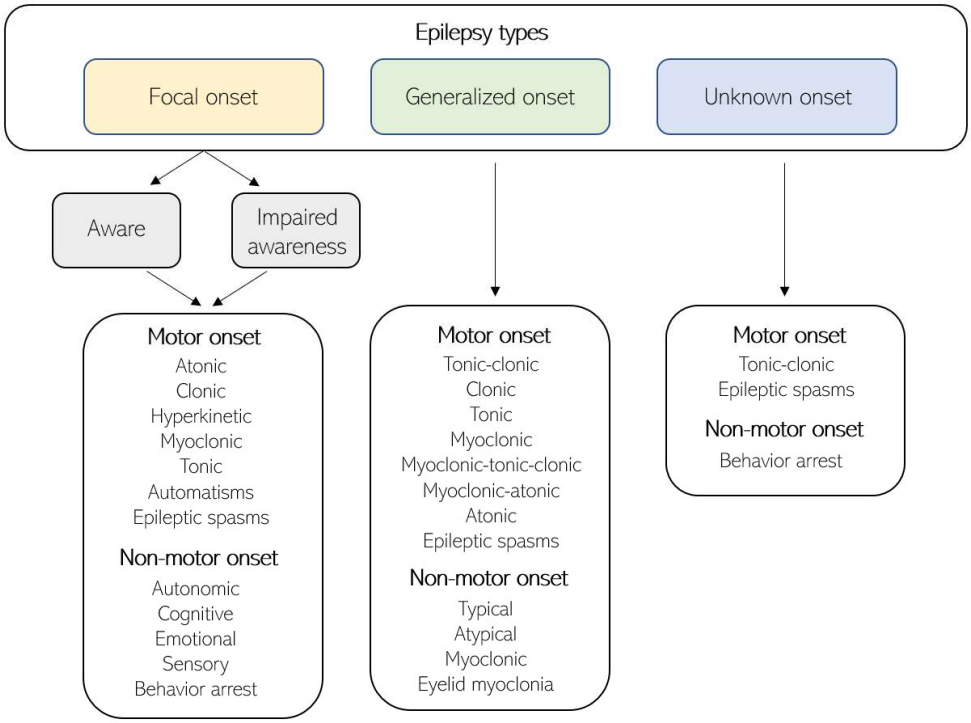

Figure 1.1 – ILAE 2017 classification of seizure types (expanded version). Adapted from (9)*.*

It is worth mentioning that patients can exhibit a combination of both generalized and focal epilepsies, a phenomenon most frequently observed in epilepsy syndromes such as Dravet and Lennox-Gastaut syndromes (9).

3. ETIOLOGY OF SEIZURES AND EPILEPSY

Different causes can lead to the occurrence of seizures and epilepsy. A **structural** etiology is identified based on brain anomalies detected using

Magnetic Resonance Imaging (MRI). Acquired structural anomalies include head trauma, stroke, tumor, neurodegenerative diseases, neural development lesions, or viral anomalies. One of the most frequent forms of structural etiologies leading to seizures and epilepsy is hippocampal sclerosis, which can be acquired, genetic, or due to an interplay between both (10). Hippocampal sclerosis is subdivided into different types based on the region presenting cell death (CA1, CA2, CA3, or CA4) and the extent of the damage (7,10). Genetic structural anomalies can also lead to seizures and epilepsy, including single-nucleotide mutations or chromosomal copy number abnormalities (7,11).

Genetic etiologies can also be the cause of epilepsy syndromes such as juvenile absences, juvenile myoclonic epilepsies, West syndrome, Dravet syndrome, or Lennox-Gastaut syndrome. The origin of the epilepsy is thought to be genetic if a known presumed genetic factor is involved in the occurrence of the seizures (7). A review article reported that 977 genes were associated with epilepsy, and this number will continue to increase in the following years with the rapid development of genetic technology (12).

Infectious etiologies of the central nervous system are also recognized as established factors contributing to seizures and epilepsies. These infectious causes include the cytomegalovirus, tuberculosis, human immunodeficiency virus, neurocysticercosis, or cerebral toxoplasmosis. Infections of the central nervous system can lead to necrosis of cortical tissues, hypoxic-ischemic injuries, cerebral infarction, or gliosis, depending on the agent involved (7,13,14).

Epilepsies with a **metabolic** etiology may result from various metabolic disorders, including hyperthermia, hyperglycemia, hypoglycemia, mitochondrial diseases, defective GABA metabolism, or leukodystrophies (7,15). While most metabolic epilepsies have a genetic origin, some of them can be acquired, e.g., pyridoxine-dependent seizures and cerebral folate deficiency-triggered seizures (7).

Finally, epilepsies are known to result from an **immune** etiology when an autoimmune-mediated central nervous system inflammation is diagnosed. These inflammations include an array of encephalitides, such as anti-N-methyl-D-aspartate (anti-NMDA) receptor encephalitis, anti-leucine-rich glioma inactivated 1 (anti-LGI1) encephalitis or Rasmussen encephalitis (16).

4. First-line treatment

Since no treatment currently exists to restore etiologically the epileptogenic activity, a pharmacological treatment remains the first-line therapy in adults to reduce antiepileptogenesis. Antiseizure medications (ASMs) are pharmacological compounds able to suppress the generation, propagation, and severity of seizures (17). ASMs administration is peculiar to the epilepsy type, the side effects, the pharmacokinetic profile of the administered compounds, the medication history of the patient, the comorbidities, the age of the patient, the willingness to have a child, and the cost (17).

The medications currently used aim to target specific molecular mechanisms. The mechanisms of action of these compounds include blocking of sodium channels, modulation of presynaptic neurotransmitter release, anti-glutamatergic activity, or a combination of them (17). More specifically, the action of ASMs can be divided into 4 different groups: (i) compounds modulating voltage-gated ion channels (e.g., sodium, calcium, and potassium channels), (ii) compounds increasing the GABA-mediated inhibitory effects by acting on $GABA_A$ receptors, GABA transporter (GAT)-1, GABA transaminase, or the GABA synthesizing enzyme glutamate decarboxylase, (iii) compounds reducing the ionotropic glutamate receptors-mediated excitatory effects by acting of the N-methyl-D-

aspartate (NMDA) or α-amino-3-hydroxy-5-methyl-4-isoxazole-propionate (AMPA) receptors, and (iv) compounds modulating the presynaptic release of neurotransmitters by acting of the SV2A and the α2δ subunit of voltage-gated calcium channels (17). Using ASMs, seizure freedom with no side effects is reached in approximately 50% of epileptic patients (17).

Different factors have been associated with seizure relapse with ASMs withdrawals in seizure-free patients, including the history of focal epilepsy, history of myoclonic seizures or multiple seizure types, presence of interictal epileptiform discharges (determined with an EEG), neural damages in the hippocampus or amygdala leading to mesial temporal sclerosis, a >50 years onset age of epilepsy, or family history of epilepsy (17,18).

5. TREATMENTS FOR DRUG-RESISTANT EPILEPSY

5.1 SURGERY

Approximately 30% of epileptic patients will develop a drug-resistant form of epilepsy (19). Patients are considered to have a refractory form of epilepsy when the use of at least two ASMs administered at the correct dosages does not make them seizure-free. These patients are referred to a specialized epilepsy center for a presurgical evaluation. Most of the patients who are candidates for surgery suffer from intractable temporal lobe epilepsy (20). For patients with mesial temporal lobe epilepsy, an anterior temporal lobectomy is performed and consists of the resection of the amygdala, hippocampus, or parahippocampus, depending on the epileptogenic zone (20). Statistics report that 66% of patients become seizure-free following this kind of surgical procedure (20,21). Other types of procedures include cortical resection of the epileptogenic focus,

hemispherectomy (usually indicated for severe, intractable epilepsies associated with a congenital hemiplegia syndrome, hemiconvulsion-hemiplegia-epilepsy syndrome, Rasmussen's syndrome, or Sturge-Weber syndrome (22)) or corpus callosotomy. Corpus callosotomy is a palliative procedure that has been showed to be effective for intractable generalized epilepsies with drop attacks (23,24).

However, for patients with a multifocal seizure onset zone, generalized epilepsy, an onset zone that lies in the eloquent cortex (i.e., brain regions critically involved in different functions including language, motor control, or higher-order cognitive functions), or for patients with a history of surgical treatment failure, other adjunctive treatments are proposed. These treatments aim at limiting the propagation, severity, and frequency of the seizures when a surgical resection of the epileptogenic zone is not possible. The existing palliative treatments for these patients include a ketogenic diet and neurostimulation techniques, namely Vagus Nerve Stimulation (VNS), Deep Brain Stimulation (DBS), and Responsive Neurostimulation (RNS). While the three techniques are approved by the U.S. Food and Drug Administration (FDA), the RNS has not been approved by the European regulatory authorities so far. A decision tree for the clinical management of patients with DRE is shown in **Figure 1.2**.

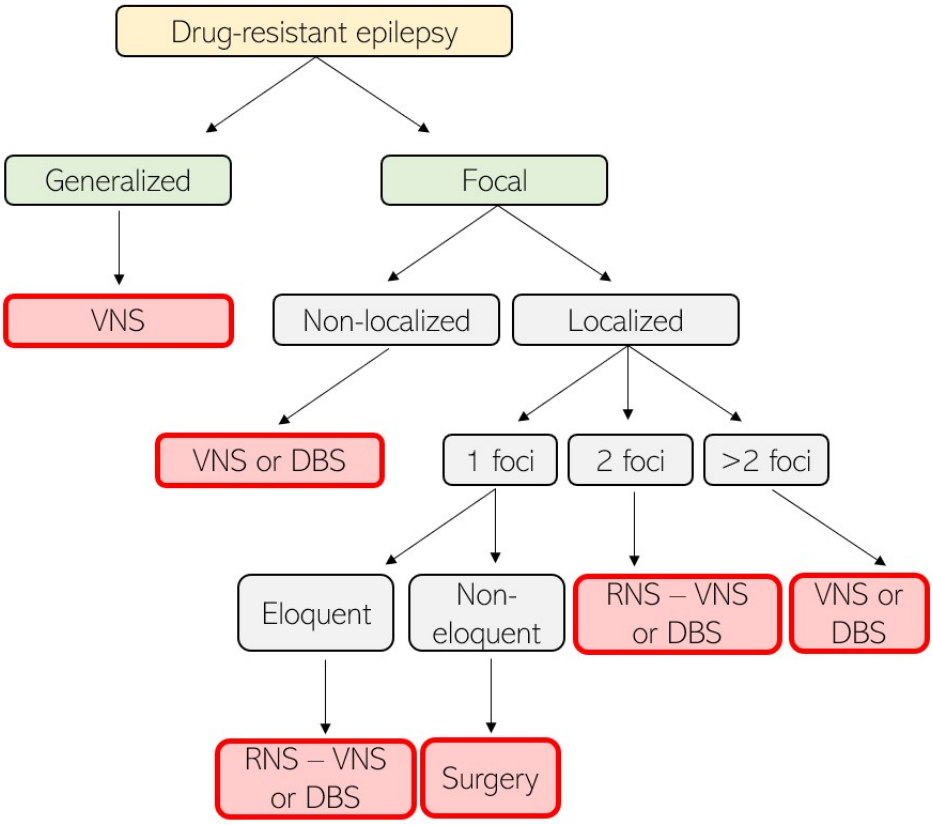

Figure 1.2 – Decision algorithm for the clinical management of drug-resistant epilepsy (DRE). Adapted from (25).

5.2 Deep brain stimulation

DBS consists of depth electrodes implanted in a specific target region that deliver a pre-established stimulation program (an open-loop strategy). A structured review of the literature that included articles from 1980 to 2018 revealed that 75% of patients implanted with a DBS device presented generalized or secondary generalized seizures, while 7.2% presented exclusively focal seizures (26).

A DBS device is composed of an Internal Pulse Generator (IPG), a lead that is inserted stereotactically in the target region, electrodes, and extension cables (**Figure 1.3**) (27). DBS can be implanted directly in the seizure onset zone or deep cortical structures (26). When implanted directly at the seizure onset zone - typically in the hippocampus, the amygdala, the hypothalamus, or specific cortical zones, DBS is known to act on the excitability of the tissues and neural synchronization, resulting in inhibitory effects. Other non-seizure-generating structures constitute targets for a DBS implantation, such as the cerebellum, basal ganglia, and the thalamus (more specifically, the anterior nucleus of the thalamus – the most common site of implantation) (26). Finally, while still in the experimental stage and not widely used in clinical practice, some studies investigated antiseizure effects of DBS by targeting deeply located fiber bundles that connect different structures of the brain, such as the corpus callosum or the fornix (26).

While the mechanisms of action of DBS are still not completely known, this therapy is known to modulate the Papez circuit that links the hippocampus to the anterior nucleus of the thalamus via the fornix and the mamillary bodies, a network involved in seizure episodes (26). Another network modulated by DBS is the cortico-thalamo-cortical relays known to disrupt the propagation of seizures (26). It is reported that 50% of patients included in clinical studies experienced a 46-90% reduction in seizure frequency when DBS is implanted in the anterior nucleus of the thalamus and 48-95% when DBS is implanted in the hippocampus (28). A previous long-term follow-up study investigating the antiseizure effects of deep brain stimulation of the anterior thalamus reported that 13.8% of patients included (4/29) remained seizure-free for at least 12 months within a follow-up period of 11 years (29).

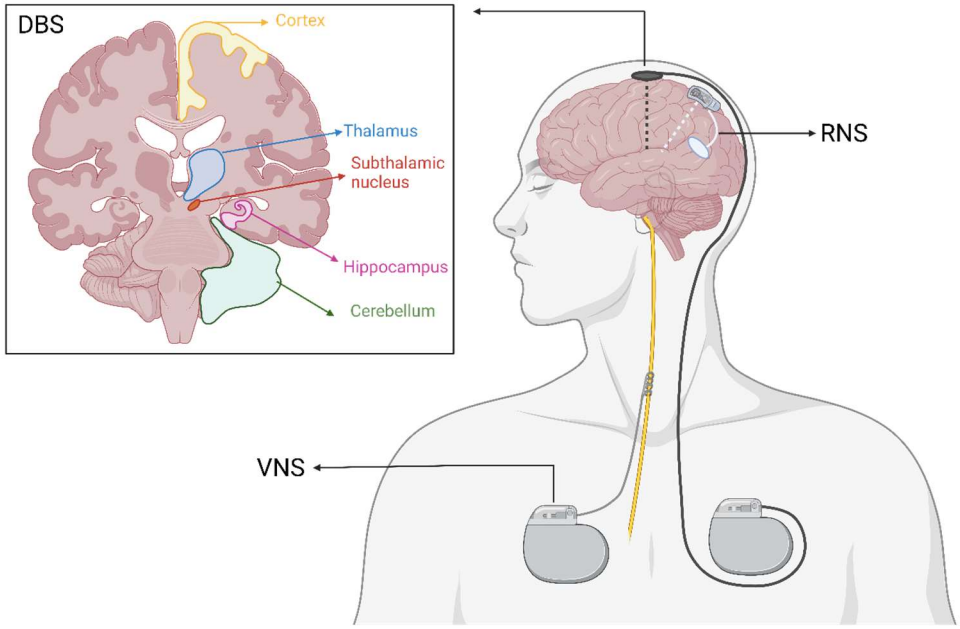

Figure 1.3 – Neurostimulation techniques proposed to patients with Drug-Resistant Epilepsy (DRE). DBS: Deep Brain Stimulation (with the different target sites highlighted in color), RNS: Responsive Neurostimulation, and VNS: Vagus Nerve Stimulation.

5.3 RESPONSIVE NEUROSTIMULATION

RNS is a technique used in drug-resistant focal epilepsy aiming at stimulating a target region in a closed-loop manner when a seizure onset is detected. This technique is proposed for patients with medically intractable focal onset seizures. The electrodes of the RNS are located at the seizure onset zones and can detect and stimulate up to two seizure foci. This device is composed of an IPG implanted within the skull with a craniotomy. The RNS device is composed of cortical strip leads that record the brain activity and one or two subdural depth leads composed of 4 electrodes

each for stimulating the seizure focus. Detection of the seizure onset is based on the identification of specific patterns of electrocorticography that are specific to the epileptic activity of the patient (30). With an acute stimulation of the seizure onset zone, RNS disrupts the synchronous activity and prevents seizure propagation (25). It has also been suggested that acute RNS may lead to a cell membrane hyperpolarization, suppressing the intracellular activity and reducing the ictal activity (25). Chronically, RNS may alter gene expression, resulting in synaptic plasticity, cortical reorganization, or neurogenesis (25). A study that included 150 epileptic patients implanted with an RNS device reported a median seizure reduction of 67%, 75%, and 82% after, respectively, 1, 2, and >3 years of treatment (31). Responder rates (>50% reduction in seizure frequency) were 66%, 77%, and 84% after 1, 2, and 3 or more years of treatment, and 18% of the patients were considered seizure-free at the last follow-up visit (after a mean of 2.3 years of treatment) (31,32). A schematic representation of the RNS device is shown in **Figure 1.3**.

5.4 VAGUS NERVE STIMULATION

As VNS in patients with DRE is the main focus of this thesis, this therapy is described in greater details in the present section.

5.4.1 IMPLANTATION

VNS has been used for over 30 years as an adjunctive treatment for patients with DRE. It consists of a helical electrode implanted around the left vagus nerve, an encapsulated IPG situated under the left clavicula, and a lead wire. Due to the asymmetry in the innervation of the left and right vagus nerves and considering that the right vagus nerve innervates

predominantly the sinoatrial node of the heart, the left side is chosen as the preferred site for VNS implantation. Indeed, a previous study conducted in dogs reported cardiac side effects such as bradycardia or asystole when the device was implanted on the right vagus nerve (33). In children, respiratory difficulties were also reported with an implantation on the right side (34,35).

While the patient is anesthetized in the supine position, an incision is performed at the level of the neck, between the mastoid and the clavicula, from the midline to the medial border of the sternocleidomastoid muscle (35). A second incision is performed at the thoracic level along the anterior axillary line, where a subcutaneous pocket is created by dissecting the tissues composed of subcutaneous fat and muscle. The electrode is placed around the left vagus nerve, and the impedance is checked to ensure good contact with the nerve. A tunneler is then inserted from the thoracic incision to the cervical incision to guide the lead and connect it to the pulse generator. The electrodes and the pulse generator are secured using, respectively, two points on non-resorbable sutures at the deep cervical fascia close to the sternocleidomastoid muscle and non-resorbable sutures to the fascia of the pectoralis muscle (35). Testing of the device is then performed before closing the incision with sutures and staples.

In a recent retrospective multicentric study that included 192 patients aged 2-66 years and implanted with a cervical VNS device, 65.6% of patients became responders (> 50% reduction in seizure frequency), including 4.7% of patients who became seizure-free (36). Although VNS has shown positive effects for all kinds of epilepsies, a better response was observed for tumor-related epilepsies and a worse response for epilepsies linked to vascular malformations and Lennox-Gastaut Syndromes (36). According to a study exploring the side effects in 60 VNS-implanted patients, the most frequent unwanted effects linked to the stimulation are voice alteration and hoarseness (experienced by 55% of patients), followed by headaches (22%), neck pain (17%), coughing (17%), dyspnea (15%),

dysphagia (13%), pharyngitis (13%), dyspepsia (10%), chest pain (7%), nausea (7%), paresthesia (7%), rash (7%), dizziness (5%), insomnia (5%), and cardiovascular palpitations (5%) (37).

5.4.2 TECHNICAL ASPECTS

In the currently available VNS devices, the pulse generator delivers a current at the level of the electrodes, depolarizing the nerve fibers and creating action potentials that travel rostrally and caudally along the nerve. For precision and safety reasons, parametrization of the VNS device is done in terms of current intensity instead of voltage to ensure a correct administration tailored to each patient (38). VNS devices are equipped with an integrated impedance measurement circuit that sends a known electrical signal into the tissues and records the voltage response from the tissue to determine the impedance. Based on the impedance measured, an estimation of the current administered in milliampere (mA) units in a train of stimulations is established. The most recent devices are composed of a pin electrode able to detect changes in heart rate and initiate stimulation to cease seizure propagation. The different stimulation parameters of a VNS device are summarized in **Figure 1.4**. These parameters include:

- **Current intensity**: amplitude of the current delivered to the nerve (expressed in mA)
- **Frequency**: number of pulses administered per second during a block of stimulations (expressed in Hz)
- **Pulse width**: duration of the pulse composing the stimulation train (expressed in µs)
- **ON time**: total duration in seconds of the stimulation period between two non-stimulating epochs where the current is set to 0 mA. **OFF time**: total duration in seconds of the non-stimulating period between two stimulation epochs where the current is set to the clinical intensity of the patient. The ON and OFF times can be

grouped into a metric called "**duty cycle**" that can be computed as (ON time + 4 s)/(ON time + OFF time). In the currently used VNS devices, 2 s ramp-up and 2 s ramp-down periods are programmed at the beginning and end of each stimulation epoch (corresponding to the 4 s in the definition of the duty cycle).

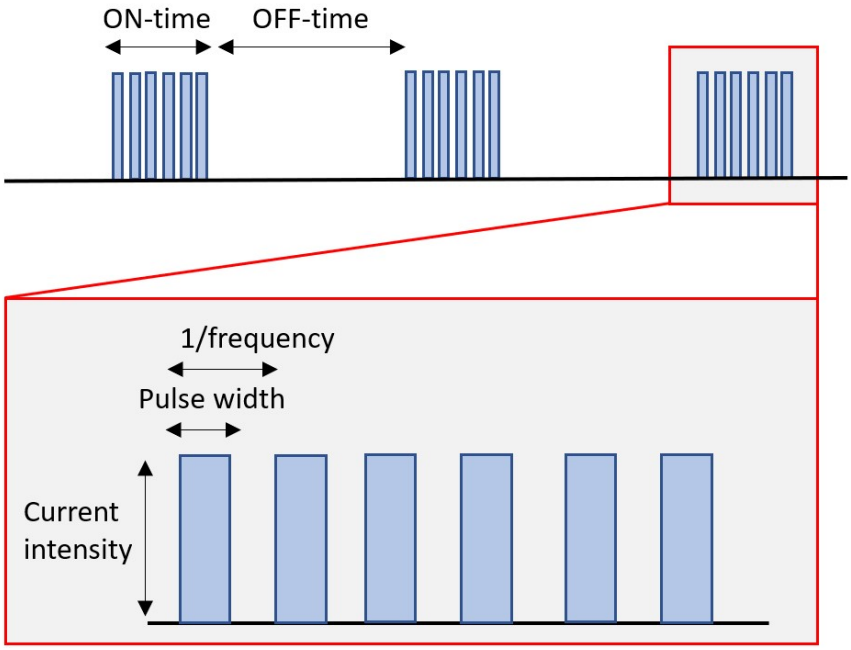

Figure 1.4 – Programmable stimulation parameters in a VNS device.

5.4.3 PHYSIOLOGICAL ASPECTS

5.4.3.1 ANATOMY OF THE VAGUS NERVE

Anatomically, the vagus nerve is the tenth of the cranial nerves and has a mixed composition. It comprises approximately 3/4 of afferent fibers carrying taste, visceral and somatic information to the central nervous

system and 1/4 of efferent fibers, which mainly conduct parasympathetic information to the heart, lungs, gastrointestinal tract, and other intra-abdominal organs but also provide motor innervation to laryngeal muscles (39,40). The composition of the vagus nerve varies across species: it was suggested that the composition of the vagus nerve of pigs is closer to humans in comparison to rats (41–43). In contrast, although the distribution of fiber caliber varies (with a higher percentage of medium-diameter fibers in humans compared to mice and pigs), it was shown that the overall percentage of myelinated fibers in the cervical vagus nerve is comparable between mice, pigs, and humans. At the functional level, it is also worth noting that while fibers with a higher degree of myelinization are activated with a lower electrical current intensity (44), other factors can influence the excitation threshold of the fibers and contribute to interspecies differences. For instance, the fibrous tissues surrounding the vagus nerve are known to increase the current needed to reach the excitation threshold, as well as the electrode design or the position of the implanted electrode used for VNS (43). Therefore, the translation of results between animals and humans is possible but should be done cautiously.

Three types of vagal fibers can be distinguished based on their functional properties: A-fibers (myelinated somatic, both efferent – Aα-, and afferent – Aβ- and Aδ- somatic fibers, 5-20 µm in diameter, stimulation intensity threshold 0.01-0.2 mA), B-fibers (myelinated, mostly efferent visceral, 1-3 µm in diameter, stimulation intensity threshold 0.04-0.6 mA) and C-fibers (unmyelinated, afferent visceral and nociceptive fibers but also preganglionic parasympathetic axons arising from the dorsal motor nucleus and mainly targeting the enteric nervous system (45), 0.4-0.2 µm in diameter, stimulation intensity threshold > 2 mA), which differ in diameter and electrical conductance (44,46–48). While a study hypothesized that maximal electrical stimulation of C-fibers could reduce seizures (49), further studies showed that the destruction of C-fibers with capsaicin did not prevent seizure suppression (50). Moreover, although efforts have been made to characterize fiber activation as a function of different VNS

parameters (51–53), it was suggested that clinically applied VNS parameters do not reach the activation threshold of C-fibers (54). Altogether, these results suggest that only A and B-fibers are effectively recruited during VNS with clinical parameters.

5.4.3.2 Modulation of the norepinephrine system with VNS

5.4.3.2.1 The locus coeruleus: a key relay at the entry of the brain

The nucleus of the solitary tract (NTS), situated in the dorsomedial medulla, is the major sensory nucleus receiving afferences from the vagus nerve (48). The NTS has wide functional efferent projections in the brain: i) within the brainstem, toward the rostral ventromedial medulla, parabrachial nucleus, raphe nuclei, and locus coeruleus (LC); ii) toward ascending structures, such as the amygdala, cerebellum, hypothalamus, and thalamus (55).

Although the LC is a small, lateralized nucleus with a cylindrical shape (~3 mm diameter x ~15 mm height) with only 15.000-20.000 neurons per side in humans, the LC is, by far, the main source of norepinephrine (NE) in the brain (56,57). It is characterized by widely diffused monosynaptic projections to both subcortical and cortical structures. The projections of the LC are small unmyelinated fibers, forming a wide antero-posterior branching network to reach the raphe nuclei, the cerebellum, and almost all areas of the midbrain and forebrain regions with very few exceptions (hypothalamus and striatum) (58). NE released by the LC may exert different effects, mostly depending on the type of receptors that are present on its target neurons (59). However, direct excitation or inhibition does not appear to be the salient characteristics of this noradrenergic pathway: the main effects of the LC-dependent NE appear through the modulation of other inputs to target neurons (60).

Located in the frontal cortex, the orbitofrontal and anterior cingulate cortex drive LC phasic activity in task-related events, through their substantial direct projections to the LC (61). Despite the vast efferent network of the LC, an injection study using tract tracers revealed that mainly two areas constituted the major LC inputs from the brainstem: the nucleus paragigantocellularis, which is part of the ventrolateral rostral medulla and the nucleus prepositus hypoglossi, in the dorsomedial rostral medulla (62). However, other minor inputs to the LC have been identified in the dorsal cap of the paraventricular nucleus of the hypothalamus, the lateral parabrachial nucleus, the spinal lamina X, the preoptic area dorsal to the supraoptic nucleus, the Kölliker-Fuse nucleus and the mesencephalic reticular formation (62,63).

The relay between the NTS and the LC is conducted through two disynaptic pathways: an excitatory pathway (via the nucleus paragigantocellularis) and an inhibitory pathway (via the nucleus prepositus hypoglossi) (48,63–65). The existence of these pathways was demonstrated through anatomical experiments in rats using retrograde tracers unilaterally injected in the LC (57). It was shown that in rats, electrical stimulation of the nucleus paragigantocellularis resulted in a phasic and excitatory response in the LC (64), while electrical stimulation of the nucleus prepositus hypoglossi yielded to the inhibition of spontaneous discharge of LC neurons (64). Additionally, in another electrophysiological study in rats, stimulation of the LC resulted in an antidromic stimulation of the neurons in the nucleus paragigantocellularis and the nucleus prepositus hypoglossi (62). The neuroanatomy of the noradrenergic pathway and the brainstem nuclei involved in the mechanisms of action of VNS are represented in **Figure 1.5**.

It is worth mentioning that other stimulation techniques have been investigated and may activate pathways that are similar to VNS. For example, trigeminal nerve stimulation has shown to reduce pentylenetetrazol-induced seizures in rats and seizure frequency in humans

(66,67). The antiepileptic effects observed with trigeminal nerve stimulation could be linked to the existing connections of the trigeminal mesencephalic nucleus with the NTS, the LC, or the lateral parabrachial nucleus (67–70). Likewise, a study conducted in rats observed anticonvulsants (or proconvulsant effects, depending on the stimulation frequency) with spinal cord stimulation (71). In the field of neuropathic pain, a study conducted with rat-spared nerve injury models observed an increased discharge rate of the LC with spinal cord stimulation in responders to the therapy (72). Although generalizing these results to epilepsy is not straightforward, the increased activity of the LC observed with spinal cord stimulation in a cohort of rats included in the study could suggest a common mechanism of action with VNS.

5.4.3.2.2 Evidence in animals

Based on the widespread connections of the noradrenergic system and the neurochemical properties of NE, VNS was hypothesized to reduce seizure development and trigger plastic changes within the brain, with the LC-NE system standing as the cornerstone of these effects. We will first review the body of evidence from animal studies, pointing at a critical involvement of NE in both the short and long-term antiepileptic effects of VNS. A summary of the results of previous animal studies presented in this section can be found in **Figure 1.5**.

5.4.3.2.2.1 Direct involvement of the locus coeruleus

In 1998, Krahl and colleagues conducted the first study that identified the LC as a key structure involved in the antiepileptic effects of VNS (73). In

this study, the LC of rats were chemically lesioned with bilateral microinfusion of 6-Hydroxy-dopamine hydrobromide (6-OHDA), leading to a significant and chronic NE depletion in cortical areas and the hippocampus, as confirmed *ex vivo* with histological examination of regional brain-dissected samples. This study used the maximal electroshock seizure (MES) model, which is categorized as a model of generalized tonic-clonic seizures that elicits hindlimb extension (HLE) and is often used to test anticonvulsant compounds (74). Using a transcorneal electrode, the MES was generated with a 60 Hz, 125 mA-alternating current delivered for 200 ms. Under active VNS (0.8 mA, 20 Hz, 500 μs pulse width), researchers showed that rats with a lesioned LC showed increased seizure severity compared to animals with an intact LC (73). Similar results were observed when the LC of rats were acutely inactivated by bilateral microinfusion of 1 μL 5% lidocaine hydrochloride into the LC for 2 minutes (73). A histological verification of the injection was conducted after the MES test, and only rats whose cannulas were located within 1 mm of the LC were included in the analyses. Therefore, it was suggested that the LC was involved in the antiepileptic effects of VNS by releasing NE, which reduces seizure susceptibility and severity. This first evidence promoted the research to further characterize the firing of the LC during acute VNS.

Likewise, another study in rats measured the activity of the LC with implanted intracerebral electrodes and revealed a direct modulation of the LC activity during VNS (75). Indeed, an increased discharge rate of the LC was observed with acute VNS (0.3 mA, 20 Hz, 500 μs pulse width) at an intensity known to maximally recruit A-fibers and some B-fibers in rats but not C-fibers (75). The discharge rate of the LC neurons was determined over three post-stimulation epochs of 30 s and was compared to the baseline activity. A statistically significant increase in the firing rate was observed over the third epoch after VNS (75). A similar study exploring firing rates of NE neurons in the LC of healthy rats after short-term (1-h, 1-day, and 3-day) and long-term (14-day, 21-day, and 90-day) VNS treatments revealed an increased firing rate after short-term and long-

term VNS (0.25 mA, 20 Hz, 500 μs pulse width, 30 s ON and 5 min OFF) (76). Finally, a study characterized the LC firing in implanted rats after 14 days and 90 days of VNS (0.25 mA, 20 Hz, 500 μs pulse width, 30 s ON, and 5 min OFF). Compared to control rats that were implanted with a dummy stimulator, the researchers found an increased percentage of NE neurons displaying burst activity, in addition to an increased number of bursts per minute in VNS-implanted rats after 14 days of VNS. The number of spikes per burst was even further increased after 90 days of VNS. It was hypothesized that this increased number of bursts per minute could be explained by a shift in the firing pattern of NE neurons toward burst discharging, therefore releasing a higher level of NE (77).

Further research supported the evidence of the VNS-activation of the LC and NTS. Ten minutes of VNS was shown to increase the presence of the activity-regulated cytoskeleton (Arc) protein, a marker of neural activity, as a result of increased gene transcription in those nuclei following VNS (1 mA, 20 Hz, 500 μs pulse width) (78). In addition, a regional induction of c-Fos, a nuclear protein expressed in highly activated neurons, was also observed in the LC following 3h of VNS administration (1 mA, 30 Hz, 500 μs pulse width, 30 s ON, 5 min OFF), while no expression of c-Fos immunoreactivity was observed in rats with a sham stimulation (79). Finally, an immunochemistry study probed the presence of short- and long-term markers of neuronal activation (c-Fos and ΔFosB, respectively) in rats that received acute (2 h) or chronic (3 weeks) VNS (0.25 mA, 20 Hz, 250 μs pulse width, 30 s ON every 5 min). Acute VNS significantly increased c-Fos in the LC, and chronic VNS led to an increased ΔFosB in the LC (80).

5.4.3.2.2.2 LOCUS COERULEUS-DEPENDENT MODULATION OF THE DORSAL RAPHE NUCLEUS

Neurochemical techniques that used tracers highlighted reciprocal connections between the LC and the Dorsal Raphe Nucleus (DRN), a major serotonin brainstem nucleus (29,63). Serotonin depletion in the brain was shown to lower the threshold of audiogenically (i.e., triggered by an acoustic stimulation), chemically and electrically evoked seizures in rats (81). Compounds that increase the extracellular level of serotonin can inhibit focal (limbic) seizures and generalized seizures (81). It is, therefore, likely that the LC and the DRN interact during VNS to confer the antiepileptic effects.

The basal firing rate of the LC and the DRN were recorded after short-term and long-term VNS (0.25 mA, 20 Hz, 500 μs pulse width, 30 s ON, and 5 min OFF) in healthy rats (76). Although the LC showed an increased firing rate after both short-term and long-term VNS, the firing rate of the DRN only showed a significant increase after long-term VNS. It was, therefore, hypothesized that the LC mediates the activity of serotonergic neurons through α_1-adrenoreceptors. Indeed, by increasing the norepinephrine tone on α_1-adrenoreceptors located on the cell body of serotonergic neurons, the LC can tonically activate serotonergic neurons in the DRN (82). This was the first evidence suggesting that while VNS activates NE neurons first, long-term stimulation can modulate the activation of other types of neurons, such as the serotonergic neurons of the DRN. The dependence of serotonergic DRN neurons on the NE modulation in VNS is further supported by a study that showed a significant increase in DRN-located serotonergic basal firing rate after 14 days of VNS (0.25 mA, 20 Hz, 500 μs pulse width, 30 s ON and 5 min OFF), which was not observed when NE neurons in the LC were priorly lesioned with a selective noradrenergic toxin DSP-4 (77).

Finally, while Cunningham and colleagues showed an increase in c-Fos production in the LC of rats after acute VNS (2h), no increase in c-Fos could be observed in the DRN after short-term VNS (80). However, a significant increase in ΔFosB was observed in both the LC and DRN after chronic VNS

(3 weeks). Therefore, the improved seizure control over time (83) could be explained by a progressive modulation of the DRN neuronal activity by the LC.

5.4.3.2.2.3 NORADRENERGIC MODULATION OF THE CEREBRAL CORTEX: HIPPOCAMPAL EFFECTS

In addition to the DRN, other studies showed that VNS increased the extracellular concentration of NE in several cortical areas (77,84,85) and in the hippocampus (84,86,87), which is part of the limbic system and often typically involved in the most common forms of temporal lobe epilepsy. Interestingly, an intensity-dependent increase in NE concentration following VNS was observed in the hippocampus of healthy rats (84). While an intensity of 0.5–1 mA showed a significant increase of NE concentration in the hippocampus, a significant increase was reached in the cortex following a VNS current intensity of 1 mA only (500 μs pulse width, 20 Hz, 30 s duration). The increased NE concentration was transient and returned to baseline after the stimulation periods ended (84). Moreover, a study that used epifluorescence to image neuronal activity in NE neurons in Thy1-GCaMP6s mice revealed a strong increase in fluorescence in NE axons within the dorsal cerebral cortex during VNS for different stimulation parameters (0.1, 0.4 and 0.8 mA, 30 Hz, 100, 500 and 800 μs applied for 5, 1 and 0.5 s), with larger and longer-lasting effects for higher intensities and longer pulse width stimulations (88).

A study characterizing the role of NE under VNS was further conducted in rats with limbic seizures evoked by intrahippocampal perfusion of the muscarinic agonist pilocarpine via a microdialysis probe (86). This study revealed an increased concentration of extracellular NE in the hippocampus during VNS (1 mA, 30 Hz, 250 μs pulse width, 7s ON and 18 s OFF). Results indicated that an increased hippocampal NE concentration of

at least 70% prevented the development of pilocarpine-induced limbic seizures. Therefore, it is reasonable to assume that a non-negligible increase in NE release (compared to the baseline NE activity) is crucial for observing antiepileptic effects with VNS. Considering that the increase of extracellular NE following VNS administration was not sufficient to prevent limbic seizures in all animals, the question of responsiveness to VNS arises. One could hypothesize that genetic and environmental inter-individual variability leads to differences in the functional or structural integrity of the noradrenergic network, therefore impacting the susceptibility of VNS to modulate the NE release to prevent seizure development. Moreover, this study emphasized the role of hippocampal NE in the antiepileptic effects delivered by VNS by administering a selective α_2-adrenoreceptor antagonist in proximity to the seizure focus. Blocking the α_2-adrenoreceptor in the hippocampus of rats responding to VNS reversed the seizure-suppressing effects (86). Another study used microelectrodes to assess the activation of post-synaptic α_2- and α_1-adrenoreceptors in the hippocampus, as well as the level of extracellular NE in cortical areas after long-term VNS (2 weeks, 0.25 mA, 20 Hz, 500 μs pulse width, 30s ON and 5 min OFF) (87). An increased level of extracellular NE was observed in the prefrontal cortex and, to a lesser extent, in the hippocampus. The results also showed an increased degree of activation of post-synaptic α_2-adrenoreceptors located in a subfield of the Cornu Ammonis (CA3) of the hippocampus following VNS administration, while the degree of activation of α_1-adrenoreceptors remained unaltered.

Finally, an electrophysiological study conducted in healthy rats showed that injection of NE in the pyramidal neurons in the CA3 reduced the firing of hippocampal neurons through the activation of the post-synaptic α_2-adrenoreceptors (89). Together, these findings indicate that the antiepileptic effects of VNS are linked to the release of NE that influences the activation of α_2-adrenoreceptors, reducing the excitability of the hippocampus and decreasing seizure susceptibility.

5.4.3.2.2.4 DOSE-DEPENDENCY OF LOCUS COERULEUS ACTIVATION

Evaluating the activation level of structures involved in the antiepileptic effects of VNS for different stimulation parameters is crucial for developing individual stimulation strategies that maximize the effects of VNS. In this context, while the implication of the LC in the antiepileptic effects of VNS appears as established (76,77), Hulsey and colleagues investigated the neural activity in the LC in response to VNS for different current amplitudes, pulse frequencies, train durations, inter-train intervals and pulse widths (90). Increasing the current intensity and keeping the other stimulation parameters constant led to a proportional significant phasic increase in the activity of the LC in both single-unit and multi-unit recordings over the entire investigated intensity range (0.1 mA – 2.5 mA). Moreover, the latency of the LC firing rate peak was independent of the stimulation intensity, compatible with the neural transmission delay from the vagal trunk to the LC. Longer trains of stimulations elicited, however, longer-lasting phasic responses, with a return to baseline firing levels occurring only after the VNS offset. Since the current intensity of 0.1 mA led to the activation of the LC, it seems that the activation of the LC resulted from the stimulation of A and B-fibers, while C-fibers were not necessary for LC activation (90). Interestingly, a plateau effect tendency was detected in a dog model for intensities beyond 1.2 mA, which corresponds to the intensities saturating A-fibers and B-fibers (91). However, translation of this observed effect to humans requires caution. There may be a close mirroring between A/B-fibers and LC dose-dependency characteristics. Nevertheless, one cannot exclude that the slight increase in LC activity reported with current intensities over the saturation threshold of A and B fibers (90) results from the onset recruitment of C-fibers (51).

In addition to varying the intensity, pulse widths were varied from 30 μs to 500 μs while keeping the current intensity constant at 0.8 mA (90). As

observed for the increasing intensity, a significant increase of neural activity in the LC was observed with an increasing pulse width. Complementary to the intensity and the pulse width, a linear relationship between charge per pulse and LC activity was observed up to 160 nC, where a plateau was then observed.

Finally, in addition to the previous parameters, the stimulation frequency was increased from 7.5 Hz to 120 Hz while other parameters were kept constant. Higher-frequency stimulation yielded a strong but transient activation of the LC, while lower-frequency trains led to a smaller but longer activation. Critically, however, histologic investigations conducted in implanted cats showed that using a stimulation frequency of 50 Hz and above can cause irreversible damage to the nerves with the development of endoneurial edema followed by early axonal degeneration of the large, myelinated fibers (92).

Taking advantage of the fact that variation in pupil diameter is a proxy to both phasic and tonic LC activity (61), studies were conducted in rodents to investigate the influence of different VNS parameters on pupil size (88,93). An increased pupil diameter was observed with increasing current intensity and duration in a dose-dependent manner, with a trend more pronounced when the arousal state of the animals was lower before the stimulation (88). A sigmoid-like relationship was found between pupil dilation and the charge per pulse (93), displaying a tendency toward saturability of pupil dilation at similar intensity ranges (0.7 – 0.9 mA), as shown from LC recordings by Hulsey et al. However, this study did not provide a statistical demonstration of a threshold above which no further pupil dilation occurs. A steeper increase in the pupil response was observed when a higher frequency of stimulation was used (20 Hz > 10 Hz > 5 Hz) (93). These results show that the stimulation frequency may induce cumulative effects, leading to a higher vagal activation when a specific charge per pulse is used. It may be, therefore, important to consider frequency when interpreting VNS experiment results. Moreover, the

frequency could be an important feature for the titration of stimulation parameters. Although other neurotransmission systems are at stake concerning pupil size modulation (particularly the cholinergic transmission), this finding warrants further exploration of parametric VNS-induced pupil dilatations in humans, in whom direct neuronal recordings of the LC are not possible.

Based on the results summarized in this section, it appears that different stimulation parameters could lead to different patterns of NE release with different functional consequences (90). This may be linked to the two disynaptic pathways that exist between the NTS and the LC (48,63–65). Indeed, the activation of the NTS with different stimulation paradigms could involve these pathways differently. Maximizing the activation of the excitatory compared to the inhibitory pathway could optimize the activation of the LC and, therefore, the subsequent release of NE. Moreover, due to inter-subject variability, different patterns of LC activation may be seen even though the same stimulation parameters are used.

5.4.3.2.2.5 EFFECTS ON NEURAL PLASTICITY

In addition to the dose-dependent response to stimulation, studies also supported the long-term neuroplastic effects of VNS. One study investigated how VNS could affect synaptic transmission in the hippocampus and evaluated the implication of the LC and β-adrenergic receptors (78). A recording electrode was placed into the CA3 region, and a stimulation electrode was placed at the perforant path. The electric field of excitatory post-synaptic potentials evoked by a single pulse stimulation of the perforant path was measured in CA3 before and after 10 minutes of VNS (1 mA, 20 Hz, 500 μs pulse width). The results revealed a persistent enhanced synaptic transmission between the perforant path and the CA3

region after VNS administration. The effects were reversed if the LC was electrolytically lesioned and if a β-adrenergic receptor antagonist was injected into the lateral ventricle. These results further emphasize the role of the LC and β-adrenergic receptors in the plasticity triggered by VNS.

Other studies hypothesized that the release of NE in cortical areas and the hippocampus could lead to neuronal plasticity and neurogenesis that may cause long-term seizure-suppressing effects (84,94). VNS was reported to increase the proliferation of progenitors in the hippocampus of adult rats (0.75 mA, 20 Hz, 250 μs pulse width, 30s ON, and 5 min OFF) (94). Moreover, VNS increased the extracellular concentration of NE in the hippocampus (1 mA, 30 Hz, 250 μs pulse width, 7s ON and 18 s OFF) (86), while a higher level of NE was associated with a higher proliferation of neural progenitors in the hippocampus (95,96). Therefore, the increased proliferation of progenitors in the hippocampus following VNS administration may be mediated by hippocampal NE activity (94). Hence, it is tempting to suggest that VNS acts via the LC-NE system to trigger molecular mechanisms in the hippocampus, leading to a tissue reorganization that restores proper cell behaviors and reduces seizure susceptibility.

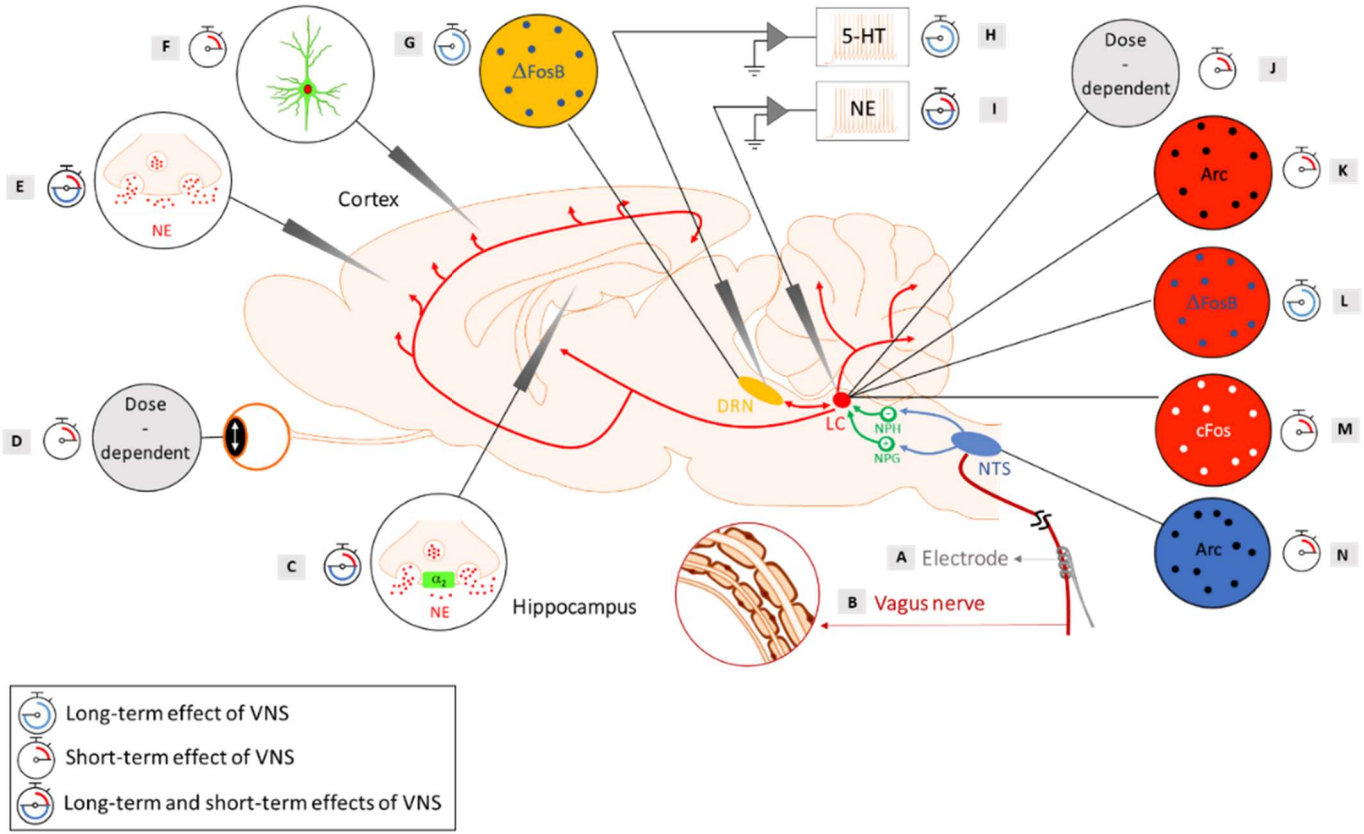
F
G
ΔFosB
5-HT
H
NE
I
Dose
-
dependent
J
E
NE
Cortex
Arc
K
ΔFosB
L
DRN
LC
NPH
NPG
NTS
cFos
M
D
Dose
-
dependent
C
NE
Hippocampus
A
Electrode
B
Vagus nerve
Arc
N
Long-term effect of VNS
Short-term effect of VNS
Long-term and short-term effects of VNS

Figure 1.5 - Evidence of the activation of the noradrenergic system in rats with short-term and long-term cervical VNS, with the neuroanatomy of the brainstem nuclei involved in the mechanisms of action of VNS. Yellow: Dorsal Raphe Nucleus (DRN), red: Locus Coeruleus (LC), green: Nucleus Prepositus Hypoglossi (NPH), an inhibitory input to the LC and the Nucleus Paragigantocellularis (NPG), an excitatory input to the LC, blue: Nucleus Tractus Solitarius (NTS). (A) A helicoidal electrode is wrapped around the vagus nerve and stimulates the nerve. (B) The vagus nerve is composed of three types of fibers: A fibers (large-diameter myelinated), B fibers (small-diameter myelinated), and C fibers (unmyelinated) fibers that have different electrical conductances. (C) An intensity-dependent increase in NE concentration following VNS was observed in the hippocampus of healthy rats for a range of intensities of 0.5–1 mA (20 Hz, 500 µs pulse width, and 30 s duration) (Roosevelt et al., 2006). Another study observed an increased concentration of extracellular NE in the hippocampus following VNS administration (1 mA, 30 Hz, 250 µs pulse width, 7 s ON, and 18 s OFF), with an increase of at least 70% preventing the development of pilocarpine-induced limbic seizures (Raedt et al., 2011). Blocking the α2-adrenoreceptor in the hippocampus of rats responding to VNS reversed the seizure-suppressing effects (Raedt et al., 2011). An increased activation of post-synaptic α2-adrenoreceptors located in a subfield of the Cornu Ammonis (CA3) of the hippocampus was observed after long-term VNS (2 weeks, 0.25 mA, 20 Hz, and 500 µs pulse width) (Manta et al., 2013). A study showed that VNS (1 mA, 20 Hz, and 500 µs pulse width) produced a persistent enhanced synaptic transmission between the perforant path and the CA3 region that was abolished when the LC was lesioned and when a β-adrenergic receptor antagonist was injected in the lateral ventricle (Shen et al., 2012). (D) During stimulation, a sigmoid-like relationship was found between the pupil dilation and the charge per pulse (Mridha et al., 2021). An increased pupil diameter was observed with an increasing current intensity and duration in a dose-dependent manner (Collins et al., 2021). (E) A significantly increased NE was reached in the cortex following VNS with

an intensity of 1 mA (20 Hz, 500 µs pulse width, and 30 s duration) (Roosevelt et al., 2006). Another study observed an increased level of extracellular NE in the prefrontal cortex after long-term VNS (2 weeks, 0.25 mA, 20 Hz, and 500 µs pulse width) (Manta et al., 2013). (F) A study using GCaMP6s imaging in Thy1-GCaMP6s mice revealed an increased fluorescence in NE axons within the dorsal cerebral cortex during VNS, with larger and longer lasting effects for higher intensities and longer pulse width stimulations (Collins et al., 2021). (G) An increase in ΔFosB was observed in the DRN after chronic VNS (3 weeks), but no increase in c-Fos was observed after acute VNS (2 h) in the DRN (0.25 mA, 20 Hz, 250 µs pulse width, 30 s ON, and 5 min OFF) (Cunningham et al., 2008). (H) An increased basal firing rate of the serotonergic neurons in the DRN was observed after long-term (14-, 21-, and 90-day) VNS treatments but not after short-term (1-h, 1-day, and 3-day) VNS treatments (0.25 mA, 20 Hz, 500 µs pulse width, 30 s ON, and 5 min OFF) (Dorr and Debonnel, 2006). Another study showed an increased basal firing rate of the serotonergic neurons in the DRN after 14 days, but the increase was abolished when the LC was lesioned (0.25 mA, 20 Hz, 500 µs pulse width, 30 s ON, and 5 min OFF) (Manta et al., 2009). (I) An increased discharge rate of the LC was observed with acute VNS (0.3 mA, 20 Hz, and 500 µs pulse width) (Groves et al., 2005). An increased firing rate of the LC was found after short-term (1-h, 1-day, and 3-day) and long-term (14-, 21-, and 90-day) VNS treatments (0.25 mA, 20 Hz, 500 µs pulse width, 30 s ON, and 5 min OFF) (Dorr and Debonnel, 2006). An increased percentage of NE neurons displaying bursts and an increased number of bursts per minute were observed in VNS-implanted rats after 14 days of VNS compared to control rats, and the number of spikes per burst was even further increased after 90 days of VNS (0.25 mA, 20 Hz, 500 µs pulse width, 30 s ON, and 5 min OFF) (Manta et al., 2009). (J) A study showed that increasing the current intensity resulted in a shorter latency to the onset of a significant driven activity of the LC. Moreover, a monotonical increase of the neural activity in the LC was observed with increasing the current intensity as well as increasing the

pulse width. Finally, higher-frequency stimulation yielded a strong but transient activation of the LC, while lower-frequency trains led to a smaller but longer activation of the LC (Hulsey et al., 2017). (K) The presence of the Arc protein was found in the LC after 10 min of VNS (1 mA, 20 Hz, 500 µs pulse width) (Shen et al., 2012). (L) A study observed ΔFosB in the LC after chronic VNS (3 weeks) (0.25 mA, 20 Hz, 250 µs pulse width, 30 s ON, and 5 min OFF) (Cunningham et al., 2008). (M) A regional induction of c-Fos in the LC was found after 3 h of VNS (1 mA, 30 Hz, 500 µs pulse width, 30 s ON, and 5 min OFF) (Naritoku et al., 1995). Another study observed c-Fos in the LC after acute VNS (2 h) (0.25 mA, 20 Hz, 250 µs pulse width, 30 s ON, and 5 min OFF) (Cunningham et al., 2008). (N) Arc proteins were observed in the NTS after 10 min of VNS (1 mA, 20 Hz, and 500 µs pulse width) (Shen et al., 2012).

5.4.3.2.3 EVIDENCE IN HUMANS

The number of studies exploring the noradrenergic system in the context of VNS is more limited in humans. This is due to (i) the difficulty in obtaining direct neuroimaging, electrophysiological, or histopathological findings on LC status; (ii) the complexity – involving a lumbar puncture – and non-established reliability of NE assessment from the cerebrospinal fluid (97); (iii) the confounding role of concomitant medications in VNS patients. Nevertheless, several studies were conducted, mostly through neurophysiological measurements that reflected the activation of the LC-NE system and its modulation by VNS. An overview of the biomarkers of short-term and long-term modulation of the LC-NE system with VNS in humans can be found in **Figure 1.6**.

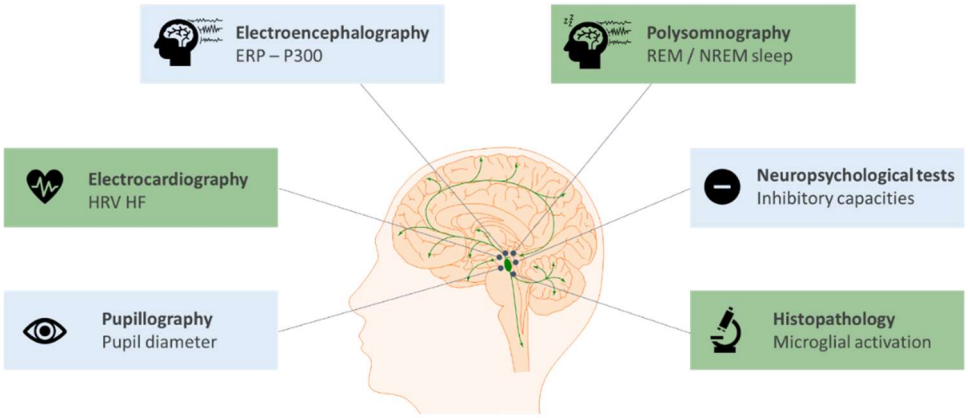

Figure 1.6 – Biomarkers of the short-term (blue) and long-term (green) modulation of the LC-NE system with cervical VNS in humans.

5.4.3.2.3.1 EVENT-RELATED POTENTIAL: P300

The effect of VNS on NE signaling was evaluated with the P300 component of event-related potentials during an oddball task paradigm (98–101). The P300, i.e., a positive EEG deflection reflecting an underlying depolarization around 300 ms post-stimulus, typically over central or parietal midline derivations, can be divided into two sub-components: an early P3a, more pronounced over the anterior regions, and a later P3b, rather detected over centro-posterior areas. The amplitude of the P300, and the P3b in particular, is considered to reflect the phasic activity of the LC-NE system indirectly (98,101). De Taeye and colleagues suggested that the P300 amplitude could be used as a non-invasive biomarker for the therapeutic efficacy of VNS: a significant increase in the P300 amplitude was observed during a VNS ON condition compared to a VNS OFF condition in responders only (98). P300 amplitude could, therefore, constitute an interesting functional biomarker of the difference between responders and non-responders to VNS. However, two other studies did not observe a

modulation of the P300 amplitude with VNS (99,100). This negative finding may be explained by the small number of subjects included (≤ 10 patients) or because responders were not differentiated from non-responders (98).

Another study further evaluated the potential of P300 features recorded during stimulation to correctly classify responders and non-responders (102). In contrast to the study of De Taeye et al. that focused on the parietal midline Pz electrode (98), measurements from 60 electrodes were incorporated (102). Analyses indicated that the P300 amplitude was significantly increased in the Pz channel and the right centro-parietal region in responders to VNS (102). A classification model was built with a cross-validation technique consisting of building a model based on a subset of patients (training set) and testing it on an independent data subset (validation set). While simply using the P300 amplitude measured by the Pz electrode led to a classification accuracy of 61%, summing the P300 amplitude measured by the CP2 electrode (right centro-parietal region) during the "VNS OFF" condition with the P300 amplitude measured by the PO5 channel (left parieto-occipital region) during the "VNS ON" condition led to a classification accuracy of 94%. However, further research is needed to determine whether the signals measured from the non-midline electrodes arise from the P300 wave or from other signals that could differ between responders and non-responders. Recently, a prospective study was conducted to measure the P3b amplitude of patients before the initiation of their treatment and after 1 year of VNS treatment (103). The P3b was observed using a three-stimuli oddball task, including not only a rare target and a frequent distractor stimulus but also a rare non-target stimulus (101). Compared to non-responders, patients who became VNS-responsive showed a significantly lower baseline P3b amplitude in the VNS OFF condition during the oddball task (103). A lower baseline P3b amplitude has been associated with a lower baseline activity of the LC-NE system, potentially implying that responders to VNS present a lower baseline NE reactivity compared to non-

responders (103), allowing a greater relative increase of NE following VNS treatment.

5.4.3.2.3.2 PUPIL DIAMETER

As in animals, pupil diameter is tightly associated with both phasic and tonic activity of the LC (104). A functional magnetic resonance imaging study indicated that the pupil diameter was positively correlated to the activity of the LC at rest and during an oddball task (105). Based on these observations, a study was conducted to evaluate how VNS may affect pupil diameter in patients with refractory epilepsy at rest and during the light reflex condition (i.e., when light stimuli were presented to evaluate whether the pupil light reflex was modified when VNS was administered) (106). A significant increase in resting pupil diameter was observed in the VNS ON condition compared to the VNS OFF condition, suggesting the influence of acute VNS toward an increased tonic LC activity. However, the time course of the pupil response compared to stimulus onset was not evaluated in the study, and this precludes from establishing whether a VNS-evoked acute response exists or not. Furthermore, no correlation with clinical response was found, nor any significant difference in the reactivity of the pupil during the light reflex conditions between VNS ON and VNS OFF conditions (106).

5.4.3.2.3.3 NEUROPSYCHOLOGICAL MARKERS: RESPONSE INHIBITION

In addition to the P300 event-related potential and the pupil diameter, the effects of VNS in response inhibition were also studied. Although the neurobiological processes involved in response inhibition are not totally elucidated yet, it was suggested that the noradrenergic system has a critical role. Indeed, the phasic activation of the LC-NE system facilitates responses to task-relevant processes (61) and is, therefore, expected to be

involved in response inhibition (107). Moreover, it was shown that acute systemic administration of atomoxetine, a NE reuptake inhibitor that rapidly increases the concentration of NE in the prefrontal cortex, leads to an increased response inhibition in rats and humans (108,109).

One study determined how VNS may influence response inhibition in a stop signal task, with the time needed for the epileptic patient to inhibit a response measured in both VNS ON and OFF conditions to compute the inhibition gain (110). VNS decreased the time needed to inhibit a response, and this effect was correlated to the clinical benefit of VNS. In addition, the P300 was also measured, as this may also reflect the response inhibition (111–113). P300 amplitudes during response inhibition were larger during VNS but were independent of the clinical efficacy of VNS. Therefore, it was hypothesized that even if VNS does not reduce seizure frequency in all patients, it could still influence neurobiological processes, such as NE transmission, without reaching clinical benefits (110).

Concerning inhibitory capacities, another study used the Eriksen Flanker test in epileptic patients with stimulation ON and OFF to measure their ability to suppress irrelevant information (114). In the Eriksen Flanker test, participants must assess the congruency of a central target (usually arrows or letters) according to their surrounding distractors. In line with previous results (110), this study showed an increased ability to suppress irrelevant information during stimulation in VNS-responders only. It is worth noting that the initial reaction time of responders in the VNS OFF condition was higher than non-responders. This slow reaction time in responders could be interpreted as a reduced NE reactivity when no stimulation is administered, which is restored in the VNS ON condition (114). These results bring new evidence of differential modulation of the norepinephrine system with VNS between individuals.

5.4.3.2.3.4 SLEEP PHYSIOLOGY

When investigating biomarkers of the effects of VNS on the LC-NE system, research has also focused on sleep characteristics. As part of the ascending activating system, the LC promotes wakefulness and needs to be partly silenced for sleep initiation. Further silencing is required to go from slow-wave sleep to Rapid-Eye Movement (REM), during which LC neurons are fully silent (115). Increases of noradrenergic signaling in the brain, such as those induced by antidepressants and mono-oxidase inhibitors, were proven to reduce REM sleep prevalence and lead to more non-REM sleep and wakefulness (116). A study investigated sleep parameters of patients with refractory epilepsy at baseline and after chronic VNS to determine whether VNS induces changes in their sleep structures (117). After chronic VNS, decreased REM sleep in implanted patients was reported (117). In addition, it was shown that VNS shortened overall nocturnal sleep duration with increased wakefulness during both the night and the day, with no apparent impact on daytime sleepiness (117). Furthermore, a reduced number of (REM) sleep episodes and duration were observed in patients with refractory epilepsy who are implanted with a VNS device (117). Therefore, one could hypothesize that VNS increases the activity of NE neurons in the LC, which leads to a reduction of REM sleep and promotes wakefulness in implanted patients. However, it should be pointed out that many factors can also influence REM sleep (e.g., medications, co-morbid depression, sleep habits, etc.). For example, some patients in this study received pharmacologic polytherapy, including carbamazepine, an antiepileptic drug that has been associated with decreased REM sleep (118,119). In children with refractory epilepsy, another study reported a significant increase in deep, slow wave sleep (non-REM 3 sleep stage) and non-REM 1 sleep stage (in percentage and duration), as well as a reduced sleep latency after 9 months of VNS compared to baseline (120). Finally, in a prospective study conducted by Hödl and colleagues, responders to VNS showed significantly higher non-REM 3 sleep compared to non-responders

before the initiation of their treatment (103). These results could reflect variability in the LC-NE system of patients with refractory epilepsy.

5.4.3.2.3.5 HEART RATE VARIABILITY

In order to find biomarkers that could refine the selection of responders to VNS, a prospective study also measured the heart rate variability (HRV) at baseline and after 1 year of VNS treatment (103). The high-frequency power of the HRV (HRV HF) reflects the parasympathetic activity and is calculated based on the fluctuation of the time between adjacent heartbeats (121,122). VNS responders showed significantly lower HRV HF compared to non-responders at baseline and after 1 year of VNS treatment. While a lower HRV HF might be associated with a higher sympathetic LC-related activity, it was suggested that a more complex network connectivity pattern recruiting other structures of the vagal afferent network could be involved (103). However, these results also suggest that a variation in the vagal afferent network exists between individuals, which could relate to the different responsiveness to VNS in patients with refractory epilepsy.

A study used machine learning to build prediction models for evaluating responsiveness to VNS therapy preoperatively based on HRV indices in wake and sleep states (123). Fifty-two HRV indices were evaluated in 30 responders and 29 non-responders before the implantation of a VNS device. After feature selection, the best outcome prediction was observed when assessing HRV indices during sleep compared to the waking state. Indeed, the model built using a univariate filtering method for feature selection of sleep indices reached an accuracy of 74.6%, while the best model in the wake state reached an accuracy of 68.8%. The HRV HF index was ranked fourth best predictor index in the sleep state and third best predictor index in the wake state.

5.4.3.2.3.6 HISTOPATHOLOGY

While immunochemistry studies evaluating the effects of VNS on the vagal afferent network in humans are scarce due to the limited number of samples available, a first study was recently conducted with the aim of extracting morphological characteristics of the nuclei linked to this network after chronic VNS (124). Neuronal cell number, astrogliosis, and microglial activation in the LC, the NTS, and the rostral pontine group of raphe nuclei were assessed in four autopsy cases with a history of refractory epilepsy treated with VNS and four chronic epilepsy cases without VNS treatment. A trend toward a decreased microglial activation was observed in the left LC (stimulated side) compared to the right LC in VNS cases. A similar trend was observed between the left LC of VNS cases and the left LC of non-VNS cases. Results were not statistically significant but could suggest a slightly decreased neuroinflammation in the LC with long-term VNS. No difference in the neuronal cell number and the number of astrocytes was observed in these nuclei. Further studies using other labels of neuronal activation and neurotransmitter concentrations could further characterize the plastic effects of long-term VNS (124).

5.4.3.2.3.7 TRANSCUTANEOUS VNS

Besides the clinically approved cervical VNS, an emerging approach to stimulate the vagus nerve non-invasively consists of the so-called transcutaneous VNS (tVNS). This non-invasive method uses a surface-electrode to stimulate the cymba conchae (i.e., inner part of the auricle, innervated by the auricular branch of the vagus nerve) (125) believed to share common patterns of brain activation with cervical VNS (126). Recent studies used psychophysiological and biological indices to provide evidence of the activation of the noradrenergic system with tVNS. Indeed, a

functional magnetic resonance imaging study showed that stimulation of the cymba conchae resulted in the activation of regions of the vagal afferent network (e.g., ipsilateral NTS, bilateral spinal trigeminal nucleus, DRN, LC, contralateral parabrachial area, amygdala, and nucleus accumbens) compared to a sham stimulation applied on the earlobe (126). A randomized, double-blind, controlled trial was conducted to assess the efficacy and safety of tVNS (127). A significant reduction in seizure frequency was observed in the tVNS group (n = 39, 25 Hz, 0.5 ± 0.47 mA, 250 μs pulse width, 30s ON, 30s OFF) after 20 weeks of tVNS therapy, which was not observed in the control group (n = 37, 1 Hz, 1.02 ± 0.83 mA, 250 μs pulse width, 30s ON and 30s OFF), while the responder rates were similar between the two groups. One recent study reported a robust tVNS-evoked pupillary dilation in healthy volunteers that was not observed under sham stimulation on the earlobe (128). In contrast, other studies did not report differences in pupil size between the tVNS ON and tVNS OFF conditions at rest and during an oddball task (129,130). Discrepancies may be partially explained by the different methodologies adopted or the different stimulation paradigms used. Indeed, Sharon and colleagues observed a pupil dilation during a task-free resting condition with short tVNS pulses (duration of 3.2 seconds) and a variable, subject-dependent maximal current intensity below the pain threshold (mean intensity of 2.2 ± 0.24 mA) (128). By contrast, the two studies that failed to observe an increased pupil diameter during stimulation used longer 30-second stimulations in healthy subjects during an oddball task with stimulation of 3 mA (25 Hz, 200 μs pulse width) (130) or 0.5 mA (25 Hz, 200-300 μs pulse width) (129) that was constant across subjects. These findings may suggest a higher impact of tVNS on the phasic LC activation (evoked by short stimulation trains) rather than on the modulation of its tonic activity, which would have been mirrored in mean pupil size differences between tVNS ON and tVNS OFF conditions, and preferentially induced by longer tVNS trains.

Another study measured the level of NE released with tVNS by means of hormonal indices such as salivary alpha-amylase and salivary cortisol

(129). Salivary alpha-amylase is a digestive enzyme known to be associated with the activity of the LC-NE system (129). The presence of this enzyme, as well as the presence of salivary cortisol, an arousal-related stress hormone, were suggested to be markers of central NE activity (131–133). Interestingly, an increased salivary alpha-amylase was observed when tVNS was used during an oddball task (129), which did not occur when a sham stimulation to the earlobe was used. Finally, in the sham condition, salivary cortisol seemed to decrease with time during the set of stimuli-discrimination tasks. It was suggested that this overall decrease in cortisol secretion could be the reflection of the mental fatigue of the participants, the activities carried out during the experiments, and other factors (129). However, when tVNS was used, this tendency of decreased salivary cortisol was abolished.

Further research is needed to establish a classification model that intends to predict responsiveness to cervical VNS based on non-invasive markers of the activity of the noradrenergic system when tVNS is delivered. If such a model reaches a high accuracy, tVNS could be an exciting avenue for assessing responsiveness to invasive VNS before the implantation of a neurostimulator and, therefore, identify more selectively VNS responders to avoid unnecessary surgery and possibly related complications.

5.4.4 ORIGINAL CONTRIBUTION

Part of the introduction (*section 5.4.3 – Physiological aspects*) was described in a review paper published as part of this thesis.

How is the norepinephrine system involved in the antiepileptic effects of vagus nerve stimulation ? **A. Berger**, S. Vespa, L. Dricot, M. Dumoulin, E. Iachim, P. Doguet, G. Vandewalle, R. El Tahry. *Frontiers in neuroscience 15:790943, 2021. doi: 10.3389/fnins.2021.790943.*

6. IMAGING AND NEUROPHYSIOLOGICAL TECHNIQUES

6.1 MAGNETIC RESONANCE IMAGING

6.1.1 GENERALITIES

MRI is a non-invasive and non-radiating imaging technique, allowing to obtain high-resolution images of an array of soft tissues and other human body parts, including the brain, spinal cord, muscles, heart, abdominal organs, blood vessels, bones, lungs, or limbs.

Given the abundant water content in the human body, the principle of MRI resides in the nuclear properties of hydrogen atoms (or protons - ^{1}H). Using a strong magnetic field, the MRI system is able to align the nuclear spins of the hydrogen atoms (i.e., an intrinsic property of the atoms corresponding to the intrinsic angular momentum of the nucleus) in the direction of the external magnetic field – or the opposite direction to a lower extent, resulting in a macroscopic magnetization of the tissues in the direction of the external magnetic field. Magnetic gradients excite a specific slice of the brain and encode spatial information by locally altering the magnetic field experienced by the hydrogen atoms. Radiofrequency (RF) pulses are used to excite the atoms and tilt the resulting macroscopic magnetization away from the direction of the external magnetic field. After applying the RF pulse, the magnetization tends to return to equilibrium by a phenomenon called “relaxation”. The relaxation signal that contains spatial and biological information about the types of tissues is measured using a receiving coil based on the principle that the varying transverse magnetization induces a sinusoidal current in the coil. Finally, the procedure is iterated across numerous slices to reconstruct the entire volume of the brain.

Different types of MRI sequences exist and can be used depending on the process or structure to be studied. Each sequence is defined by specific parameters such as the timing between successive RF pulses, the duration of the RF pulse - that determines the tilt angle of the macroscopic magnetization, and the strength or direction of the gradients applied. The most common structural images are obtained with a T1-sequence, which creates an image based on the relaxation of longitudinal macroscopic magnetization, or “spin-lattice” relaxation. The image obtained contains high anatomical details with a good contrast between the brain's white matter, gray matter, and cerebrospinal fluid (CSF). T1-weighted images are often used to identify lesions in the brain. A T2-weighted sequence allows the reconstruction of an image that represents the relaxation of the transverse macroscopic magnetization (or “spin-spin” relaxation) and provides valuable insight for identifying a tumor, inflammation, or edema.

6.1.2 FUNCTIONAL MAGNETIC RESONANCE IMAGING

Functional MRI (fMRI) is a technique used to study the activation of brain areas during a task or at rest. FMRI is a dynamic acquisition, in the sense that multiple brain volumes are acquired during a specific period of time lasting the duration of the task, in the case of a task-based paradigm. The images acquired have a T2* contrast, i.e., a T2 contrast accounting for inhomogeneities in the magnetic field due to susceptibility effects and the presence of paramagnetic substances.

The T2* contrast captures changes in oxygen concentration in the blood in brain areas that are activated during a task. Indeed, when neurons in a specific brain area are firing, an increased flow of oxygenated blood occurs to ensure a sufficient supply of oxygen and nutrients (e.g., glucose) to meet the energy demands that are necessary for the intended brain activity. The relationship between increased activity of neurons in a specific

area leading to an increased oxyhemoglobin concentration and a decreased deoxyhemoglobin concentration is known as “neurovascular coupling”. The neurovascular coupling is represented in **Figure 1.7**.

When brain areas are activated, the over-representation of oxyhemoglobin locally influences the magnetic field due to the paramagnetic properties of oxygen. This local change is reflected in an increased T2* relaxation in brain-activated regions. This local increased T2* is reflected by a brighter signal in the images acquired, and is known as the Blood Oxygenation Level Dependent (BOLD) signal. During the analysis of fMRI data, the intensity of each voxel is evaluated over the course of the experiment. The Hemodynamic Response Function (HRF) is commonly used to model the BOLD signal and fit the time series of every voxel (i.e., a three-dimensional volume element of the tissue being imaged). The commonly used HRF function consists of a Gamma distribution composed of (**Figure 1.7**):

- *An initial dip*: reflecting the initial oxygen consumption in the activated area before observing the increased flow of oxygenated blood.
- *A rising phase*: reflecting the increased blood flow of oxygenated blood to supply the required oxygen and nutrients and meet the metabolic demand.
- *A falling phase*: reflecting a return to the baseline blood flow and oxygenation level.
- *An undershoot*: reflecting the imbalance and regulation of the blood flow.

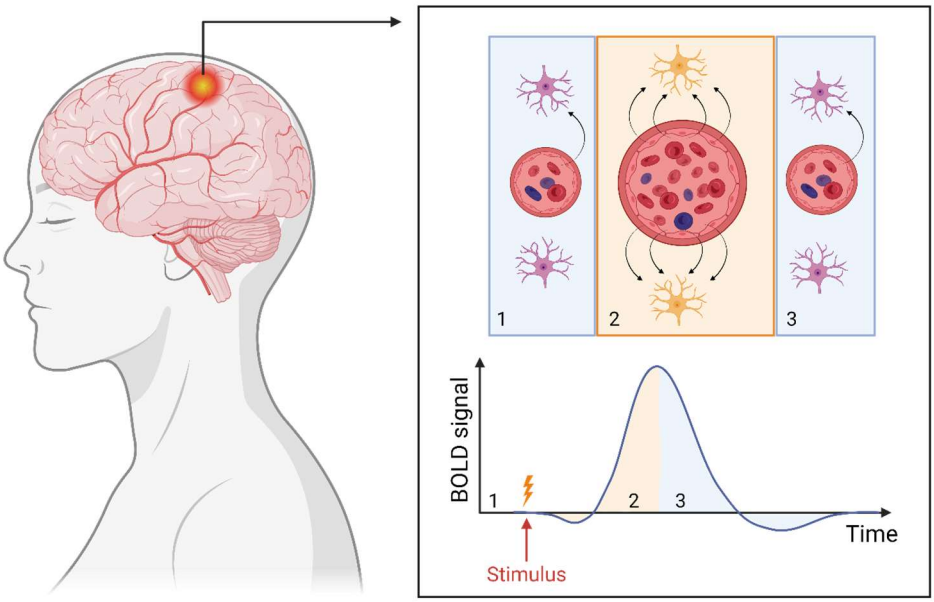

Figure 1.7 – Principles of functional MRI (fMRI). (1) Brain activity at rest is characterized by a regular and controlled consumption of nutrients by the neurons. (2) Increased flow of oxygenated blood following an increased activity of neurons in a specific brain region, reflected in the rising phase of the BOLD signal. (3) Return to a baseline activity with an undershoot reflecting the imbalance and regulation of blood flow.

6.1.3 DIFFUSION MAGNETIC RESONANCE IMAGING

Water molecules within the tissues experience a Brownian motion - a random movement of the molecules due to their thermal energy. A Pulsed Gradient Spin Echo (PGSE) sequence is used to extract the diffusion characteristics of these molecules by applying two diffusion-sensitizing gradients. The first diffusion gradient dephases the spins proportionally to their position as they will experience a different magnitude of the magnetic field while the second gradient has a rephasing role. By extracting the

phase and magnitude of the signal measured, one can obtain characteristics about the diffusion of the water molecules within the brain. The signal measured is the attenuation of the T2* signal and is specific to the microstructure of the tissues. The PGSE sequence is characterized by a b-value expressed in s/mm^2 that reflects the degree of diffusion applied with the diffusion-sensitizing gradients. The b-value is defined as:

$$b_{PGSE} = (\gamma G \delta)^2 \left(\Delta - \frac{\delta}{3}\right)$$

Where:

- γ is the gyromagnetic ratio (42.57 $MHz \cdot T^{-1}$ for ^1H).
- G is the amplitude of the diffusion gradients (expressed in $T \cdot m^{-1}$).
- δ is the duration of the diffusion gradients (expressed in s).
- Δ is the time between the dephasing and rephasing gradients (expressed in s).

For high b-values, the diffusion in the CSF is high leading to a large reduction in the signal being measured, making the CSF to appear dark on the diffusion images acquired with such a b-value. Since diffusion in the CSF is highly isotropic, a large diffusion will occur in the CSF independently on the direction of the diffusion-sensitizing gradients being applied. However, the diffusion in the white matter is highly anisotropic compared to the CSF. When the diffusion-sensitizing gradient is applied in the direction of the white matter fibers, an important diffusion occurs due to the unrestricted nature of the diffusion along the tracts. Conversely, when the gradient is applied perpendicularly to the direction of the fibers, the diffusion of the water molecules is highly restricted. Therefore, the signal measured contains microstructural information about the brain tissues and is dependent on the magnitude of the diffusion-sensitizing gradients and the direction of the gradients.

6.1.3.1 DIFFUSION TENSOR IMAGING

Based on the diffusion data, models were built to extract structural information from the tissues being imaged. DTI estimates the three-dimensional diffusion of water molecules that can be represented by a 3x3 symmetrical tensor by repeating the PGSE sequence using different orientations of the diffusion-sensitizing gradients. The 3x3 symmetrical tensor can be expressed as:

$$D = \begin{pmatrix} D_{xx} & D_{xy} & D_{xz} \\ D_{yx} & D_{yy} & D_{yz} \\ D_{zx} & D_{zy} & D_{zz} \end{pmatrix}$$

Diagonalization of the tensor leads to a matrix composed of 3 eigenvectors (λ_1, λ_2, λ_3) on the diagonal and zeroes for the off-diagonal entries:

$$D = X\Lambda X^{-1}$$

$$\Lambda = \begin{pmatrix} \lambda_1 & 0 & 0 \\ 0 & \lambda_2 & 0 \\ 0 & 0 & \lambda_3 \end{pmatrix}$$

Based on the diagonalized tensor, DTI metrics can be estimated and are defined as:

- *Axial Diffusivity (AD)*: characterized by λ_1, this metric represents the rate of diffusion of the water molecules along the preferential diffusion direction (expressed in $mm^2 \cdot s^{-1}$). In the case of a theoretically perfect isotropic diffusion, $\lambda_1 = \lambda_2 = \lambda_3$.
- *Radial Diffusivity (RD)*: computed as $(\lambda_2 + \lambda_3)/2$, this metric represents the rate of diffusion perpendicularly to the preferential direction of diffusion (expressed in $mm^2 \cdot s^{-1}$).
- *Mean Diffusivity (MD)*: computed as $(\lambda_1 + \lambda_2 + \lambda_3)/3$, this metric represents the overall rate of diffusion of the water molecules regardless of the direction of diffusion (expressed in $mm^2 \cdot s^{-1}$).

- *Fractional Anisotropy (FA)*: computed as $\sqrt{\frac{3}{2}}\frac{\sqrt{(\lambda 1-MD)^2+(\lambda 2-MD)^2+(\lambda 3-MD)^2}}{\sqrt{\lambda 1^2+\lambda 2^2+\lambda 3^2}}$, this metric represents the extent to which water molecules are constraint in space, considering all directions of diffusion (no unit).

As mentioned before, diffusion in the white matter is highly anisotropic. It can be represented by an ellipsoid tensor reflecting a preferential direction of diffusion. In contrast, diffusion in the CSF is highly isotropic (unrestricted) and can be represented by a spherical tensor (**Figure 1.8**).

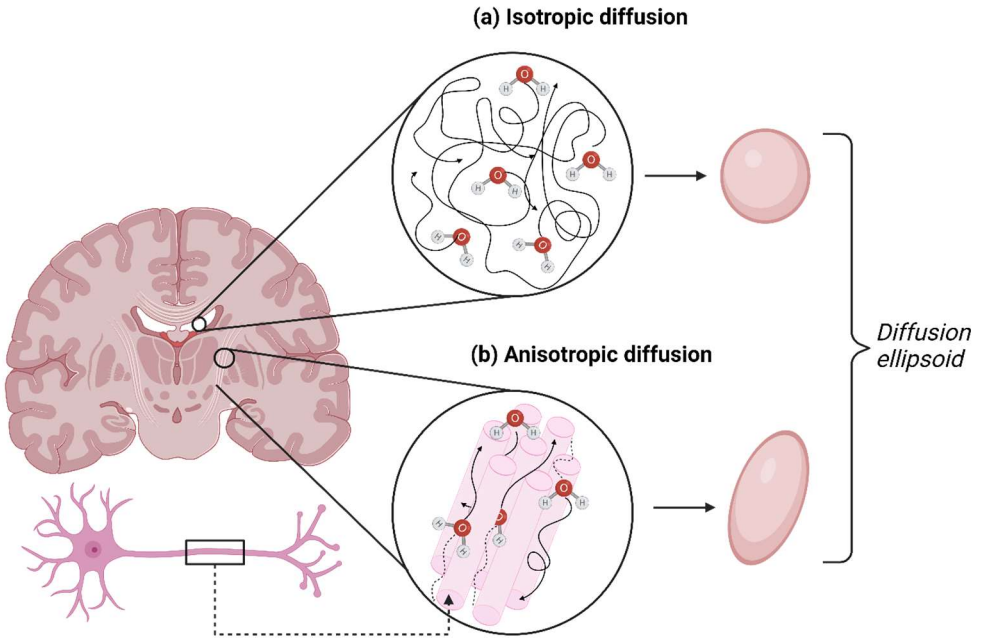

Figure 1.8 – Schematic representation of the diffusion of water molecules in (a) the CSF where the diffusion is isotropic, leading to an estimated spherical tensor, and (b) the white matter, a highly anisotropic medium due

to the restricted diffusion along the axons, leading to an estimated tensor represented by an ellipsoid with a preferential direction of diffusion.

6.1.3.2 Neurite Orientation Dispersion and Density Imaging

Neurite Orientation Dispersion and Density Imaging (NODDI) is a microstructural imaging technique where different compartments are considered, including non-tissue (i.e., CSF) and tissue (i.e., gray matter and white matter) compartments. The tissue compartment is further divided into intra-neurite (space bounded by the cellular membrane of the axons or the dendrites) and extra-neurite (space around the cellular membrane) compartments (134,135). The decomposition of the diffusion MRI signal is shown in **Figure 1.9**.

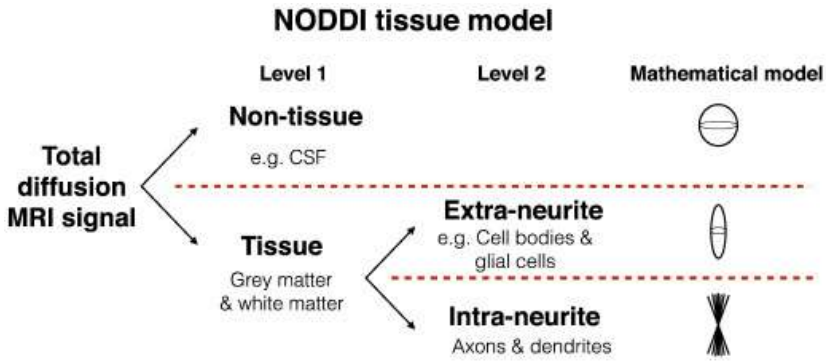

Figure 1.9 – Decomposition of the diffusion MRI signal into different compartments with the Neurite Orientation Dispersion and Density Imaging (NODDI) tissue model.

The total diffusion signal measured arises from a combination of independent compartments. Therefore, the total normalized diffusion signal *S* can be decomposed as (135):

$$\mathrm{S} = (1 - \upsilon_{\mathrm{iso}})(\nu_{\mathrm{ic}}\,\mathrm{A}_{\mathrm{ic}} + (1 - \nu_{\mathrm{ic}})\mathrm{A}_{\mathrm{ec}}) + \nu_{\mathrm{iso}}\mathrm{A}_{\mathrm{iso}}$$

Where:

- v_{iso} is the volume fraction of the isotropic compartment (CSF).
- v_{ic} is the volume fraction of the intracellular compartment (or the Neurite Density Index – NDI).
- v_{ec} is the volume fraction of the extra-cellular compartment.
- A_{iso} is the normalized signal of the isotropic compartment (CSF).
- A_{ic} is the normalized signal of the intracellular compartment.
- A_{ec} is the normalized signal of the extra-cellular compartment.

A different mathematical expression models the signal arising from each compartment. The intracellular compartment is modeled by cylinders with zero radii, representing the highly restricted diffusion perpendicularly to the axons but not in the direction of the axons (134,135). The signal arising from this compartment is expressed as (for axons with an orientation 'n' and a magnetic gradient 'g' applied):

$$A_{ic1} = e^{-b_{\parallel} d_{i,\parallel}} = e^{-|\hat{g}\cdot\hat{n}|\,(\gamma\delta G)^2\left(\Delta-\frac{\delta}{3}\right) d_{i,\parallel}}$$

Where:

- $d_{i,\parallel}$ is the axial diffusivity along the axons, in the intra-neurite space.

Integration over all possible orientations of the sticks leads to the expression:

$$A_{ic} = \int f(\boldsymbol{n})\, s^{-b d_{i,\parallel}(\boldsymbol{g}\cdot\boldsymbol{n})^2} d\boldsymbol{n}$$

With:

$$f(n) = M\left(\frac{1}{2}, \frac{3}{2}, \kappa\right)^{-1} e^{\kappa(\boldsymbol{\mu} \cdot \boldsymbol{n})^2}$$

Where:

- *f(n)* is the orientation distribution based on the Watson distribution that describes a spherical distribution of the sticks that is characterized by μ (the principal orientation of the Watson distribution), and κ (the concentration parameter measuring the extent of orientation dispersion around the principal direction of orientation).
- *M* is the confluent hypergeometric function (or the Kummer's function).

The signal from the extracellular compartment is characterized by the mathematical expression:

$$A_{ec} = e^{-bg^T(\int f(\boldsymbol{n})\, D(\boldsymbol{n})\, d\boldsymbol{n})\, \boldsymbol{g}}$$

Where:

- *D(n)* expresses a tensor with '*n*' as the principal direction of diffusion and characterized by an axial diffusivity ($d_{e,\parallel}$) hypothesized to be equal to the axial diffusivity of the intra-neurite compartment $d_{i,\parallel}$.

Finally, the mathematical expression that models the isotropic diffusion is:

$$A_{iso} = e^{-bd_{iso}}$$

In this model, some assumptions are made, and parameters are fixed a priori based on typical *in vivo* values (136):

- $d_{iso} = 3 * 10^{-3}$ [mm^{2}s^{-1}]

- $d_{e,\parallel} = d_{i,\parallel} = 1.7 * 10^{-3}$ [mm^2s^{-1}]
- $d_{e,\perp} = d_{e,\parallel}\,(1 - v_{ic})$, according to the tortuosity model.

The diffusion metrics estimated by the model include the NDI (as mentioned before) and the Orientation Dispersion Index (ODI), defined as:

$$ODI = \frac{2}{\pi} \arctan\,(1/\kappa)$$

Based on the estimation of these metrics, it is hypothesized that a higher ODI represents highly dispersed neurites, while a lower value will be found in highly aligned axons (134,135). One of the main limitations of the model is that it considers only one type of fibers represented by axons of zero radii without characterizing each crossing fascicle independently. Moreover, fixing some parameters a priori remains a limitation as these parameters may vary in different brain regions and/or across individuals, especially in patients presenting a neurologic disorder. However, this model remains very powerful as multiple compartments are modeled individually in opposition to DTI, which only estimates a single tensor for characterizing the diffusion in each voxel.

6.1.3.3 Microstructure Fingerprinting

Microstructure Fingerprinting (MF) is a multi-compartment model based on Monte Carlo simulations of the diffusion of water molecules (137). This model is based on the superposition principle that assumes that the signal measured in a voxel arises from disjoint and independent structures. This means that it is hypothesized that no exchange of water occurs between the fascicles during the acquisitions. Following this principle, the signal arising from a voxel where K fascicles are crossing, and a partial CSF volume is present can be decomposed as (137):

$$S = M_0 \cdot \left[\sum_{k=1}^{K} v_k A_{fasc}(\boldsymbol{\Omega}_k, \mathbf{T}_k, \mathbf{u}_k ; \boldsymbol{g}) + v_{CSF} A_{CSF}(\mathrm{D}_{CSF}, \mathbf{T}_{CSF} ; \boldsymbol{g}) \right]$$

$$= \sum_{k=1}^{K} w_k A_k + w_{CSF} A_{CSF}$$

Where:

- M_0 is the net initial magnetization of the signal within the voxel.
- w_k is the weight (contribution) of the apparent signal of the k-th fascicle and is equal to $M_0 v_k$.
- $A_k = A_{fasc}(\boldsymbol{\Omega}_k, \mathbf{T}_k, \mathbf{u}_k; \mathbf{g})$ is the normalized diffusion-weighted MRI signal of the k-th fascicle, modeled by Monte Carlo simulation of the random self-diffusion of molecules in an environment characterized by the microstructural properties $\boldsymbol{\Omega}_k$ (with the axons being represented by hexagonal packing of cylinders), with $\mathbf{u}_k$ representing the orientation of the k-th fascicle and $\mathbf{T}_k$ capturing the relaxation properties of the tissue (such as T1, T2, and proton density).
- $v_k = \frac{w_k}{\sum_{i=1}^{K+1} w_i}$ is the fraction of the physical volume of the voxel occupied by the k-th fascicle. Correspondingly, v_{CSF} is the fraction occupied by the CSF, such that $v_1 + \ldots + v_K + v_{CSF} = 1$.
- D_{CSF} is the diffusivity in the CSF.
- $\boldsymbol{g}$ is related to the gradient profile used in the diffusion sequence (a specific gradient duration and time between the diffusion-sensitizing gradients).

This model can estimate the properties of crossing fascicles within a voxel, while DTI cannot characterize them independently. In this model, axons are represented by a hexagonal packing of cylinders with specific microstructural features reflecting the underlying biology of the tissues (i.e., the distance between the axons, the apparent axonal radius, and the specific orientation). Using Monte Carlo simulations of the random

diffusion of water molecules, one can extract the expected signal for a specific microstructural environment (after discretization of the Ω-space into microstructural parameters of interest: Ω_1, …, Ω_N). Therefore, a dictionary containing the simulated signals (or fingerprints) of N-selected microstructural configurations for a fascicle of direction u_0 is built:

$$F^0 = [A_1^0, \dots, A_N^0]$$

Based on the computation of F^0, the single fascicle dictionary is computed for fascicles with K orientations: F^1, …, F^K. An external routine is used to evaluate the number and orientation of fascicles within each voxel. The inverse problem is then solved, leading to an optimal combination of fascicles in every voxel, leading to the minimum difference between the acquired and the simulated signals. This optimization problem is solved under sparsity constraints that do not allow a mixture of fingerprints to reconstruct the signal arising from a single fascicle of axons (137). This constraint may constitute a limitation for cases where special sub-regions within fascicles present different microstructural features (137). Solving the sparse optimization problem can be mathematically defined as:

$$(\widehat{j_1}, \dots, \widehat{j_k}) = \underset{1 \le j_{1,\dots,} j_K \le N}{\operatorname{argmin}} \min_{\boldsymbol{w} \ge 0} \left\| \boldsymbol{y} - \left[\boldsymbol{A}_{j_1}^1 | \dots | \boldsymbol{A}_{j_K}^K | \boldsymbol{A}_{CSF} \right] \cdot \begin{bmatrix} w_1 \\ \dots \\ w_K \\ w_{CSF} \end{bmatrix} \right\|_2^2$$

Where:

- *y* is the diffusion-weighted MRI signal.
- $\widehat{j_k}$ is the optimal fascicle with specific microstructural parameters $\widehat{\boldsymbol{\Omega_k}}$ selected from $\mathbf{F^k}$, the single-fascicle dictionary with orientation k.

After estimation of the optimal combination of fingerprints within each voxel, MF metrics can be computed. MF estimates the fraction of occupancy of the crossing fascicles within each voxel and their

corresponding fiber volume fraction (or axonal density). Considering the hexagonal packing of cylinders used to model the axons within a fascicle, the fiber volume fraction of a fascicle defined by an apparent axonal radius (r) and a spacing between the axons (s) can be defined as (**Figure 1.10**):

$$fvf_{fasc} = \frac{A_{axons \subset hexagon}}{A_{hexagon}} = \frac{2\pi}{\sqrt{3}} \left(\frac{r}{s}\right)^2$$

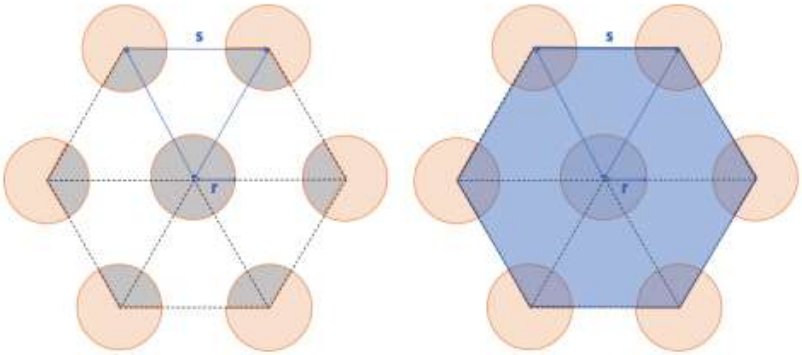

Figure 1.10 – Schematic representation of a hexagonal packing of axons within a fascicle, characterized by an apparent axonal radius (r), and a spacing between the axons (s). The fiber volume fraction is computed as the ratio between the gray area and the blue area ($\frac{A_{axons \subset hexagon}}{A_{hexagon}}$ *). Adapted from* (134).

Finally, the weighted Fiber Volume Fraction (wFVF) in each voxel where the external routine estimated the presence of two crossing fascicles, can be defined as:

$$wFVF_i = \frac{\nu_{1,i} \cdot fvf_{1,i} + \nu_{2,i} \cdot fvf_{2,i}}{\nu_{1,i} + \nu_{2,i}}$$

Where:

- *i* is the index of the voxel.
- $v_{1,i}$ is the fraction of occupancy of fascicle 1 in the voxel i (and $v_{2,i}$ for fascicle 2).
- $fvf_{1,i}$ is the fiber volume fraction of fascicle 1 in the voxel i (and $fvf_{2,i}$ for fascicle 2).

The computational cost for creating the dictionary containing the fingerprints increases for a finer resolution of microstructural parameters. However, this model is biologically more interpretable than DTI since Monte Carlo simulations are known to provide exact signals for any tissue geometry (137).

6.1.4 LOCUS COERULEUS IMAGING

The LC is involved in numerous processes, including regulating anxiety and alertness, gating sleep, detecting salient changes in the environment, and cognition over various domains (138). Moreover, LC alteration has been reported in an array of psychiatric and neurological diseases, including Alzheimer's disease dementia (139), Parkinson's disease (140), rapid eye movement sleep behavior disorder (141), insomnia disorder (142), pathological anxiety (143), late-life depression (144) or schizophrenia (145). Knowing that the LC shows alterations in different conditions, efforts have been made to characterize this nucleus structurally and functionally using non-invasive techniques. Recently, MRI sequences have been developed to visualize the LC *in vivo*, opening new avenues in better understanding the progression of diseases and developing biomarkers of pathological processes. The LC appears as hyperintense on the images obtained, allowing us to segment it and study its characteristics (e.g., its contrast, computed as the mean signal intensity within the LC compared to

a reference region usually located anteriorly to the LC in the pons). Different techniques, from manual to semi-automatic or automatic methods, have been used to extract the LC based on these images. However, semi-automatic and automatic techniques often require an LC template, inducing possible bias in the LC extraction. Therefore, although manual delineation of the LC in the subject's space may suffer from subjectivity, this technique remains the gold standard for LC delineation.

The exact biological interpretation of the LC contrast as observed using specific MRI sequences remains debated (146). Previous studies suggested that a higher LC contrast was associated with a higher concentration of neuromelanin (a by-product of NE that accumulates inside the cell body of noradrenergic neurons), as confirmed in a study that used a combination of histology and *postmortem* MRI (56). However, a recent study showed that LC contrast was still observable on images obtained using a sequence with magnetization transfer in mice that were genetically engineered to have 70% fewer LC cells (147). It has been suggested that MRI sequences may set the LC apart from its surroundings due to the specific transfer of magnetization between different pools contained in noradrenergic neurons, i.e., the intracellular water content of the LC with the presence of paramagnetic ions, such as neuromelanin (147,148). Overall, and despite the current debate and investigations, the LC contrast is accepted as an indicator of LC integrity (148), with a higher contrast reflecting better integrity depending on the age of assessment and excluding potential prodromal stages of degenerative brain disorders (139,149).

6.2 IMAGING BIOMARKERS OF VNS RESPONSE

Although limited, previous studies used imaging techniques to investigate possible functional and structural brain differences between responders and non-responders to VNS. Using DTI, a study conducted in

children found higher integrity (as reflected with a higher FA) in the left-lateralized limbic, association, and projection fibers (150). These tracts included the internal capsule (anterior limb and retrolenticular part), the external capsule, the corona radiata (anterior, superior, and posterior), the posterior thalamic radiation, the fornix, the stria terminalis, the superior longitudinal fasciculus, the inferior longitudinal fasciculus, and the inferior fronto-occipital fasciculus. However, no difference was found in the other DTI metrics (MD, RD, and AD). Based on DTI data, a Support Vector Machine (SVM) classifier was built and reached a classification accuracy of 89.5%, with an Area Under the Curve (AUC) of 0.96, a true positive rate of 96%, and a true negative rate of 73% (150).

Another study conducted in a cohort of 21 children with intractable epilepsy investigated whole-brain fMRI connectivity to thalamic regions before the implantation of a VNS device (151). A higher presurgical thalamocortical connectivity to the anterior cingulate and insular cortices was found in patients with a better response to VNS. Based on the intrinsic connectivity, an SVM classifier was built to classify responders and non-responders to VNS and demonstrated an 88% accuracy in an external cohort composed of 8 children.

Finally, preoperative Positron Emission Tomography (PET) data using 2-deoxy-2[^{18}F]fluoro-D-glucose (FDG - a marker of the metabolic brain activity based on glucose consumption) was collected in 66 children before undergoing VNS implantation (152). An Independent Component Analysis (ICA) computed different independent components (IC) generating independent sets of brain regions. They found that IC9 (which is composed of the anterior cingulate gyrus, the cerebellum, and the brainstem - overlapping the NTS, the LC, and the dorsal raphe nucleus) was significantly correlated with IC25 (that includes the thalamus, cerebellum, lingual gyrus of the occipital lobe and the medial orbitofrontal gyrus) in patients with a poorer response to VNS. In contrast, no correlation was found in responders to VNS. In non-responders only, another component that

showed metabolic connectivity with IC9 was IC27, which is composed of the precentral gyrus, the middle cingulate gyrus, and the supramarginal gyrus. Therefore, knowing that VNS may have desynchronizing effects on the brain, poorer VNS seizure outcomes may result from a stronger baseline metabolic connectivity of pathways composing the vagal afferent network (152).

6.3 LARYNGEAL MOTOR EVOKED POTENTIALS

The larynx is innervated by two collaterals of the vagus nerve: the superior laryngeal nerve (subdivided into an internal and an external branch) and the recurrent (or inferior) laryngeal nerve. The recurrent laryngeal nerve branches off the vagus nerve at the level of the aortic arch (**Figure 1.11**). These low-threshold motor fibers innervate the laryngeal muscles (except the cricothyroid) and part of the pharynx (153). The recurrent laryngeal nerve carries motor, sensory, and parasympathetic afferents to the larynx.

Stimulation of the vagus nerve co-activates the recurrent laryngeal nerve and triggers recordable Laryngeal Motor Evoked Potentials (LMEPs) with the activation of low threshold Aα-fibers (154). Indeed, studies that estimated the conduction velocity of the fibers responsible for the LMEP found values consistent with the known physiological properties of motor fibers (± 45 m/s) (155,156). It is known that antiseizure effects of VNS are mediated by higher threshold fibers (Aβ-, Aδ- and/or B-fibers – while antiseizure effects have been observed in animal studies for current intensities below the activation threshold of B-fibers) (73,86,157,158). However, knowing that properties of fibers are intrinsically related, recruitment properties of Aα-fibers could indirectly inform about excitation properties of fibers involved in antiseizure effects of VNS (49,159).

Previous studies successfully recorded LMEPs invasively in VNS-implanted rats (154,157) and humans through intra-operative vocal cord recording or using needle electromyography during laryngoscopy (160,161). The invasive measurement of LMEPs is a laborious procedure that could be performed only during the implantation of a VNS device. To overcome this problem, a technique that uses two surface electrodes in a horizontal neck derivation was proposed. This technique allows non-invasive LMEP recording in humans (155). Based on this technique, studies successfully recorded LMEPs in chronically and acutely implanted patients with DRE and hypothesized that LMEPs could be used as a biomarker of genuine vagal A-fiber activation (155,156).

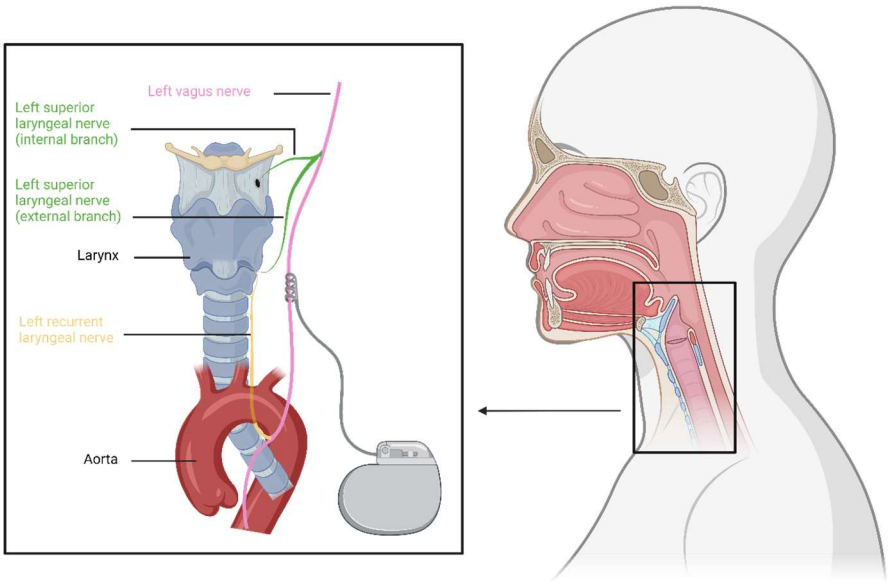

Figure 1.11 – Schematic representation of the collaterals of the left vagus nerve (the left superior laryngeal nerve and the left recurrent laryngeal nerve) innervating the intrinsic muscles of the larynx.

CHAPTER 2. OBJECTIVES OF THE THESIS

The primary focus of the research conducted within this thesis revolved around optimizing the VNS treatment for individuals suffering from DRE. In this context, part of the research aimed at developing and proposing a novel approach for the titration of the stimulation parameters that relies on physiological indicators of fiber engagement instead of the current empirical titration based on the subjective tolerance of the patients to the stimulation. Additionally, the research sought to develop response biomarkers using different techniques: electrophysiological recordings and muti-modal MRI acquisitions. This segment of the research aimed to deepen our current knowledge about the biological requisites necessary for the therapeutic benefits of VNS and to advance our understanding of the mechanisms of action of this therapy.

Chapter 3 *(Study 1)* focuses on peripheral investigations with the recording of VNS-triggered LMEPs using an easy-to-record and cost-effective technique. The neurophysiological properties of VNS-activated low-threshold motor fibers were compared between responders and non-responders to VNS. Moreover, the clinically programmed stimulation intensity of each patient was compared to the intensity leading to saturation of the motor fibers in search for possible under- or overstimulation in the cohort of patients included in the study. These analyses aimed at investigating whether LMEPs features could be used as an indicator of fiber engagement and help to guide the titration of the stimulation parameters. Finally, machine learning techniques were used to build a model based on LMEPs characteristics to classify responders and non-responders to VNS. Therefore, *Study 1* aims to answer the following questions: (1) ***Using LMEPs recordings, can a new titration technique based on a physiological indicator of fiber engagement be proposed?*** (2) ***Are LMEPs-related recruitment features linked to VNS response?***

Although not directly linked to epilepsy, **Chapter 4** *(Study 2)* focuses on developing a methodology for characterizing the LC functionally and structurally using a MAGNETOM Terra^{TM} Ultra-High Field (UHF) 7T MRI (Siemens Healthineers, Erlangen, Germany). This study was critical for the conceptualization and realization of *Study 3*. This body of work was conducted as part of a project of the Sleep and Chronobiology Lab of the GIGA Institute (Cyclotron Research Center – Human Imaging group, University of Liège). In this study, a combination of structural MRI (using a dedicated sequence – previously optimized in the center - allowing the visualization of the LC *in vivo*, as it appears hyperintense on the reconstructed images) and fMRI were used to extract LC characteristics in young and late middle-aged healthy individuals. Aside from creating a pipeline for analyzing LC characteristics, this project sought to investigate the potential relationship between LC response and LC reactivity, as assessed during a mismatch negativity task. Furthermore, this study aimed to ascertain whether the functional response of the LC underwent changes as a result of healthy aging. Investigating structural and functional features of the LC in healthy individuals is critical to detect and better characterize pathological conditions affecting the LC in clinical populations.

Based on the methodology developed in the previous chapter, **Chapter 5** focuses on assessing the structural and functional characteristics of the LC in patients with DRE and implanted with a VNS device. First, a preliminary work is presented in this chapter and consists of developing and optimizing an MRI sequence allowing the visualization of the LC *in vivo* using the SIGNA^{TM} Premier 3T MRI system (GE Healthcare, Milwaukee, WI, United States) of Saint-Luc University Hospital. Qualitative and quantitative analyses were conducted to identify the final LC sequence that will be used in *Study 3*. The best-performing sequence was selected by two independent raters by evaluating the easiest and most reproductible LC delineation and confirmed with a quantitative characterization of the LC intensity compared to the surrounding tissues. Secondly, *Study 3* is presented, where LC features are compared between non-responders and

responders/partial responders to VNS therapy. Moreover, based on multi-shell diffusion MRI data, DTI and MF (a multi-compartment diffusion model) were used to extract microstructural features of white matter tracts arising from the LC and projecting to the hippocampus and compare them between non-responders and responders/partial responders. All the investigated metrics were also correlated with duration of the therapy in search of potential neuroplasticity effects occurring in the brain following VNS administration. Therefore, *Study 3* aims to answer the following questions: (1) ***Are structural and functional features of the LC linked to VNS response or VNS therapy duration?*** (2) ***Are microstructural features of white matter tracts arising from the LC and projecting to the hippocampus linked to VNS response or VNS therapy duration?***

Further structural connectivity analyses were conducted in **Chapter 6** (*Study 4*). Considering the broadness of thalamocortical white matter tracts constituting a complex network that could disrupt the synchronous and abnormal activity of neurons, structural integrity in different subsegments of these tracts was explored in DRE patients. Based on high-gradient multi-shell diffusion MRI data, single- (i.e., DTI) and multi-compartment models (i.e., NODDI and MF) were used to determine how the extracted microstructural features could discriminate patients responding and not responding to VNS. Based on the microstructural metrics estimated, an SVM model was built to determine how accurately patients could be classified based on their response to VNS. Clinical features were also incorporated into the SVM classifier to determine their potential utility in conjunction with diffusion metrics in distinguishing responders/partial responders and non-responders. Therefore, *Study 4* aims at answering the following questions: (1) ***Are microstructural features of thalamocortical tracts linked to VNS response?*** (2) ***Can clinical features improve the classification of patients based on their response to VNS?***

Chapter 7 encompasses the industrial part of this thesis that was realized in collaboration with Synergia Medical, a company specializing in

the development of fully MRI-compatible optoelectronic neurostimulators. Within this context, this chapter tackles the specifications, complete development, and validation of the Optical Communication Device (OCD). The OCD serves the purpose of awakening the implant, establishing communication with it to adjust the stimulation parameters, and initiating stimulation remotely from the command room while the implant is placed inside an MRI system. The development of this device paves the way for future research opportunities using fMRI, aiming to better understand the acute effects of VNS administration and optimize this therapy by tuning the stimulation parameters to maximize the recruitment of structures involved in the antiseizure effects. Therefore, this study aims to answer the following question: ***Can a robust system be developed to control the stimulation parameters of an optoelectronic neurostimulator remotely in an MRI environment?***

CHAPTER 3. VNS-INDUCED LARYNGEAL MOTOR EVOKED POTENTIALS

1. INTRODUCTION AND OUTLINE OF THE CHAPTER

As mentioned in the introductory chapter, VNS is known to trigger recordable LMEPs due to the co-activation of the recurrent laryngeal motor fibers that branch off the vagus nerve at the level of the aortic arch. The goal of *Study 1* presented in this chapter was to record LMEPs in VNS-implanted patients using a non-invasive, easy-to-record, and cost-effective technique that has been previously described (155), to assess the neurophysiological properties of VNS-activated low threshold motor fibers in responders and non-responders to VNS. Within that framework, single compound motor action potential features and recruitment-related characteristics were extracted based on LMEP recordings and compared between responders and non-responders to VNS. This analysis was performed under the hypothesis that abnormal vagus nerve activation with VNS could be detected in LMEP recordings with deviant features. Therefore, one could hypothesize that an abnormal activation of the vagus nerve could – at least partially – explain the poor response to the treatment reported in a subgroup of patients who are known as non-responders. Based on the characteristics of the LMEPs extracted, a multi-feature analysis was conducted, and an SVM classifier was built to determine how accurately recruitment-related features could discriminate responders from non-responders.

Moreover, the clinically applied stimulation currents used as part of the treatment of the patients were compared to the intensity leading to the saturation of the laryngeal motor fibers in order to explore possible under

or over-stimulation in patients with lower therapeutic efficacy of VNS. Indeed, the currently used titration strategy, which consists of setting the stimulation intensity based on the subjective tolerance of the patients to the stimulation, remains empirical. In this context, we postulate that LMEPs saturation properties could help to titrate the stimulation parameters based on a physiological indicator of fiber engagement and give deeper insight into the optimal dose to be delivered to maximize the antiseizure effects.

2. Study 1 : Vagus nerve stimulation-induced laryngeal motor evoked potentials for response prediction and intensity titration in drug-resistant epilepsy

Abstract

The objective of the study was to record LMEPs in VNS-implanted patients suffering from DRE. Based on these recordings, LMEPs characteristics were evaluated and compared between responders and non-responders. Finally, possible under- or over-stimulation was assessed based on a physiological indicator of fiber engagement. Mean dose-response curves were compared between responders and non-responders. An SVM model was built based on both LMEP and dose-response curve features to discriminate responders from non-responders. For the exploration of possible under- or over-stimulation, a ratio between the clinically applied stimulation intensity and the intensity yielding to LMEP saturation was computed for each patient. A trend toward a greater excitability of the nerve was observed in responders compared to non-responders to VNS. The SVM classifier discriminated responders and non-responders to VNS with an accuracy of 80%. An ineffective attempt to overstimulate at current levels above what is usually necessary to obtain clinical benefits was suggested in non-responders. The SVM model built emphasizes a possible link between vagus nerve recruitment characteristics and treatment effectiveness. Most of the clinically responding patients receive VNS at a stimulation intensity of 1-fold and 2-fold the intensity inducing LMEP saturation. LMEP saturation could be a practical help in guiding the titration of the stimulation parameters using a physiological indicator of fiber engagement.

2.1 MATERIAL AND METHODS

2.1.1 DATA ACQUISITION

2.1.1.1 PATIENTS

Patients included in the present study were recruited from the VNS database of the Center for Refractory Epilepsy of Saint-Luc University Hospital, Brussels, Belgium. Data included in the study are from patients who met the following criteria: (i) DRE diagnosis; (ii) treated with VNS (DemiPulse® Model 103 or DemiPulse Duo® Model 104, AspireHC® Model 105 or AspireSR® Model 106; LivaNova, Inc., London, United Kingdom) for at least three months and (iii) aged between 18 and 75 years. Exclusion criteria consisted of severe side effects due to VNS therapy, such as dyspnea or severe pain in the neck or the ear region. In total, 45 patients were eligible and were recruited for the study. The clinical response evaluation was determined at the last follow-up visit. All patients signed the informed consent prior to any investigation. The Ethics Committee of Saint-Luc Hospital approved the study procedures (reference nr. 2018/07NOV/416).

2.1.1.2 RECORDING METHOD

Patients numbered 1-11 were included in a formerly published study by Vespa et al. (155), in which an EEG/EP digital acquisition system (Matrix 1005, Micromed, Mogliano Veneto, Italy) was used for recording LMEPs. For the other patients (numbered 12-45), LMEPs were recorded using the Biosemi (Amsterdam, Netherlands) EEG/EP acquisition system. The sampling rate was set at 4096 Hz. Signals were high pass filtered at 0.5 Hz.

LMEPs were recorded with two recording surface electrodes in a horizontal bipolar derivation (LMEP+/LMEP-), as described in (155).

2.1.1.3 STIMULATION PROTOCOL

The impedance of the VNS lead was checked before and after the session. Patients were instructed to minimize neck movements and to abstain from speaking except to report discomfort or pain due to the stimulation. The therapeutic parameters, including the stimulation current (I_{stim} expressed in mA), frequency (Hz), pulse width (µs), and duty cycle (%), were checked at the beginning of the session. For the initial phase, I_{stim} was set to 0 mA (VNS OFF), while the frequency remained unchanged. The pulse width used in patients numbered 1-11 previously included in (155) (and also included in the present study) was set to 250 µs. For the remaining patients (numbered 12-45), the pulse width was kept at the clinically programmed pulse width (250 or 500 µsec). The external magnet was programmed to stimulate at gradually increasing intensities, with 0.25 mA increments up to 0.125 or 0.25 mA higher than the clinically applied stimulation current (**Figure 3.1A**), depending on the tolerance of the patient.

Using the external magnet, six trains of 14 s were delivered for each stimulation intensity level, three in the ascending and three in the decremental phase (**Figure 3.1A**). Ramp-up and ramp-down phases occurred at the initiation and at the end of each simulation and lasted 2 s each. Therefore, each stimulation train lasted 18 s in total (**Figure 3.1B**). A period of 40 s of VNS OFF was taken between each stimulation train. At the end of the experiment, I_{stim} was reset to the clinically applied output current, and the lead impedance was checked to be under 5 kΩ.

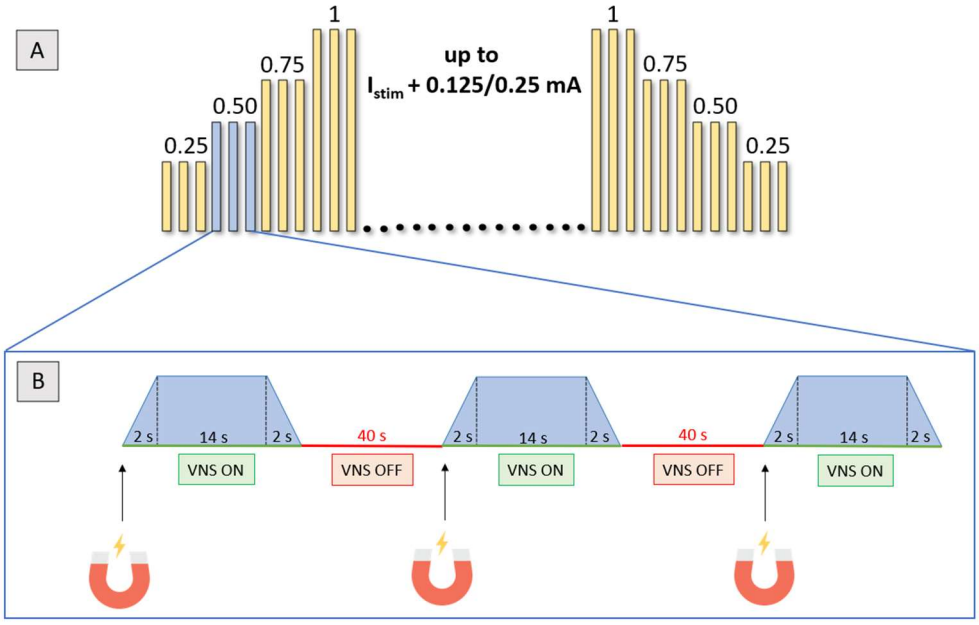

Figure 3.1 - (A) Timeline of the stimulation protocol. (B) Magnet-induced stimulations and duration of each stimulation block. I_{stim}: clinically applied stimulation current, mA: milliamperes, s: seconds, VNS: Vagus Nerve Stimulation.

2.1.2 DATA ANALYSIS

2.1.2.1 DEMOGRAPHIC AND CLINICAL FEATURES

Demographic and clinical features of patients included in the study, including sex, age, type of epilepsy, epilepsy onset age, duration of VNS therapy, VNS current, VNS frequency, VNS pulse width, and VNS duty cycle are reported in **Table 3.1**. These features were statistically compared between responders and non-responders, using Mann-Whitney U-tests.

Variables	*NR (n = 20)*	*R (n = 22)*	*p-value*
Sex	9 M - 11 F	9 M - 13 F	0.79
Age	40.8 (± 15.59)	42.04 (± 16.58)	0.80
Epilepsy onset age	18.95 (± 13.54)	13 (± 9.47)	0.10
Duration of VNS therapy (months)	66.7 (± 47.74)	82 (± 70.41)	0.41
Mean VNS output current (mA)	1.5 (± 0.40)	1.41 (± 0.34)	0.38
Mean VNS frequency (Hz)	24.75 (± 4.44)	24.77 (± 4.75)	0.98
Mean VNS pulse width (μs)	300 (± 102.6)	295.45 (± 98.7)	0.88
*Rapid duty cycle **	2 (14 s ON/66 s OFF – 23 %) (30 s ON/66 s OFF – 35 %)	1 (14 s ON/66 s OFF – 23%)	
Epilepsy type:			
Focal epilepsy	18	16	
Generalized epilepsy	2	6	

*Table 3.1 - Demographic and clinical characteristics of the study population (n = 42, 20 Non-Responders - NR, 22 Responders - R). M: Male, F: Female. *Duty cycles are determined based on previously reported definitions* (162–165).

2.1.2.2 LMEP FEATURES

After the recording, signals were analyzed using MATLAB 2018a software (MathWorks, Natick, MA, United States). To remove data

acquired during the ramp-up and ramp-down phases, the 2 s at the beginning and at the end of each stimulation block were discarded. Fifty consecutive stimulations were time-marked for each VNS train administered, starting 1 s after the ramp-up period, to ensure stabilization by using an automatic VNS stimulation artifact identification algorithm. Thereafter, the selected 50 trains were segmented into epochs according to the method described in (155). A visual analysis was conducted to ensure that possible movements did not impact the recordings. The peak-to-peak (P2P) amplitude value was computed for each single LMEP waveform as the difference between the largest positive and negative deflections occurring after the stimulation artifact. The following P2P values were averaged, obtaining a P2P mean value and standard deviation (SD) for each stimulation epoch. Finally, P2P amplitudes were averaged across the epochs corresponding to the same stimulation current values (6 epochs in total), resulting in a mean P2P amplitude and SD for each current intensity and for each subject.

The LMEP latency, extracted after computation of the first derivative of the signal (when clinical stimulation parameters are used, such as I_{stim} and the pulse width), was defined as the time between the initial peak of the stimulation artifact and the initial deflection of the motor response (155). The measured LMEP latency was normalized by the patient's height to take differences in nerve length into account. The height-corrected latency (L_c) of a patient was computed as follows: *(latency/height of the patient) * (average height of the patients in the investigated cohort)*. The value of the maximal LMEP amplitude, corresponding to the plateau of the recruitment curve (Y_{sat}), was measured for all the patients included in the study. Recruitment-unrelated LMEP characteristics (L_c and Y_{sat}) were extracted in all patients with recordable LMEPs and were compared between responders and non-responders using Mann-Whitney U-tests.

2.1.2.3 *LMEP RECRUITMENT : DOSE-RESPONSE CURVES*

A Boltzmann sigmoid function was used to fit LMEPs amplitudes as a function of the stimulation charge (current x pulse width) (166). Since the charge rather than the stimulation current alone is known to better reflect the actual activation of the nerve fibers, the charge instead of the current amplitude alone was used for the fitting. The recruitment curves (or dose-response curves) were obtained for each patient using the MATLAB 2018a Curve Fitting Toolbox. The corresponding LMEP amplitude, as a function of the stimulation charge (C_S), was modeled as:

$$LMEP\ amplitude = \frac{Y_{sat}}{\left[1 + e^{\frac{(C_{50} - C_S)}{k}}\right]} \quad (1)$$

The Boltzmann fit was considered to be good whenever the curve showed an $R_2 > 0.95$ and ≥ 2 points on the ascending part of the curve (155,156). Only patients with a good fit of the dose-response curve, and for whom a pulse width of 250 µs was used, were candidates to extract the following features, which were subsequently compared between responders and non-responders to VNS:

- C_{50} – Charge for an output current value at which the LMEP amplitude reaches half its maximal amplitude [nC].
- C_{98} – Charge for an output current value leading to 98% recruitment of the fibers [nC].
- k – Recruitment slope value corresponding to the fiber excitability homogeneity.
- C_5 – The charge leading to 5% recruitment of the fibers is taken as a theoretical threshold for LMEP induction.

2.1.2.4 *Optimal range of therapeutic current based on fibers saturation*

Regardless of the goodness of the Boltzmann fit based on the criteria mentioned above, the curve enabled us to obtain confidence intervals (CI) for the levels of Y_{sat} (since saturation is observed independently of the slope of the curve). Hence, by using such intervals, the lowest output current value administered that fell within the range of the CI of Y_{sat} was determined and used to estimate the intensity needed for LMEP saturation (I_{sat}) in *all* patients. The ratio between the routinely used output current and the previously described estimate of LMEP saturation, defined as I_{stim}/I_{sat} was compared between responders and non-responders for all the patients included in the study. In that regard, the mean and standard deviation of the I_{stim}/I_{sat} ratio was computed for responders and non-responders, and the Probability Density Function (PDF) of this ratio was estimated for responders and non-responders using a kernel density non-parametric method ("ksdensity" MATLAB 2018a built-in function) (167). Eventually, the probability (the area under the PDF curve) that the I_{stim}/I_{sat} ratio lies in a given range of integer values (0-1, 1-2, 2-3, 3-4, and 4-5) was computed for responders and non-responders using trapezoidal numerical integration ("trapz" MATLAB 2018a built-in function).

2.1.2.5 *SVM and multi-feature classification*

Only subjects showing a good fit of the Boltzmann curve (and for whom a pulse width of 250 µs was used during the stimulation protocol) were included in the discovery cohort used to train the SVM classifier. The SVM model was built using the Scikit-learn machine learning library (French Institute for Research in Computer Science and Automation, Rocquencourt, France) implemented in Python (168).

Feature selection was conducted using a recursive feature elimination technique. A wrapper feature selection method that uses an internal filter-based feature selection was used to rank the features by importance. Therefore, (i) six features of interest (Y_{sat}, C_{50}, C_{98}, k, C_5, L_c) were ranked based on their p-value computed with Mann-Whitney U-tests between the two groups (responders and non-responders), then (ii) a model was fitted using all the features of interest and (iii) features were recursively discarded based on their p-value, before refitting the model. When fitting an SVM model, it is common to use kernel functions to implicitly map the data into a higher-dimensional space. This technique is used to make non-linear data linearly separable in a higher dimensional space, where a linear classifier can be used to separate the data. Different kernel functions were used (linear kernel, polynomial kernel, Radial Basis Functions – RBF, and sigmoid kernel) and compared in terms of accuracy to select the most suited SVM classifier.

The classifier accuracy was evaluated using the Leave-One-Out (LOO) cross-validation technique. Grid search (a technique used to tune and identify the optimal hyperparameters in a model) was used to select the regularization parameter (C) and the gamma-kernel coefficient (γ - only applicable for the polynomial kernel, RBF and sigmoid kernel) for fitting the soft-margin SVM model. The C parameter ensures a tradeoff between misclassifications and maximization of the margin hyperplane for a better generalization of the model to unknown data. The γ parameter controls the distance of influence of a single training point and, therefore, influences the curvature of the decision boundary. Grid search was conducted by searching over values of C = [2^{-5}, …, 2^{2}]. The optimal model (i.e., the best-performing kernel function, the best subset of features, and the most-suited hyperparameters) was selected based on the classification accuracy of the different models tested. Thereafter, the confusion matrix reporting the true positive (TP), true negative (TN), false positive (FP), and false negative (FN) predictions were computed. The sensitivity (or true positive

rate) defined as TP/(TP+FN) and the specificity (or true negative rate), i.e., TN/(TN+FP), finally led to an estimation of the AUC of the Receiver Operating Characteristic (ROC) curve of the best SVM classifier.

2.2 RESULTS

2.2.1 LMEP RECORDING AND SINGLE FEATURE ANALYSIS

In total, 45 patients were eligible and recruited. The LMEPs could not be recorded in three patients. One of them (a non-responder) presented a history of postsurgical laryngeal nerve lesion. However, no history of injured left laryngeal nerve or vocal cord dysfunction was reported in the two other patients (one responder and one non-responder). Therefore, 42 patients in whom LMEPs were successfully recorded were finally included in the study (22 responders and 20 non-responders). The demographic and clinical characteristics of the included patients are reported in **Table 3.1**.

LMEPs features were extracted and summarized in **Table 3.2A**. Although not significant (at the level $p < 0.05$), a slight increase in the latency was observed in non-responders (7.70 ± 1.36 ms) compared to responders (7.61 ± 0.98 ms). Moreover, a trend toward a lower Y_{sat} was observed in non-responders (191.77 ± 88.9 µV) compared to responders (209.85 ± 97.7 µV).

The Boltzmann curve was successfully fitted in 17/42 patients (9 responders and 8 non-responders), including 15 patients for whom a pulse width of 250 µs was used. Recruitment-related LMEPs characteristics of these patients are summarized in **Table 3.2B**. The mean dose-response curve of patients showing a good fit of the Boltzmann curve was computed for responders and non-responders, as shown in **Figure 3.2**. Although not significant, a trend toward an earlier rising flank of the dose-response curve was observed in responders compared to non-responders, as

reflected by a lower C_5 in responders (56.42 ± 38.94 nC) compared to non-responders (68.93 ± 50.1 nC). Moreover, a trend toward a lower C_{50} was observed in responders (129.97 ± 31.19 nC) compared to non-responders (154.83 ± 49.27 nC) without reaching a significance at level $p < 0.05$.

A. Recruitment-unrelated characteristics (42 subjects)	***NR (n = 20)***	***R (n = 22)***	***p-value***
L_c (ms)	7.70 (± 1.36)	7.61 (± 0.98)	0.81
Y_{sat} (µV)	191.77 (± 88.9)	209.85 (± 97.7)	0.53
B. Recruitment-related characteristics (15 subjects)	***NR (n = 7)***	***R (n = 8)***	***p-value***
k (slope)	29.17 (± 8.91)	24.97 (± 8.55)	0.34
C_{50} (nC)	154.83 (± 49.27)	129.97 (± 31.19)	0.34
C_{98} (nC)	268.37 (± 66.58)	227.18 (± 46.92)	0.34
C_5 (nC)	68.93 (± 50.1)	56.42 (± 38.94)	0.69

Table 3.2 - Comparison of Laryngeal-Motor Evoked Potentials (LMEPs) characteristics between Responders (R) and Non-Responders (NR). (A) Recruitment-unrelated features extracted in all patients (42 patients, 20 NR, 22 R) with recordable LMEPs, and (B) Recruitment-related LMEP features in patients with a good fit of the Boltzmann curve and for whom a pulse width of 250 µs was used as part of the stimulation protocol (15 patients, 7 NR, 8 R). The mean (and standard deviation) values are reported in the table.

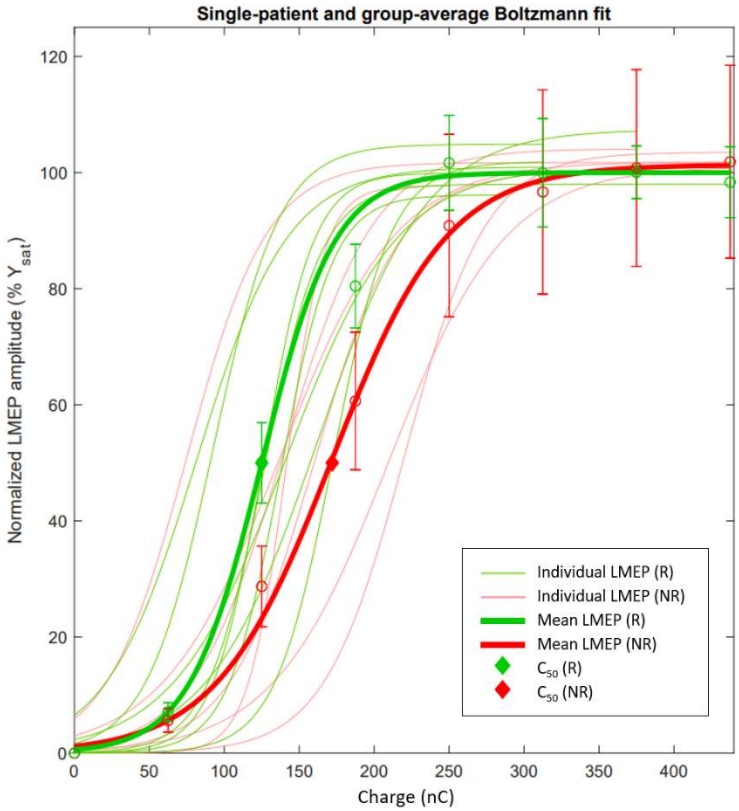

Figure 3.2 - Normalized (% Y_{sat} – the value of the maximal LMEP amplitude, corresponding to the plateau of the recruitment curve) single-patient dose-response curves and normalized fitted Laryngeal-Motor Evoked Potential (LMEP) values averaged across Responders (R, green, n = 8) and Non-Responders (NR, red, n = 7). C_{50}: Charge for an output current value at which the LMEP amplitude reaches half its maximal amplitude [nC].

2.2.2 Optimal range of therapeutic current based on fibers saturation

The PDF of the I_{stim}/I_{sat} ratio was estimated for each patient. The estimated PDF for responders and non-responders are shown in **Figure 3.3**. In the responding group, the distribution of I_{stim}/I_{sat} is sharper than the

distribution for non-responders, which spreads over a wider range of values instead. Moreover, probabilities of I_{stim}/I_{sat} to lie within different ranges of integer ratios were computed for responders (**Figure 3.3B**) and non-responders (**Figure 3.3C**). According to the results, there is a probability of 68.5% that patients predisposed to becoming responders to VNS will have a clinical output current set to a value within a range of 1-fold and 2-fold the intensity that induces LMEP saturation. This probability drops to 38.27% for the non-responding group.

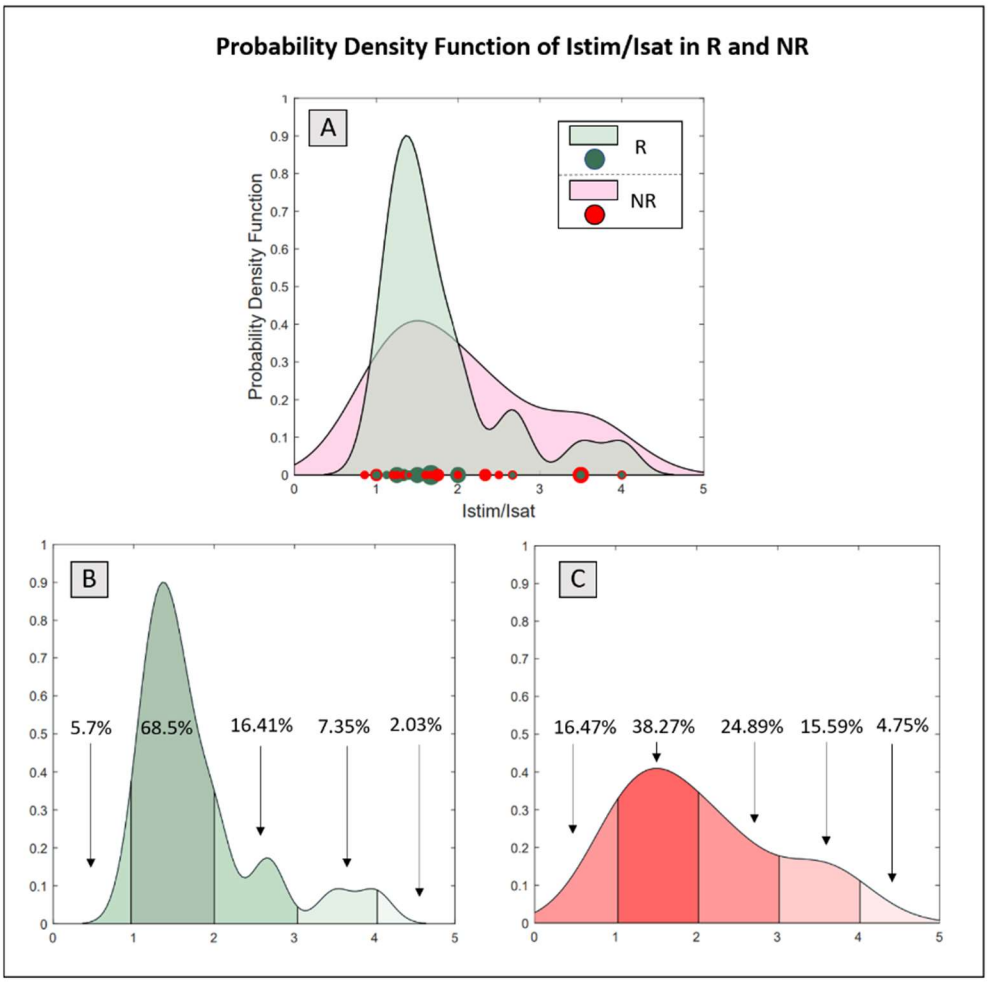

Figure 3.3 - Probability Density Function (PDF) of the ratio between the routinely used output current (I_{stim}) and the intensity needed for LMEP saturation (I_{sat}) estimated in Responders (R, green, n = 22) and Non-Responders (NR, red, n = 20). (A) The ratios I_{stim}/I_{sat} of the patients are represented by circles, with the size being proportional to the number of patients with the same ratio. (B) Probability that I_{stim}/I_{sat} lies within different ranges of integer ratios for R and (C) NR.

2.2.3 SVM AND MULTI-FEATURE CLASSIFICATION

The ranking of the features extracted from the Boltzmann fit was: k (p = 0.34), C_{50} (p = 0.34), C_{98} (p = 0.34), Y_{sat} (p = 0.46), C_5 (p = 0.69), and L_c (p = 1). Since three features presented the same p-value, the recursive feature elimination was conducted until the three most discriminatory features were used for the classification. The best-performing model used the sigmoid kernel function for mapping the data and the top four features for the classification, including k, C50, C98, and Y_{sat} (**Figure 3.4A**). A summary of the performance of the different models (subsets of features with the corresponding best-performing hyperparameters) can be found in **Supplementary Materials S3.1**.

Grid search over the hyperparameters suggested a top-performing classification for values of C = 4 and γ = 1 (**Figure 3.4B**). The corresponding sensitivity and specificity for the best-performing hyperparameters are also shown in **Figure 3.4B**. The confusion matrix that summarizes the classification predictions and the ROC curve of the best-performing model are shown in **Figure 3.4C**. Using this model, the classifier reached an accuracy of 80%, a sensitivity of 75%, and a specificity of 85.71%. Finally, based on the ROC curve, the final SVM classifier reveals an AUC of 82.1%. It is worth mentioning that a model using a sigmoid kernel and six features for the classification also reached a classification accuracy of 80%, with a

corresponding sensitivity of 87% and a specificity of 71.41%. Due to the lower specificity of the model compared to the previous one and the poor corresponding AUC (64.3%), the final model used for the classification is the one using four features.

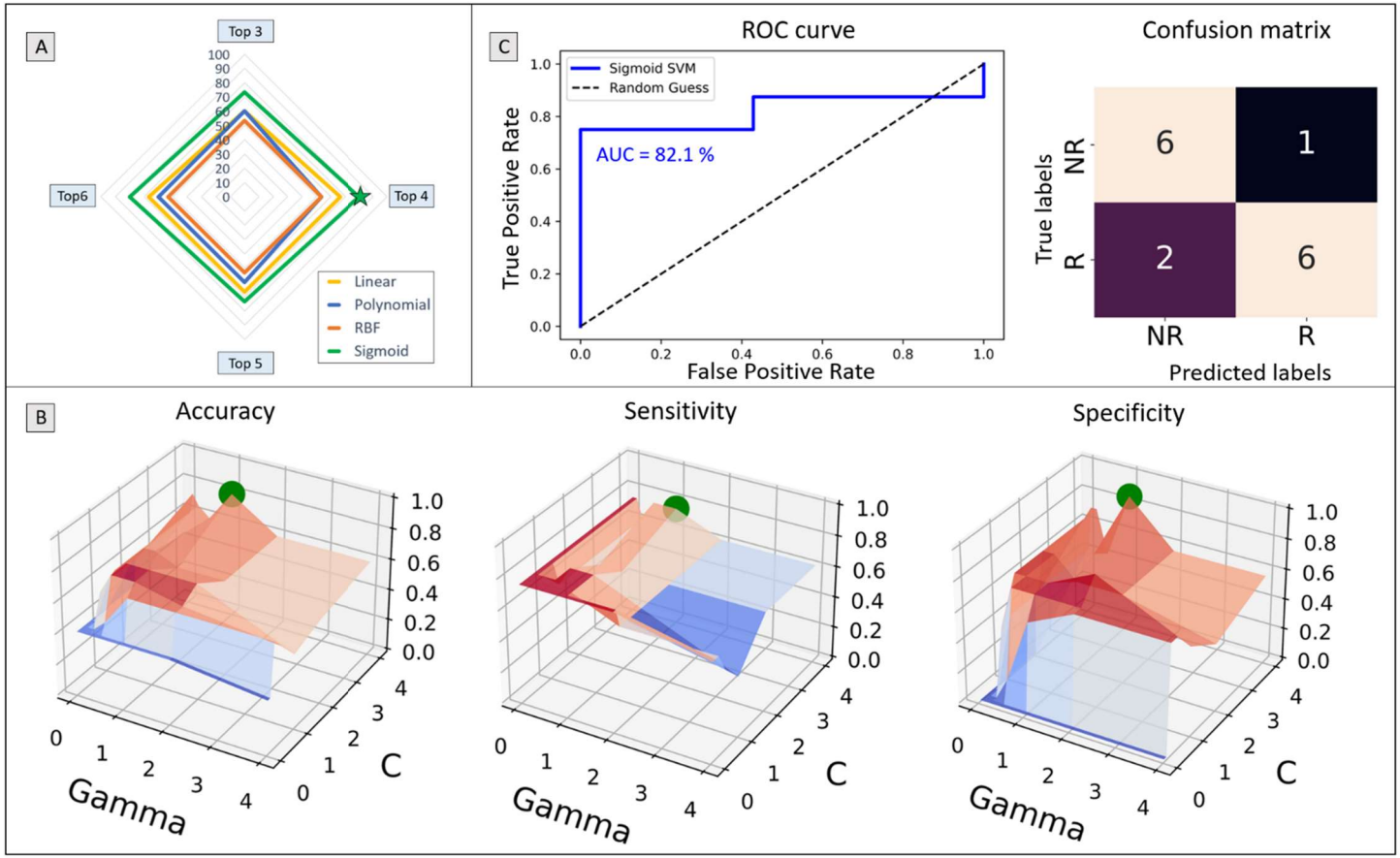
A
Top 3
Top4
Top 5
Top6
100
90
80
70
60
50
40
30
20
10
0
Linear
Polynomial
RBF
Sigmoid
C
ROC curve
Sigmoid SVM
Random Guess
AUC = 82.1 %
True Positive Rate
False Positive Rate
0.0
0.2
0.4
0.6
0.8
1.0
Confusion matrix
True labels
NR
R
6
1
2
6
Predicted labels
B
Accuracy
Sensitivity
Specificity
Gamma
C
0
1
2
3
4

Figure 3.4 - Model selection: (A) Recursive Feature Elimination (RFE) for the top 3 features, top 4 features, top 5 features, and all 6 features with the corresponding maximum accuracy of classification for models when different kernels (linear kernel, polynomial kernel, Radial Basis Function - RBF and sigmoid kernel) are used. (B) For the model with the best accuracy (80%, sigmoid kernel function), details of the grid search over the hyperparameters (C and γ) are shown. The green sphere represents the [C, γ] combination leading to the best accuracy. The corresponding sensitivity and specificity are also shown. (C) Receiver Operating Characteristic (ROC) curve of the final Support Vector Machine (SVM) classifier, with an Area Under the Curve (AUC) of 82.1% and the confusion matrix of the final SVM classifier (top 4 features, sigmoid kernel, C = 4, γ = 1), showing 6 true positive predictions, 6 true negative predictions, 1 false positive prediction and 2 false negative predictions, resulting in a sensitivity of 75%, and a specificity of 85.71%.

2.3 DISCUSSION

In the current study, LMEPs were successfully recorded in 42/45 patients, showing a good reproducibility of the recording technique that was previously described in (155). The mean I_{stim}/I_{sat} ratio was larger in the non-responding group than in the responding group, suggesting in the non-responding group an ineffective attempt to overstimulate at current levels above what is usually necessary to obtain clinical benefits. The peak-like PDF of the I_{stim}/I_{sat} ratio observed in responders may suggest that, given the stimulation level of motor fiber saturation, an optimal range of stimulation current with antiseizure effects could be estimated in these patients. When looking at the I_{stim}/I_{sat} ratio in non-responders, a rather dispersed distribution was observed, reflecting the heterogeneity of causes behind the non-response. Indeed, non-responders with a ratio lower than the optimal range of output currents related to saturation of low-threshold A-

fibers could correspond to more sensitive patients who do not tolerate VNS well and, therefore, are not stimulated at current intensities sufficient to observe antiseizure effects. Alternatively, if an adequate treatment remains inefficient despite intensities in the effective range, more central mechanisms must be considered. In this case, other parameters affecting the synaptic transmission, such as the pulse frequency or train length, could be adapted (169). A previous study that used a generalized linear mixed model to ascertain the relationship between key stimulation parameters and clinical outcome in 1178 patients has demonstrated a population-level optimal target output current and duty cycle at 1.61 mA and 17.1 % (170). In addition to this target dose, an inverted-U relationship has been reported between VNS intensity and brain plasticity in specific areas. This principle was demonstrated in studies where VNS was paired with motor training in rats to improve recovery after neurological injury. Intracortical microstimulation was used to infer plasticity effects based on the movement representations in the motor cortex (171–173). Other studies in the field of stroke recovery and fear conditioning for Posttraumatic Stress Disorder (PTSD) also suggested an inverted-U relationship as assessed respectively with motor tasks and behavioral tests (174,175). In opposition to the sigmoid relationship found for the VNS-induced LMEPs, it could be hypothesized that the inverted-U relationship found at the central level may be due to the additional recruitment of a high-threshold inhibitory or desensitizing system.

We should acknowledge that no significant differences in single LMEP features were found between responders and non-responders, which is concordant with results reported by Bouckaert et al. (156). Nevertheless, individual dose-response curves reveal a trend toward greater excitability of the nerve fibers in responders compared to non-responders. Indeed, a trend toward an earlier rising flank of the dose-response curve, a lower charge leading to half-saturation of the fibers, and a lower excitability threshold were observed in responders compared to non-responders. A multi-feature analysis using SVM was conducted to evaluate whether

features extracted from the dose-response curve could accurately discriminate non-responders from responders. Using four features for the classification (i.e., the slope of the dose-response curve, the charge leading to 50% saturation of the fibers, the charge leading to 98% saturation of the fibers and the amplitude of the LMEP at the plateau phase of the recruitment curve), the SVM model reached a classification accuracy of 80%, a sensitivity of 75%, a specificity of 85.71% and an AUC of the ROC curve of 82.1%. Despite the difficulty of interpreting our machine learning forecast in clinical terms, the model built in the present study emphasizes a possible link between vagus nerve recruitment characteristics and treatment effectiveness.

It was previously suggested that a low stimulation current (ranging from 0.25 to 0.75 mA for a pulse width of 250 µs) was sufficient to record LMEPs (156). This observation was confirmed in the present study, where the mean theoretical threshold reflecting the charge needed for the recruitment (5 % saturation) of motor fibers was approximately 69 nC (corresponding to an output current of 0.27 mA for a pulse width of 250 µs) and 56 nC (corresponding to an output current of 0.22 mA for a pulse width of 250 µs) in non-responders and responders, respectively. It is worth mentioning that these values were recorded for VNS devices composed of a similar spiral electrode placed around the vagus nerve. The values could differ for another electrode design, such as a cuff electrode. In addition, a previous study showed that the threshold current for minimal response induction was stable over time (156). Therefore, LMEPs could give insight into the state of the nerve and the nerve-electrode contact early after the implantation of a VNS device. In responders, an average charge of approximately 130 nC was found to recruit half the motor fiber population. Since a pulse width of 250 µs was used in these patients, this charge corresponds to an output current of 0.51 mA. Therefore, almost all motor fibers are probably responding at approximately 1 mA. However, on average, our results suggest that full recruitment in non-responders requires approximately 155 nC, corresponding to 1.2 mA. The higher

threshold in non-responders could be due to a partially damaged nerve (demyelination), anatomical differences such as the relative position of fibers within the nerve, the electrode contact position, or the local tissue gliosis (156). Although a broad spectrum of causes may underlie non-response, these results reinforce the idea that a reduced nerve excitability leading to an inadequate activation could be involved in (at least part of) non-responders included in the present study.

However, the current study presents several limitations. In 3/45 patients, no LMEP recording was possible. The absence of LMEP recording may be explained by different physiological problems (e.g., an inefficient activation of vagal fibers due to postsurgical scarring or gliosis, axonal degeneration, or a concomitant pathology) or technical difficulties during the recording. One of the patients (a non-responder) in whom LMEPs were not recorded presented a history of left recurrent laryngeal nerve injury after a thoracic surgery unrelated to VNS therapy. For the two other patients (one responder and one non-responder), no clinical history of injured left laryngeal nerve or vocal cord dysfunction was reported, but no laryngoscopy was performed. A second limitation is the fact that a successful fitting of the Boltzmann curve (at least two points on the rising flank of the curve) was achieved in 17/42 patients only. Newer versions of VNS devices should allow for smaller stimulation intensity increments and, therefore, more points on the rising flank for a better fitting of the dose-response curve. The cohort in the present study included patients chronically implanted for up to 10 years, when VNS devices only allowed titration steps of 0.25 mA.

In future studies, an independent cohort of patients could be used as a validation cohort to further evaluate the reproducibility of the proposed SVM classifier on unknown data. Moreover, further investigations are necessary to study the relationship between the recruitment of low-threshold motor fibers and the afferent central antiepileptic fibers of the vagus nerve. Non-invasive techniques such as fMRI, EEG, or pupillometry

could be used to build a classification model combining efferent markers of effective nerve stimulation with afferent markers of central VNS effects involved in the antiseizure effects of the treatment. Building such a model could help to deepen our current knowledge about the (possibly co-acting) mechanisms responsible for non-response in approximately 1/3 of implanted patients and help to stratify these patients better.

2.4 CONCLUSION

Using a non-invasive, easy-to-record, reproducible, and cost-effective technique, LMEPs were recorded in VNS-implanted patients suffering from refractory epilepsy. Clinically applied stimulation levels in responders and non-responders have been compared with the recorded motor response in the recurrent nerve branch. The results suggested that most of the clinically responding patients receive VNS at a stimulation intensity of 1-fold and 2-fold the intensity inducing LMEP saturation. Our results clearly indicate that non-response can have several different causes, as reflected by the inhomogeneity in the non-responding group. When a stimulation below that *"optimal"* level is used in non-responders, one could suggest an ineffective stimulation of the vagus nerve where the stimulation intensity should be increased, given that no side effect prevents it. For non-responders with a stimulation level above the usually effective range might reflect a desperate attempt to obtain a response by increasing the intensity. Based on these results, we support the idea that scaling the stimulation intensity as a function of the LMEP saturation could be a practical help in guiding the titration of the stimulation parameters using a physiological indicator of fiber engagement. Indeed, measuring LMEPs could provide a stimulus strength reference in a single patient and indicate when increasing the intensity or pulse duration becomes useless. Therefore, knowing that the nerve is activated effectively can then be the rational basis on which the clinician can try to further improve an

ineffective treatment by changing the pulse train duration or frequency: two stimulation parameters known to be involved in the central effects of VNS by acting on central synapses. In the future, LMEPs could be used in the clinical context to give early hints on the success of implantation, monitor the evolution of the recovery of the nerve, and perhaps improve the adequacy or effectiveness of VNS.

2.5 ORIGINAL CONTRIBUTION

Vagus nerve stimulation-induced laryngeal motor evoked potentials for response prediction and intensity titration in drug-resistant epilepsy. **A. Berger**, E. Carapancea, S. Vespa, V. Danthine, P. Doguet, J. Delbeke, A. Nonclercq, R. El Tahry. *Clinical Neurophysiology 147, 2023. doi: 10.1016/j.clinph.2023.01.009.*

CHAPTER 4. LOCUS COERULEUS FEATURES IN A HEALTHY POPULATION : A METHODOLOGICAL STUDY USING ULTRA-HIGH FIELD 7T MRI

1. INTRODUCTION AND OUTLINE OF THE CHAPTER

The research presented in this chapter constitutes a methodological approach for assessing structural and functional features of the LC in a healthy population. Developing a methodology to study the structural and functional characteristics of the LC was critical for investigating them in patients with DRE (Chapter 5).

In the context of healthy aging, studies reported that the LC contrast increases in adulthood up to about 60 years and declines thereafter (139,176,177). The variability of the LC contrast in aging may be related to the presence of Alzheimer's disease pathology, altering the structural integrity of the LC (139). A recent *in vivo* 3T fMRI study that used a visual novelty paradigm in humans further reported that lower activity and functional connectivity of the LC were associated with amyloid-related cognitive decline in cognitively unimpaired older individuals (178). However, whether LC functional response changes with healthy aging has not been established. Likewise, it has not been investigated whether age-related changes in LC contrast are associated with a detectable change in its functional response.

Here, we first tested whether the functional response of the LC during an auditory oddball task – a robust paradigm used to recruit the LC (105) – differed between young and late middle-aged healthy individuals.

Based on previous electrophysiology and fMRI studies that reported a reduced brain response to oddball events in aging (179,180), we expect a more prominent response in the LC of younger adults. We further investigated whether the LC response was related to the LC integrity, as assessed through its contrast, to determine if a structural-functional relationship may exist in the nucleus. Overall, this work aims to further our current knowledge about the effect of healthy aging on LC physiology and anatomy. A better functional and structural characterization of this nucleus in healthy individuals could help to detect abnormal features in different medical conditions. This could help to improve the detection of LC-related disorders and diseases in young and late middle-aged individuals, better characterize their evolution, and potentially help to develop therapies that target the LC-NE system.

2. Study 2 : Structural and functional characterization of the locus coeruleus in young and late middle-aged individuals

Abstract

The brainstem LC influences a broad range of brain processes, including cognition. The so-called LC contrast is an accepted marker of the integrity of the LC that consists of a local hyperintensity on specific MRI structural images. The small size of the LC has, however, rendered its functional characterization difficult in humans, including in aging. A full characterization of the structural and functional characteristics of the LC in healthy young and late middle-aged individuals is needed to determine the potential roles of the LC in different medical conditions. Here, we wanted to determine whether the activation of the LC in a mismatch negativity task changes in aging and whether the LC functional response was associated with the LC contrast. We used UHF 7T fMRI to record brain response during an auditory oddball task in 53 healthy volunteers, including 34 younger (age: 22.15 ± 3.27 years; 29 females) and 19 late middle-aged (age: 61.05 ± 5.3 years; 14 females) individuals. Whole-brain analyses confirmed brain responses in the typical cortical and subcortical regions previously associated with mismatch negativity. When focusing on the brainstem, we found a significant response in the rostral part of the LC probability mask generated based on individual LC images. Although bilateral, the activation was more extensive in the left LC. Individual LC activity was not significantly different between young and late middle-aged individuals. Importantly, while the LC contrast was higher in older individuals, the functional response of the LC was not significantly associated with its contrast. These findings may suggest that the age-related alterations of the LC structural integrity may not be related to changes in its functional response. The

results further suggest that LC responses may remain stable in healthy individuals aged 20 to 70.

2.1 MATERIAL AND METHODS

2.1.1 PARTICIPANTS

A sample of 53 healthy participants of both sexes, composed of 34 healthy young (age: 22.15 ± 3.27 years, 29 females) and 19 late middle-aged (age: 61.05 ± 5.3 years, 14 females) individuals were included in this study. A summary of the demographic data can be found in **Table 4.1**. This study was approved by the Faculty - Hospital Ethics Committee of the University of Liège. All participants provided their written informed consent and received financial compensation.

The exclusion criteria were as follows: history of major neurologic or psychiatric disease or stroke; recent history of depression and anxiety (< 5 years); sleep disorder; use of any medication affecting the central nervous system; smoking; excessive alcohol (> 14 units/week) or caffeine (> 5 cups/day) consumption; night shift work in the past 6 months; travels in a different time zone during the last two months; Body Mass Index (BMI) ≤ 18 and ≥ 29 (for the older participants) and ≥ 25 (for the younger participants); clinical symptoms of cognitive impairment for older subjects (Mattis Dementia Rating Scale score < 130; Mini-Mental State Examination score < 27) (181,182) and MRI contraindications. Due to miscalculation at screening, one older participant had a BMI of 30.9, and one of the younger participants had a BMI of 28.4. Since their BMI did not deviate substantially from the criteria and BMI was used as a covariate in our statistical models, these participants were included in the analyses. Depression, anxiety, sleepiness, and sleep quality were assessed with the Beck Depression

Inventory (BDI) (183), Beck Anxiety Inventory (BAI) (184) and the Pittsburgh Sleep Quality Index (PSQI) (185), respectively.

The LC-NE system has been recognized as a neuromodulator during sleep (186). Moreover, knowing that the LC exhibits a circadian rhythm and is involved in regulating the sleep-wake cycle (187), the younger participants were requested to maintain a loose fixed sleep-wake schedule (± 1h) for one week before fMRI acquisitions. This instruction was intended to reduce prior sleep deprivation and favor similar circadian entrainment across participants while keeping realistic daily life conditions. Adherence to the schedule was verified using a wrist actimetry device (AX3, Axivity Ltd, Newcastle, UK). Older participants were requested to avoid unusual late sleep time for three days prior to their participation. Adherence was verified using sleep diaries.

FMRI recordings were completed in the morning, 2 to 3h after wake-up time, to control for time-of-day effects. Prior to entering the MRI scanner, all participants were maintained in dim light (10 lux) for at least 45 min during which they received instructions about the following MRI sessions. The fMRI sessions consisted of a 10 min visual task followed by a 10 min auditory oddball task. The present paper only deals with the auditory task. Structural MRI data were acquired in a separate MRI session completed within one week before or after the fMRI session.

	Late middle-aged cohort (n = 19)				**Young cohort (n = 34)**				
	Mean	**SD**	**Min**	**Max**	**Mean**	**SD**	**Min**	**Max**	**p-value**
Age (years)	61.05	5.3	53	70	22.15	3.27	18	29	0.000
BMI (kg/m^2)	24.9	3.52	19.4	30.9	21.96	3.11	17.2	28.4	0.005

Education (years)	14.58	2.63	9	19	14.41	2.28	12	20	0.81
BDI	5.58	4.05	0	14	6.97	4.4	0	20	0.26
BAI	3.16	3.13	0	9	4	2.9	0	11	0.33
PSQI	3.95	2.22	0	8	4.65	1.95	1	9	0.24
Sex (F - M)	14 F – 5 M				29 F – 5 M				0.15

Table 4.1 *- Characteristics of the study population. The p-values shown in the table correspond to two-sample t-tests comparing the characteristics between the young and late middle-aged cohorts. The education level is expressed in years of study. BMI stands for Body Mass Index and is expressed in kg/m^2. BDI score, BAI score, and PSQI, respectively, stand for the Beck Depression Inventory score (180), Beck Anxiety Inventory score (181), and Pittsburgh Sleep Quality Index* (185)*. F: Female and M: Male. All characteristics were compared using two-sample t-tests, except for sex composition, which were compared using a Chi-square test.*

2.1.2 AUDITORY ODDBALL TASK

The task consisted of rare deviant target tones (1000 Hz sinusoidal waves, 100 ms) composing 20% of the tones that were pseudorandomly interleaved within a stream of standard stimuli (500 Hz sinusoidal waves, 100 ms). The task included 270 auditory stimuli in total (54 target tones). Auditory stimuli were delivered to the participants with MRI-compatible headphones (Sensimetrics, Malden, MA). The interstimulus interval was set to 2000 ms. Participants were instructed to press with the right index finger on an MRI-compatible keyboard (Current Designs, Philadelphia, PA) as quickly as possible at the appearance of target sounds. The experimental paradigm was designed using OpenSesame (*version 3.2.8*) (188). The MRI

session started with a short volume calibration session to ensure an optimal perception of the stimuli.

2.1.3 MRI DATA ACQUISITIONS

MRI data were acquired using a MAGNETOM Terra 7T MRI system (Siemens Healthineers, Erlangen, Germany), with a single-channel transmit and 32-channel receive head coil (1TX/32RX Head Coil, Nova Medical, Wilmington, MA). To reduce dielectric artifacts and homogenize the magnetic field of RF pulses, dielectric pads were placed between the head of the participants and the coil (Multiwave Imaging, Marseille, France). Foam pads were used to stabilize the head of the participants and limit the motion during the acquisition.

BOLD fMRI data were acquired during the task, using the CMRR multi-band (MB) Gradient-Recalled Echo - Echo-Planar Imaging (GRE-EPI) sequence: TR = 2340 ms, TE = 24 ms, flip angle = 90°, matrix size = 160 × 160, 86 axial 1.4 mm-thick slices, MB acceleration factor = 2, GeneRalized Autocalibrating Partial Parallel Acquisition (GRAPPA) acceleration factor = 3, voxel size = (1.4 x 1.4 x 1.4)mm^3. The cardiac pulse and respiratory movement were recorded concomitantly using a pulse oximeter and a breathing belt (Siemens Healthineers, Erlangen, Germany). The fMRI acquisition was followed by a 2D GRE field mapping sequence to assess B0 inhomogeneity with the following parameters: TR = 5.2 ms, TEs = 2.26 ms and 3.28 ms, FA = 15°, bandwidth = 737 Hz/pixel, matrix size = 96 × 128, 96 axial 2.0 mm-thick slices, voxel size = (2 x 2 x 2)mm^3, acquisition time = 1:38 min.

A Magnetization-Prepared with 2 RApid Gradient Echoes (MP2RAGE) sequence was used to acquire T1-weighted anatomical images: TR = 4300 ms, TE = 1.98 ms, FA1/FA2 = 5°/6°, TI1/TI2 = 940 ms/2830 ms, bandwidth = 240 Hz/pixel, matrix size = 296 × 256, 224 axial 0.75 mm-thick slices,

GRAPPA acceleration factor = 3, voxel size = (0.75 x 0.75 x 0.75)mm^3, acquisition time = 9:03 min (189). The LC-specific sequence consisted of a 3D high-resolution Magnetization Transfer-weighted Turbo-FLash (MT-TFL) sequence with the following parameters: TR = 400 ms, TE = 2.55 ms, FA = 8°, bandwidth = 300 Hz/pixel, matrix size = 480 × 480, number of averages = 2, turbo factor = 54, MTC pulses = 20, MTC FA = 260°, MTC RF duration = 10000 µs, MTC Inter RF delay = 4000 µs, MTC offset = 2000 Hz, voxel size = (0.4 x 0.4 x 0.5)mm^3, acquisition time = 8:13 min. Sixty axial slices were acquired and centered for the acquisitions perpendicularly to the rhomboid fossa (i.e., the floor of the fourth ventricle located on the dorsal surface of the pons) (**Figure 4.1**).

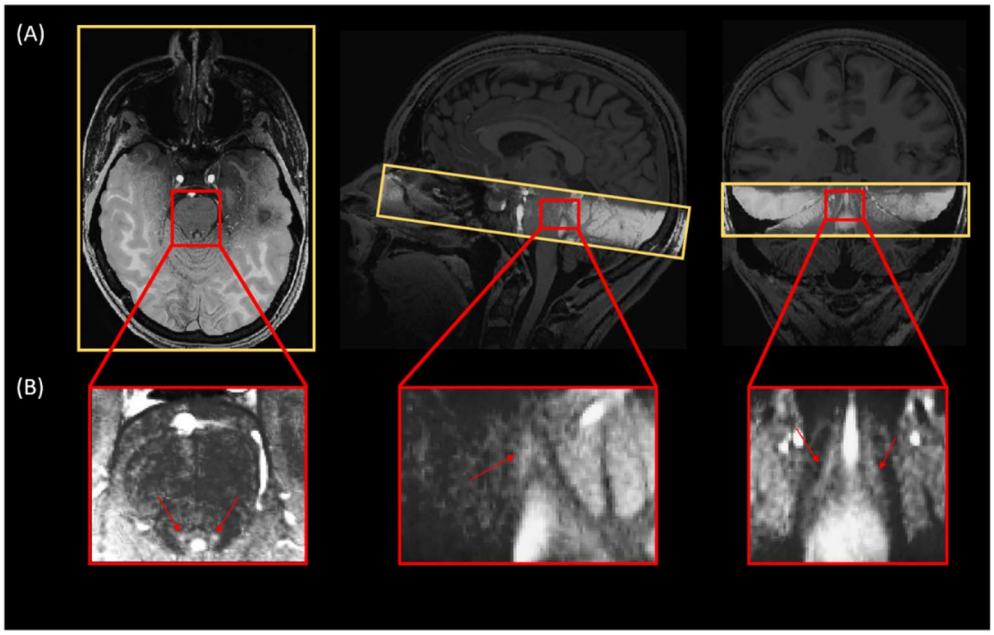

Figure 4.1 - (A) Realigned LC slab on the anatomical T1-weighted image and (B) LC hyperintensity on the MT-TFL image.

2.1.4 MRI DATA PRE-PROCESSING

EPI images were realigned and unwarped using the Statistical Parametric Mapping toolbox (SPM12, *https://www.fil.ion.ucl.ac.uk/spm/software/download/*). Although this procedure should, in principle, control for all movement-related bias, only volunteers with head movement of < 3 mm and < 3° were included (no subject had to be removed using this criterion). In order to make sure that a possible head motion difference between young and late middle-aged individuals did not bias brain-related activations, head motion was compared between the two groups as an image quality control. For each movement parameter (translation in x, y, z, and rotations: pitch, roll, yaw), a metric characterizing the movement during the acquisition was computed as (for example, for the x-translation):

$$overall\ x-translation = \int_{volume\ 1}^{volume\ end} |x-translation|$$

Each movement parameter was statistically compared between young and late middle-aged individuals using a two-sample t-test. No difference between the two groups was observed (translation in x: p = 0.14, y: p = 0.39, z: p = 0.62 ; pitch: p = 0.54, roll: p = 0.69, yaw: 0.61). No difference was observed when computing the mean translation and rotation of each participant (translation: p = 0.62 and rotation: p = 0.95).

EPI images underwent brain extraction using *'BET'* from the FMRIB Software Library suite (FSL, *https://fsl.fmrib.ox.ac.uk/fsl/fslwiki*), and the final images were spatially smoothed with a Gaussian kernel characterized by a full-width at half maximum of 3 mm.

The background noise in MP2RAGE images was removed using an extension of SPM12 (extension: *https://github.com/benoitberanger/mp2rage*) (190). The denoised image

was then automatically reoriented using the *'spm-auto-reorient'* SPM function and corrected for intensity non-uniformity using the bias correction method implemented in the SPM segmentation. Brain extraction was then conducted on the denoised-reoriented-biased-corrected image using both the Advanced Normalization Tools (ANTs, *http://stnava.github.io/ANTs/*) (191) with the *'antsBrainExtraction'* function and the RObust Brain EXtraction tool (ROBEX, *https://www.nitrc.org/projects/robex*) (192). The method yielding the best extraction for each individual, as assessed by visual inspection, was used for subsequent steps. A whole-brain T1 group template was created using ANTs, based on preprocessed MP2RAGE images of all subjects except for one, the MP2RAGE image of whom was not adapted due to a bad positioning of the slices during the acquisitions. Finally, the preprocessed MP2RAGE image of each subject was normalized to the Montreal Neurological Institute (MNI) space [MNI152 - with a (1 x 1 x 1)mm^3 image resolution]. The purpose of using a template that is specific to our dataset was to improve the registration into the MNI space using an intermediate space. The transformation parameters obtained from normalization were later used for registering first-level statistical maps into the MNI space to conduct group-level fMRI analyses. While the LC reactivity was extracted in the native space of the subject (see Statistical Analyses section), a group analysis was conducted to evaluate the general oddball effects.

In order to extract LC contrast, T1 structural images in the native space of the subject (after removing the background noise) were upsampled by a factor 2 [(0.375 x 0.375 x 0.375)mm^3] to avoid losing in-plane resolution when registering the LC slab to the T1 image. The upsampling was done using the '*nii_scale_dims'* function from an extension of SPM12 (extension: *https://github.com/rordenlab/spmScripts*). The complete LC contrast extraction was done in the native space of the subject. The MT-TFL image of each subject was registered with the whole brain upsampled T1 image by means of a two-step process: (i) a rough manual registration to extract the parameters for an initial transformation using ITK-SNAP (193) and (ii)

an automatic affine registration based on the initial transformation parameters, using ANTs (**Figure 4.1A**). MT-TFL data of one subject was not usable due to an excessive motion of the participant, leading to a registration failure. The LC appearing hyperintense on registered MT-TFL images (**Figure 4.1B**) was manually delineated by two expert raters, and the intersection of the LC masks of the two raters was computed as the final LC mask for each individual. The LC mask was skeletonized by only keeping the voxel with the highest intensity in each axial slice. Based on the skeletonized LC mask, the LC contrast was computed after normalization of each LC slice intensity to a slice-corresponding 2D reference region [a 15 x 15 voxels region, corresponding to a (5.5 x 5.5)mm^2 square region] situated anteriorly (and centrally) in the pons, in the pontine tegmentum. For example, the left LC contrast was defined as:

$$Contrast\ LC_{Left} = \underset{i}{\text{mean}}\left(\frac{LC_{Left,i} - mean(2D\ pons_i)}{mean(2D\ pons_i)}\right)$$

Where:

- i is the slice index along the (left) LC.
- $LC_{Left,i}$ is the intensity of the voxel with the highest intensity in the axial slice with index i.
- mean(2D $pons_i$) represents the mean intensity in the 2D reference region corresponding to the axial slice with index i.

The LC contrast was computed as the mean LC contrast between the left and right LC. Individual skeletonized LC masks were used for extracting the LC activity during the oddball task in the structural space of the subject (statistical output was identical when using the full individual LC masks rather than the skeletonized masks).

In order to investigate the activation of the LC at the group level, an LC probabilistic template was created. The LC mask of each volunteer was

normalized to the structural group template and then to the MNI [MNI152 – (1 x 1 x 1)mm^3]. This was done using the *'antsApplyTransforms'* ANTs command, with the transformation parameters estimated (i) when registering the subject-specific MP2RAGE image to the structural template and (ii) the transformation parameters estimated when registering the structural template to the MNI. The final LC probabilistic template was created as the sum of all masks divided by the number of subjects included in the analysis.

2.1.5 STATISTICAL ANALYSES

Statistical analyses were conducted using SPM12. A high-pass filter with a 128 s cutoff was applied to remove slow signal drifts. The timing vector with the appearance of the target tones was convolved with the canonical HRF to model the event-related response and was used as the main condition in a General Linear Model (GLM). The PhysIO Toolbox (*https://www.tnu.ethz.ch/en/software/tapas/documentations/physio-toolbox*) was used to compute physiology-related voxel-wise signal fluctuations based on respiratory and cardiac pulsation data (194) that was available in 48 volunteers (physiological data was not available for 5 volunteers). The Fourier expansion of the cardiac and respiratory phases computed with the toolbox, as well as the realignment parameters, were used as multiple regressors of no interest in the GLM. To avoid any registration-induced error, the first-level statistical analysis was conducted in the native space of the subject.

The mean functional image was registered to the MP2RAGE image to extract the corresponding transformation matrix used to register the first-level statistical map of each subject to the structural image. Therefore, for all subjects, statistical maps corresponding to the appearance of target sounds were registered to the structural native space, normalized to the

group template space, and then to the MNI space. A second-level analysis was then conducted in the MNI space (to report coordinates of activation clusters), where age, sex, and BMI were used as covariates. Whole brain activation was first assessed following voxel-level Family-Wise Error (FWE) correction based on random field theory for $p < 0.05$. For the sake of simplicity, only clusters with a size of at least 20 voxels were reported (an extensive table without minimum cluster size and all significant voxel clusters are available upon request). Structures showing peak activation foci were identified using the Harvard-Oxford Subcortical and Cortical structural Atlases (195). The probabilistic mask of the LC was then used to assess specific activation of the LC. Due to the small size of the nucleus, LC activation was not expected to survive stringent whole-brain FWE correction. Therefore, a small-volume correction using the LC template was conducted using SPM12 to report voxel-level FWE-corrected results within the LC mask.

REX Toolbox (*https://web.mit.edu/swg/software.htm*) was then used to extract the activity estimates (betas) associated with the appearance of the target sounds in the skeletonized LC mask of each subject in the native space to avoid possible registration errors that may occur with normalization (196). Therefore, the LC mask was resampled to the dimension of functional images when extracting the LC reactivity with the REX Toolbox. This procedure ensured that any potential displacement and bias introduced by the normalization step into the common MNI space did not affect individual activity estimates. Statistical analyses using these activity estimates were performed in RStudio (*version 2022.07.1*; *https://www.rstudio.com/*). For all models, a multivariate linear modeling approach was used, using sex, BMI, and education as covariates. LC response and contrast followed Gaussian distributions. The three models of interest investigated in the present study were: (i) $LC_{contrast} \sim$ age + covariates, (ii) $LC_{response} \sim$ age + covariates, and (iii) $LC_{response} \sim LC_{contrast}$ + age + ($LC_{contrast}$ x age) + covariates. The first and second models were designed to assess age-related changes in LC contrast and LC response, respectively.

The third model was intended to seek a relationship between functional response and LC contrast. Given our sample size, we computed a prior sensitivity analysis to get an indication of the minimum detectable effect size in our main analyses. According to G*Power (*version 3.1.9.4*) (197) taking into account a power of 0.8, an error rate α of 0.05, and a sample size of 52 (33 + 19), we could detect medium effect sizes r > 0.33 (one-sided; absolute values; CI: 0.06 – 0.55; $R^2 > 0.11$, R^2 CI: 0.003 – 0.3) within a linear multiple regression framework including one tested predictor (LC activity) and three or four covariates (depending on the statistical model).

2.2 RESULTS

The LC contrast across the entire length of the nucleus was extracted for each individual based on MT-TFL images. The multivariate linear model using the LC contrast averaged over both LCs as dependent variable found a significant main effect of age (**p = 0.038***, t = 2.13, 95% CI interval [3.45e-05, 0.0013]) but no main effect for BMI (p = 0.456), sex (p = 0.565) and education (p = 0.943) (**Figure 4.2A**). When adding age-group in addition to age to the model to take into account the fact that age was not truly continuous in our sample, these statistical outputs remain significant (main effect of age: **p = 0.012***, t = 2.6, 95% CI interval [7.4e-4, 5.8e-3]; main effect of age-group: **p = 0.035***, t = -2.16, 95% CI interval [-0.2, -0.007]). Boxplots of the LC contrast in young and late middle-aged individuals are shown in **Figure 4.2B**. The same model was then computed separately for the left LC contrast (p = 0.053) and the right LC contrast (p = 0.15). We further explored potential differences in LC contrast in late middle-aged individuals aged 60 or less and 61 or more in a multivariate linear model similar to the preceding and found no main effect of age subgroups (p = 0.16). Boxplots of the LC contrast in subgroups of the late-middle-aged cohort are shown in **Figure 4.2C**.

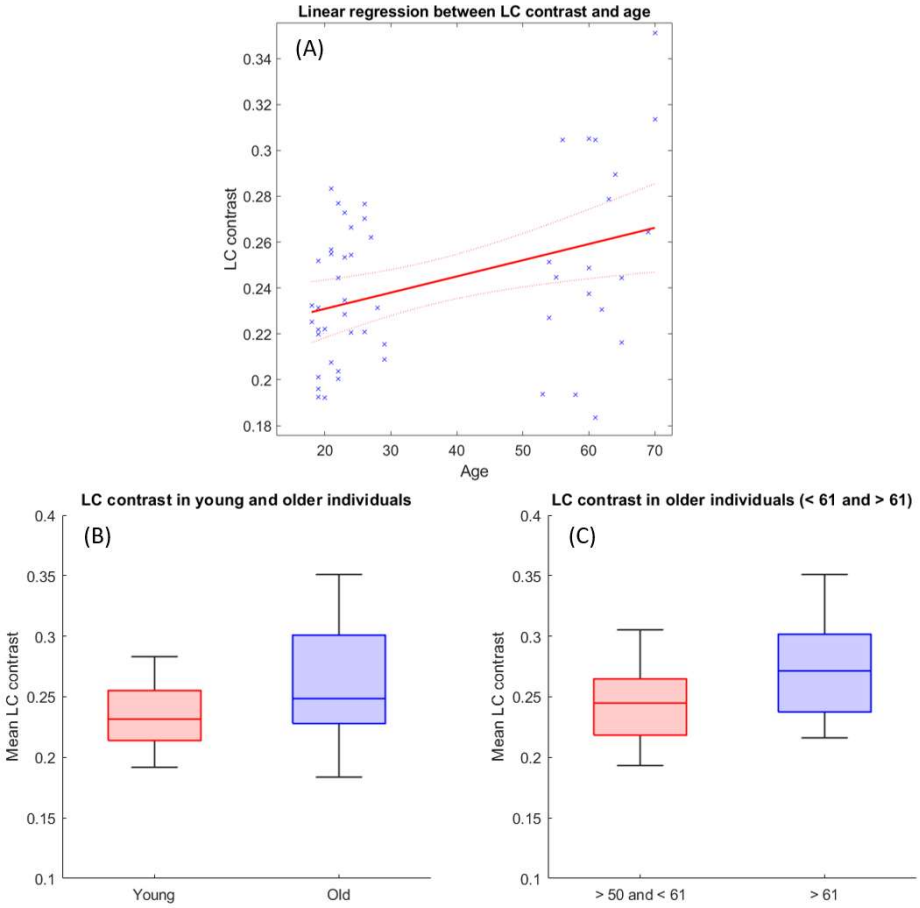

Figure 4.2 - LC contrast variation with age. (A) Linear regression plot of LC contrast and age. Solid line: regression line; Dashed lines: 95% confidence interval ; (B) LC contrast in young and older individuals and (C) LC contrast in subgroups of the older cohort (< 61 and > 61 years). The horizontal line at the mid-point of the data represents the median, and the colored box (without the whiskers) represents the interquartile range (50% of observations).

During the fMRI recordings, the participants completed the task correctly (mean accuracy: 97.1%, SD: 10.4%). FMRI data analyses over the entire brain showed that the target tones were associated with a significantly greater BOLD signal in a wide set of areas (**Figure 4.3**). At the cortical level, significant activation foci ($p_{FWE} < 0.05$) were detected bilaterally over the cerebellum, the posterior cingulate gyrus, the insular cortex, the precuneus, the middle temporal gyrus, the middle frontal gyrus, the frontal pole, unilaterally over the anterior cingulate gyrus (left), the planum polare (left), the lateral occipital cortex (right), the cuneal cortex (left), the superior frontal gyrus (left), the precentral gyrus (left) and the lingual gyrus (right) (**Figure 4.3A**). At the subcortical level, a significant activation was detected bilaterally over the thalamus and the caudate. These results are in line with the reported neural correlates of mismatch negativity tasks and support the validity of our procedure (198–202). A detailed list of brain activations highlighted using a stringent statistical threshold controlling for multiple comparisons is provided in the supplementary materials and may serve as a reference for future 7T MRI investigations using the same task (**Supplementary Material S4.1**). No significant activation difference was observed between healthy young and late middle-aged individuals (for a statistical threshold $p_{FWE} < 0.05$).

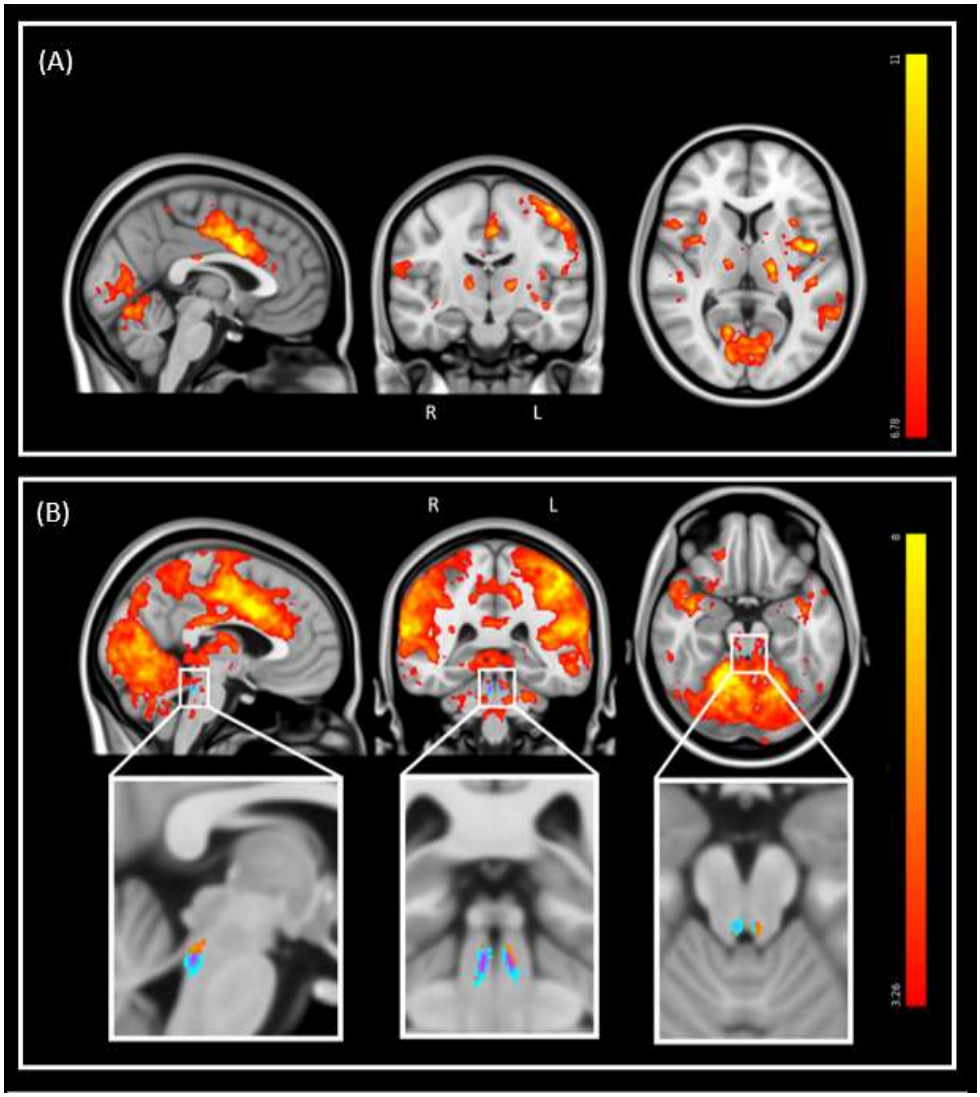

Figure 4.3 - Whole-brain and LC response to the target sounds during the auditory oddball task. Sagittal, coronal, and axial views (MNI coordinates: [-3 -15 7]). The legend shows the t-values associated with the color maps. The images are shown with the radiological convention for the orientation. (A) Whole-brain results using a significance threshold of p < 0.05 FWE-corrected (p < 3.34e-8 uncorrected; t > 6.35) and a minimum cluster size of 20 voxels. Refer to ***Supplementary Material S4.1*** *for a detailed list of coordinates. (B) Same results displayed using an uncorrected threshold of p*

< 0.001 (t > 3.26). Insets at the bottom show the LC probabilistic template and the significant activation detected within this mask (p < 0.05 FWE-corrected within LC mask). Refer to ***Table 4.2*** *for detailed coordinates.*

We then focused on the LC. Given the small size of the structure, we did not expect that activation would survive the conservative $p_{FWE} < 0.05$ statistical threshold over the whole brain. Correction for multiple comparisons $p_{FWE} < 0.05$ was rather considered within the study-specific probabilistic template of the LC in the MNI space. Following this procedure, five significant local peak intensity clusters were detected in the rostral part of the LC (**Table 4.2**). Although a significant activation was detected bilaterally, the activation clusters were larger over the rostral left LC (**Figure 4.3B**).

Brain region (Peak MNI coordinates)	Cluster size	T_{49}	p-FWE	MNI coordinates (x, y, z) in mm		
Locus coeruleus L	25	4.93	0.001	-4	-36	-20
	6	4.87	0.001	-8	-38	-32
Locus coeruleus R	2	4.42	0.003	8	-37	-32
	4	3.57	0.03	6	-35	-28
	2	3.4	0.046	4	-36	-19

Table 4.2 *- Activation foci within the LC at the appearance of target sounds, for a statistical threshold of p < 0.05 FWE-corrected after small-volume correction using the LC template as search region. R: Right, L: Left.*

Further analyses were conducted in the structural native space of each subject, where the individual LC activity was extracted. The multivariate linear model for the bilaterally averaged estimates of the LC activity did not yield significant main effects for age ($p = 0.57$, $t = 0.57$, 95% CI interval [-0.010, 0.019]), BMI ($p = 0.13$), sex ($p = 0.49$) or education ($p = 0.7$). Boxplots of the LC reactivity in young and late middle-aged individuals are shown in **Figure 4.4A**. Similar statistical outputs were obtained when computing the same model separately with the activity estimate of the left and right LC (main effects for age: left LC, $p = 0.92$, $t = 0.01$, 95% CI interval [-0.017, 0.017], right LC, $p = 0.3$, $t = 1.05$, 95% CI interval [-8e-3, 0.027]) or when adding age group to the model (main effect for age and group: left LC, $p > 0.3$, right LC, $p > 0.5$).

We then used a multivariate linear model to assess the link between LC activity, as dependent variable, and LC contrast. The model did not reveal a significant main effect of LC contrast ($p = 0.77$, $t = -0.29$, 95% CI interval [-22.22, 16.64]), nor an LC contrast by age interaction ($p = 0.77$, $t = 0.77$, 95% CI interval [-0.33, 0.44]) on the LC response (**Figure 4.4B**). Similar statistical outputs were obtained when computing the same model separately with the activity estimate and contrast of the left and right LC, respectively (main effects for LC contrast - left LC: $p = 0.85$, $t = -0.19$, 95% CI interval [-16.47, 13.61]; right LC: $p = 0.13$, $t = -1.51$, 95% CI interval [-22.82, 3.27]), or when adding age group to the model (main effect for age and group: left LC, $p > 0.4$, right LC, $p > 0.3$).

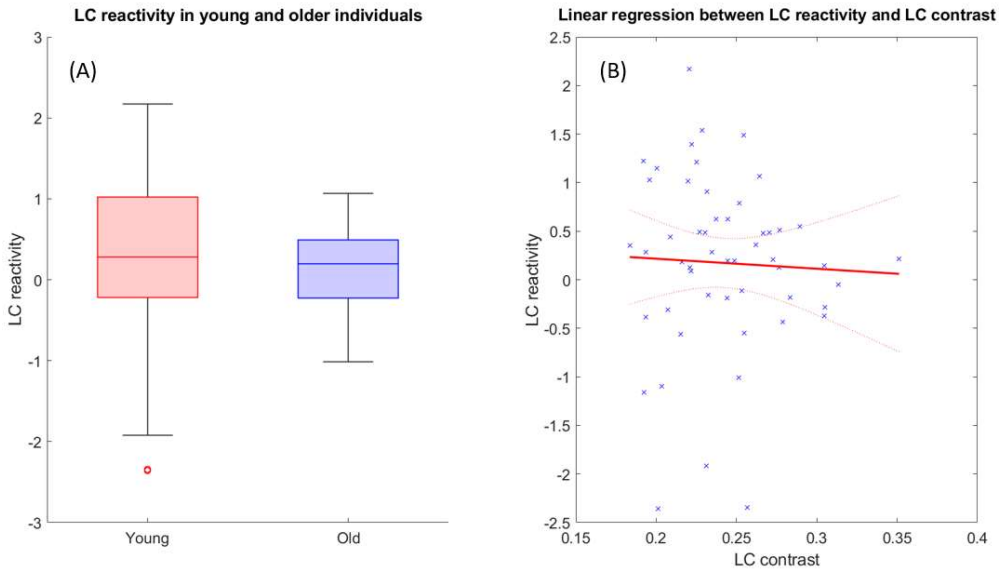

Figure 4.4 - (A) LC reactivity in young and late middle-aged individuals. The horizontal line at the mid-point of the data represents the median, and the colored box (without the whiskers) represents the interquartile range (50% of observations). (B) Association between LC activation and LC contrast. Linear regression plot of LC activity and LC contrast. Solid line: regression line; Dashed lines: 95% confidence interval.

2.3 DISCUSSION

A better characterization of structural and functional characteristics of the LC in healthy individuals is critical (i) to detect abnormal early features occurring in an array of diseases and disorders affecting the LC, (ii) to characterize their possible evolution, and (iii) potentially help in the development of therapies targeting the LC-NE system. We assessed the LC functional response and LC contrast in a cohort of 53 healthy individuals aged 18 to 30 years and 50 to 70 years using a UHF 7T MRI system. We did not find an association between age and LC response, as assessed during

an auditory oddball task. While we found the expected age-related increase in LC contrast, this accepted marker of LC integrity was not significantly related to its functional response.

Although widely studied, the exact source of the LC contrast as extracted using specific MRI sequences remains debated (146). It was hypothesized that LC contrast was related to the progressive increase in neuromelanin that accumulates inside the cell bodies of noradrenergic neurons, as confirmed in *postmortem* studies (203,204). Histology combined with *postmortem* 7T MRI acquisitions revealed that regions with T1-hyperintensities within the LC colocalized with the presence of neuromelanin-rich neurons (205) such that LC contrast might reflect the density of neuromelanin-containing noradrenergic neurons within the LC (176,206). Recent investigations further showed that the LC contrast obtained using a T1-weighted MRI sequence with magnetization transfer was still detectable in mice genetically engineered to have about 70% fewer LC cells (147). Therefore, the LC contrast may not be directly linked to the accumulation of neuromelanin itself but rather to the specific microstructure of noradrenergic neurons (147). Overall, while the LC contrast is deemed to reflect the integrity of the LC (i.e., its neuronal density), lipid accumulation and inflammation have also been suspected to influence the LC contrast (207).

In line with the literature, an expected age-related difference in LC contrast was observed in the present study (206,208). A previous study hypothesized that the increased LC contrast with age may be linked to a related shrinkage of cells within the LC (176). However, a study using staining methods also indicated that the volume of the LC and its neuron population were not affected by normal aging (age range: 47-83 years) (209). We found no indication of a potential plateau or a decreased LC contrast starting after 60 years in our sample, which would be compatible with the previously reported inverted-U relationship between contrast and age, with a maximum contrast found at around 60 years (176,177). This

may be due to a lack of sensitivity as our sample of late middle-aged individuals was relatively young and small: 19 individuals in total with only 10 participants with > 60 years and a range of ages 50-70 years. This may also come in part from the stringent exclusion criteria, which led to a sample of very healthy individuals in which LC integrity could presumably be better preserved. However, this does not mean they could not harbor presymptomatic pathologies such as tauopathy (176). For example, a lower LC contrast is related to higher tau deposition in the entorhinal cortex in cognitively unimpaired individuals (139). Therefore, when studying the effect of normal aging, one cannot exclude that participants included are in a prodromal phase of age-related diseases. Indeed, based on autopsy data, knowing that approximately 50% of individuals between 30 and 40 years present an accumulation of abnormal tau proteins within the LC (210,211), some participants in the current study could already be in a Braak stage I/II. However, a tau PET examination would be needed to determine the Braak stage in our cohort of cognitively intact participants.

The LC is known to be involved in novelty or salience detection (105,212,213). It is reciprocally connected with the cortical salience network to enhance processing behaviorally important stimuli (214). The salience network is involved in high-level cognitive control to detect unexpected stimuli and reorient attention (215). In the present study, a reliable LC response was detected with the UHF 7T MRI system during an auditory oddball paradigm, which mimics novelty and/or salience detection. In contrast to a prior study where pupil response – an accepted output of LC phasic activity – was recorded and used as a regressor to isolate LC response during an auditory oddball task (105), no pupil measurement was required in the present study to extract the LC response. We detected a bilateral activation in the rostral LC – a part of the nucleus densely connected to associative regions (216) – that was mostly left-lateralized. While there is no clear consensus on the presence of lateralization in the LC, there is increasing evidence of regional specialization of the LC in terms of cell composition and projections (217).

Previous tracing studies conducted in rats showed that rostral LC projections innervate a multitude of brain areas, including the hippocampus, the septum, the caudate-putamen (218) and the hypothalamus (218,219). While intense labeling was observed in the caudal LC after the injection of tracers into the thalamus, scattered cell labeling in the rostral LC was also reported (218,220). Although translation to humans may not be straightforward, these results support that the LC subparts are not uniform in terms of projections to the different brain areas. Therefore, it is plausible that the rostral activation reflects, at least in part, a true functional regional effect related to the ongoing cognitive process during the oddball task rather than sensitivity issues (that we cannot, however, rule out).

The fact that the LC response remained stable in late middle-aged individuals compared to young adults was not in line with our expectations. Once again, these results could be due to the very healthy and relatively young nature of our sample or the inability of fMRI to capture subtle LC response differences between individuals during an auditory oddball task. The oddball task may also be too cognitively undemanding to trigger true age-related differences. Despite this, our results suggest that the age-related increase in LC contrast does not necessarily translate into a detectable change in functional response. This observation is further reinforced by the absence of correlation between LC contrast and LC response - at least in a simple auditory mismatch negativity task. Although longitudinal data could confirm this causality, our results may support the idea that LC contrast is more sensitive to aging or takes place before functional changes. One could hypothesize that a compensation mechanism takes place to counter age-related alterations in the LC structure, as reflected by a change in LC contrast. This compensation mechanism would, however, need to scale out exactly the consequence of the structural alteration so that no difference between age groups can be detected. This cannot be ruled out, though compensatory mechanisms to

sustain cognition in aging most often result in higher activation or bilateralization of brain responses (221).

The activity of the LC neurons is known to follow tonic and phasic modes. While the tonic activity of LC neurons is known to be involved in task disengagement and search for alternative behaviors (*'exploration'*), the phasic activity during a goal-oriented task facilitates task-related behaviors to maximize performance (*'exploitation'*) (61). A trade-off between these two modes allows for the maximization of the reward and the utility (61). Since the auditory oddball paradigm in the present study did not require the search for alternative behaviors at the expense of task performance optimization, one could hypothesize that only the phasic activity of the LC was investigated with our protocol. However, the repetition time used for our acquisitions (i.e., 2.34 s) is relatively long compared to the fast burstiness of LC neurons, such that tonic activity or interactions between tonic and phasic activity could contribute to our findings. However, future studies should evaluate the relationship between age-related changes in LC contrast and tonic activity. Other analyses could also probe a potential link between LC contrast and resting-state functional connectivity using the LC as a seed region (222).

It is worth mentioning that while linear patterns are sought in the present study, no individual between the age of 30-50 was sampled, constituting a limitation. A study with a less discretized data sample could confirm our results. Moreover, the sexes of the participants were unbalanced since only 5 males were recruited in each group (young and late-middle-aged individuals). Future studies may also want to use individually tailored HRF to assess LC response. While the canonical HRF we used to model activity over the entire brain seems suitable to model average LC response over a group of participants, individual LC responses can vary substantially across individuals (178).

Given the critical involvement of the LC in cognitive and behavioral processes such as learning and memory (223,224), attention (225),

regulation of sleep and vigilance (115), or addiction (226), assessing its response could be useful to evaluate the integrity of the LC-NE system in a vast array of psychiatric, neurologic, and neurodegenerative disorders. For example, alterations in the activity and/or connectivity of the LC were reported to contribute to the development of depression (227,228) and the symptomatology of schizophrenia (229). Aside from the early tauopathy of the LC that appears to contribute to Alzheimer's disease (139), synucleinopathy contributing to LC degeneration was also detected in prodromal dementia of Lewis bodies (149). Finally, concerning existing therapies targeting the LC-NE system, it was suggested that the functional integrity of this system may be linked to responsiveness to VNS in patients with inoperable DRE (98,103,230). In the context of healthy aging, our results indicate that, while LC contrast changes with age, LC responsiveness may remain stable such that any abnormal response may constitute an early sign of an unhealthy trajectory.

2.4 ORIGINAL CONTRIBUTION

Structural and functional characterization of the locus coeruleus in young and late middle-aged individuals. **A. Berger**, E. Koshmanova, E. Beckers, R. Sharifpour, I. Paparella, I. Campbell, N. Mortazavi, F. Balda, Y.J. Yi, L. Lamalle, L. Dricot, C. Phillips, H. IL. Jacobs, P. Talwar, R. El Tahry, S. Sherif, G. Vandewalle. *Frontiers in neuroimaging 2:1207844, 2023. doi: 10.3389/fnimg.2023.1207844.*

CHAPTER 5. LOCUS COERULEUS FEATURES IN PATIENTS WITH DRUG-RESISTANT EPILEPSY

1. INTRODUCTION AND OUTLINE OF THE CHAPTER

In this chapter, MRI was used to assess features of the LC in patients with DRE in order to refine our current knowledge about the LC-dependent mechanisms of action of VNS and explore the possible relationship between these features and response to VNS. Indeed, as extensively described in the introduction, a great interest has been brought to the LC, as this nucleus constitutes the main source of norepinephrine in the brain, a neurotransmitter known to confer antiseizure effects. Although the recent development of MRI sequences allowed an *in vivo* visualization of this nucleus, these techniques have never been used to investigate LC properties in DRE patients implanted with a VNS device.

The first part of this chapter deals with LC sequence optimization. Magnetic Resonance (MR) sequences allowing the visualization of the LC are not part of clinically available MRI sequences and are dependent on the MRI system used. Therefore, this sequence had to be developed and optimized before being used for *Study 3*. In this context, qualitative and quantitative analyses were conducted to select the sequence leading to the best LC visualization.

The second part of the chapter focuses on the actual analysis of LC characteristics in DRE patients implanted with a VNS device using a multimodal MRI approach. The primary goals of *Study 3* were to test whether MRI-based LC contrast and functional response were related to

the therapeutic efficacy of VNS. For the structural analysis, the sequence developed and optimized in the first part of the chapter was used and allowed to extract the LC contrast. The functional response of the LC was assessed with fMRI during an auditory oddball task - a task known to recruit the LC, as demonstrated in Chapter 4. We further explored whether these LC characteristics were related to the duration of VNS therapy in the search for potential neuroplasticity effects. Moreover, knowing that long-term suppression of seizures may be due to the release of norepinephrine in the hippocampus (84,86,94), the structural integrity of the white matter tracts arising from the LC and projecting to the hippocampus was explored. The integrity of white matter tracts was inferred based on multi-shell diffusion MRI data and the use of two diffusion models described in Chapter 1: DTI and MF. We hypothesize that a relationship between integrity in these tracts and therapeutic efficacy may exist.

2. LOCUS COERULEUS MRI SEQUENCE OPTIMIZATION

For conducting the analyses in this chapter, preliminary work consisted of developing and optimizing an MRI sequence to visualize the LC *in vivo* using the GE 3T SIGNA™ Premier MRI system of Saint-Luc University Hospital. When developing an MR sequence, changing parameters of an MRI sequence such as TR or TE, lead to a different image contrast. Different MRI sequences are used in the literature to image the LC, including Fast Spin Echo (FSE), T1-weighted Fast Low Angle Shot (FLASH), 3D Spoiled Gradient Recalled echo with Magnetization Transfer (SPGR MT), Turbo Spin Echo (TSE), Inversion Recovery (IR), T1-weighted Magnetization Transfer (T1-MT), Magnetization Transfer Turbo-FLash (MT-TFL) and Spin Echo (SE) sequences – each of them being specific to the constructor of the MRI system (141,176,177,205,231–238). While TSE and MT-TFL sequences are the most widely used MR sequences to image the LC, previous data suggested that sequences with MT can achieve a higher spatial resolution than TSE sequences using a 3T MRI system (237). In this context, different sequences were tested and optimized using the GE 3T SIGNA™ Premier MRI system (as summarized in **Table 5.1**).

Sequence	Flip angle (°)	TR (ms)	TE (ms)	Voxel size (mm^3)	Number of slices	Averages
1. MT-TFL	8	81	4	0.39 x 0.39 x 1.5	28	1
2. MT-TFL	8	54	4	0.39 x 0.39 x 1.2	28	1
3. MT-TFL	8	54	5	0.39 x 0.39 x 1.7	28	1
4. MT-TFL	12	54	5	0.39 x 0.39 x 1.7	28	1
5. MT-TFL	16	54	5	0.39 x 0.39 x 1.7	28	1
6. MT-TFL	16	68	5	0.39 x 0.39 x 1.7	28	1
7. MT-TFL	20	68	5	0.39 x 0.39 x 1.7	28	1
8. MT-TFL	16	68	10	0.39 x 0.39 x 1.7	28	1

Table 5.1 – Parameters of MR sequences (Magnetization Transfer Turbo-FLash – MT-TFL) tested for LC sequence optimization. Corresponding images can be found in ***Figure 5.1****.*

The MRI sequence leading to the best LC visualization was determined based on qualitative and quantitative analyses. Concerning the qualitative analysis, two raters inspected each MT-TFL sequence carefully and independently and determined the one leading to the best LC visualization – i.e., the sequence allowing the easiest LC delineation. Using sequences MT-TFL 1-4, the cerebrospinal fluid appears as hyperintense as the LC (**Figure 5.1**). Although the LC is visible on the axial and coronal slices, its delineation is rendered more difficult. On the opposite, the signal from the cerebrospinal is lower for sequences MT-TFL 5-8, making it appear darker on the images and facilitating the LC extraction. The two raters independently selected the MR sequence MT-TFL 7 as the sequence leading to the easiest LC delineation. The sequence chosen is characterized by the highest flip angle and leads to the best contrast between the LC and the surrounding tissues and structures.

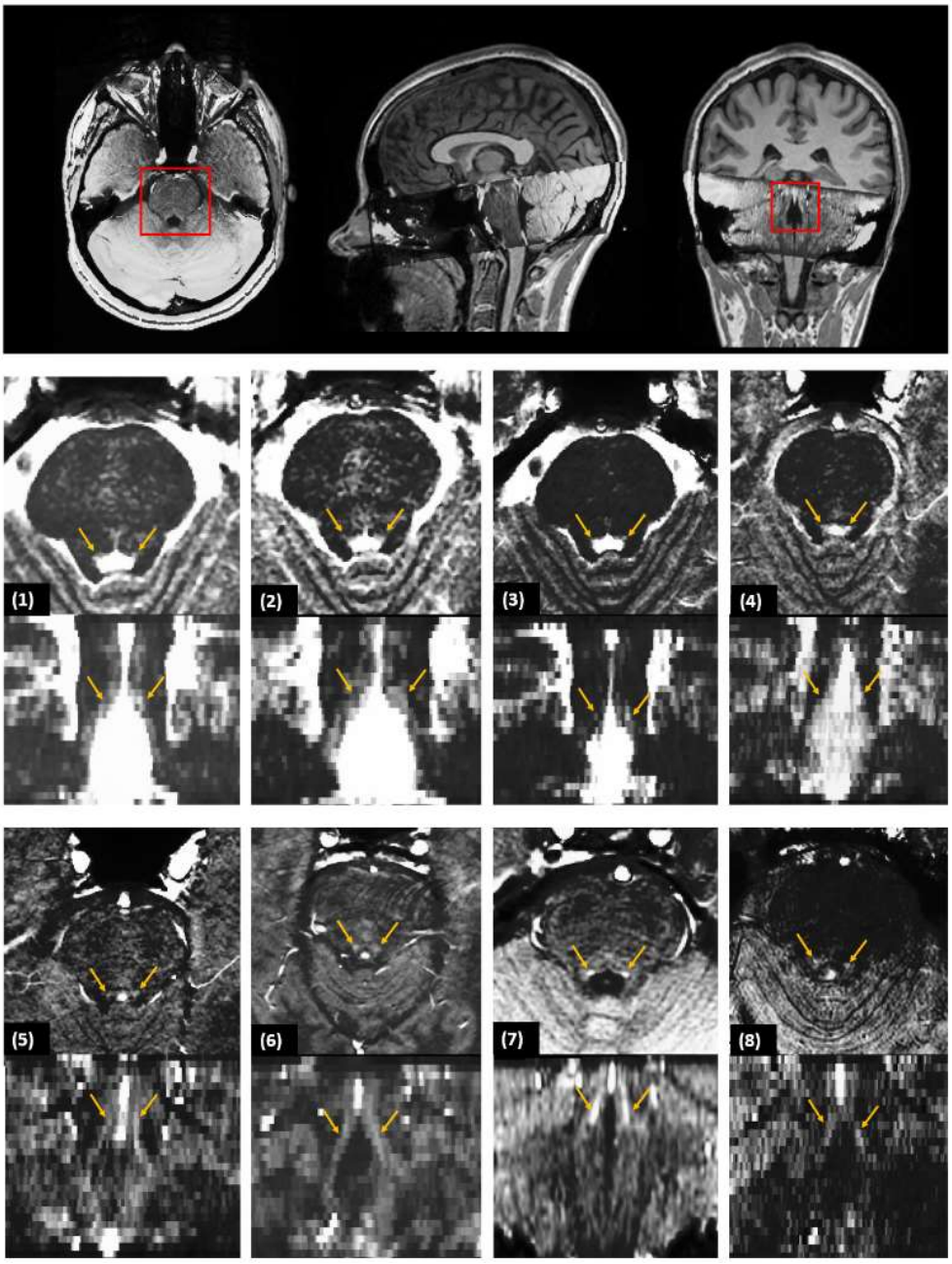

Figure 5.1 – Visualization of the locus coeruleus (LC) with the different Magnetization Transfer Turbo-FLash (MT-TFL) MRI sequences tested. Parameters of the sequences are: (1) FA = 8°, TE = 4 ms and TR = 81 ms ; (2)

FA = 8°, TE = 4 ms and TR = 54 ms, (3) FA = 8°, TE = 5 ms and TR = 54 ms, (4) FA = 12°, TE = 5 ms and TR = 54 ms, (5) FA = 16°, TE = 5 ms and TR = 54 ms, (6) FA = 16°, TE = 5 ms, and TR = 68 ms, (7) FA = 20°, TE = 5 ms and TR = 68 ms, (8) FA = 16°, TE = 10 ms and TR = 68 ms.

In order to confirm the selection of the LC sequence based on the qualitative analysis, the intensity was evaluated in four landmarks for each sequence, with interest points positioned in the left and right LC - in the axial slice with the highest LC intensity, the CSF and the anterior-most part of the rhomboid fossa (**Figure 5.2**). MT-TFL 7 gives the best discrimination between the two LC and the landmarks, confirming the sequence selection of the two raters (**Figure 5.3**).

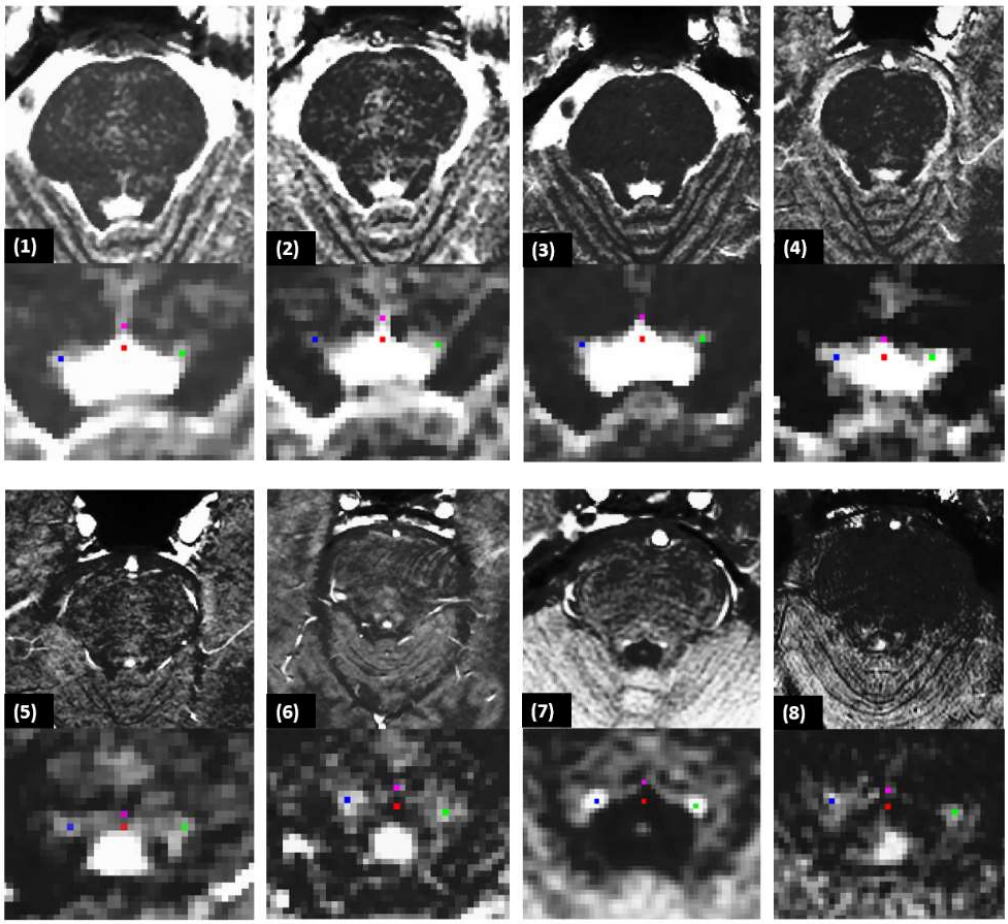

Figure 5.2 – LC sequence selection - landmarks for each MT-TFL sequence: CSF (red), right LC (blue), left LC (green), and the anterior-most part of the rhomboid fossa (pink).

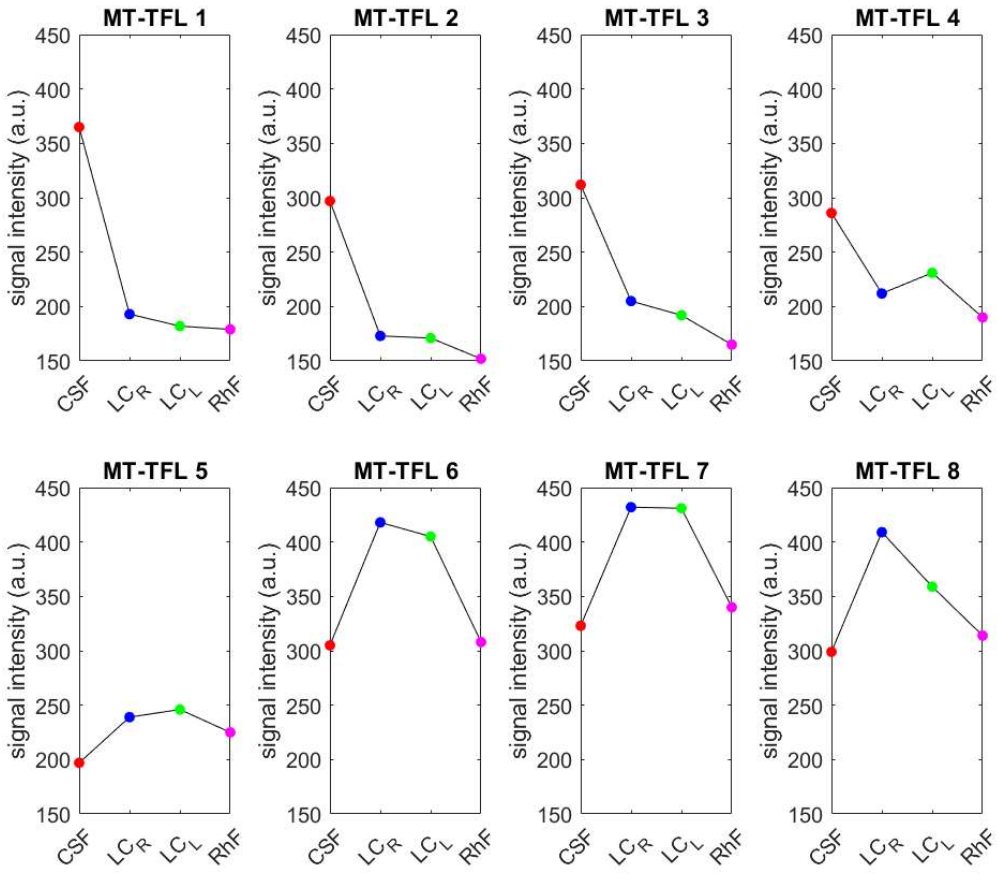

Figure 5.3 – LC sequence selection - intensity in the landmarks to study the contrast between the LC and the surrounding tissues for the different MT-TFL sequences tested. CSF: cerebrospinal fluid, LC_R: right locus coeruleus, LC_L: left locus coeruleus, and RhF: anterior-most part of the rhomboid fossa.

Finally, after the data acquisition of LC images of 23 subjects (37.26 ± 12.91 years, 13 females) with the selected MRI sequence, LC masks were manually created by two independent raters (more information about the LC mask creation in the next section). In order to validate the MRI sequence selected, the Sørensen-Dice Similarity Coefficient between the masks of the two raters was computed for each subject as:

$$DSC = 2 * \frac{\sum_{i=1}^{N}(LC_{rater\ 1,i} * LC_{rater\ 2,i})}{\sum_{i=1}^{N}(LC_{rater\ 1,i} + LC_{rater\ 2,i})}$$

Where:

- $LC_{rater\ 1,i}$ is the i^{th} voxel in the binary LC mask created by rater 1 (and correspondingly $LC_{rater\ 2,i}$ for rater 2).
- N is the total number of voxels.

Based on the manual LC delineations of 23 subjects, the mean DSC values for the right and left LC were respectively 0.63 (± 0.15) and 0.65 (± 0.11). Moreover, for the right and left LC, 78.5% and 74% of DCS values were greater than 0.6. In lesion studies, delineations of lesions on MRI images are thought to show a good similarity for DSC values between 0.6-0.8, with 0.7 or higher known to reflect a high similarity (239). Therefore, our analyses demonstrate a good reproducibility of LC mask creation using the selected MT-TFL sequence. Previous 3T MRI studies where LC delineation of healthy subjects was performed manually by two experienced raters reported mean DSC values of 0.499 (240), 0.6 (241) and ranged between 0.54-0.64 in a test-retest reliability study that included multiple scan sessions (242). It is worth mentioning that comparing DSC values reported in studies with LC segmentation in healthy subjects or in patients with a possible alteration of this nucleus should be done cautiously.

The manual segmentations of the LC done by the two independent raters in our study are, therefore, in the upper-high range of similarity measurements compared to the values found in the literature. Although manual delineation may have a part of subjectivity, this technique is still considered the gold standard for LC mask creation. To remove a part of the subjectivity, the intersection of the LC masks was computed for analyzing LC features in *Study 3*. The computation of DSC values in the present section only aimed at giving an indication of LC visibility and reproducibility

for LC mask creation using the selected MT-TFL sequence. Therefore, although the sequence used in the present study shows good LC visibility as assessed with qualitative and quantitative analyses, future studies could aim to tune MR sequence parameters further to continue improving LC imaging using the GE 3T SIGNA^{TM} Premier MRI system.

3. Study 3 : Locus coeruleus features are linked to vagus nerve stimulation response in drug-resistant epilepsy

Abstract

The LC-NE system is thought to be involved in the clinical effects of VNS. This system is known to prevent seizure development and induce long-term plastic changes, particularly with the release of NE in the hippocampus. However, the requisites to become responder to the therapy and the mechanisms of action are still under investigation. Using MRI, we assessed the structural and functional characteristics of the LC and microstructural properties of LC-hippocampus white matter tracts in patients with DRE responding or not to VNS therapy. Twenty-three DRE patients with cervical VNS were recruited for this pilot study, including 13 responders or partial responders and 10 non-responders. A dedicated structural MRI acquisition allowed in vivo localization of the LC and computation of its contrast (an accepted marker of LC integrity). LC activity was estimated using fMRI during an auditory oddball task. Finally, multi-shell diffusion MRI was used to estimate the structural properties of LC-hippocampus tracts. These characteristics were compared between responders/partial responders and non-responders, and their association with therapy duration was also explored. In patients with a better response to the therapy, trends toward a lower activity and a higher contrast were found in the left medial and right caudal portions of the LC, respectively. An increased LC contrast, bilaterally over its medial portions, correlated with the duration of the treatment. Finally, a higher integrity of LC-hippocampus connections was found in patients with a better response to the treatment. These new insights into the neurobiology of VNS may provide novel markers of the response to the

treatment and may reflect neuroplasticity effects occurring in the brain following VNS implantation.

3.1 Material and methods

3.1.1 Participants

Patients were recruited from the VNS database of the Center for Refractory Epilepsy of Saint-Luc University Hospital, Brussels, Belgium. The patients met the following criteria: (i) DRE diagnosis, (ii) treated with VNS (DemiPulse® Model 103 or DemiPulse Duo® Model 104, AspireHC® Model 105 or AspireSR® Model 106; LivaNova, Inc., London, UK) for at least six months, (iii) able to understand the study protocol and (iv) aged 18 years or older. Exclusion criteria consisted of severe side effects of VNS reported by the patients, such as dyspnea, pain in the neck/ear region, gastrointestinal complaints, history of alcohol or drug abuse, the presence of psychiatric illnesses, hearing problems reported by the patients, travel in a country with a different time zone over the last month and any MRI contraindication. The clinical response to VNS was determined by the neurologist at the last follow-up visit. Based on these criteria, 23 patients were recruited, including 10 non-responders, 5 partial responders and 8 responders, presenting, respectively, < 30%, 30–50% (with seizure-suppressing effects reported with the magnet mode – when swiping the magnet in front of the generator) and > 50% reduction in seizure frequency (**Table 5.2**). In four non-responders, the VNS was off for several reasons: (i) two patients were explanted four months and 2.4 years before the experiment, (ii) in one patient the device was turned off completely for almost two years due to side effects, and a lack of response, and (iii) in one patient the battery was empty and not replaced since no positive effect was observed. All patients signed the informed consent prior to any

investigation. The study received approval by the Ethical Committee of Saint-Luc University Hospital (reference nr. 2021/18FEV/086).

Characteristics	**NR (n = 10)**	**R/PR (n = 13)**	**p-value**
Age (years)	35.1 ± 15.19	38.92 ± 11.22	0.49
Sex	6 Females 4 Males	7 Females 6 Males	1.00
Therapy duration of VNS (months)	91.1 ± 52.15	72.54 ± 83.54	0.54
Epilepsy type	10 Focal 0 Generalized	11 Focal 2 Generalized	0.48
Epilepsy duration (years)	24 ± 11.32	28.31 ± 13.62	0.49
Number of ASMs (number of patients)	2 ASMs : 4 3 ASMs : 3 4 ASMs : 3	2 ASMs : 6 3 ASMs : 6 4 ASMs : 1	0.22
Benzodiazepine (daily) intake (number of patients)	2	1	0.18
VNS intensity (mA) [a]	1 mA : 0/6 1.125 mA : 0/6 1.25 mA : 0/6 1.50 mA : 1/6 1.75mA : 3/6 2 mA : 2/6	1 mA : 2/13 1.125 mA : 1/13 1.25 mA : 2/13 1.50 mA : 5/13 1.75 mA : 1/13 2.00 mA : 2/13	0.03
VNS frequency (Hz) [a]	20 Hz : 4 25 Hz : 2 30 Hz : 0	20 Hz : 5 25 Hz : 2 30 Hz : 6	0.15

VNS pulse width (µs) [a]	250 µs : 5 500 µs : 1	250 µs : 11 500 µs : 2	1.00
Rapid duty cycle [a,b]	0	2	0.91

Table 5.2 - Demographic and clinical characteristics of the study population. [a] Values reported after excluding 4 NR (see text). [b] The duty cycle is defined as (ON time + 4 s)/(ON time + OFF time), and a rapid duty cycle is defined as an OFF time ± 1.1 min while keeping the duty cycle ± 50% (162). *NR: non-responder, R: responder, PR: partial responder, ASM: antiseizure medication.*

3.1.2 ODDBALL PARADIGM

Knowing that the auditory oddball task recruits the LC (243,244), this paradigm was chosen to extract the functional response of the LC in a VNS OFF condition in the current study. The task was administered during fMRI acquisitions and consisted of rare target stimuli (1000 Hz sinusoidal waves, 100 ms) appearing approximately 20% of the time and pseudorandomly interleaved in a stream of standard sounds (500 Hz sinusoidal waves, 100 ms). Two hundred and twenty stimuli were administered in total, including 46 target tones (interstimulus interval: 2500 ms). The experimental paradigm was designed using OpenSesame 3.3.8 (188). MRI-compatible headphones (NeuroNordicLab, Bergen, Norway) were used to deliver the stimuli. Participants were instructed to press a button box (ResponseGrip, NeuroNordicLab, Bergen, Norway) with the right index finger as soon as possible at the appearance of target sounds. A test sequence composed of 35 stimuli, including 8 target sounds, was performed during an MRI

acquisition to ensure an optimal perception of the stimuli and comprehension of the instructions.

3.1.3 IMAGING PARAMETERS

The MRI acquisitions were realized following the LivaNova guidelines for MRI (setting the output current to 0 mA and turning off sensing). Imaging data were acquired using the SIGNA^{TM} Premier 3T MRI system (GE Healthcare, Milwaukee, WI, USA) with a 48-channel head coil. T1-anatomical images were acquired using a Magnetization Prepared — RApid Gradient Echo (MPRAGE) sequence: TR = 2186 ms, TE = 2.95 ms, FA = 8°, TI = 900 ms, bandwidth = 244.14 Hz, matrix size = 256 × 256, 156 axial slices, imaging frequency = 127.77 Hz, voxel size = (1 × 1 × 1)mm^3, acquisition time = 5:26 min.

A high-resolution MT-TFL sequence was used to visualize the LC: TR = 68 ms, TE = 5 ms, FA = 20°, bandwidth = 65.12 Hz, matrix size = 512 × 512, 28 axial slices, voxel size = (0.39 × 0.39 × 1.7)mm^3, acquisition time = 11:40 min. For this axial acquisition, the LC slab was centered perpendicularly to the rhomboid fossa, i.e., the floor of the fourth ventricle. BOLD fMRI data were acquired with a multiband EPI sequence: acceleration factor = 3, TR = 1700 ms, TE = 30 ms, FA = 90°, bandwidth = 3906.2 Hz, matrix size = 128 × 128, 75 axial slices, voxel size = (1.7 × 1.7 × 2)mm^3, number of volumes acquired = 335, acquisition time = 9:41 min. Diffusion MRI data were acquired with a PGSE sequence: TR = 4837 ms, TE = 80.5 ms, and flip angle = 90°. A high-gradient multi-shell diffusion scheme was used and consisted of 64 gradients at b = 1000 [s · mm^{-2}] and 32 gradients at b = 2000, 3000, and 5000 [s · mm^{-2}], interleaved with 7 b0 images. The in-plane field-of-view was 220 × 220 mm^2, the matrix size was 110 x 110, and the data contained 68 axial slices with a 2-mm thickness (no inter-slice gap, 2-mm isotropic voxels). A multi-slice excitation scheme was used during the

acquisition with a hyperband slice factor of three to reduce the acquisition time. The total acquisition time was 13:33 min. Finally, a T2-weighted image was acquired to improve the patient-specific segmentation of the hippocampus. The T2-weighted image was acquired using a SE sequence: TR = 2.5 ms, TE = 91 ms, FA = 90°, matrix size = 255 × 255, 141 sagittal slices, voxel size = (1 × 1 × 1)mm^3, acquisition time = 2:01 min.

3.1.4 DATA ANALYSIS

3.1.4.1 LC CONTRAST EXTRACTION

T1-anatomical images were upsampled by a factor of three, ending up with a resolution of (0.33 × 0.33 × 0.33)mm^3, to avoid losing in-plane resolution when registering the LC slab to the T1 image. The MT-TFL image of each subject was registered to the whole brain upsampled T1 image by means of a two-step process: (i) a rough manual registration to extract the parameters for an initial transformation using ITK-SNAP (245) and (ii) an automatic registration based on the initial transformation parameters, using the advanced normalization tools (ANTs, Penn Image Computing and Science Laboratory, UPenn, USA, *https://stnava.github.io/ANTs/*) (**Figure 5.4-A**). Two trained raters (AB and EB) manually delineated the LC independently. The intersection of the LC masks of the two raters was computed (**Figure 5.4-B**). Each LC mask was then divided into different subregions (25% rostral, 50% medial, and 25% caudal portions of the LC) (**Figure 5.4-C**). Other studies investigating LC integrity in different clinical conditions also used subdivisions of the LC based on the fact that the LC is topographically organized in regions composed of cells projecting to different areas of the brain (232,246–250). It was suggested that the rostral part of the LC would project to the forebrain, including the hippocampus, while the medial and caudal portions would project to the basal ganglia,

cerebellum, and spinal cord (218,219,251,252). While no evidence currently exists on how VNS could differentially activate or modulate each of these subregions and how each region could be individually involved in the antiseizure effects of VNS, subdivisions of the LC were used in the present study to investigate more specific differences that could be hidden when considering the LC as a whole.

For each axial slice of the LC subpart masks, a 5-voxel cross was centered on the voxel with the highest intensity (**Figure 5.4-D,E**). For each LC slice, the LC intensity was normalized to a slice-corresponding 2D reference region [a 15 × 15 voxels region, corresponding to a (4.95 × 4.95)mm^2 square region] situated anteriorly to the LC in the pons, in the pontine tegmentum (**Figure 5.4-F**). Therefore, the complete reference region is a 3D region composed of (number of LC slices × 15 × 15) voxels. The LC contrast was computed as the mean normalized intensities over the length of the LC. Therefore, for each LC subpart, the contrast was computed as follows (e.g., for left LC):

$$Contrast\ LC_{Left-Rostral} = \frac{1}{n} \sum_{i=1}^{n=|LC_{Left-Rostra}|} \left(\frac{\overline{LC}_{Left-Rostral,i}}{\overline{pons}_i} - 1 \right)$$

Where:

- *i* is the slice index along the LC subpart.
- *n* is the number of slices along the LC subpart.
- $\overline{LC}_{Left-Rostra\ ,i}$ is the mean intensity within the 5-voxel cross for the LC slice with index i.
- $\overline{pons}_i$ is the mean intensity within the corresponding 2D reference region (15 x 15 voxels) for the LC slice with index i.

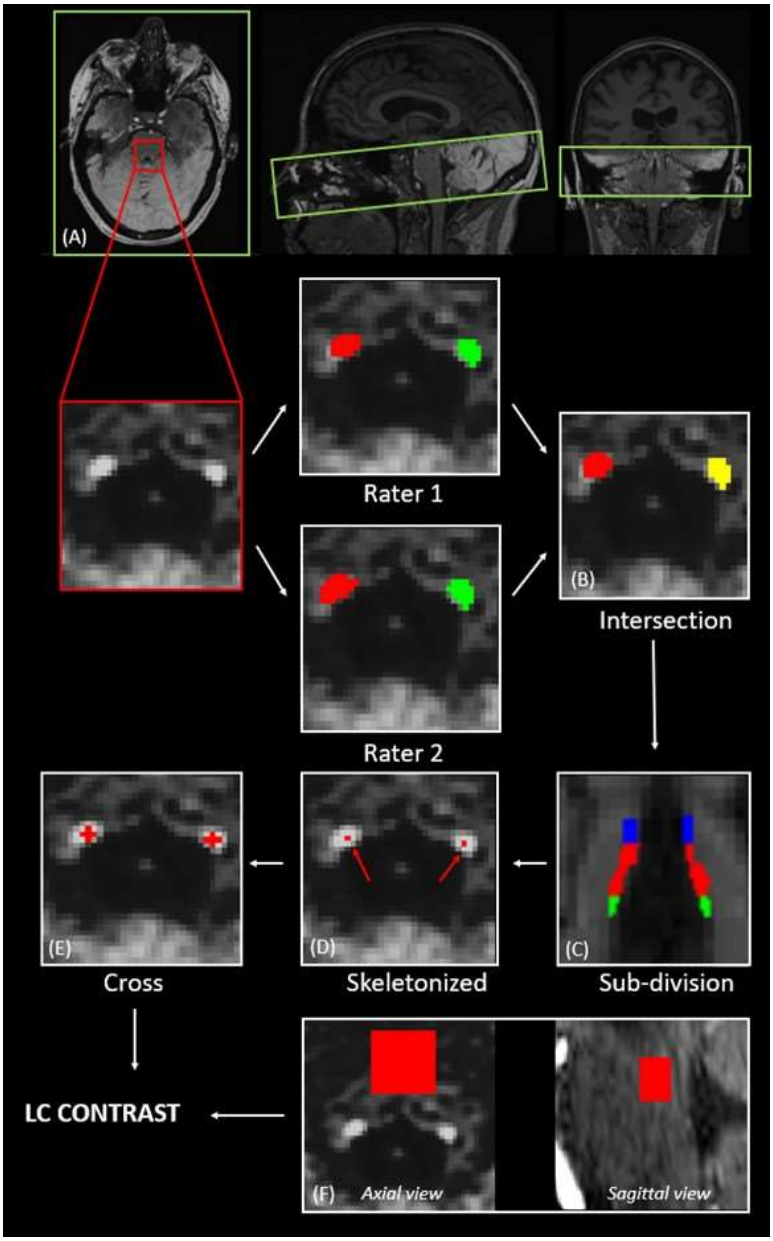

Figure 5.4 - Extraction of the LC contrast. (A) Registration of the LC slab to the structural T1-weighted anatomical image (axial, sagittal and coronal views) ; (B) Computation of the intersection of the LC masks of two independent raters ; (C) Subdivision of the LC into rostral – 25 upper %

(blue), medial – 50 middle % (red), and caudal – 25 lower % (green); (D) Selection of the voxel with the highest intensity for each axial slice ; (E) Centering of a 5-voxel cross on the voxel with the highest intensity ; (F) Definition of a slice-corresponding reference region in the pons (axial view), and final 3D reference region (sagittal view).

3.1.4.2 FUNCTIONAL PREPROCESSING AND LC ACTIVITY EXTRACTION

BrainVoyager (Brain Innovation B.V., Maastricht, Netherlands) was used to process EPI images. First, slice scan time correction was applied using the cubic spline interpolation. Three-dimensional motion correction was applied with a trilinear/sinc interpolation, using the first volume as the reference volume. Temporal high pass filtering was applied using the GLM approach with the Fourier basis set to remove slow-frequency drift. A default cut-off of 3 cycles was used, meaning that sine and cosine functions with cycles < 3 are modeled in the design matrix and removed from the voxel's time course. Registration of fMRI data to the structural space was realized after conducting brain extraction on the T1 image. For the registration, the initial alignment was conducted before a fine-tuning alignment based on the intensity of the images using multi-scale rigid-body transformations. The timing vector containing the appearance of target sounds was convolved with the standard two-gamma HRF and used as the main condition in a GLM. Realignment parameters (three translations and three rotations) were used as multiple regressors of no interest. All predictors were z-transformed before fitting the model. A region-of-interest (ROI) analysis was conducted in the space of the subject. Based on the ROI signal time course, the beta values associated with the target appearance were extracted in the left and right LC subparts for each subject.

3.1.4.3 MICROSTRUCTURAL FEATURES OF LC-HIPPOCAMPUS CONNECTIONS

Diffusion data of 18 patients were available, including data of 7 non-responders and 11 responders/partial responders. Due to an amygdalohippocampectomy performed in the right hemisphere of one patient (a non-responder), LC-hippocampus connections were extracted in 17 patients for the right hemisphere and in 18 patients for the left hemisphere. Data preprocessing was done using ElikoPy (*https://github.com/hyedryn/elikopy*). Preprocessing steps included: skull stripping [using the Diffusion Imaging In Python library—DiPy, *https://dipy.org/*, (253)], Rician denoising [using the Marcheko–Pastur Principal Component Analysis–MPPCA (254)], Eddy currents, susceptibility distortion, and motion corrections [Eddy command of the FMRIB Software Library — FSL, *https://fsl.fmrib.ox.ac.uk/fsl/fslwiki* (255)]. DTI maps (FA, MD, AD, and RD) were reconstructed using DiPy. **A** multi-compartment fingerprinting model (known as MF) based on Monte Carlo simulations of diffusion MRI signals was also used to extract quantitative microstructural features of white matter (137). As described in Chapter 1, MF is a powerful multi-compartment model that does not make assumptions about the tissues and the diffusion processes (137). MF estimates the occupancy fraction of the crossing fascicles within each voxel and their corresponding fiber volume fraction [or axonal density (256)]. Therefore, the wFVF value estimated in each voxel is defined as:

$$wFVF_i = \frac{\nu_{1,i} * fvf_{1,i} + \nu_{2,i} * fvf_{2,i}}{\nu_{1,i} + \nu_{2,i}}$$

Where :

- *i* is the index of the voxel.
- $\nu_{1,i}$ is the fraction of occupancy of fascicle 1 in voxel *i* (and $\nu_{2,i}$ for fascicle 2).
- $fvf_{1,i}$ is the fiber volume fraction of fascicle 1 in voxel *i* (and $fvf_{2,i}$ for fascicle 2).

All diffusion maps were registered to the structural space of the subject after registering the FA map to the T1-weighted image using the *'antsRegistration'* function from ANTs and applying the transformation parameters to the other diffusion maps. In order to extract the mean diffusion metrics along the LC-hippocampus connections, DSIstudio (*https://dsi-studio.labsolver.org/*) was used for the reconstruction of the fiber direction, using generalized Q-sampling imaging (QSI) (257) with a default diffusion sampling length ratio of 1.25. The left and right LC masks were dilated by one voxel in every direction using DSIstudio. Segmentation of the left and right hippocampi was conducted with Freesurfer (Linux — centOS *version 7.2*) in the structural space of the subject using the T1- and T2-weighted images to improve segmentation of pial surfaces. The dilated left and right LC masks were used as seed regions, with the left and right hippocampal masks used as end regions, respectively. The quantitative anisotropy was used as the tracking index, and default lengths of minimum of 30 mm and maximum of 300 mm were used for the tractography. The deterministic fiber tracking was done with the Runge–Kutta method, using a seed count of 10 million as the terminative criterion. For each patient, the final tractography was visually and carefully inspected by a neurosurgeon (VJ), and false fibers were excluded to clean the tracts. The mean diffusion metrics (DTI: FA, MD, RD, AD, and MF: wFVF) were then extracted in the left and right LC-hippocampus connections.

3.1.4.4 STATISTICAL ANALYSIS

Statistical analyses were conducted using RStudio (*version 4.2.1*). The demographic and clinical characteristics were compared between non-responders and responders/partial responders using Mann–Whitney U-tests or Fisher's exact tests for categorical variables (**Table 5.2**). After conducting Shapiro-Wilk normality tests without rejection of the null

hypothesis (normality of the data) for the LC contrast, LC activity and diffusion metrics in LC-hippocampus connections, two linear models (LM) were used to model these features in terms of response and therapy duration (total duration between the implantation day and the MRI acquisition), controlling for age, sex, ASM intake, epilepsy duration and benzodiazepine intake – as they may lead to cognitive dysfunctions ascribed to sedation or inattention (258), making this covariate particularly important for an attentional task. In this pilot study, two models were used to assess independently the relationship between the LC features and VNS response or therapy duration to avoid possible multicollinearity issues. Indeed, it has been reported that the response rate to VNS increases with therapy duration (259). In addition, while no difference in therapy duration was found between responders/partial responders and non-responders in the present pilot study, the statistical approach considering independently VNS response and therapy duration in the models may be useful in studies with larger cohort of patients, where these two variables may not be independent. False discovery rate (FDR) correction was conducted for each LC metric to correct for multiple comparisons. Results of the statistical tests were considered significant for $p_{FDR} < 0.05$, while only a trend is considered for uncorrected $p < 0.05$. In order to avoid fitting problems with the LM due to possible multicollinearity of the predictors, the variance inflation factor (VIF) was computed for the predictors included in each model and VIF values were lower than 5 (low correlation between the predictors).

3.2 RESULTS

3.2.1 ACCURACY OF THE ODDBALL TASK

FMRI data was not available for one non-responder, for whom MRI acquisitions were stopped after the structural acquisitions due to the occurrence of a seizure during the acquisitions. The mean accuracy to the oddball task was 85.44 ± 29.94% when all patients were considered, which we consider reasonable given the patients population. Four patients (two responders and two non-responders) had relatively low accuracy to the task (< 90%). Excluding these patients led to an accuracy of 98.30 ± 2.58%. Results of the statistical analyses are reported for the complete sample of patients and with the reduced sample, including patients with a good accuracy to the task only (> 90% detection of target sounds). Group-level analysis of the general oddball effects for validating the paradigm can be found in **Supplementary Material S5.1** and **Supplementary Material S5.2**.

3.2.2 LOCUS COERULEUS RESPONSE

The output of all the statistical models can be found in **Supplementary Material S5.3**. The LM using LC response as dependent variable, revealed a trend toward a significant relationship (not significant after FDR correction) between VNS response and LC response in the medial portion of the left LC (N = 22, p = 0.01*, p_{FDR} = 0.05 and N = 18, p = 0.03*, p_{FDR} = 0.11, when only patients with good accuracy are included), after controlling for age, sex, ASM intake, benzodiazepine intake and epilepsy duration (**Supplementary Material S5.3-A**). For visual purposes, boxplots of the response in LC subparts in responders/partial responders and non-responders are shown in **Figure 5.5**. No significant main effect of therapy duration was observed for the response in the medial portion of the left LC (N = 22, p = 0.72; and N = 18, p = 0.57, when only including patients with good accuracy) (**Supplementary Material S5.3-B**).

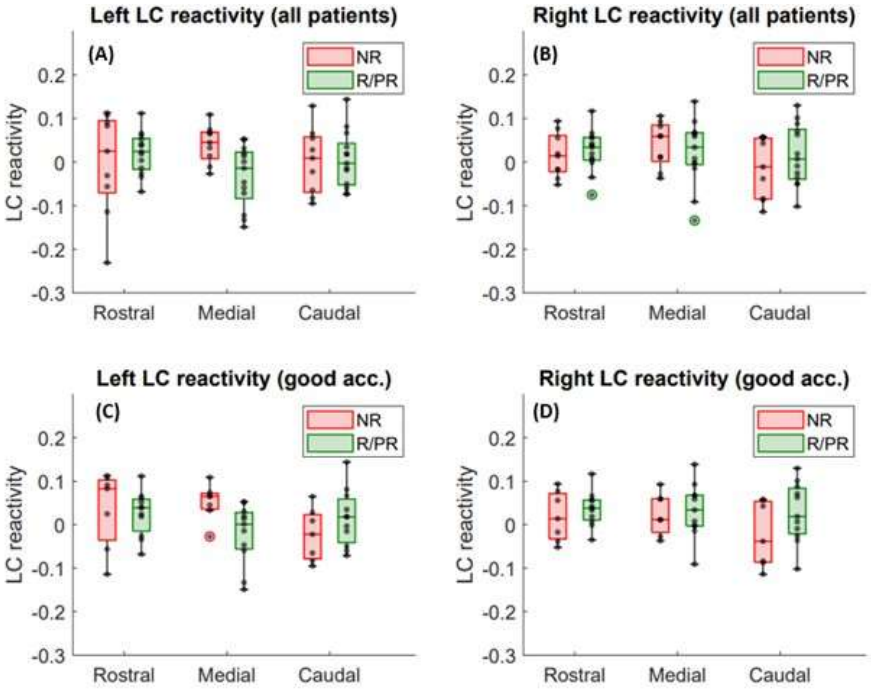

Figure 5.5 - LC response to target stimuli in patients responding (or partially responding) and not responding to VNS treatment. Activity in the rostral, medial, and caudal portions of the (A) left LC (all patients included), (B) right LC (all patients included), (C) left LC (only patients with a good accuracy to the task, i.e., > 90%) and (D) right LC (only patients with a good accuracy to the task, i.e., > 90%), in Non-Responders (NR) and Responders (R)/Partial Responders (PR). Refer to text and ***Supplementary Material S5.3*** *for full statistical output of the LM.*

3.2.3 LOCUS COERULEUS CONTRAST

A trend toward a significant relationship (not significant after FDR correction) was found between VNS response and LC contrast in the caudal portion of the right LC ($p = 0.03^*$, $p_{FDR} = 0.08$) (**Supplementary Material S5.3-C**). Moreover, a trend toward a significant effect of therapy duration

on the contrast in the medial portion of the left and right LC was observed (left: p = 0.03*, p_{FDR} = 0.11 and right: p = 0.04*, p_{FDR} = 0.11— **Supplementary Material S5.3-D**). For visual purposes, regressions between the contrast of LC subparts and therapy duration are shown in **Figure 5.6**.

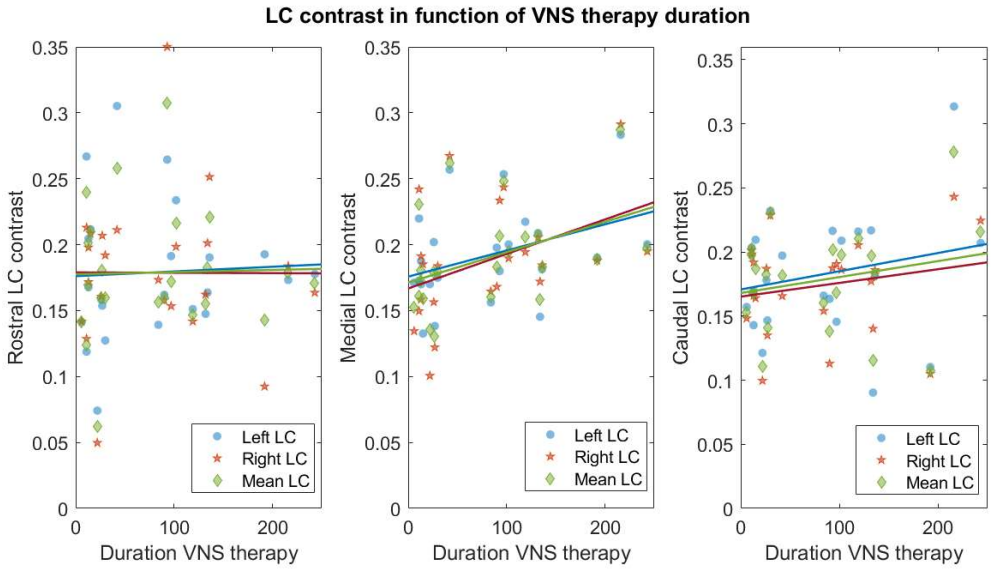

*Figure 5.6 - Linear regressions between the contrast in LC subparts and therapy duration. Linear regressions for the rostral, medial, and caudal left (blue circles), right (orange stars), and mean over left and right (green diamond) LC and therapy duration (expressed in months). Refer to **Supplementary Material S5.3** for full statistical output of the LM.*

3.2.4 LOCUS COERULEUS – HIPPOCAMPUS MICROSTRUCTURE

Due to the small size of the LC and the resolution of the diffusion data, the left and right LC masks were used without rostro-caudal subdivisions for the tractography. The tractography between the LC and the

hippocampus yielded two bundles reaching, respectively, the head and the tail of the hippocampus (**Figure 5.7**). This corresponds to the described anatomy of the ascending noradrenergic bundles (260). Both bundles were considered jointly in our analyses. Individual tracking of LC-hippocampus connections realized in all patients can be found in **Supplementary Material S5.4**.

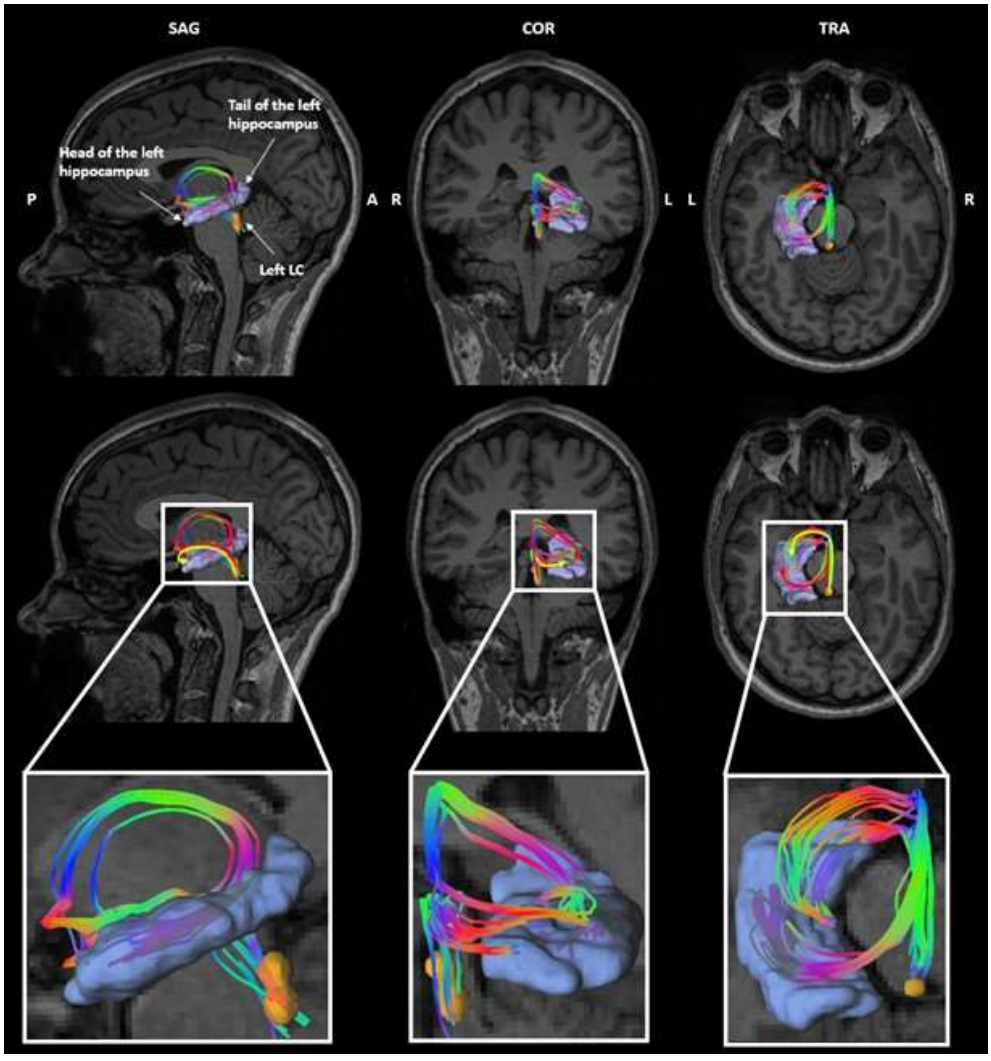

Figure 5.7 - Tractography of the left LC-hippocampus connections in a representative subject. Orange: left LC, purple: left hippocampus. The color of the tracts reflects the directionality of the fibers.

In the left LC-hippocampus connections, a significantly higher MD (p = 1.23e-3*, p_{FDR} = 3.07e-3*) and a higher AD (p = 0.02*, p_{FDR} = 0.03*) were found in non-responders (**Figure 5.8**). Moreover, a significantly higher RD (p = 1.49e-5*, p_{FDR} = 7.43e-5*) and a lower wFVF (p = 0.02*, p_{FDR} = 0.03*) were found in the left LC-hippocampus connections of non-responders (**Supplementary Material S5.3-E**). Finally, in the right LC-hippocampus connections, a significantly higher MD (p = 0.01*, p_{FDR} = 0.03*) and higher RD (p = 0.003*, p_{FDR} = 0.01*) were found in non-responders. For visual purposes, boxplots showing the diffusion metrics in non-responders and responders/partial responders are shown in **Figure 5.8**. No significant main effect of therapy duration on diffusion metrics was found (**Supplementary Material S5.3-F**).

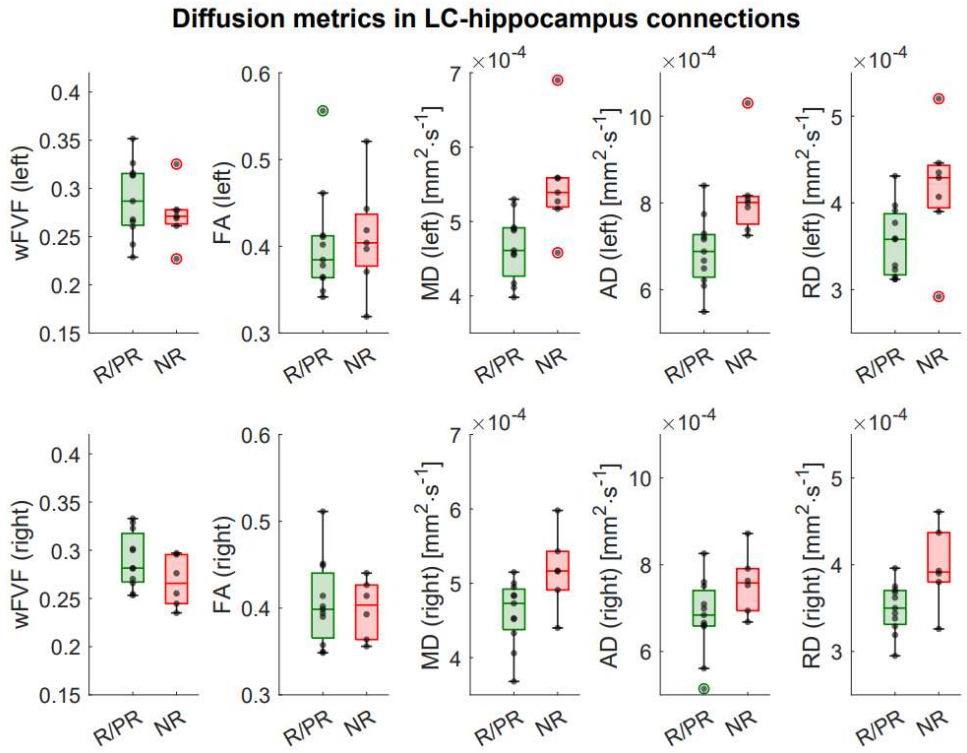

Figure 5.8 - Integrity of LC-hippocampus connections in patients responding (or partially responding) and not responding to VNS treatment. First row: Boxplots showing the difference in diffusion metrics in left LC-hippocampus connections between responders (R)/partial responders (PR) and non-responders (NR). Second row: Boxplots showing the difference in diffusion metrics in right LC-hippocampus connections between R/PR and NR. Refer to text and ***Supplementary Material S5.3*** *for full statistical output of the LM.*

3.3 Discussion

Several animal and human studies suggested that the LC-NE system is a critical player in the antiseizure effects of VNS in patients with DRE

(84,86,98,103). Previous studies investigated non-invasive biomarkers of the modulation of the LC-NE system to demonstrate its implication in the antiseizure effects of VNS and also to understand the variability in response to the treatment across patients. However, no *in vivo* imaging study was conducted to assess the functional and structural characteristics of the LC directly and investigate potential differences in patients with DRE implanted with a VNS device.

The results of this pilot study suggested a trend toward a lower response in the medial portion of the left LC at the appearance of target sounds during an auditory oddball task in responders/partial responders compared to non-responders to VNS (with the VNS being turned off). These functional findings may be in line with previous indirect assessments of LC-related measures. A previous study that measured the P3 event-related potential (i.e., a positive EEG deflection occurring around 300 ms post-stimulus) during an auditory oddball task found a higher amplitude in non-responders to VNS in a VNS OFF condition (98). Another study that recorded the amplitude of the P3b component 2–4 weeks post-implantation but before any stimulation revealed a lower baseline amplitude in patients who became responders to VNS after one year of treatment (103). Therefore, it could be hypothesized that patients with DRE show a different functional state of the vagal afferent network (and, more specifically, the LC-NE system), as suggested by Hödl and colleagues. Individuals with a lower baseline activity could, therefore, constitute good candidates for a therapy targeting the LC-NE system, compared to individuals with a less modulable network.

Previous studies suggested rostro-caudal and antero-posterior regional specializations of the LC in terms of cell types and projections (217). Whether the link between response to VNS therapy and LC activity found in the medial portion of the left LC reflects true lateralization or is due to statistical insensitivity over the right LC is unclear. However, knowing that the left vagus nerve (i.e., the VNS implantation side) projects – mainly, but

not only – to the ipsilateral NTS, one could expect an effect mostly localized in the left LC. The NTS projects to the LC through two disynaptic pathways: an excitatory pathway with a relay within the nucleus NPG (261) and an inhibitory pathway with a relay within the NPH (63,64,262). These anatomical connections were confirmed through a simulation study of the LC, where antidromic activations of the NPG and NPH were observed (62). Since no known monosynaptic connections have been reported between the left and right LC (63), it has been suggested that the contralateral response recorded when the LC is stimulated unilaterally may be due to a putative interplay between the excitatory and/or inhibitory drive generated from the LC stimulation, via an antidromic activation of bilateral brainstem afferents (263). Tracing studies revealed bilateral interconnections between the two NPH (264) and the two NPG (265).

Therefore, it is not surprising that VNS may modulate the brain bilaterally, as potentially reflected in the trends toward an effect of therapy duration on the contrast in the medial portion of the left and right LC. Studies conducted in rats suggested that the NPG projects to the medial (and ventral) portion of the LC (266). Moreover, studies found that thalamic-projecting cells were mainly located caudally in the LC of rats (266). Interestingly, we found a trend toward a relationship between LC contrast in the caudal portion of the right LC and VNS response. Whether the trend observed in the caudal right portion is a true regionalization or is due to noise-related sensitivity issues in the other portions remains to be explored. Although the translation of animal results to humans is not straightforward, our results together could possibly suggest that the functional and structural characteristics of the medial and caudal portions of the LC could differ between patients with DRE and may reflect the modulatory effects of this therapy on the LC-NE system.

The exact biological interpretation of LC contrast as observed using specific MRI sequences remains debated (146). Previous studies suggested that a higher LC contrast, as observed using specific T1-weighted MRI

sequences, was associated with a higher concentration of neuromelanin (a by-product of NE that accumulates inside the cell body of noradrenergic neurons), as confirmed in a study that used a combination of histology and *postmortem* MRI (56). However, a recent study showed that LC contrast was still observable on images obtained using a sequence with magnetization transfer in mice that were genetically engineered to have 70% fewer LC cells (147). It has been suggested that MRI sequences with magnetization transfer effects (such as the sequence used in the present study) may set the LC apart from its surroundings due to the specific transfer of magnetization between different pools contained in noradrenergic neurons, i.e., the intracellular water content of the LC with the presence of paramagnetic ions, such as neuromelanin (147,148). Overall, and despite the current debate and investigations, the LC contrast is accepted as an indicator of LC integrity (206), with a higher contrast reflecting a better integrity depending on the age of assessment and excluding potential prodromal stages of degenerative brain disorders (139,149). Therefore, the biological interpretation of our finding showing a trend toward an increased contrast in the medial portion of the LC over time with VNS may be that VNS triggers plastic effects that could improve or restore LC functions. Future studies, including longitudinal assessments, are needed to elucidate this question.

Bilaterally, we found a significantly lower MD and RD in the LC-hippocampus connections in responders/partial responders compared to non-responders. Moreover, a lower AD and higher wFVF were found in responders/partial responders compared to non-responders, mainly localized in the left LC-hippocampus connections. These diffusion-related findings suggested a higher integrity of the LC-hippocampus connections in patients with DRE with a better response to the treatment. Indeed, it has been suggested that a lower MD and RD indicated healthier axons (267,268), and a higher fiber volume fraction reflected a higher axonal density (256). While DTI metrics showed higher statistical differences between responders/partial responders and non-responders than the MF

metric, wFVF is known to be biologically more interpretable and specific to the microstructural features of the fibers. Indeed, this model provides near-ground truth for diffusion-weighted MRI signals for crossing fascicles (137), while DTI is not able to capture characteristics of crossing fibers individually and is based on a simplified model of diffusion (a larger diffusion tensor is estimated for crossing fascicles). Therefore, MF offers supplementary information by disentangling the individual influence of crossing fascicles and confirming the interpretation of DTI metrics.

A previous tracing study that used horseradish peroxidase suggested the existence of strong fiber connections between the LC and the hippocampus in rats (219,269). Another study conducted in non-human primates suggested that connections between the LC and the hippocampus could exist through an indirect pathway that includes the central tegmental tract and the medial forebrain bundle projecting toward the amygdala (270). Previous studies conducted in primates and rats have extensively reported structural and functional interconnections between the amygdala and the hippocampus (271–275), making the amygdala a potential relay between the LC and the hippocampus in the vagal afferent network. We used default tracking parameters (e.g., the step size or the angle threshold), which are known to limit the occurrence of false-positive tracts. In addition, the tracts were visually inspected to avoid tracts with unrealistic shapes. The connections highlighted in the present study were visually consistent across patients, providing further support that they do not reflect spurious tracts. However, quantifying the coherence of the tracts at the group level poses a challenge due to the inclusion of patients with congenital brain malformations or patients who underwent brain surgery. This complexity precludes the use of a common space and constitutes a limitation in the present study. Future studies should nevertheless further investigate the consistency between tractography and *postmortem* data in humans.

In previous studies, an intensity-dependent increase of NE was measured in the hippocampus of healthy rats following VNS administration (84), and a sufficient increase – of at least 70% prevented the development of pilocarpine-induced seizures in rats (86). Furthermore, NE concentration has been associated with the proliferation of neural progenitors in the hippocampus (95,96). Therefore, one could speculate that a better integrity of the tracts arising from the LC and projecting to the hippocampus may allow a higher release of NE within the hippocampus during VNS administration and could be associated with a better response to the treatment and/or to greater neuroplasticity effects onto hippocampal structures.

Although our sample is acceptable for a population of patients with DRE and implanted with a VNS device, it remains relatively small for statistical analyses. In addition, including a sample of healthy subjects could be interesting to compare structural and functional characteristics of the LC with VNS-implanted DRE patients to gain further insight into the specific characteristics of this system in DRE and better understand the biological requisites to become responder to the therapy. On a methodological level, respiratory and heart rate signals could be recorded in future studies, to regress out possible confounding effects of physiological noises for the fMRI analyses. When exploring the LC contrast, analyses could include a standard reference region for the normalization to minimize possible errors linked to the manual placement of the region and increase the reproducibility of the procedure (276–278).

Future longitudinal studies are needed to assess the evolution of the LC contrast/activity and the structural integrity of the LC-hippocampus connections over time after the implantation of a VNS device and compare the pre- and post-implantation characteristics. Such studies would provide deeper insight into the modulatory effects of the therapy on the LC and could help to establish new biomarkers of VNS efficacy. Other mechanisms of action for the seizure-suppressing effects of VNS have been previously

suggested. Exploring the structural and functional characteristics of the DRN (a nucleus composed of serotoninergic neurons) or the concentration of inhibitory (e.g., gamma-aminobutyric acid) and excitatory (e.g., glutamate or aspartate) metabolites in the brain of DRE patients using spectroscopy, could serve as a promising direction for future investigations (99,279,280).

3.4 ORIGINAL CONTRIBUTION

Locus coeruleus features are linked to vagus nerve stimulation response in drug-resistant epilepsy. **A. Berger**, E. Beckers, V. Joris, G. Duchêne, V. Danthine, N. Delinte, I. Cakiroglu, S. Sherif, EIG. Morrison, AT. Sánchez, B. Macq, L. Dricot, G. Vandewalle and R. El Tahry. *Frontiers in Neuroscience – Brain Imaging Methods*, 2024; 18:1296161. *doi: 10.3389/fnins.2024.1296161*

CHAPTER 6. THALAMOCORTICAL MICROSTRUCTURAL FEATURES IN PATIENTS WITH DRUG-RESISTANT EPILEPSY

1. INTRODUCTION AND OUTLINE OF THE CHAPTER

It was suggested that VNS could modulate the activity of the thalamus which could disrupt the genesis of pathological activity in the brain (79,281–284).

FMRI has been previously used to show that functional connectivity was increased in a network encompassing the left thalamic, insular, and temporal nodes in patients with a better response to VNS (150). Likewise, an increased connectivity of the thalami to the anterior cingulate cortex and the left insula as assessed before the implantation was associated with better seizure control with VNS in children with DRE (151). Based on these connectivity metrics in children, an SVM model was built and was able to discriminate responders to VNS from patients with a < 50% reduction in seizure frequency with an accuracy of 88% in an external cohort of patients (151). The potential role of the thalamus in mediating VNS efficacy was reinforced using DTI for the assessment of the brain microstructure in DRE patients (150). Larger FA - i.e., a marker of structural integrity - was found in different tracts in responders to the therapy compared to non-responders, including within left thalamocortical, limbic, and association fibers. Using DTI metrics in these tracts, an SVM was built to classify

patients based on their responses to VNS and reached a classification accuracy of 89.5%.

In the study presented in this chapter, we argue that the role of the thalamus in VNS efficacy may be better understood using diffusion MRI. Diffusion MRI is a powerful imaging modality for characterizing the microstructure of white matter tracts, but this technique remains underexploited in the field of DRE. To our knowledge, while a previous study used single-shell diffusion MRI (150), no study used high-gradient multi-shell diffusion MRI to extract microstructural features of white matter tracts in DRE patients implanted with a VNS device. Multi-shell diffusion MRI uses multiple b-values (corresponding to gradient strengths and durations) and allows the assessment of more complex aspects of the tissue microstructure using multi-compartment models, in opposition to classical models such as DTI. Therefore, the goal of the present study was to assess whether microstructural features in subsegments of thalamocortical tracts extracted based on multi-shell diffusion MRI data could help to distinguish patients responding and not responding to VNS. Moreover, we explored whether multi-compartment models could provide a finer biological interpretation of microstructural differences in white matter tracts among patients responding or not responding to VNS.

Classical DTI metrics were computed in DRE patients and multi-compartment diffusion models were used to better characterize microstructural features of crossing fascicles. These models included NODDI and MF. MF is a model known to provide near-ground truth for diffusion-weighted MRI signals and compute metrics that are biologically more interpretable (137,285). We hypothesize that a higher integrity of thalamocortical tracts will be found in patients demonstrating greater therapeutic efficacy. Using an SVM classifier based on DTI, NODDI, and MF metrics, we explored how responders and non-responders to VNS could be accurately discriminated from each other, despite the limited size of our

sample. Finally, clinical features were incorporated into the SVM model to assess their potential utility in classifying patients.

2. STUDY 4 : IDENTIFYING RESPONDERS TO VAGUS NERVE STIMULATION BASED ON MICROSTRUCTURAL FEATURES OF THALAMOCORTICAL TRACTS IN DRUG-RESISTANT EPILEPSY

ABSTRACT

The mechanisms of action of Vagus Nerve Stimulation (VNS) and the biological prerequisites to respond to the treatment are currently under investigation. It is hypothesized that thalamocortical tracts play a central role in the antiseizure effects of VNS by disrupting the genesis of pathological activity in the brain. This pilot study explored whether in vivo microstructural features of thalamocortical tracts may differentiate Drug-Resistant Epilepsy (DRE) patients responding and not responding to VNS treatment. Eighteen patients with DRE (37.11 ± 10.13 years, 10 females), including 11 responders or partial responders and 7 non-responders to VNS, were recruited for this high-gradient multi-shell diffusion Magnetic Resonance Imaging (MRI) study. Using Diffusion Tensor Imaging (DTI) and multi-compartment models - Neurite Orientation Dispersion and Density Imaging (NODDI) and Microstructure Fingerprinting (MF), we extracted microstructural features in 12 subsegments of thalamocortical tracts. These characteristics were compared between responders/partial responders and non-responders. Subsequently, a Support Vector Machine (SVM) classifier was built, incorporating microstructural features and 12 clinical covariates (including age, sex, duration of VNS therapy, number of antiseizure medications, benzodiazepine intake, epilepsy duration, epilepsy onset age, epilepsy type - focal or generalized, presence of an epileptic syndrome - no syndrome or Lennox-Gastaut syndrome, etiology of epilepsy - structural, genetic, viral, or unknown, history of brain surgery, and presence of a brain lesion detected on structural MRI images). Multiple diffusion metrics consistently demonstrated significantly higher white matter fiber integrity

in patients with a better response to VNS (p_{FDR} < 0.05) in different subsegments of thalamocortical tracts. The SVM model achieved a classification accuracy of 94.12%. The inclusion of clinical covariates did not improve the classification performance. The results suggest that the structural integrity of thalamocortical tracts may be linked to therapeutic effectiveness of VNS. This study reveals the great potential of diffusion MRI in improving our understanding of the biological factors associated with the response to VNS therapy.

2.1 MATERIAL AND METHODS

2.1.1 PARTICIPANTS

Patients were recruited from the Center for Refractory Epilepsy of Saint-Luc University Hospital. Inclusion criteria were (i) adult participants, (ii) with a diagnosis of DRE (persistent seizures despite the use of at least two ASM administered at correct dosages) (iii) able to understand the study protocol, (iv) implanted for at least six months with one of the following VNS models: DemiPulse® Model 103, DemiPulse Duo® Model 104, AspireHC® Model 105, or AspireSR® Model 16 (LivaNova, Inc., London, UK), and (v) patients whose medication did not influence assessment of VNS response. Exclusion criteria were: occurrence of a seizure < 24h prior to the MRI acquisitions, severe side effects of VNS reported by the patients such as dyspnea, pain in the neck/ear region, or gastrointestinal complaints, history of alcohol or drug abuse, the presence of psychiatric illness, inability to understand the study protocol, and any MRI contraindication. Response to VNS was determined by the reference neurologist with the following criteria: patients are considered as responders if a > 50% reduction in seizure frequency is observed, partial responders demonstrate a reduction in seizure frequency between 30-50%

with positive effects observed when swiping the magnet in front of the generator manually, and non-responders present a < 30% reduction in seizure frequency. The reference neurologist estimated response to VNS based on the seizures reported over a three-month period before the implantation. Moreover, a screening of medical records was conducted to ensure that no change in medication could have positively influenced the evaluation of response to VNS. In the present study, 18 patients were recruited, including 5 partial responders, 6 responders, and 7 non-responders. Since therapeutic effects were found in partial responders – although, to a lower extent, these patients were grouped with responders for statistical analyses. Demographic data can be found in **Table 6.1**. In 3 non-responders, the VNS was off for several reasons: (i) two patients were explanted four months and 2.4 years before the experiment, and (ii) in one patient, the device was turned off completely for almost two years due to side effects and a lack of response. The study received approval by the Ethical Committee of Saint-Luc University Hospital (reference nr. 2021/18FEV/086). All patients signed the informed consent prior to any investigation.

Characteristics	**NR (n = 7)**	**R/PR (n = 11)**	**p-value**
Age (years)	37.14 ± 12.82	37.09 ± 8.71	0.61
Sex	3 Females 4 Males	7 Females 4 Males	0.63
Therapy duration of VNS (months)	109.28 ± 46.98	61.27 ± 71.50	0.10
Epilepsy type	7 Focal 0 Generalized	9 Focal 2 Generalized	0.50
Epilepsy duration (years)	24.71 ± 8.85	26.64 ± 13.09	0.84
Epilepsy onset age (years)	16.71 ± 10.14	10.45 ± 8.00	0.18

Epileptic syndrome	Lennox-Gastaut : 1/7 No syndrome : 6/7	Lennox-Gastaut : 1/11 No syndrome : 10/11	1.00
Brain surgery	Brain surgery : 3/7 No surgery : 4/7	Brain surgery : 1/11 No surgery : 10/11	0.25
Etiology of epilepsy	Structural : 3/7 Viral : 1/7 Genetic : 0/7 Unknown : 3/7	Structural : 4/11 Viral : 0/11 Genetic : 2/11 Unknown : 5/11	0.76
Lesion on brain MRI	Lesion : 5/7 No lesion : 2/7	Lesion : 5/11 No lesion : 6/11	0.37
Number of ASMs (number of patients)	2 ASMs : 2/7 3 ASMs : 2/7 4 ASMs : 3/7	2 ASMs : 5/11 3 ASMs : 5/11 4 ASMs : 1/11	0.30
Benzodiazepine (daily) intake (number of patients)	2	1	0.53
VNS intensity (mA) [a]	1 mA : 0/4 1.125 mA : 0/4 1.25 mA : 0/4 1.50 mA : 0/4 1.75 mA : 2/4 2 mA : 2/4	1 mA : 1/11 1.125 mA : 1/11 1.25 mA : 1/11 1.50 mA : 5/11 1.75 mA : 1/11 2.00 mA : 2/11	0.05
VNS frequency (Hz) [a]	20 Hz : 3/4 25 Hz : 1/4 30 Hz : 0/4	20 Hz : 4/11 25 Hz : 2/11 30 Hz : 5/11	0.21

VNS pulse width (µs) [a]	250 µs : 3/4 500 µs : 1/4	250 µs : 9/11 500 µs : 2/11	1.00
Rapid duty cycle [a,b]	0/4	2/11	0.58

Table 6.1 - Demographic and clinical characteristics of the study population. [a] Values reported after excluding 3 NR (see text); [b] The duty cycle is defined as (ON time + 4s)/(ON time + OFF time), and a rapid duty cycle is defined as an OFF time < 1.1 min while keeping the duty cycle < 50% (286). *NR: Non-Responder, R: Responder, PR: Partial Responder, ASM: Antiseizure medication.*

2.1.2 IMAGING PARAMETERS

Imaging data were acquired using the SIGNA Premier 3T MRI system (GE Healthcare, Milwaukee, WI, USA), following the LivaNova guidelines for MRI. Before entering the MRI room, the output current of the VNS device was set to 0 mA, and the AutoStim mode was turned off (according to the LivaNova guidelines for MRI). Imaging data were acquired using the SIGNA Premier 3T MRI system (GE Healthcare, Milwaukee, WI, USA) with a 48-channel head coil. T1-anatomical images were acquired with a MPRAGE sequence: TR = 2186 ms, TE = 2.95 ms, FA = 8°, TI = 900 ms, bandwidth = 244.14 Hz, matrix size = 256 x 256, 156 axial slices, imaging frequency = 127.77 Hz, voxel size = (1 x 1 x 1)mm^3, acquisition time = 5:26 min. Diffusion MRI data were acquired with a PGSE sequence: TR = 4837 ms, TE = 80.5 ms, and flip angle = 90°. A high-gradient multi-shell diffusion scheme was used and consisted of 64 gradients at b = 1000 $s{\cdot}mm^{-2}$ and 32 gradients at b = 2000, 3000, and 5000 $s{\cdot}mm^{-2}$, interleaved with 7 b0 images. The in-plane field-of-view was (220 x 220)mm^2, the matrix size was 110 x 110, and the data contained 68 axial slices with a 2-mm thickness (no inter-slice gap, 2-mm isotropic voxels). A multi-slice excitation scheme was

used during the acquisition with a hyperband slice factor of three to reduce the acquisition time. The total acquisition time was 13:33 min. A T2-weighted image was acquired to improve the patient-specific segmentation of cortical areas. The T2-weighted image was acquired using a SE sequence: TR = 2.5 ms, TE = 91 ms, FA = 90°, matrix size = 255 x 255, 141 sagittal slices, voxel size = (1 x 1 x 1)mm^3, acquisition time = 2:01 min.

2.2 DATA ANALYSIS

2.2.1 PREPROCESSING AND DIFFUSION MODELS

Preprocessing of the diffusion data was performed using the ElikoPy pipeline (*https://github.com/Hyedryn/elikopy*) (287). The preprocessing steps included skull stripping (using the Diffusion Imaging in Python library – DiPy, *https://dipy.org/* (253)), Rician denoising (Marchenko-Pastur Principal Component Analysis (254)), Eddy currents correction, susceptibility distortion correction and motion correction (255).

DTI maps were computed using DiPy. The DTI metrics investigated in this study included FA, MD, AD, and RD. Multi-compartment diffusion models were used to characterize crossing fascicles, i.e., NODDI and MF, a model known to provide near-ground truth for diffusion-weighted MRI signals and compute metrics that are biologically more interpretable (137,285). NODDI maps were computed with the Diffusion Microstructure Imaging in Python (DMIPY, *https://github.com/AthenaEPI/dmipy*) toolbox (288). Two NODDI metrics were investigated: the ICVF, also known as the NDI, and the ODI. This model requires two values that are fixed a priori: the isotropic diffusivity for the CSF (default value of $3*10^{-3}$ mm^2s^{-1}) and the axial diffusivity of the intra-neurite space (default value of $1.7*10^{-3}$ mm^2s^{-1}).

Finally, MF is a multi-compartment model based on Monte Carlo simulations of the random walk of water molecules within the brain. The MF metric computed in the present study is the wFVF corresponding to the axonal density of the fibers and is defined as :

$$wFVF_i = \frac{\nu_{1,i} * fvf_{1,i} + \nu_{2,i} * fvf_{2,i}}{\nu_{1,i} + \nu_{2,i}},$$

Where:

- *i* is the index of the voxel.
- $\nu_{1,i}$ is the fraction of occupancy of fascicle 1 in voxel *i* (and $\nu_{2,i}$ for fascicle 2).
- $fvf_{1,i}$ is the fiber volume fraction of fascicle 1 in voxel *i* (and $fvf_{2,i}$ for fascicle 2).

2.2.2 TRACTOGRAPHY

A Fiber Orientation Distribution (FOD) was estimated with the Multi-Shell Multi-Tissue Constrained Spherical Deconvolution (MSMT-CSD) implemented in MRtrix3 (289). Tractography was performed with the *tckgen* function of MRtrix3 in the diffusion space of the patients. A second-order integration over FOD - a probabilistic algorithm - was used to reconstruct the streamlines. A 5-tissue-type segmented image (including cortical gray matter, subcortical gray matter, white matter, cerebrospinal fluid and pathological tissues) was computed using the *5ttgen* command of MRtrix3 and used for constraining anatomically the tractography and improve it using biological realistic priors. Streamlines were truncated and re-tracked during the tractography to avoid poor structural terminations. Tracking parameters included: tracking step size = 0.5 x voxel size (2-mm isotropic voxel), maximum angle = 15° for all tracts except tracts projecting

to the parietal lobe where 10° was used, minimum length = 2 x voxel size, maximum length = 100 x voxel size, 1000 as the maximum number of sampling trials at each point, FOD amplitude cut-off value for terminating tracks = 0.05, and the number of selected streamlines after all selection criteria have been applied = 10000.

Twelve subsegments of thalamocortical tracts were reconstructed for each subject (6 left-lateralized and 6 right-lateralized tracts), including the anterior thalamocortical tracts, the superior thalamocortical tracts, the posterior thalamocortical tracts (projecting to the parietal cortex, or to the occipital cortex), and the inferior thalamocortical tracts (projecting to the temporal cortex or to the insular cortex) (290). Candidate gray matter regions used as inclusion regions for the tractography were extracted in the structural space of the subjects with Freesurfer (Linux – centOS *version 7.2*), using the T1 and T2-weighted images for the segmentation of the whole brain. All ROIs were warped into the diffusion space of the subject after registering the skull-stripped T1-weighted image to the diffusion space, using the *'bbregister'* function from Freesurfer, and applying the transformation parameters to the segmented ROI using the *'mri_vol2vol'* function from Freesurfer. This step included a 6-parameter rigid body transformation with the '*-no-resample'* option to avoid losing resolution due to resampling of the structural image. For the tracking, white matter inclusion regions (defined based on anatomical knowledge of thalamocortical tracts (290)) were also used as ROI to improve the tractography. These regions were obtained after registration of the parcellation from the Johns Hopkins University – International Consortium for Brain Mapping (JHU ICBM) DTI-152 Atlas in the diffusion space of the subject with a two-step process: (i) registering the template image - ICBM152 (1 x 1 x 1)mm^3 to the T1-weighted image (using the Advanced Normalization Tools toolkit - ANTs, Penn Imaging Computing and Science Laboratory, UPenn, USA, *http://stnava.github.io/ANTs/*) of the subject and applying the transformation parameters to warp the white matter labeled ROI into the structural space of the subject, and (ii) applying the

transformation parameters obtained when registering the T1-weighted image into the diffusion space of the subjects.

For tracking all thalamocortical tracts, the Freesurfer-segmented left and right thalami were used as seed regions for tracking left and right thalamocortical tracts, respectively. The inclusion ROIs and END regions used for tracking the subsegments of the thalamocortical tracts were based on regions previously defined (290) (all regions are summarized in **Table 6.2**). The final tracts are shown in **Figure 6.1**.

Thalamocortical tracts	**Inclusion ROIs**	**END**
Anterior	Anterior limb of the internal capsule	Frontal lobe: superior frontal cortex, rostral and caudal middle frontal cortex, pars opercularis, pars triangularis, pars orbitalis, lateral and medial orbitofrontal cortex and frontal pole
Superior	Posterior limb of the internal capsule	Central gyrus
Posterior		
Projecting to parietal lobe	Posterior limb of the internal capsule	Parietal lobe: superior parietal cortex, inferior parietal cortex and precuneus
Projecting to the occipital lobe	Posterior limb of the internal capsule	Occipital lobe: lateral occipital cortex, lingual gyrus, cuneus and pericalcarine gyrus
Inferior		
Projecting to the temporal lobe	Retrolenticular part	Temporal lobe: superior,

	of the internal capsule	middle, and inferior temporal cortex, banks of the superior temporal sulcus, fusiform gyrus, transverse temporal cortex, and entorhinal cortex
Projecting to the insular cortex	Retrolenticular part of the internal capsule	Insular cortex

Table 6.2 - Inclusion brain regions (ROI: Region-Of-Interest and END regions) used for the tracking of thalamocortical tracts.

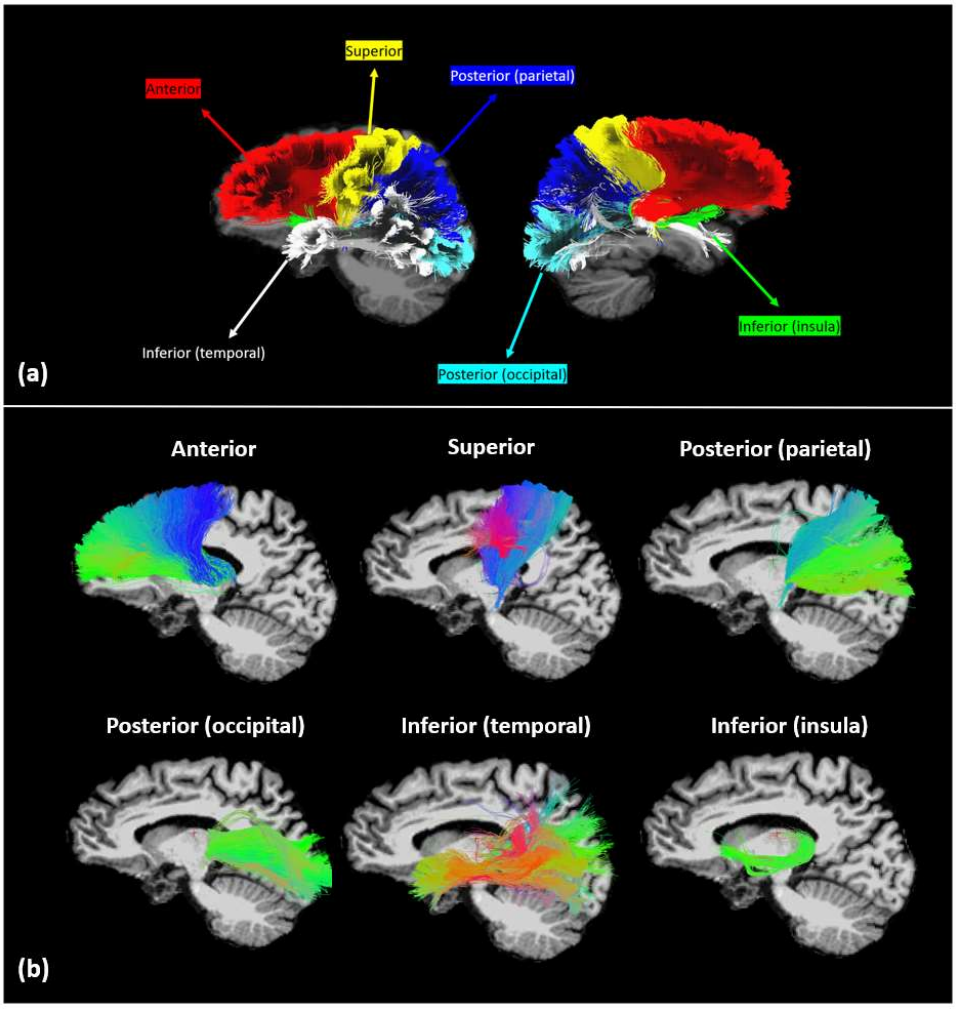

Figure 6.1 - Example of the tractography of thalamocortical tracts extracted in one patient. (a) All subsegments of thalamocortical tracts superimposed with a color index, and (b) individual thalamocortical subsegments, with the color reflecting the orientation of the fibers.

2.2.3 STATISTICAL ANALYSIS

Statistical analyses were conducted using RStudio (*version 4.2.1*). Demographic and clinical features summarized in **Table 6.1** were statistically compared between responders/partial responders and non-responders using Wilcoxon Mann-Whitney tests for continuous variables and Fisher's exact test for nominal data.

Using multivariate linear regressions, diffusion MRI metrics were modeled in terms of VNS response, using age, sex, ASM intake, epilepsy duration, VNS therapy duration, and benzodiazepine intake as covariates.

The VIF values were computed for the predictors included in the linear models to avoid fitting problems. VIF values of all predictors were < 5 (low correlation between predictors), with a maximum VIF value of 2.06 found for the sex of the patients. FDR correction was applied for all the tracts investigated to correct for multiple comparisons (12 tests). Results were considered as significant for $p_{FDR} < 0.05$. Trends towards significance were considered for $p < 0.05$. For visual purposes, boxplots of diffusion metrics in responders/partial responders and non-responders were shown. Tracking of the right posterior thalamocortical tract projecting to the parietal lobe failed for one patient (a non-responder) due to a right amygdalohippocampectomy associated with a resection of temporo-occipital dysplasia. Therefore, the diffusion metrics were investigated in 18 patients for all tracts, except for the right posterior thalamocortical tracts projecting to the parietal lobe, for which 17 patients were included in the analysis.

2.2.4 SUPPORT VECTOR MACHINE

Seventeen subjects were included in the discovery cohort - the patient for whom the tractography failed for the right posterior thalamocortical tract projecting to the parietal lobe was excluded for consistency purposes in the features used to train the SVM model. An SVM model was chosen

over other existing classification models, as it is known to perform well on small datasets (291). The Scikit-Learn Python library (French Institute for Research in Computer Science and Automation, Rocquencourt, France) was used to build the SVM model (168). Data was mean-centered and scaled to unit variance to reduce sensitivity to the feature scale and have a faster convergence when fitting the SVM model.

A recursive feature elimination approach was used to determine the optimal combination of features by removing the least important feature before refitting the model. A wrapper feature selection approach was conducted, with an internal filter-based feature selection using the '*SelectKBest*' function that uses F-statistics to classify features based on their contribution to the target variable – i.e., response to VNS therapy. Therefore, a model was built using all features and recursively eliminating the least important feature; the model was rebuilt until one feature (i.e., the most important feature for discriminating responders/partial responders and non-responders) remained. Eighty-four diffusion MRI features were considered (12 tracts – 6 in each hemisphere; 7 metrics in total – 4 DTI metrics, 2 NODDI metrics, and 1 MF metric). Clinical features were incorporated into the set of features used for the classification to evaluate their potential influence in the classification of the patients. The following clinical features were included: age, sex, duration of VNS therapy, number of ASM, benzodiazepine intake, epilepsy duration, epilepsy onset age, epilepsy type (focal or generalized), presence of an epileptic syndrome (no syndrome or Lennox-Gastaut syndrome), etiology of epilepsy (structural, genetic, viral, or unknown), history of brain surgery, and presence of a brain lesion detected on structural MRI images. Therefore, 96 features were considered in total for building the SVM model. All clinical features that could be retrospectively extracted from medical records were added in the present study. The inclusion of these features in the model to evaluate their potential to discriminate R/PR and NR constitutes interesting investigations, as (i) response rate to VNS is known to increase with the duration of the therapy (170), (ii) white matter integrity of tracts

composing the vagal afferent network may present specific abnormalities in different epilepsy types, or epilepsies with different etiologies, (iii) patients with a shorter history of epilepsy could show a higher likelihood to respond to VNS (170), and that (iv) lesions detected on MRI or history of brain surgery could explain changes in white matter microstructure in fibers composing the vagal afferent network (292,293).

A common practice in machine learning is to use kernel functions to implicitly map the data into a higher-dimensional space to solve a non-linear classification problem using a linear classifier. Therefore, different kernel functions were used during the model selection process to investigate the most suitable function for the classification: linear, polynomial, Radial Basis Functions – RBF, and sigmoid kernel functions. Grid search over the hyperparameters was realized for the regularization parameter (to ensure a trade-off between misclassifications and maximization of the margin hyperplane) and the gamma-kernel coefficient (defining the curvature of the decision boundary - only applicable for polynomial, RBF, and sigmoid kernel functions). Tuning of the hyperparameters was done with a nested Leave-One-Out (LOO) cross-validation to select the best-performing model while avoiding overfitting and bias for the estimation of the ability of the model to generalize to unseen data. Grid search over these parameters (inner cross-validation loop) was realized over classically reported values: C = [10^{-4}, 10^{-3},…, 10^{2}] and γ = [‘*scale’*, ‘*auto’*, 10^{-4}, 10^{-3},…, 10^{2}]; with scale = 1/(number of features * data variance) and auto = 1/(number of features).

Due to the small nature of our dataset, the classification accuracy was also evaluated using the LOO cross-validation technique (outer cross-validation loop). The confusion matrix reporting the true positive (TP), true negative (TN), false positive (FP), and false negative (FN) predictions was computed. The final model (best subset of features, most suitable kernel function, and hyperparameters) was chosen based on a multi-criterion evaluation that includes:

- F1-score, defined as: 2*(*precision* * *recall*)/(*precision* + *recall*), with *precision* = TP/(TP + FP) and *recall* = *sensitivity* = TP/(TP + FN).
- Classification accuracy defined as: (TP + TN)/(TP + TN + FP + FN).

For the best-performing model, the ROC curve was plotted, and the AUC was computed based on the prediction scores using the '*roc_auc_score'* function.

2.3 RESULTS

2.3.1 DIFFUSION TENSOR IMAGING

The linear model using the DTI metrics as dependent variables and controlling for several potential confounds (see Materials and Methods) revealed a significantly higher MD in non-responders compared to responders/partial responders bilaterally in the left inferior thalamocortical tracts projecting to the temporal lobe (left: $p = 0.001$, $p_{FDR} = 0.01$*, right: $p = 0.002$, $p_{FDR} = 0.01$*), in the left posterior thalamocortical tracts projecting to the parietal lobe ($p = 0.01$, $p_{FDR} = 0.03$*), right inferior thalamocortical tracts projecting to the insular cortex ($p = 0.007$, $p_{FDR} = 0.02$*), and right posterior thalamocortical tracts projecting to the occipital cortex ($p = 0.004$, $p_{FDR} = 0.01$*) (**Figure 6.2**). Moreover, a significantly higher RD was found in non-responders compared to responders/partial responders in the right inferior thalamocortical tracts projecting to the insular cortex ($p = 0.007$, $p_{FDR} = 0.02$*), right inferior thalamocortical tracts projecting to the temporal lobe ($p = 0.007$, $p_{FDR} = 0.02$*), and right posterior thalamocortical tracts projecting to the occipital lobe ($p = 0.002$, $p_{FDR} = 0.02$*). Linear models of diffusion metrics of models showing significant results after FDR correction ($p_{FDR} < 0.05$) or trends of significance ($p < 0.05$) are reported in **Supplementary Material S6.1**.

Moreover, while the duration of VNS therapy was used as a covariate in the statistical models to remove a possible influence on the diffusion metrics, no significant effect of therapy duration was found in any statistical model.

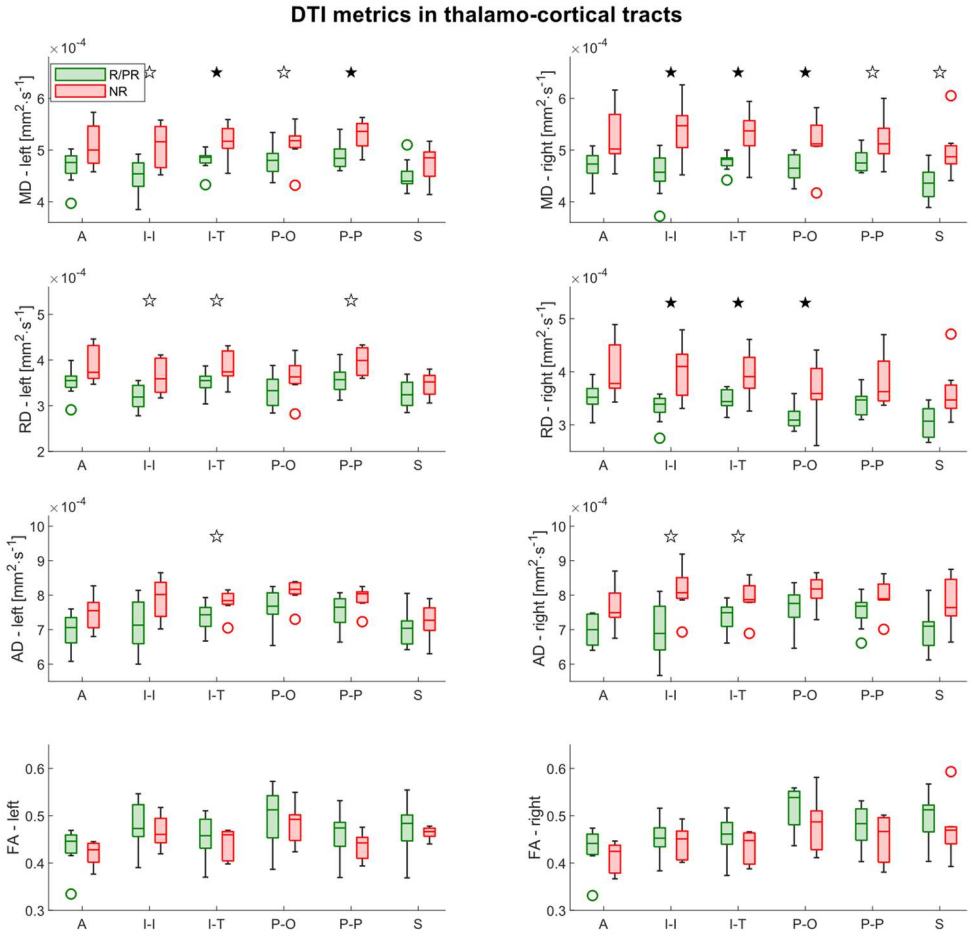

Figure 6.2 - Boxplots of DTI metrics in thalamocortical tracts in Responders (R)/Partial Responders (PR) and Non-Responders (NR). Filled stars represent the results of the linear models that remained significant after FDR correction; Empty stars represent the results of the linear models that were

significant without correction only. AD: Axial Diffusivity, FA: Fractional Anisotropy, MD: Mean Diffusivity, RD: Radial Diffusivity, A: Anterior thalamocortical tracts, I-I: Inferior thalamocortical tracts projecting to the insular cortex, I-T: Inferior thalamocortical tracts projecting to the temporal lobe, P-O: Posterior thalamocortical tracts projecting to the occipital lobe, P-P: Posterior thalamocortical tracts projecting to the parietal lobe, S: Superior thalamocortical tracts.

2.3.2 NEURITE ORIENTATION DISPERSION AND DENSITY IMAGING

The linear model using the NODDI metrics as dependent variables yielded a significantly higher ICVF (or NDI) bilaterally in responders/partial responders compared to non-responders in the inferior thalamocortical tracts projecting to the insular cortex (left: $p = 0.02$, $p_{FDR} = 0.04$*, right: $p = 0.01$, $p_{FDR} = 0.04$*), inferior thalamocortical tracts projecting to the temporal lobe (left: $p = 0.005$, $p_{FDR} = 0.02$*, right: $p = 0.004$, $p_{FDR} = 0.02$*), posterior thalamocortical tracts projecting to the occipital lobe (left: $p = 0.02$, $p_{FDR} = 0.04$*, right: $p = 0.004$, $p_{FDR} = 0.02$*), and left posterior thalamocortical tracts projecting to the parietal lobe ($p = 0.02$, $p_{FDR} = 0.04$*) (**Figure 6.3**).

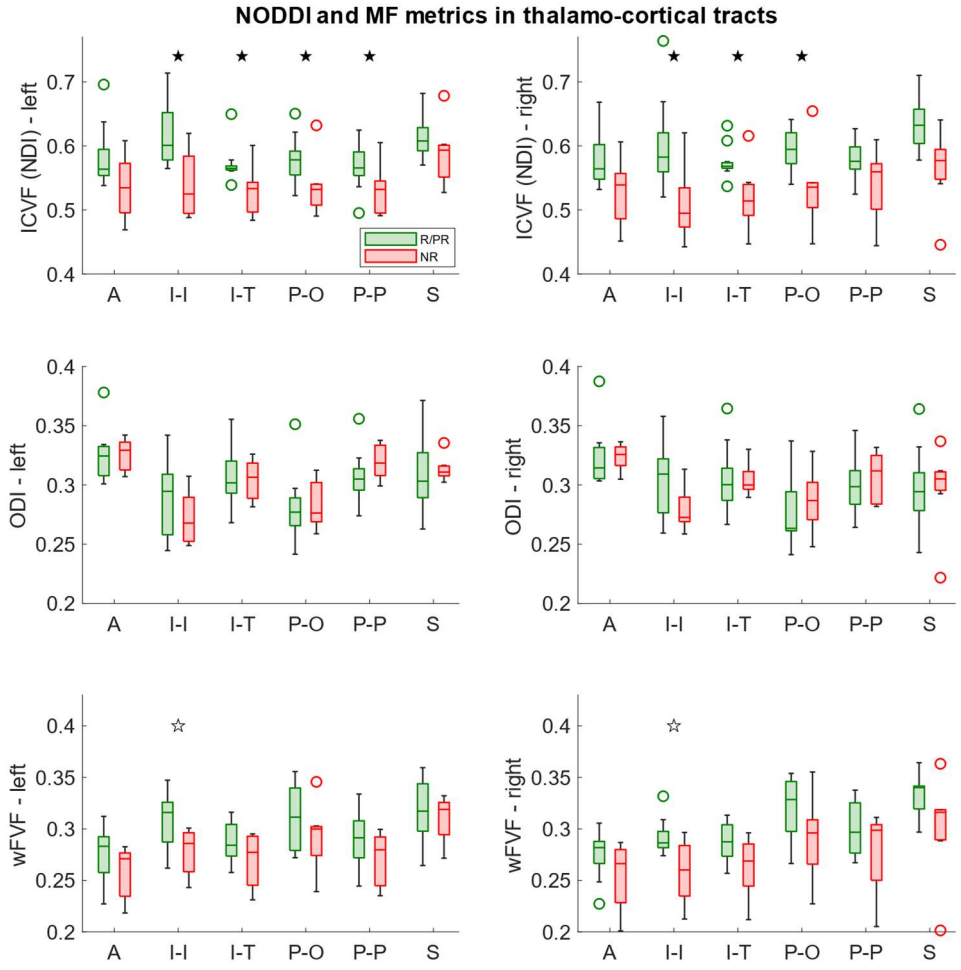

Figure 6.3 - Boxplots of NODDI and MF metrics in thalamocortical tracts in Responders (R)/Partial Responders (PR) and Non-Responders (NR). Filled stars represent the results of the linear models that remained significant after FDR correction; Empty stars represent the results of the linear models that were significant without correction only. ICVF: Intracellular Volume Fraction, NDI: Neurite Density Index, ODI: Orientation Dispersion Index, wFVF: weighted Fiber Volume Fraction. A: Anterior thalamocortical tracts, I-I: Inferior thalamocortical tracts projecting to the insula, I-T: Inferior thalamocortical tracts projecting to the temporal lobe, P-O: Posterior thalamocortical tracts projecting to the occipital lobe, P-P: Posterior

thalamocortical tracts projecting to the parietal lobe, S: Superior thalamocortical tracts.

2.3.3 MICROSTRUCTURE FINGERPRINTING

The linear model for the MF metrics led to no significant difference after FDR correction. However, a trend toward a higher wFVF in responders/partial responders compared to non-responders was found bilaterally in the inferior thalamocortical tracts projecting to the insular cortex (left: p = 0.04, right: p = 0.02) (**Figure 6.3**).

2.3.4 SUPPORT VECTOR MACHINE

The feature selection technique highlighted different models that led to the highest classification accuracy and the associated F1-score. The best model that included the least number of features only used the five best discriminatory features for the classification. This model reached a classification accuracy of 94.12% and an F1-score of 95.65%. The selected features were: MD in left inferior thalamocortical projecting to the insular cortex ($score_{SelectKBest}$: 12.25, $p_{SelectKBest}$ = 0.003), MD in right inferior thalamocortical tracts projecting to the insular cortex ($score_{SelectKBest}$: 11.50, $p_{SelectKBest}$ = 0.004), RD in right inferior thalamocortical tracts projecting to the insular cortex ($score_{SelectKBest}$: 11.11, $p_{SelectKBest}$ = 0.004), RD in left inferior thalamocortical tracts projecting to the insular cortex ($score_{SelectKBest}$: 9.65, $p_{SelectKBest}$ = 0.007) and MD in the right superior thalamocortical tracts ($score_{SelectKBest}$: 9.56, $p_{SelectKBest}$ = 0.007).

The same performance (classification accuracy and F1-score) was found when using the 13, 63, 64, and 65 best features (**Figure 6.4a**). Moreover, the accuracy remained high regardless of the number of features chosen

for the classification, providing evidence of stability of the model, and hints that the model is not overfitting. The classification accuracy and F1-score remained consistently high during the features selection technique, indicating the stability of the selected model when features are added for the classification. Hence, to (i) prevent overfitting, (ii) optimize the computational efficiency, and (iii) enhance the generalization properties of the model, the final model chosen was the one showing the best performance and the minimal number of features for the classification (i.e., 5 best discriminatory features). At each iteration of the LOO cross-validation technique, the sigmoid kernel was selected as the best-performing model, and grid-search over the hyperparameters suggested a top-performing classification for the default values of C = 1, and γ = 1/(number of features * data variance) = 0.2. These values promote good generalization by balancing the complexity and smoothness of the decision boundary, which is essential for preventing overfitting in small datasets. Using this model, the AUC = 87.88%, the sensitivity = 100%, and the specificity = 83.33%. The corresponding ROC curve and confusion matrix can be found in **Figures 6.4b** and **Figure 6.4c**, respectively.

The most discriminatory clinical feature selected was the number of ASM, selected at the 39th position out of 96 features (with a higher number of ASM in patients with a poorer response to VNS, which was not significant when comparing groups in the demographic data table – **Table 6.1**).

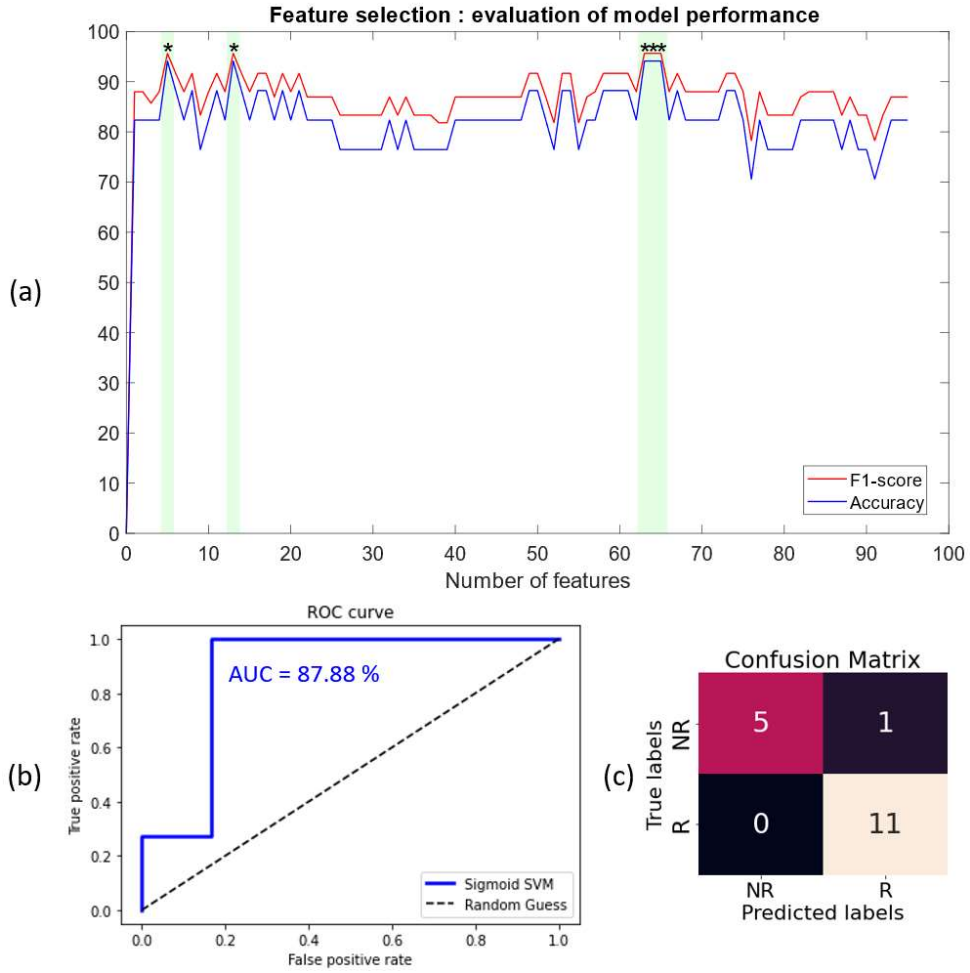

Figure 6.4 - Model and feature selection techniques for building the final SVM model. (a) Evolution of the classification accuracy and F1-score of the best-performing model during the recursive feature elimination; (b) Receiver Operating Characteristics (ROC) curve of the final Support Vector Machine (SVM) classifier, with an Area Under the Curve (AUC) of 87.88%; (c) Confusion matrix of the final SVM model, showing 5 true negative (TN) predictions, 11 true positive (TP) predictions, 0 false negative (FN) prediction and one false positive (FP) prediction.

2.4 DISCUSSION

Considering the broadness of projections arising from the thalamus and projecting to the cortex, modulation of this circuitry with VNS could disrupt the abnormal and synchronous activity of neurons (294). The present pilot study aims to increase our current understanding about the possible implication of thalamocortical tract integrity in the interindividual differences in response to VNS using diffusion MRI. Based on the diffusion metrics extracted, our results suggested a lower integrity in different subsegments of thalamocortical tracts in patients with a poorer response to VNS.

The thalamus may be a central player in the antiseizure effects of VNS (79,281–284). In addition to the rationale provided in the introduction, an immunochemistry study carried out in rodents found an increased nuclear Fos immunolabelling - a marker for high neuronal activation - in the habenular nuclei of the thalamus with VNS (79). Moreover, previous positron emission tomography studies conducted in humans found a bilateral increased cerebral blood flow in the thalami following VNS administration (281–283). Interestingly, the increased cerebral blood flow measured in one of these studies correlated with decreased seizure frequency (282). Using functional MRI, an increased activation in different cortical areas was found with VNS, while an increase in the thalamus was reported in 2 out of 5 patients – those who demonstrated improvement in seizure control after the implantation (284). Moreover, previous studies explored the connectivity features of thalamocortical relays in DRE patients (79,151,282–284). Indeed, a functional MRI study found an increased connectivity of the thalami to the anterior cingulate cortex and the left insula before the implantation, which was associated with a higher therapeutic efficacy of VNS (151). Finally, a previous diffusion MRI study found an increased FA in the left thalamocortical, limbic, and association

fibers in responders to the therapy compared to patients with a < 50% reduction in seizure frequency (150).

In the present study, higher MD and RD were found mainly in subsegments of the inferior and posterior thalamocortical tracts in non-responders. Although not specific, higher MD and RD could indicate reduced fiber integrity, including a reduced density of axons and/or lower myelination (295–297). Since DTI may suffer from strong assumptions and poor specificity, multi-compartment models were used to give further insights into microstructural differences across DRE patients.

High-gradient multi-shell diffusion MRI allowed us to use NODDI and MF, two multi-compartment models, for extracting microstructural metrics. While NODDI has been used to characterize white matter microstructure in an array of neurologic and psychiatric diseases, including Alzheimer's disease (298), Parkinson's disease (299), epilepsy (292), or schizophrenia (300), this study constitutes the first study investigating NODDI and MF metrics in DRE patients implanted with a VNS device. The lower NODDI-based ICVF found in subsegments of the inferior and posterior thalamocortical tracts in non-responders could suggest that the lower integrity suspected based on MD and RD may arise from a reduced fiber density. Since trends toward lower MF-based wFVF values were also found in the inferior thalamocortical tracts (projecting to the insular cortex), the results from the MF analysis further support the interpretation of the results obtained from the other diffusion models. Therefore, this pilot study could suggest that metrics from multi-compartment models may provide additional insight into microstructural differences without suffering from the strong assumptions of DTI.

The accuracy of 94.12% reached with the best SVM model only included classical DTI metrics, suggesting that they may be the best diffusion metrics to date to support clinical decisions. The best features selected for the SVM classification mainly involved diffusion metrics in the inferior thalamocortical tracts projecting to the insular cortex, i.e., tracts

that also showed significant differences between responders/partial responders and non-responders in the multiple regression analyses. Interestingly, a functional MRI study of the acute effects of VNS found a bilateral activation of the thalami – but more robustly left-lateralized – and insular cortices, suggesting the involvement of these brain areas in the antiseizure effects of VNS (301). Since a lower integrity of white matter tracts connecting these regions was found in non-responders in the present study, one could suggest that a lower integrity of these tracts could result in a lower therapeutic efficacy due to possibly impaired communication. While only DTI metrics were selected for the SVM model, the statistical models that included multi-compartment features provided additional information on the microstructural properties of thalamocortical tracts and confirmed the interpretation of DTI metrics. However, more research is necessary to determine whether multi-shell diffusion MRI could guide clinical decisions in the future.

Importantly, the best SVM model did not select clinical features. These findings reinforce the idea that clinical characteristics may not be useful for improving the prediction of VNS response (150). In line with our results, another 11-year retrospective study that included 365 pediatric patients built a prediction model and suggested that clinical features alone were not sufficient to accurately predict VNS response (302). Furthermore, this reflects the value of diffusion MRI metrics as markers of VNS response and the potential use of our classification model to patients implanted with a VNS device for whom clinical data is incomplete. Indeed, the performance of this model will remain unaffected by challenges related to the availability of clinical data. Our findings are similar to a previous DTI study where an SVM model was built (using metrics from various white matter tracts based on a tract-based spatial statistics analysis) and reached a classification accuracy of 89.5% when discriminating non-responders and responders. Adding clinical features did not improve the classification (150). This contrasts with another study that used EEG-based connectivity measures to build a classification model and suggested that clinical data

were useful for predicting VNS response (303). Although the comparison between techniques and studies is difficult, one could argue that DTI connectivity metrics are more powerful than EEG connectivity metrics in predicting response to VNS, as they may not require a full clinical characterization of the patients. Future prospective studies including an extensive clinical characterization of the patients could confirm these findings. Indeed, a previous study indicated that IQ deficiency may be a predictor for responding to VNS (304). However, including this feature – among others – in the classifier developed by Mithani and colleagues, did not improve the classification of patients (150).

Although the number of patients included in the present study is considered acceptable for a population of DRE patients implanted with a VNS device, it is important to note that the sample size remains relatively small. Therefore, while the present pilot study aimed at investigating differences of structural integrity in a pathway involved in antiseizure effects of VNS between patients showing a good and poor response to the treatment, a replication of these results is highly needed in a more extensive cohort of patients with DRE. Moreover, using an external cohort of patients to validate the SVM classifier built in the present study is warranted to evaluate the generalization, robustness, and practical relevance of the model. Besides these limitations, which are inherent to our study design, whether the differences observed in the present study (i) reflect an inherent inclination to respond more favorably to VNS, (ii) are linked to seizure activity - given that patients with a poorer response to the treatment may tend to experience seizures more frequently - or (iii) reflect the direct and more prominent impact of VNS in reorganizing tracts in patients with a better response, remains to be clarified. Indeed, a previous study suggested an increased MD in patients with drug-resistant temporal lobe epilepsy compared to controls in fasciculi carrying temporal lobe connections that could reflect astrogliosis and microstructure derangement related to seizure activity in the vicinity of the seizure focus (305,306). One of these studies found a higher MD that was associated with a shorter

interval between the last seizure and DTI (306). In their study, 24 patients had an average of 50 ± 54h between the last seizure and DTI examination, and 6 patients underwent MRI acquisition as outpatients: 5 had a seizure one week before the examination, and one patient had a seizure 10 min before (306). While our exclusion criteria involved excluding patients who had a seizure within 24h prior to the MRI examination to control for the possible impact of seizures on microstructural derangement, further studies incorporating hospitalized patients could provide insight into the potential influence of seizures on diffusion metrics of multi-compartment models. For our study design, knowing the exact time of the latest seizure prior to the MRI examination could be useful to control for possible seizure-related effects. Moreover, including a benchmark cohort of epileptic patients characterized by the same seizure burden as our cohort could be valuable for future research to extract the effect of VNS and remove possible effects of seizures on thalamocortical integrity. Further studies could only include patients thoroughly maintaining a seizure diary to precisely evaluate the reduction of seizure frequency. This could help to refine the categorization of patients, by using a continuous variable characterizing VNS response instead of using a binary classification. Longitudinal studies assessing diffusion metrics both before the implantation and throughout the treatment could be interesting to evaluate the modulatory effect of VNS on the integrity of thalamocortical tracts. Interestingly, the effect of different stimulation paradigms on thalamocortical integrity could be explored longitudinally. These investigations could help to better select stimulation parameters to maximize the neuromodulatory effects of VNS. For example, microburst stimulation – a paradigm that aims to stimulate with high-frequency bursts of stimulation – is believed to improve the modulation of the thalamus (307,308). Comparing the effect of microburst VNS on thalamocortical integrity with classical stimulation paradigms could validate the potential of microburst VNS to improve neuroplasticity effects in the brain. However,

further studies are needed to evaluate the potential effect of this paradigm in improving the response to VNS.

Pre-implantation acquisitions are needed to evaluate the value of diffusion metrics within thalamocortical to predict VNS response. However, this pilot study constitutes interesting insights into the variability in response across implanted patients. Finally, investigations of the structural-functional associations in DRE patients using a multimodal approach that includes high-gradient multi-shell diffusion and, for instance, functional MRI could refine the understanding of the biological prerequisites for responding to VNS.

Overall, our study highlighted the significant potential of single- and multi-compartment diffusion MRI models in elucidating interindividual differences in biological features that could be associated with VNS response. Investigation of the predictive value of multi-compartment models in a clinical context, and their potential to unravel the neuromodulatory effects of VNS on thalamocortical tracts could be investigated in pre-implantation and longitudinal studies utilizing the methodology described in this pilot study. These imaging techniques could contribute to medical decision-making, patient management, and the innovation of novel clinical treatments in the future.

2.5 ORIGINAL CONTRIBUTION

Identifying responders to vagus nerve stimulation based on microstructural features of thalamocortical tracts in drug-resistant epilepsy. **A. Berger**, M. Cerra, V. Joris, V. Danthine, B. Macq, L. Dricot, G. Vandewalle, N. Delinte, R. El Tahry. *Neurotherapeutics (2024), in press*.

CHAPTER 7. SYNERGIA MEDICAL : A NEW OPTOELECTRONIC NEUROSTIMULATOR

1. INTRODUCTION

This doctoral thesis included an industrial part realized in collaboration with Synergia Medical. Synergia Medical is a start-up founded in 2014 that is developing optoelectronic neurostimulators for patients suffering from drug-resistant epilepsy.

As this device is MRI-compatible, it has the potential to ease the clinical management of epileptic patients undergoing MRI acquisitions. Unlike other commercially available VNS devices, the optoelectronic neurostimulator does not need to be turned off during MRI acquisitions. Indeed, compared to other VNS devices, this optoelectronic neurostimulator is not composed of electrical wires but optical fibers. Moreover, the casing of the Synergia Medical implant is composed of glass, a diamagnetic and non-conducting material that makes the casing not sensitive to magnetic field attraction or heating. This new generation neurostimulator opens significant avenues for better understanding the mechanisms of action of VNS, as patients can be acutely stimulated during fMRI acquisitions. Research about the VNS-activated brain areas could lead to the personalization of the stimulation parameters by setting the parameters that lead to the highest activation of areas that are critically involved in the antiseizure effects of VNS. Moreover, knowing that the device does not have to be turned off before MRI acquisitions constitutes a time-saving advantage. Indeed, there is no necessity for a trained

individual to deactivate the device before entering the MRI room, nor is there a delay associated with deactivation. That is particularly useful for emergency situations, such as strokes. Previous commercially available devices require the MRI iso-center to be outside of an exclusion zone covering an area delimited by C7 and L3. This may constitute a limitation for patients who have to undergo MRI acquisitions in the context of cancer (e.g., breast cancer, heart cancer, spinal cord tumor), spine issue, preoperative MRI (e.g., shoulder), or structural and functional investigations of the heart.

The Synergia Medical device comprises an IPG that sends optical pulses and a battery that can be recharged transcutaneously. The wireless control system used to recharge the battery of the IPG is known as the Smart Charger (SC). This device communicates with the IPG through near-infrared (NIR) light. The SC will also be used by the reference neurologist to change the stimulation parameters of the implant after encoding the parameters in the clinical programmer, a software developed by the firm and accessible on a tablet. The electronic of the IPG includes a stimulation unit that generates optical pulses by driving Vertical-Cavity Surface-Emitting Lasers (VCSELs), that deliver NIR light characterized by a wavelength of 850 nm. The Optical Lead (OL) carries the NIR light to the electrode. In turn, the electrode sends electrical impulses to the vagus nerve by converting light pulses into electrical current using a photovoltaic cell unit composed of an absorbing material. The corresponding current activates photodiodes that send a feedback signal to the IPG. The different components of the Synergia Medical optoelectronic neurostimulator are shown in **Figure 7.1**.

In order to communicate with the implant remotely from the command room during fMRI acquisitions, a system needs to be developed. Development of this system is critical to study precisely the acute effects of VNS using fMRI. Part of the research conducted in this thesis consisted in developing this system and is described in the present chapter.

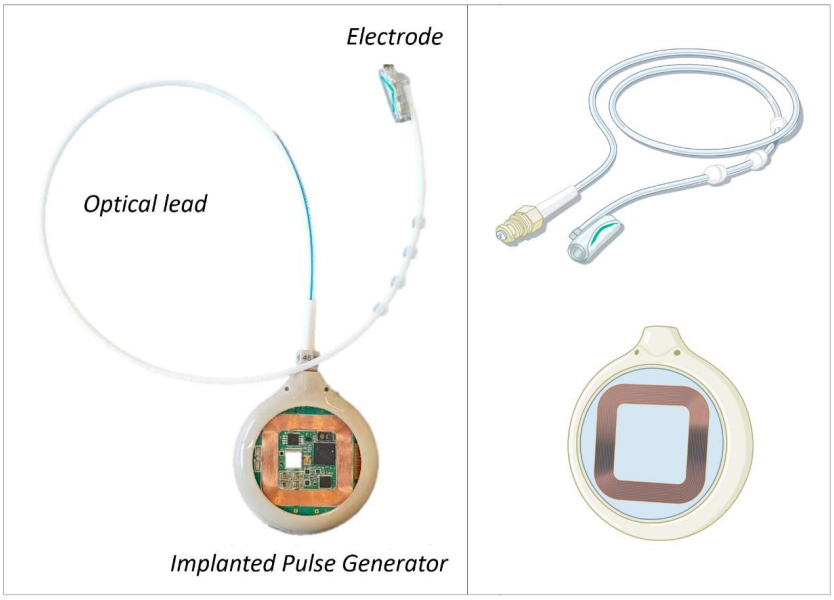

Figure 7.1 – Components of the Synergia Medical optoelectronic neurostimulator.

2. Optical Communication Device

2.1 Overview and specifications

The device used to control the implant remotely from the command room during fMRI acquisitions is called the Optical Communication Device (OCD) and is composed of optical fibers. The OCD acts as a communication bridge between the SC and the IPG. A patent was granted for this device on June 1st, 2022, and is currently active in all European countries (EP3930828B1), the United States (*US2023147433A1*), Japan (*JP2023515700A*), China (*CN115485015B*), Canada (*CA3170535C*), Brazil (*BR112022021614A2*) and Australia (*AU2020446167B2*) (309). In the

patent documentation, the OCD is defined as a kit of parts, including processing units and communication means that allow safe, reliable, and reproducible control of the functions of the Active Implanted Medical Device (AIMD) exposed to MR-image acquisition conditions (309).

The requirements for this device are:

- The device must be transportable.
- The device should communicate with the implant at approximately 10 m.
- The device should transmit enough optical power to overcome the diffusion in the human skin tissues.
- The device should transmit enough optical power to overcome possible loss within the fibers and at the extremities of the fibers.
- The device should transmit enough optical power to overcome noise in the MRI room.

As described in the patent, the OCD serves as an optical communication lead. It establishes communication between (i) the implanted source of communication light of the IPG and the external communication photodetector of the SC and (ii) the external source of communication light of the SC and the implanted photodetector of the IPG (309) (**Figure 7.2**)

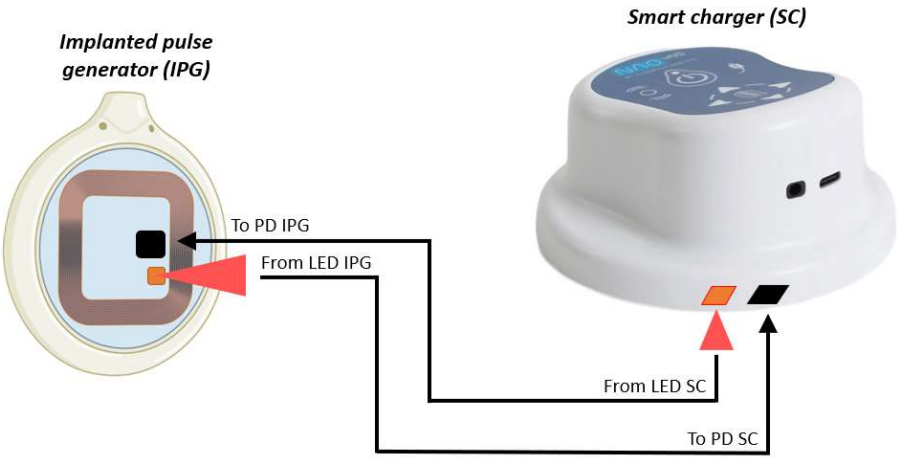

Figure 7.2 – Schematic representation of the communication between the IPG and the SC. IPG: implantable pulse generator, SC: smart charger, LED: light-emitting diode, PD: photodiode.

The OCD is composed of an embodiment that is placed in the command room and another in the MRI room. The proximal interface part (in the command room) is designed so that the optical fibers can be inserted and coupled to the SC and aligned with the photodetector and the external source of light of this unit. The distal interface part, placed on the patient's skin lying in the MRI system, enables the alignment of the optical fibers with the photodetector and the implanted source of NIR light of the IPG. Using a software designed to control the stimulation parameters, the computer communicates with the SC (via a USB-C connection or Bluetooth). The SC, in turn, sends the commands to the implant through the optical fibers. The OCD is also composed of a custom-made computer-controllable electronic system and optical fibers used for the optical wake-up of the implant. While this section aimed at giving an overview of the different components of the OCD, technical details about the two systems composing the OCD, and the experiments conducted to design the OCD

parts are provided in *section 2.2 – Optical wake-up system*, and *section 2.3 – Communication system*). The different subparts of the final OCD in an MRI environment are shown in **Figure 7.3**. Details about each sub-system can be found in the following sections.

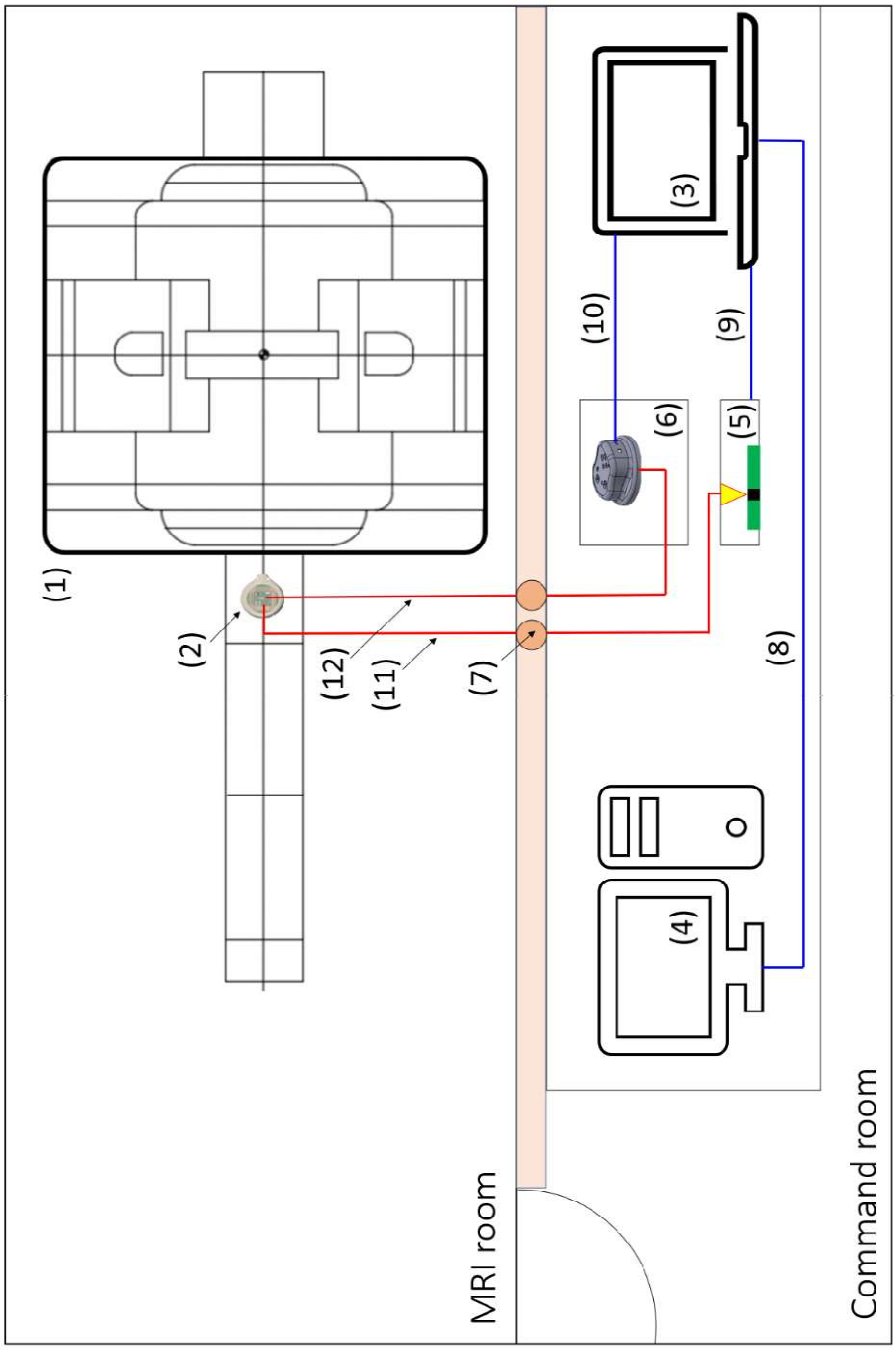
(1)
(2)
(12)
(11)
(7)
(3)
(10)
(9)
(6)
(5)
(8)
(4)
MRI room
Command room

Figure 7.3 – Schematic representation of the Optical Communication Device (OCD) setup. (1) MRI system. (2) Implantable Pulse Generator (IPG). (3) SC/IPG communication interface. (4) MR controller. (5) Vertical-Cavity Surface-Emitting Lasers (VCSELs) composing the optical wake-up system. (6) SC/IPG communication system. (7) Feedthrough holes for MRI room/command room communication. (8) Connection between MR-controller and SC/IPG communication interface for functional MRI (fMRI) synchronization with stimulation. (9) Connection between SC/IPG communication interface and optical wake-up system. (10) Connection between the SC/IPG communication interface and SC. (11) Optical fibers composing the optical wake-up system. (12) Optical fibers composing the SC/IPG communication system. Optical wake-up system : (5) + (11). Communication system (12).

2.2 OPTICAL WAKE-UP SYSTEM

To establish communication with the implant, the communication mode of the IPG must be activated with a wake-up command. The IPG is composed of four photodiodes, and a minimum quantity of NIR light has to be detected by each of the four photodiodes to result in the optical wake-up of the implant. The use of four photodiodes instead of a single one with a unique threshold prevents false detections. The optical wake-up is usually achieved using the SC, which generates an optical wake-up signal - one burst of NIR light with an 850 nm wavelength lasting 19 ms - detected by the implant. In an MRI environment, the implant must be awakened from the command room using the OCD. After researching and testing various optical solutions, the optical wake-up part of the OCD has been optimized. For this application, a 15 m-long, 5 mm-diameter bundle that is composed of glass optical fibers with a diameter of 70 µm is used (Oplatek Bevenic) (**Figure 7.4**). The use of glass optical fibers instead of plastic fibers was needed for this application to limit optical losses and allow long-distance

transmission of NIR light. Moreover, the use of small-diameter fibers of 70 µm makes the bundle flexible, which is an important criterion for transporting the OCD and installing this system between the command room and the MRI room.

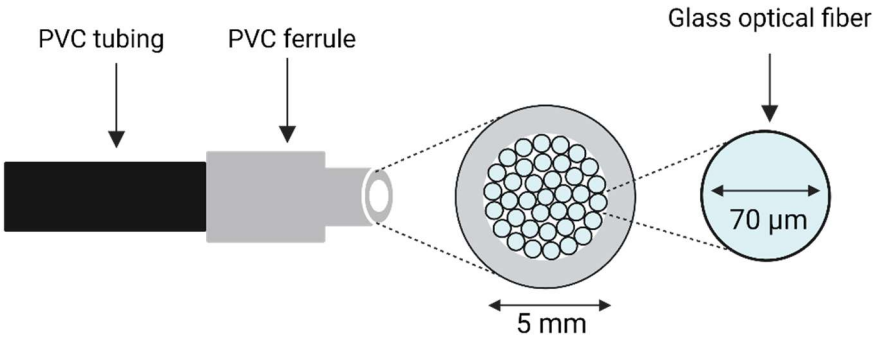

Figure 7.4 – Schematic representation of the bundle of optical fibers used as part of the optical wake-up system of the OCD.

Given the important optical losses when a simple NIR LED is used for the optical wake-up part of the OCD, VCSELs were used for the final version. VCSELs allow a narrower beam of light compared to classical LEDs, leading to a better focus of the light in the bundle of optical fibers. Moreover, since VCSELs have smaller physical dimensions than LEDs, more VCSELs can be coupled at the entry of the bundle of fibers. These properties of VCSELs allow maximizing the power transmitted through the bundle of optical fibers to overcome optical losses.

The NIR light-emitting VCSELs were controlled with a custom computer-controllable electronic system (**Figure 7.5-1/2**). The operation of the custom electronic system is controlled using a computer application, which communicates instructions to an Arduino (i.e., a Printed Circuit Board – PCB). In our set-up, the Arduino controls four sources of current (**Figure**

7.5-2/3). These sources of current drive independently four VCSELs (high-power HV85-2000P1, narrow beam, 2 W optical output power, Optowell) that are mounted inside a 3D-printed piece (**Figure 7.5-4**), designed to prevent direct contact with the eyes and avoid potential damages. The optical fiber bundle (**Figure 7.5-5**) was fixated in a connector of the 3D-printed piece in front of the VCSELs to gather the NIR light transmitted to the MRI room for waking up the implant. In turn, the transmitted NIR light signal is detected by the photodiodes mounted on the IPG responsible for detecting the optical wake-up signal (**Figure 7.5-8**).

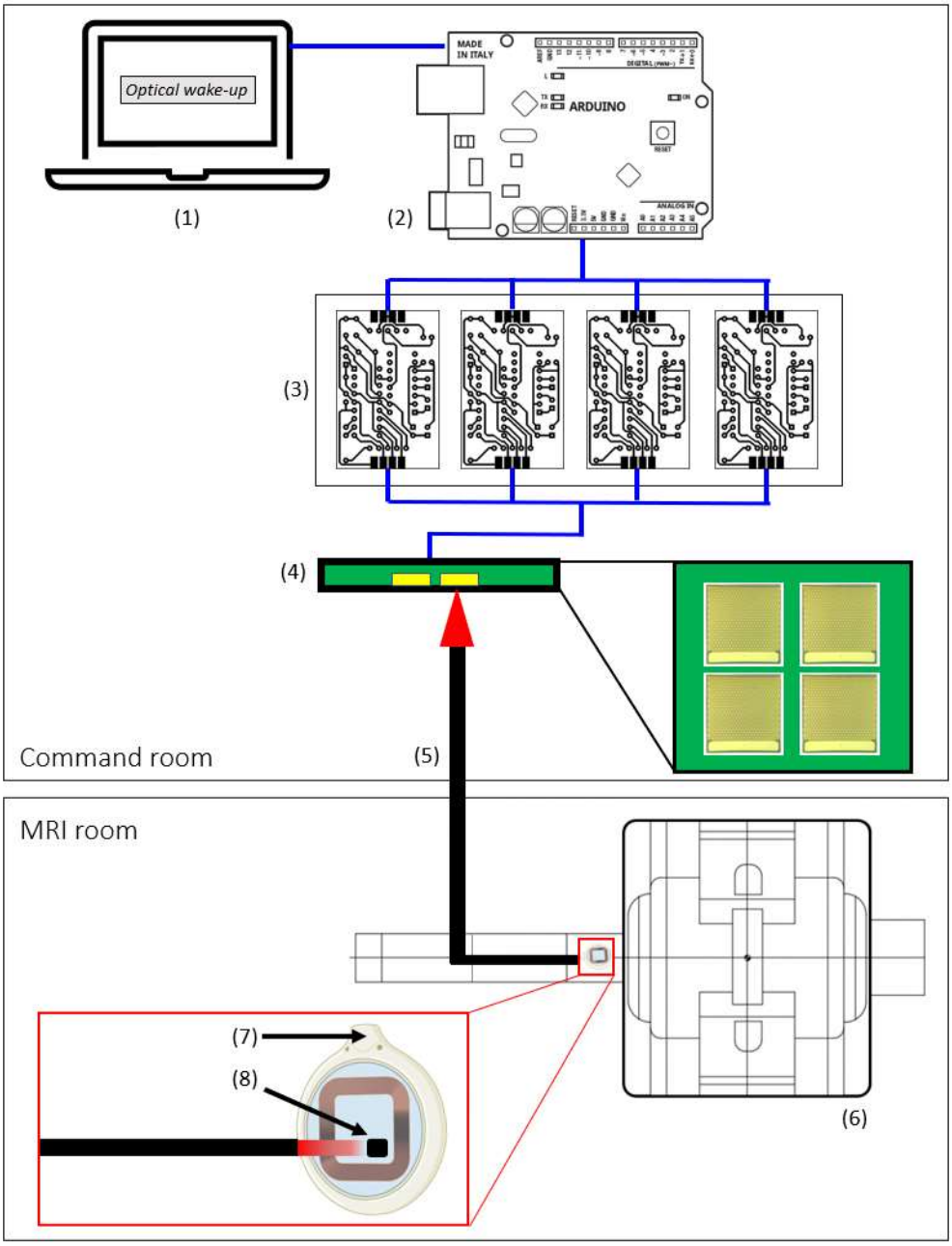

Figure 7.5 - Schematic representation of the optical wake-up system. (1) Software that controls commands sent to the Arduino. (2) Arduino that controls four sources of current. (3) Sources of current that drive near-

infrared (NIR) Vertical-Cavity Surface-Emitting Lasers (VCSELs). (4) 3D-printed piece containing four VCSELs. (5) Bundle of optical fibers that send optical wake-up commands to the MRI room. (6) MRI system. (7) Implanted Pulse Generator (IPG) placed in the head coil of the MRI in front of the bundle of optical fibers. (8) Photodiode of the IPG that detects the optical wake-up signal.

2.3 COMMUNICATION SYSTEM

Aside from the optical wake-up system of the OCD that intends to wake up the communication mode of the IPG, the second part of the OCD consists of establishing communication between the SC (in the command room) and the IPG (inside the MRI system). This communication is crucial to ensure a connection of the implant with the SC for tuning the parameters remotely and initiating stimulation. An overview of this system can be found in **Figure 7.6.**

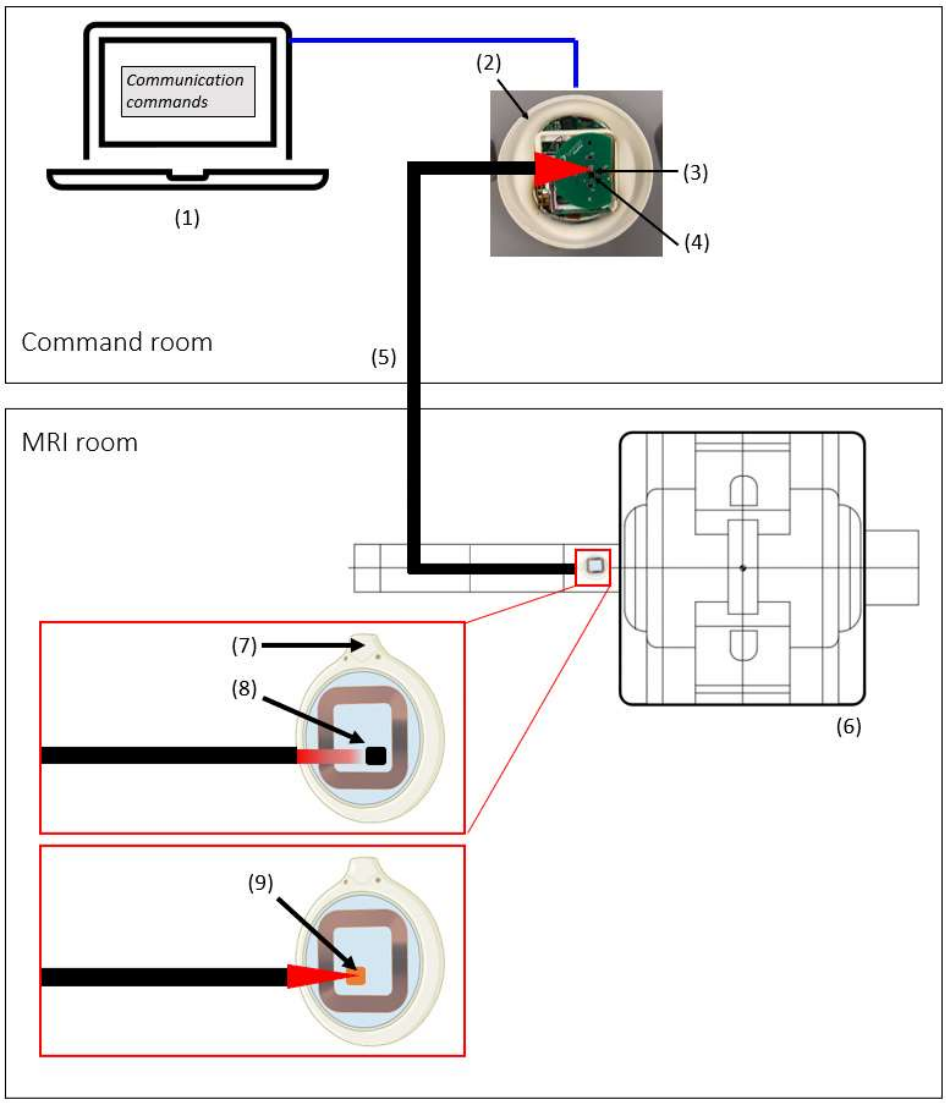

Figure 7.6 - Schematic representation of the communication system. (1) SC/IPG communication interface. (2) (boosted) SC. (3) NIR LED of the (boosted) SC. (4) Photodiode of the SC detecting the signal from the IPG. (5) Bundle of optical fibers that send communication commands to the MRI room. (6) MRI system. (7) Implanted Pulse Generator (IPG) placed in the head coil of the MRI in front of the bundle of optical fibers. (8) Photodiode

of the IPG that detects the communication commands. (9) NIR LED of the IPG sending a signal back to the SC to establish proper communication.

In order to maximize the optical power sent from the SC to the command room, a boosted version of the SC was created and is composed of a high-power NIR LED (SFH 4451, 850 nm, MIDLED®, driving pulsed current of maximum 1 A, driven with a pulsed current of 450 mA for the OCD application). Bidirectional communication between the SC and the IPG is needed to ensure a good connection of the implant. The boosted SC is controlled using the computer software and transmits NIR light through the bundle of optical fibers (Oplatek Bevenic), which forms the communication channel of the OCD system. The 10 m long optical bundle consists of two optical cables, each with a 5 mm core diameter and made up of optical fibers with a 70 µm diameter. These two cables merge into a larger 7.1 mm-diameter optical cable on the extremities of the bundle (**Figure 7.7**). The signal transmitted through the optical bundle is detected by the photodiode mounted on the IPG responsible for communication with the implant. If the implant correctly receives the signal, the IPG sends an NIR light signal back to the SC to ensure a proper implant connection. Therefore, a NIR LED mounted on the IPG transmits a signal that goes through the skin and the bundle of optical fibers guiding the NIR light to the photodiode of the SC.

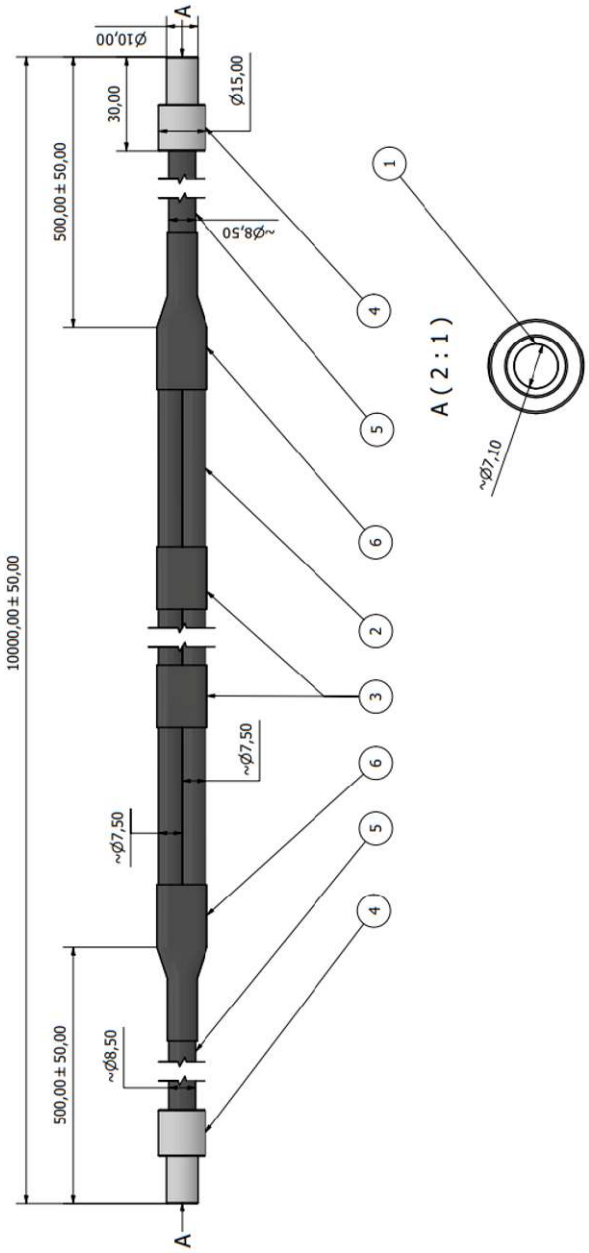

Figure 7.7 - Custom-made bundle of optical fibers used to communicate between the SC and the IPG (Oplatek Bevenic). (1) Merged fibers. (2) SCHOTT® Fiber Optic Light Cables (LKS) composed of 70 µm-diameter optical fibers. (3) Heat shrink tubing to bundle cables together. (4) PVC

ferrule. (5) PVC tubing. (6) Heat shrink tubing to protect the bifurcation part.

2.4 Experimental testing of optical wake-up system

2.4.1 Minimum optical power required to wake up the implant

2.4.1.1 Methods

The minimum optical power required to wake up the implant was measured before assessing the optical loss within the fibers transmitting the signal from the command room to the MRI room. To achieve this, a NIR LED (L852P50 – 848-856 nm, optical output power: 50 mW, diameter 5.6 mm, Thorlabs) was powered by various current amplitudes using a 2450 SourceMeter (Keithley) and placed in front of the detection photodiodes of the IPG (**Figure 7.8**). When properly awakened, the implant emits a visible flashing light (that will be removed for the implantable version of the IPG), and the minimum optical power needed to wake up the implant can be measured. This was done using a thermal power sensor (S310C, 10W, 20-mm diameter, Thorlabs) and a digital power and energy meter (PM100D, Thorlabs). The thermal power sensor head comprises thermopile-based sensors for measuring the spectra of the NIR light emitted. Emitting NIR light produces a temperature change converted into an electrical signal, and the power meter console estimates the optical power based on the measured signal (**Figure 7.8**).

2.4.1.2 Results

Increasing the current until a visible flashing light is observed on the IPG and placing a thermal power sensor in front of the NIR LED allowed us to determine that an approximated optical power of 10 mW is required to wake up the implant.

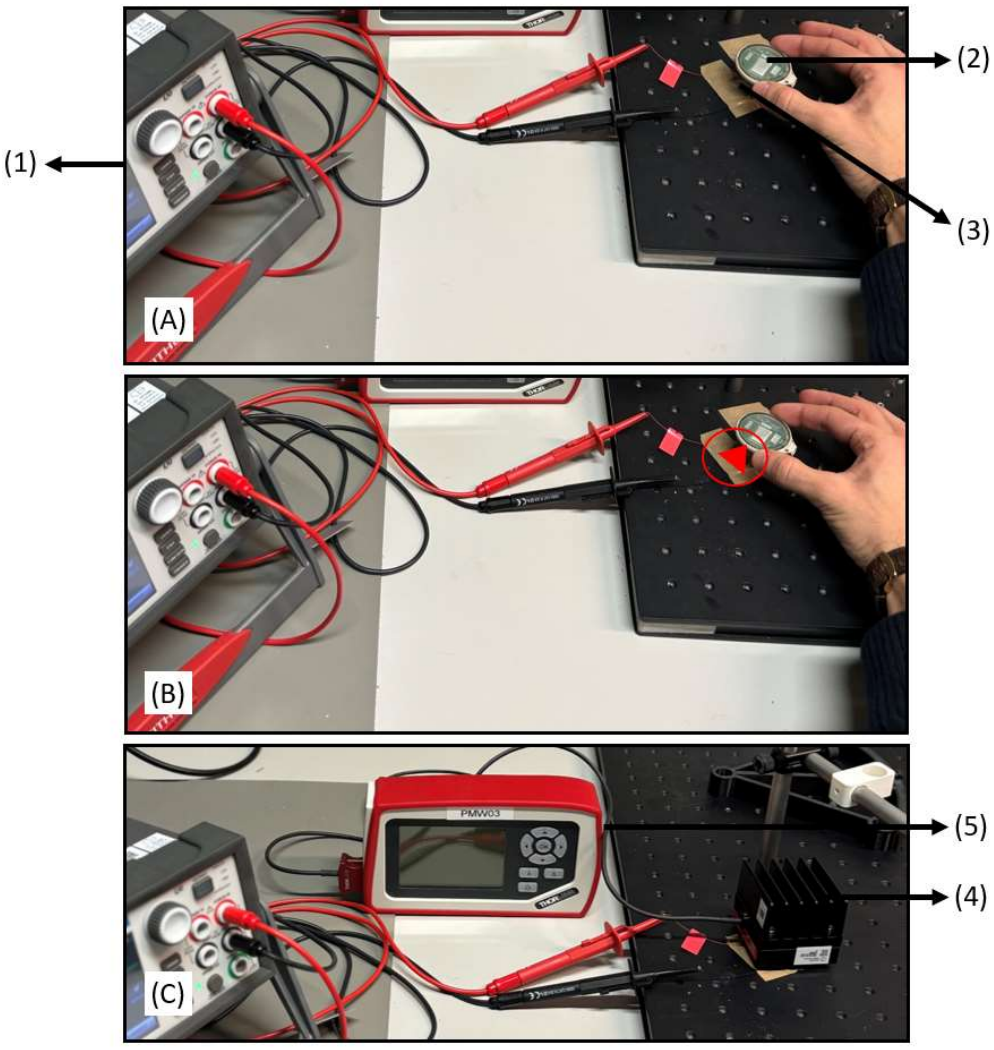

Figure 7.8 - Experimental setup to measure the minimum optical power needed to wake the Implantable Pulse Generator (IPG). (A) Increase of the

current supplied to the near-infrared (NIR) light-emitting diode (LED). (B) For sufficient optical power delivered by the NIR LED when increasing the current, the IPG wakes up as indicated with a flashing red light. (C) Measurement of the minimum optical power that led to the optical wake-up of the implant. (1) 2450 SourceMeter Keithley, (2) IPG, (3) L852P50 NIR LED (848-856 nm), Thorlabs, (4) Thermal power sensor, (5) Digital power and energy meter - PM100D, Thorlabs.

2.4.2 Optical power loss assessment

2.4.2.1 Methods

New tests were conducted to determine the optical losses within the bundle of optical fibers used for the optical wake-up and through the skin outside an MRI environment. These tests are necessary to evaluate whether the system would be robust enough for long-distance and *in vivo* communications.

A high-power NIR LED (L1I0-0850060000000, 850 nm, 1A, 1.35 W LUXEON IR Series, Lumileds) was driven with different current intensities, and the optical power was measured using the same experimental set-up depicted in **Figure 7.8**. The same tests were conducted with the optical fiber bundle used for the optical wake-up alone and with skin samples of 2 mm or 3 mm thickness placed between the LED and the entry of the optical fiber. The specimens consisted of pig skin measuring approximately 10 cm by 10 cm that were prepared and vacuum-sealed for preservation (using FFS015X - JCS).

2.4.2.2 Results

Results showing the optical power measured in these different conditions are shown in **Figure 7.9**. Optical power values in the different conditions are reported in **Supplementary Material S7.1**.

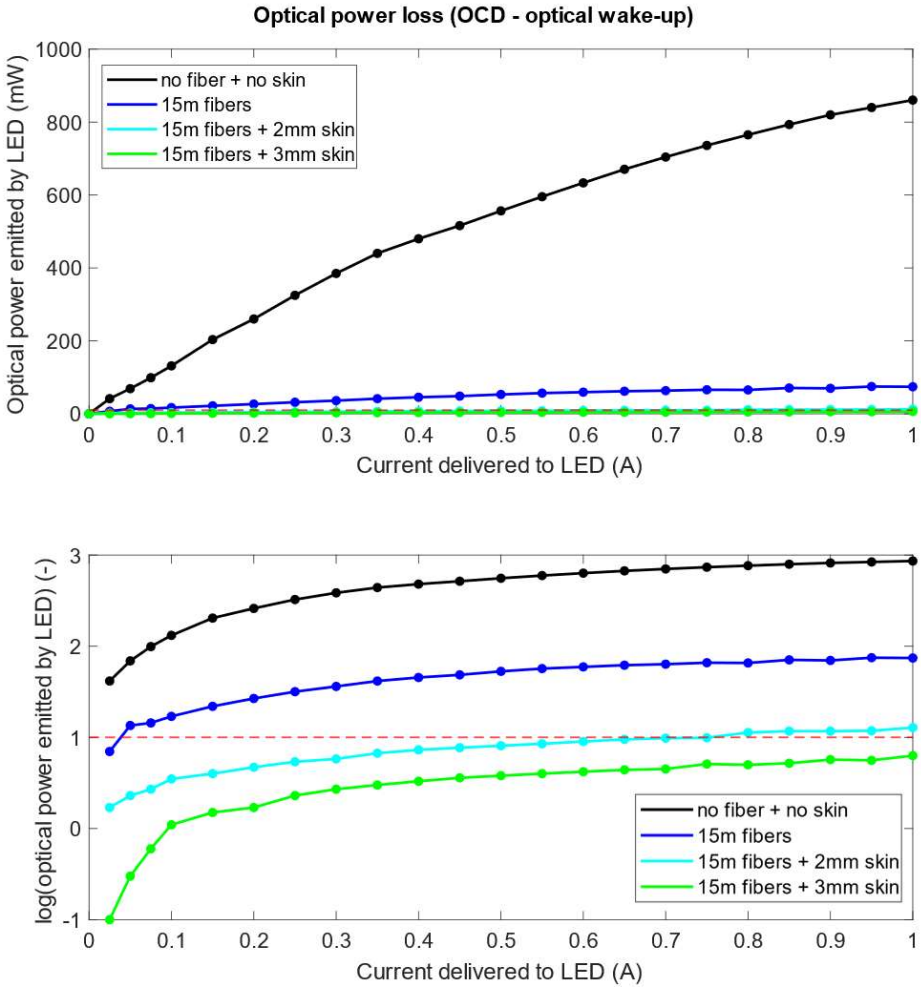

Figure 7.9 - Measurement of optical power losses within the bundle composed of optical fibers and skin of different thicknesses for the optical wake-up of the implant. Discontinuous red line: estimated optical threshold for optical wake-up of the implant.

Losses within the fibers, attributed to the coupling at the extremities and through the skin, remain important. However, considering that a minimum optical power of approximately 10 mW is required to wake up the implant and that other NIR light-emitting systems with higher optical power could be used (*see section 2.2.4 – Sensitivity to MRI static field*), the overall loss remains acceptable.

2.4.3 SENSITIVITY TO MRI STATIC FIELD

2.4.3.1 METHODS

Tests were conducted to evaluate the sensitivity of the system to the static field of the MRI (SIGNA™ Premier 3T system, GE Healthcare, Milwaukee, WI, USA). The IPG was positioned at different distances from the entry of the MRI bore (100, 80, 60, 40, 20, and 0 cm), and the optical wake-up commands were sent from the command room to the MRI room through the OCD. A 5 mm-thick sample of pig skin was placed between the optical wake-up part of the OCD and the implant to simulate *in vivo* conditions.

2.4.3.2 RESULTS

Depending on the application, one to four VCSELs can be turned on by the system. However, the experiments conducted as part of this project showed that one VCEL provides sufficient optical power for the optical wake-up of the implant. **Irrespective of the distance from the entry of the bore and the presence of the skin sample, all optical wake-up commands successfully woke up the implant (Figure 7.10).**

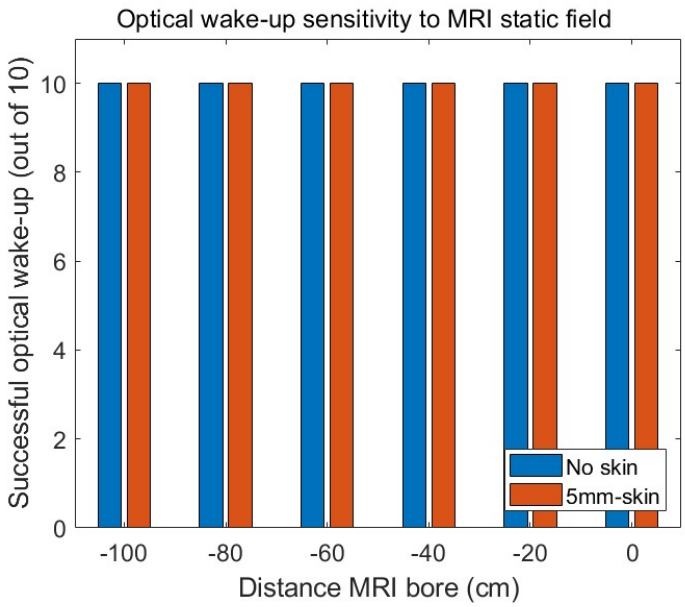

Figure 7.10 - Evaluation of the optical wake-up sensitivity to the MRI static field at different distances from the MRI bore.

2.5 EXPERIMENTAL TESTING OF COMMUNICATION SYSTEM

2.5.1 OPTICAL POWER LOSS ASSESSMENT

2.5.1.1 METHODS

An experiment was conducted to characterize the optical power losses associated with the fibers (transmission and coupling) and the diffusion of the light through the skin outside of an MRI environment. A schematic representation of the experimental set-up used is shown in **Figure 7.11**. Communication commands were sent using the computer software (**Figure**

7.11-A). A message was displayed on the interface, indicating whether the connection to the IPG was successful (**Figure 7.11-B**).

2.5.1.2 RESULTS

When using the optical fiber bundle alone, 100% of connection commands passed the communication test. When a 10 mm-thick skin sample was placed between the bundle of optical fibers and the IPG to simulate an extreme – and unrealistic – *in vivo* situation, 100% of the commands successfully connected with the IPG.

These tests demonstrate the robustness of the communication system of the OCD outside of an MRI environment.

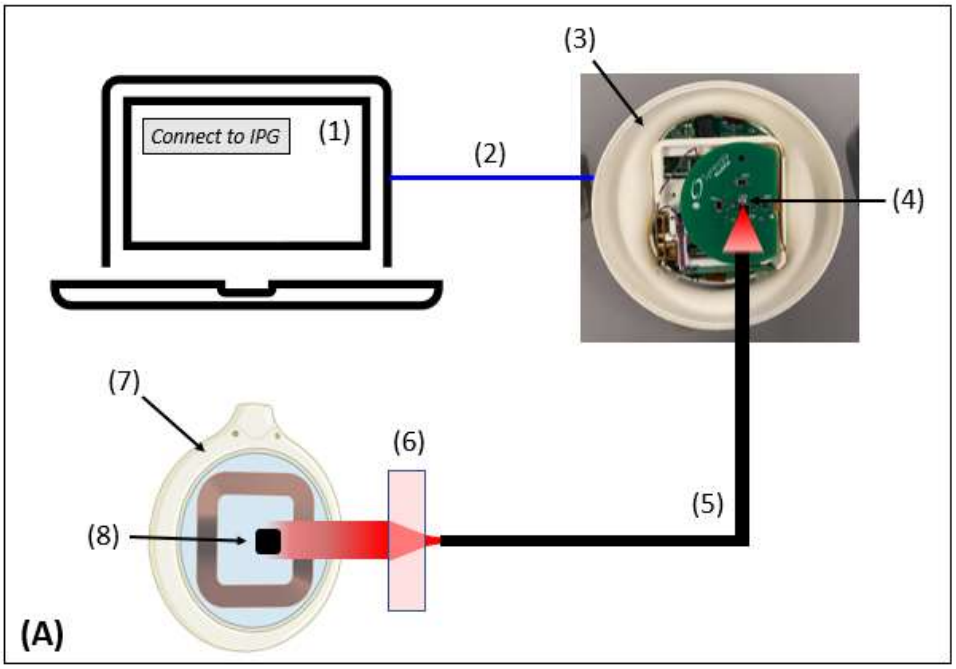
(3)
Connect to IPG
(1)
(2)
(4)
(7)
(6)
(5)
(8)
(A)

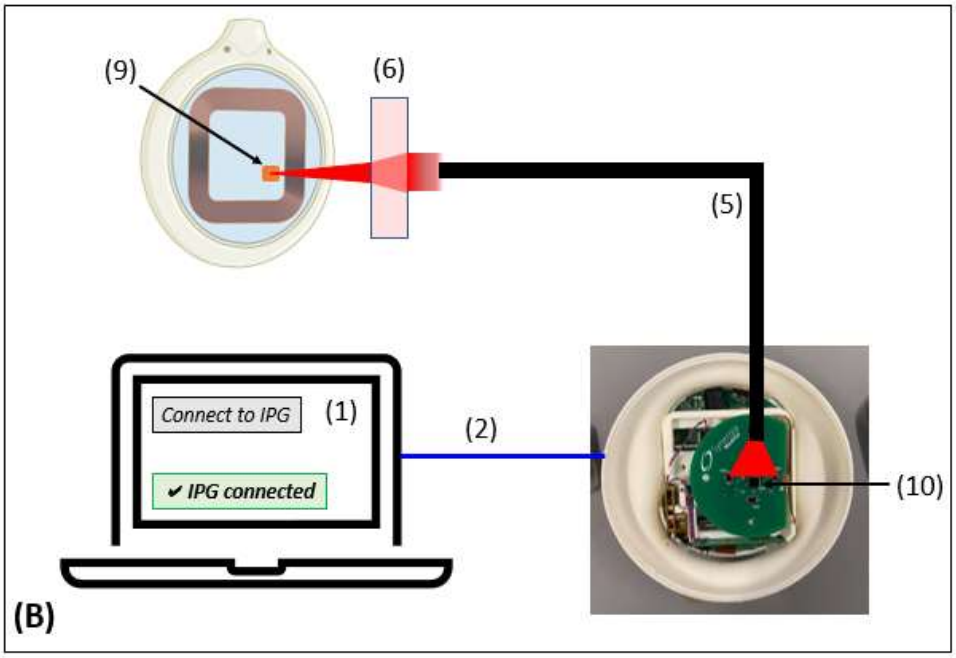
(9)
(6)
(5)
Connect to IPG
(1)
(2)
✔ IPG connected
(10)
(B)

Figure 7.11 - Schematic representation of the experimental set-up used for assessing the robustness of the communication between the SC and the IPG through the OCD (laboratory setting), with (A) the signal programmed on the interface and sent from the boosted SC to the IPG and (B) the signal arising from the IPG and detected by the SC. (1) SC/IPG communication interface. (2) Connection of the boosted SC to the SC/IPG interface. (3) SC. (4) NIR LED of the SC (SFH 4451, 850 nm, MIDLED®, driven with a pulsed current of 450 mA for the OCD application). (5) Bundle of optical fibers. (6) Skin samples of 10 mm-thickness. (7) Implanted Pulse Generator (IPG). (8) Photodiode of the IPG. (9) NIR LED of the IPG. (10) Photodiode of the SC.

2.5.2 SENSITIVITY TO MRI STATIC FIELD

2.5.2.1 METHODS

To test the sensitivity of the communication with the implant in an MRI environment, the IPG was positioned at various distances from the entry of the MRI bore (100, 80, 60, 40, 20, and 0 cm). The SC was connected to the computer software via a USB-C connector, and connection commands were sent between the SC and the IPG (bidirectional communication). If missing bits of information lead to a connection failure of the IPG, an error message is displayed on the computer interface. This was implemented for safety reasons, to ensure perfect communication between the IPG and the SC before adapting stimulation parameters, removing the possibility of false detections. The same experimental set-up represented in **Figure 7.11** was used, with the IPG placed inside the static field of the MRI.

2.5.2.2 RESULTS

Without using samples of pig skin between the IPG and the OCD, all the commands passed the communication tests, independently of the distance of the IPG to the entry of the bore (**Figure 7.12**). When placing a 5 mm-thick sample of pig skin between the IPG and the OCD, all communication commands correctly passed the tests when the IPG was placed up to 40 cm from the entry of the bore. However, 7/10 and 6/10 commands passed the tests when the IPG was positioned at 20 cm and 0 cm from the entry of the MRI bore, respectively, with a 5 mm-thick sample of pig skin placed between the IPG and the OCD (**Figure 7.12**).

These results demonstrate that using the OCD, the communication between the SC and the IPG is sensitive to the static field of the MRI. The sensitivity remains acceptable for fMRI acquisitions, as multiple commands can be sent until a successful connection is established and the stimulation is initiated.

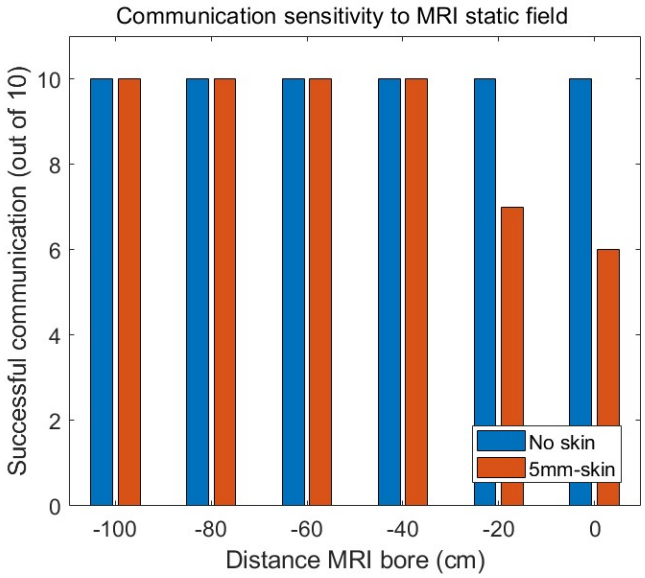

Figure 7.12 - Evaluation of the SC/IPG communication sensitivity to the MRI static field at different distances from the MRI bore.

3. DISCUSSION

Research about the mechanisms of action of VNS using fMRI has faced challenges due to the presence of ferromagnetic materials in these devices. Indeed, it was suggested that the static field of the MRI, RF pulses, and MRI gradients could cause the generator to vibrate and VNS devices to malfunction (310). Therefore, while previous studies investigated the acute effects of VNS using fMRI, some precautions have been implemented to avoid device deactivation during MRI acquisitions. In this context, previous 1.5 T MRI studies (i) used a transmit/receive RF head coil during the MRI acquisitions and (ii) implanted the VNS device with a specific orientation to avoid adverse events (311,312). Indeed, when conducting MRI acquisition with an active VNS device, it was suggested that the placement of the IPG should be such that the reed switch inside the pulse generator (i.e., a sensor able to detect a magnetic field, and used in the manual VNS mode to trigger or stop stimulation when swiping a magnet in front of the generator in commercially available devices) is oriented parallel to the static field of the MRI. This is done to ensure that the VNS device continues to operate during fMRI acquisitions (313,314). While it was suggested that orientation of the reed switch may not be imperative if the electrode inputs remain oriented parallel to the orientation of the static field to minimize the chance of inducing electrical currents, it does not prevent inhibition or induction of the stimulation while the patient is entering the MRI room (312). Therefore, as recommended in the physician manual, the stimulation should be completely turned off during MRI examinations (1.5T and 3T systems). For UHF 7T MRI systems or higher, more technical research is needed to evaluate the safety of these examinations for VNS patients.

In opposition to previous commercially available VNS devices, the optoelectronic neurostimulator developed by Synergia Medical is composed of optical fibers instead of electrical wires, making this device

fully MRI-compatible. The development of this device opens up new opportunities to (i) evaluate the acute effects of VNS on brain structures using fMRI when different stimulation parameters are used and (ii) develop new titration strategies by selecting stimulation parameters that are maximally recruiting structures of the vagal afferent network.

In this context, part of the research presented in this thesis consisted of developing the OCD, a system used to control the stimulation parameters and initiate stimulation from the command room while the implant is inside an MRI system. In the context of a study investigating the effect of different stimulation parameters at the central level, the use of this device would increase the comfort of the patient by enabling adjustments of the stimulation parameters while the patient remains inside the MRI system. Moreover, this device is needed to synchronize stimulation to the fMRI acquisitions. The final version of the OCD consists of two main components: (i) an optical wake-up system comprising a high-power VCSEL and an optical bundle that transmits the signal to the MRI room, and (ii) a communication system, which includes a boosted version of the SC with a high-power NIR LED and an optical bundle. This system ensures bidirectional communication between the implant and the SC for entering in a communication mode with the IPG from the command room. In an MRI environment and simulating an *in vivo* condition using samples of skin, the optical wake-up system of the OCD is highly robust. While the communication system of the OCD in a simulated *in vivo* condition seems to be sensitive in the static field of the MRI, this sensitivity remains acceptable for fMRI acquisitions in the context of a pilot study conducted in sheep that would be anesthetized.

Further development could improve communication robustness with the implant using the OCD. However, possible paths of optimization are beyond the scope of this thesis, as they may necessitate adjustments in the SC/IPG software interface. Indeed, a bidirectional communication is

required between the IPG and the SC to connect the implant. The communication fails if a few bits of information are missing.

However, in the context of fMRI acquisitions, only a small portion of the exchanged bits are needed to meet the requirements for this application. For instance, bits of information exchanged between the SC and the IPG to read the status of the battery are not needed in an MRI context, as this can be checked beforehand. Therefore, adapting the software for the IPG connection to ignore missing bits of information that are not necessary in the context of fMRI acquisitions could help improve the robustness of the OCD communication system in an MRI environment. A the hardware level, adding redundant communication could help to correct for transmission failure. The final validation of this system involves testing the OCD outside and inside an MRI environment in real *in vivo* situations. This will be conducted initially in implanted sheep and ultimately in patients once the first implantations are achieved.

CHAPTER 8. DISCUSSION

This chapter is structured into two main sections: dosing biomarkers and response biomarkers. While the results of the studies conducted as part of this thesis were discussed in depth in the corresponding chapter, the present chapter aims to summarize the main findings, address the limitations, and provide a further discussion about the practical implications of this work and the contributions to the field.

1. DOSING BIOMARKERS

1.1 DEVELOPMENT OF A NEW TITRATION STRATEGY BASED ON LARYNGEAL MOTOR-EVOKED POTENTIALS RECORDINGS

A new titration technique aiming to use physiological indicators of fiber engagement was proposed, in contrast to the empirical method currently used and based on the subjective tolerance of the patients to the stimulation.

In the context of VNS, the term *"dosing biomarkers"* refers to biological measurements used to guide the dose to be delivered (or the stimulation parameters that should be used) to optimize the therapeutic efficacy of the therapy. These markers can help to give insight into the level of engagement of the vagal fibers for different stimulation parameters. These biomarkers are needed to select stimulation parameters that optimally recruit the vagal fibers while limiting the side effects of the therapy. Compared to other treatments – and more specifically, pharmacotherapies

where the dose-response curves of pharmacologic compounds are well established, dosing biomarkers in the field of VNS remain limited. Therefore, biomarkers that allow the determination of the clinically relevant dose to be administered to each patient are lacking, preventing the development of individualized and biologically informed titration strategies.

LMEPs can be easily recorded using two surface electrodes and reflect a genuine activation of low threshold vagal Aα-fibers, as determined by studies evaluating the conduction velocity of fibers responsible for the LMEPs induction (155,156). While antiseizure effects are conferred by fibers with a higher threshold (more specifically Aβ-, Aδ- and/or B-fibers) but, knowing that properties of fibers are intrinsically related, recruitment properties of low-threshold fibers could give indirect information about the recruitment state of fibers involved in the antiseizure effects of VNS (49,159). Previous modeling studies investigating the effect of stimulation on the recruitment of myelinated fibers show that thresholds are proportional to the square of the fiber diameter (315). Therefore, if fibers with antiseizure effects have a threshold at most twice that of Aα-fibers, then their diameter would be smaller by a factor of at most $\sqrt{2} = 1.41$. Moreover, it is worth mentioning that previous animal studies that reported antiseizure effects with VNS used current intensities below the recruitment threshold of B-fibers (73,86,158).

In this context, a clinical exploration of VNS parameters was conducted in ***Study 1***, where the clinically used stimulation intensity was compared to the intensity leading to LMEPs saturation. It was shown that most of the responders to VNS showed a stimulation intensity in a range between 1-fold and 2-fold the intensity inducing LMEP saturation. Conversely, patients with a poor response to VNS showed a high inhomogeneity in the ratio between the clinical intensity used and the intensity leading to LMEP saturation. These results emphasize the drawback of the empirical titration that will tend to increase the current intensity beyond a possible *"optimal*

level" (i.e., a level of stimulation that should be sufficient to obtain clinical benefit where most of the clinically responsive patients are found) in non-responders and try to maximize the antiseizure effects as long as no side effects prevent such an increase.

Based on these findings, a novel titration strategy was proposed, where LMEPs measurements could be used as a physiological indicator of fiber engagement. During the titration process, antiseizure effects should be expected upon achieving what could be considered as the *"optimal level"* of stimulation for each patient (an intensity found within the range of 1-fold to 2-fold the intensity leading to LMEP saturation). Indeed, above this level of recruitment, the chance of observing sufficient therapeutic efficacy will be limited. Setting this personalized optimal range could help to prevent overstimulating patients with current intensities above what is necessary to observe clinical benefits. In addition to the programmed stimulation current used clinically as part of the patient's treatment, the *AutoStim* mode is also available in three models of VNS devices, including AspireSR® 106, SenTiva® 1000, and 1000-D (LivaNova, Inc., London, United Kingdom). This feature detects an elevated heart rate associated with the potential onset of a seizure and delivers an extra dose of VNS accordingly. Some patients who were included in the investigations presented in this thesis were implanted with the AspireSR® 106 model. It is worth mentioning that this mode imparts additional beneficial effects in patients in whom it is activated (316–318). Therefore, setting the clinically used current intensity within the ideal range and using the optimal range to set the current used in the *AutoStim* mode and the manual mode (when swiping the magnet manually in front of the generator) - considering that no side effects prevent its use - could maximize the chance of observing antiseizure effects with VNS.

Based on the new titration method proposed, if the reduction of seizure frequency is not sufficient despite the use of intensities in an effective range, other stimulation parameters could be tuned to modulate

the effects at the central level. Indeed, it was suggested that changing the stimulation frequency or the pulse width could modulate the synaptic transmission at the central level (169). Further research is needed to investigate the potential of fine-tuning these parameters in patients exhibiting a poor response to VNS despite using a current intensity within the effective range. If no clinical efficacy is observed, one may suggest a VNS-resistant form of epilepsy with altered integrity at the central level, preventing sufficient antiseizure effects with VNS. In this situation, the development of new treatments aiming at controlling epilepsy in these patients is needed.

However, one cannot exclude that patients may exhibit varying levels of tolerance to the stimulation, such that patients with a lower tolerance may not support a stimulation intensity in the effective range. For these patients, the distinction between *"real non-responders"* - who would not respond even if an intensity in the effective range was used, or *"false non-responders"* - who simply do not tolerate the stimulation but would be considered as responders if a higher intensity was used, remains impossible. Therefore, while reducing the frequency and pulse width of the clinical stimulation or increasing the *AutoStim* threshold could reduce the side effects, the decision to keep them implanted or keep the VNS device active may have to be evaluated by the reference epilepsy center. A summary of the novel titration strategy proposed in ***Study 1*** is shown in **Figure 8.1**. It is worth mentioning that some patients may present a non-functional implant (electrode not positioned on the nerve or broken electrodes). For these patients, replacement of the device should be considered, and the titration technique proposed in ***Study 1*** would not be applicable.

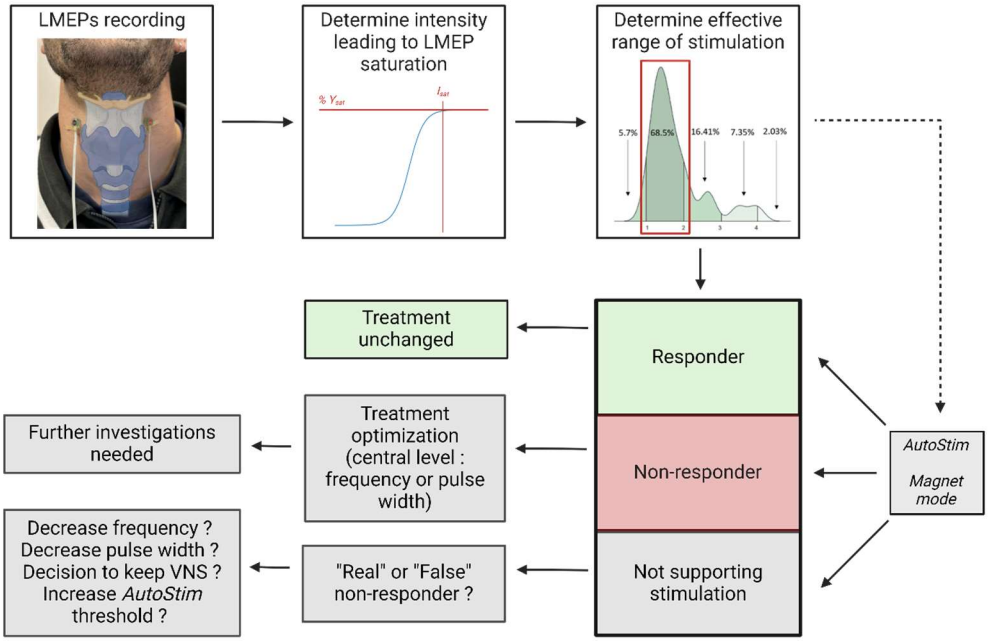

Figure 8.1 – Summary of the novel titration strategy proposed, and based on a physiological indicator of low threshold fiber engagement.

One of the main limitations when recording the LMEPs is the relatively coarse increment steps of current used for building the dose-response curve. While newer versions of VNS devices allow titration steps of 0.125 mA, obtaining an acceptable fitting of the Boltzmann curve in patients with older versions of VNS devices remains difficult. Using incremental steps of < 0.125 mA could greatly improve the fitting of the dose-response curve and the estimation of the recruitment characteristics. Moreover, while the novel titration technique presented in the current study would be useful to determine an effective range of current intensities, future studies are needed to determine how the LMEPs may evolve over time after implantation. Indeed, the titration technique presented in ***Study 1*** may be useful only when LMEPs are stabilized in time after the implantation – if

the patients present a temporary demyelination for example, and that the optimal range can be computed when the nerve is completely recovered. According to an ongoing study carried out in our laboratory, the stimulation intensity for LMEP induction seems to evolve up to 3 months after the implantation in some but not all patients (319). However, the evolution of the recruitment characteristics of LMEPs over time after implantation is still under investigation, and a definitive pattern of evolution is yet to be established. If it turns out that LMEPs features remain consistent over time after the implantation, the titration technique proposed in this section could be used as soon as LMEPs become recordable. Conversely, if changes in LMEP features occur after the implantation, the proposed titration technique would be discouraged until the LMEPs stabilize and allow the computation of the patient-specific optimal range of stimulation intensity. In that situation, the ongoing investigations will provide clarity on the temporal dynamics of changes in LMEPs features and the average duration required for them to stabilize after the implantation. Naturally, this titration technique remains suitable for patients in whom LMEPs can be recorded only. Therefore, it is not suitable for patients with postsurgical laryngeal nerve lesions or vocal cord paralysis. Considering that these adverse effects can appear in approximately 1% of patients after the implantation, the titration technique outlined in the present section could still serve as a tool for dosing VNS intensity in most patients.

Based on the findings presented in this thesis, a clinical study could be conducted to demonstrate the feasibility of using LMEPs as dosing biomarkers. To achieve this, fMRI could be used to evaluate the central activation corresponding to different stimulation intensities derived from LMEPs. For instance, patients could be stimulated with current intensities resulting in (i) LMEP induction, (ii) 50%-saturation of LMEPs, (iii) 100%-saturation of LMEPs, and (iv) 150%-saturation of LMEPs. Subsequently, the central activation could be compared across these different stimulation conditions. Undertaking such clinical studies investigating the relationship

between peripheral recordings, central activation, and clinical outcome is critical to validate the utility of LMEPs as effective dosing biomarkers. However, one cannot exclude that VNS effects could also be observed with fMRI in patients in whom LMEPs are not recordable. One hypothesis could be linked to the heterogeneity of the vagus nerve, such that low-threshold motor fibers are not being correctly stimulated in these patients while higher-threshold fibers involved in antiseizure effects could be accurately recruited with VNS. Moreover, it is possible that stimuli applied on the vagus nerve diffuse to structures pertaining to the trigeminal territory - a branch that could also lead to antiseizure effects when stimulated, although to a lower extent (320). Although determining the appropriate number of patients to be included in such studies is challenging given the scarcity of literature on the subject – mainly due to the presence of ferromagnetic materials in current VNS devices preventing acute stimulation during fMRI acquisitions, a pilot study that includes 10 patients may already provide preliminary results. Indeed, a study conducted by Lomarev and colleagues where central VNS effects for two different stimulation paradigms (two frequencies of stimulation) were investigated only included 6 patients (311). Moreover, conducting a pilot study with 10 patients could supply valuable information for the calculation of the sample size for a larger clinical study.

1.2 Development of a device for exploring dose-response effects in an MRI environment

A system was developed to activate and communicate remotely with the Synergia Medical optoelectronic neurostimulator in an MRI environment.

The development of a fully MRI-compatible optoelectronic neurostimulator by Synergia Medical opens new avenues of research to study how different stimulation parameters modulate structures of the vagal afferent network. As part of this thesis, a patented device called the OCD was developed to enable the realization of fMRI studies that will be conducted with this new-generation VNS device. The final version of the OCD is composed of two main embodiments, allowing it to operate from the command room while the implant is in the MRI system. The first embodiment is responsible for the optical wake-up of the implant, and the other allows to connect to the implant and communicate with it to tune the stimulation parameters and start stimulation. Technical details and validation of the OCD outside and inside an MRI environment are described in depth in ***Chapter 7***. While the optical wake-up of the implant is highly robust, the communication part of the OCD remains sensitive when combining a simulated *in vivo* situation using samples of skin with the placement of the implant in an MRI environment. However, while the sensitivity remains acceptable for conducting the fMRI tests, it could be optimized by providing adaptations in the SC/IPG interface. However, these modifications remain beyond the scope of this thesis.

In future studies, the use of the OCD during fMRI acquisitions could be useful to confirm the hypotheses described in ***Study 1***. Indeed, knowing that most responsive patients show a stimulation intensity between 1-fold and 2-fold the intensity required for LMEP saturation, one could evaluate whether structures of the vagal afferent network are optimally activated in this range of stimulation intensities. In particular, using the methodology described in ***Study 2*** and ***Study 3***, functional characteristics of the LC could be extracted for different stimulation intensities with acute VNS administration. We expect that stimulation intensities within the optimal range will lead to maximum activation of the LC.

Although overstimulating patients can lead to more pronounced side effects and a reduced battery life, high stimulation intensities might also

recruit inhibitory or desensitizing systems at the central level. Indeed, the existence of a desensitizing system has already been suggested in a study where dilation of the pupil - an accepted readout of the LC activity - was measured in different conditions of stimulation and used as a dosing biomarker of the central effects of VNS (321). They found a drop in pupillary response for high stimulation intensities, particularly for 2 mA. They suggested that moderate stimulation intensities induce stronger modulatory effects than low or excessively high intensities (321). These results align with a previous study conducted in rats, suggesting that low-to-moderate output currents were sufficient to reduce seizure activity (322). Indeed, while values of current intensities cannot be directly translated to humans due to the different diameters of the fibers, myelination processes, or electrodes – cuff vs. helical electrodes, stimulating the vagus nerve with a current of 0.25 mA was sufficient to reduce the cortical excitability, and was even slightly more efficient than stimulating with an intensity of 1 mA (322).

Therefore, fMRI could confirm or reject the hypothesis of whether a reduced activation appears at the central level for stimulation intensities above the optimal range of currents. If a reduced activation is observed for current intensities beyond an optimal range, different potential factors could be considered to contribute to this effect. It is possible that high current intensities may initiate the recruitment of unmyelinated high-threshold C-fibers, which could, in turn, facilitate the activation of inhibitory systems. It was suggested that a minimum threshold of 2 mA is needed for recruiting C-fibers (44), which aligns with the reduction in pupillary response found for this intensity (321). In rats, the intensity threshold for C-fiber recruitment is approximately 400 µA, and all C-fibers are recruited for intensities between 600 and 800 µA (49). Therefore, previous results showing a slight decrease in efficiency for reducing cortical excitability when a 1 mA stimulation is administered in rats may indicate that recruitment of C-fibers - and saturation in this case - may lead to the onset of recruitment for desensitizing systems (322). Moreover, a study

investigated the response elicited by VNS in pyramidal neurons of the parietal association cortex in rats, a region that provides afferent input to widespread cortical regions, including the temporal cortex that is frequently involved in seizure initiation (323–325). Investigations in the parietal association cortex were conducted since it was hypothesized that these neurons may respond to VNS as suggested by a previous *c-fos* immunolabeling study (79). Therefore, different stimulation intensities were used, and responses in these neurons were recorded using *in vivo* intracellular recordings (323). They found that low-intensity trains of VNS (100 µA, 30 Hz, 500 µs pulse width) were efficient in reducing the excitability of neurons, by inducing slow vagal hyperpolarization. However, higher intensities of VNS (200- and 500 µA) were less efficient in reducing the excitability of neurons. The authors suggested that low-intensity currents mainly recruit myelinated fibers in the range of Aδ-fibers, as established by an analysis of the compound action potential of the cervical vagus nerve that estimated a conduction velocity of 2 m/s. On the opposite, current intensities of 200- and 500 µA recruited unmyelinated C fibers in addition. Based on their findings they suggested that the recruitment of unmyeliated fibers attenuated the inhibitory cortical projections originating from myelinated fibers through subcortical mechanisms (323).

As presented in the introduction, the vagus nerve projects to the NTS that, in turn, sends projections to the LC through two disynaptic pathways: an excitatory pathway with a relay in the nucleus paragigantocellularis and an inhibitory pathway with a relay in the nucleus prepositus hypoglossi (57,64). While further electrophysiological and immunochemistry studies are needed to investigate how different VNS parameters may modulate the contribution of each system in the LC activation, it is possible that increasing stimulation intensities above an optimal range will cause an augmented contribution of the inhibitory system, which could counterbalance the excitatory input to the LC.

Moreover, it is important to consider the effect of stimulation intensities on NE release by the LC, which could lead to different functional consequences. It was first suggested that high-affinity α2-adrenergic receptors (G protein-coupled receptors) in the LC play a critical role in modulating the responsiveness of LC neurons to excitatory stimulation (326). An excess of endogenous NE could lead to decreased NE firing due to the presence of α2-adrenergic autoreceptors on the terminals of NE neurons, as binding of NE onto these receptors leads to a reduced release of NE in the synaptic cleft (76). This is supported by a study that measured the regulation of NE release in the cingulate cortex of rats following the local application of α2-adrenoreceptor antagonist into the LC. They found that α2-adrenoreceptors in the LC exert a tonic autoinhibition on NE release in the cingulate cortex (327). Furthermore, *in vivo* recordings showed that intracellular activation of an LC neuron leads to a biphasic response: an initial short burst of impulses followed by a period of quiescence or post-stimulation inhibition (PSI) (328,329). They found that blockade of the α2-adrenergic autoreceptors decreased the PSI that followed the burst of activity (328,329).

Baral et al. developed an experimentally validated neuronal model of NE cells to study the NE-mediated modulatory effects between LC neurons (330). Due to the presence of α2-adrenergic receptors in the somatic area and the unusually close proximity of the soma of NE neurons that are highly packed in the LC, neighboring neurons could modulate each other via volume transmission of NE (330). In addition, knowing that LC neurons projecting to different brain areas may show different sensitivity to α2-receptor agonists and that LC neurons are topographically organized in terms of projection targets, it could be postulated that volume-mediated inhibition of specific neighboring neurons with different targets leads to specific functional consequences (330).

Therefore, one could speculate that moderate VNS current intensities could lead to an adapted balance between a sufficient release of NE that

contributes to antiseizure effects through a low autoinhibition effect on α2-adrenergic autoreceptors and a controlled inhibition on neighboring LC neurons without adversely affecting therapeutic effects of VNS. Conversely, high stimulation intensities of VNS could lead to an excess release of NE, leading to a dominant autoinhibitory effect on the stimulated NE neurons and neighboring NE neurons projecting to different brain areas (**Figure 8.2**). Consecutively, this could lead to reduced firing of NE neurons, reduced release of NE in terminals, and an increased PSI. Finally, while more research is needed to elucidate the effects of VNS on tonic LC activity, it is worth mentioning that heightened tonic activity of the LC has been associated with undesired cognitive effects, including distractibility and anxiety (61).

Future electrophysiological and computational studies considering the LC as a topographically organized nucleus instead of a whole are needed to elucidate which subpopulations of NE neurons are activated with VNS. This could help to better understand the functional specificity of LC subnetworks and the functional consequences of different VNS current intensities to better characterize and predict a possible inhibition loop effect. While it is crucial to acknowledge that there may be other factors that could explain the desensitization at the central level when high stimulation intensities are used, further fMRI studies could explore the recruitment optimization of structures of the vagal afferent network, particularly the LC, by fine-tuning other parameters such as the frequency, pulse width, train duration or duty cycle (90,169,311,331–333).

Moreover, a new stimulation strategy has recently emerged and aims to stimulate with high-frequency bursts of stimulation. This paradigm, called “microburst VNS”, is believed to improve the modulation of the thalamus (334). During microburst stimulation, bursts of 4-7 pulses with a 100-500 µs pulse width are delivered with a frequency between 250-350 Hz and interleaved with inter-burst intervals of 0.5-2.5 s (334). An exploration of the central effects of microburst VNS could greatly benefit

from the use of the OCD and the optoelectronic neurostimulator. An open-label multicenter phase I clinical trial with an investigational VNS device (M1000C µB SenTiva® VNS therapy system) is ongoing (*ClinicalTrials.gov identifier : NCT03446664*) (334). This study aims to assess the potential risk-benefit profile of microburst VNS and explore the impact of this stimulation paradigm on the activity of the thalamus using fMRI.

Finally, assessing the central effects of VNS when physiologically guided stimulation paradigms are used could constitute an interesting way of optimizing this therapy. A previous study explored the brainstem responses of acute tVNS using a UHF 7T MRI, with the stimulation delivered during exhalation or inhalation (335). Hypotheses behind this exploration were based on the knowledge that activity of the NTS is modulated by respiration through (i) a bottom-up afference from pulmonary stretch receptors and aortic baroreceptors and (ii) a top-down control from ventral respiratory group nuclei in the medulla (335). They found that in-phase stimulation with exhalation led to a higher functional response in regions consistent with the NTS, LC, median, and dorsal DRN. Such stimulation paradigms could be investigated with the administration of cervical VNS using fMRI. For example, using fMRI during a task where the patient is asked to breathe in and breathe out (e.g., 5 s inhalation and 5 s exhalation) in a synchronized manner with VNS administration could help investigate such effects. Development of such studies could also benefit from the use of the OCD.

In conclusion, the development of the optoelectronic neurostimulator, combined with the use of the OCD for performing fMRI research, unveils thrilling research prospects for VNS optimization. Developing dosing biomarkers is critical to ensure an adapted administration of VNS therapy and maximize the chance of observing antiseizure effects. However, interindividual differences may exist and could result in a different therapeutic efficacy despite delivering an adapted treatment. The following section of the thesis deals with the development of response biomarkers.

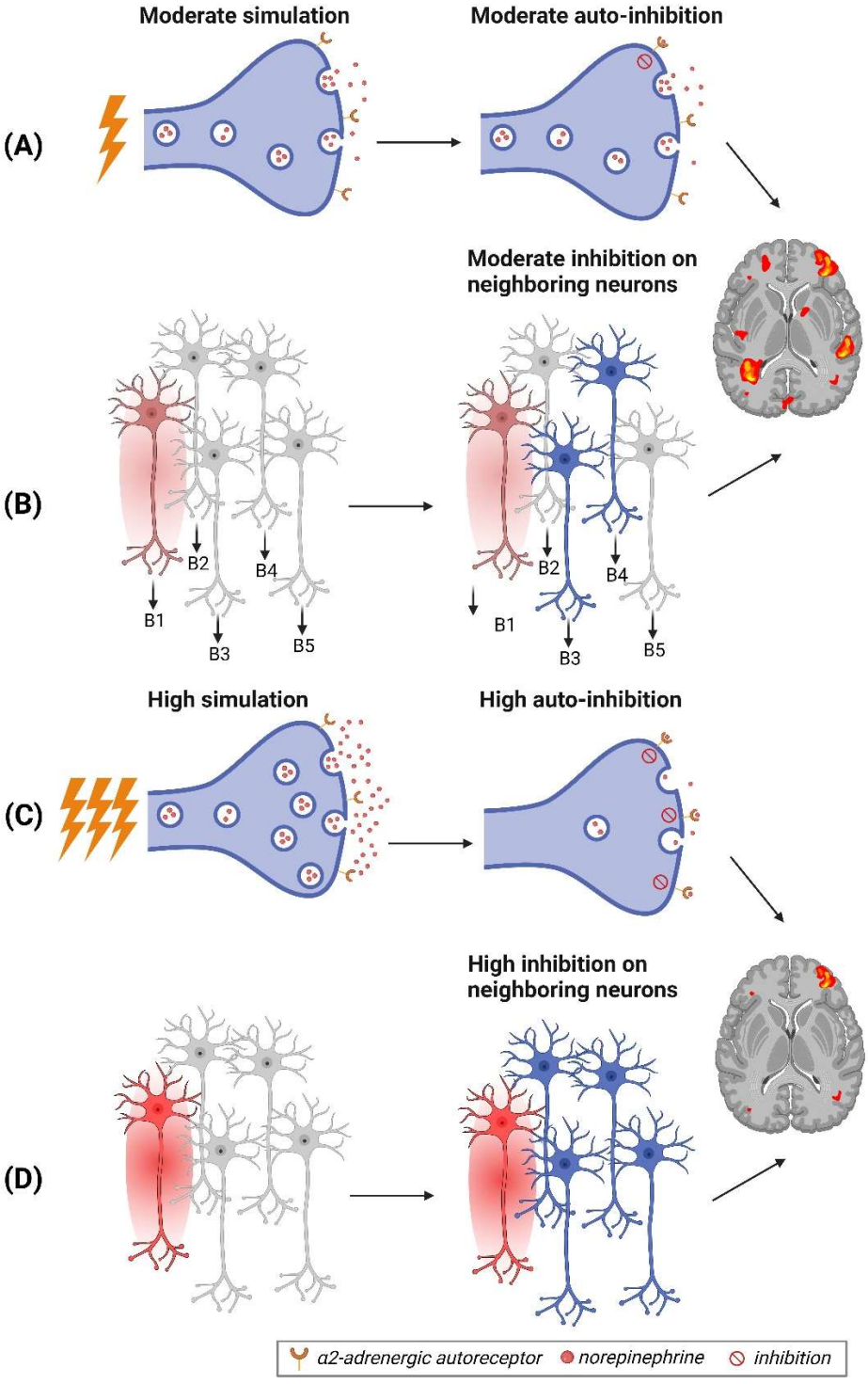
Moderate simulation
Moderate auto-inhibition
(A)
Moderate inhibition on neighboring neurons
(B)
B1
B2
B3
B4
B5
High simulation
High auto-inhibition
(C)
High inhibition on neighboring neurons
(D)
α2-adrenergic autoreceptor
norepinephrine
inhibition

Figure 8.2 – Possible explanations for the proposed hypothesis of reduced central effects for high stimulation intensities of VNS. (A) Moderate stimulation leads to moderate auto-inhibition through α2-adrenergic autoreceptors. (B) Moderate stimulation of an LC neuron could lead to a moderate inhibition of neighboring neurons within the LC. (C) High stimulation leads to a high auto-inhibition through α2-adrenergic autoreceptors. (D) High stimulation of LC neurons could lead to a high inhibition of neighboring neurons within the LC. Red neuron: activated neuron. Blue neuron: Inhibited neuron. Grey neuron: neuron whose activity is not altered. B1-B5: Projections to different brain areas.

2. RESPONSE BIOMARKERS

Another objective of this thesis was to develop response biomarkers that are essential to improve the assessment of VNS response using biological indicators of peripheral nerve recruitment and central markers of VNS efficacy. These markers hold the potential to deepen our current knowledge about the variable response across patients and to improve the differentiation between responders and non-responders to VNS. In turn, the development of response biomarkers could (i) help to prevent unnecessary re-implantations in non-responders who are not showing physiological signs of VNS response and (ii) improve the stratification of different drug-resistant forms of epilepsy.

2.1 PERIPHERAL MARKERS OF THERAPEUTIC EFFICACY

Using peripheral recordings of the nerve excitability to extract recruitment characteristics of the nerve, we were able to discriminate responders and non-responders to VNS.

In order to observe antiseizure effects, it is crucial to ensure that the nerve is accurately recruited and does not present pathological recruitment characteristics. As mentioned before, since LMEPs characteristics may indirectly reflect recruitment characteristics of fibers conferring antiseizure effects, evaluation of the features of the dose-response curve built based on LMEPs measurements was conducted as part of ***Study 1***. In this study, it was hypothesized that patients with a better response to the treatment could show higher excitability of the vagus nerve compared to patients with a lower response to the treatment. In terms of recruitment features, a higher excitability of the vagus nerve could be reflected in lower LMEPs latencies, higher LMEPs amplitudes, lower intensity threshold for LMEPs induction, and/or higher slope of the dose-response curve. On the opposite, a post-surgical pathology of the nerve - e.g., a damaged nerve, scarring, or gliosis - or a defective activation of the nerve - e.g., possibly due to a suboptimal interface between the nerve and the electrode - would tend to show opposite trends in these features.

In accordance with previous studies (156), no difference in LMEPs features was found here, but a trend toward a greater excitability of the nerve was found in patients with a better response to the treatment. Indeed, trends toward an earlier rising flank of the dose-response curve, a lower charge leading to half-saturation of the fibers, and a lower excitability threshold were observed in responders compared to non-responders. However, while results suggested that programming the output current to 1 mA may be sufficient to fully recruit motor fibers in responders, an average of 1.2 mA was found in non-responders, possibly reflecting different nerve excitability between patients. Knowing that a combination of features could offer a more comprehensive exploration of the differences existing across patients as each feature could reflect different physiological states of the nerve, a multi-feature analysis was

conducted to determine how accurately LMEP features could discriminate responders from non-responders when taken together. An SVM model was built, and correctly classified patients based on their response to VNS with an accuracy of 80% (sensitivity = 75%, specificity = 85.71%, and AUC = 82.1%). Although providing a physiological interpretation of the combination of features used for the classification is beyond the scope of the current work, the findings suggest that the vagus nerve recruitment characteristics could be linked to the treatment efficacy. SVM is a powerful technique for classification purposes; it is suitable for small datasets, is not sensitive to noise in the data, and demonstrates good generalization and regularization properties. For these reasons, the SVM constitutes an interesting solution to our classification problem. However, other classification algorithms exist (e.g., random forest, K-Nearest Neighbors, or Naive Bayes) and could be compared to determine the most suitable models for classifying VNS patients based on LMEPs features. While VNS research is limited by data availability, the continuously increased influx of data in the clinical domain, the growing number of patients being implanted each year, and the implementation of large datasets from multi-centric studies promise a transformative shift in the methodology employed. Eventually, with a large amount of data, deep learning algorithms, including multiple layers-deep neural networks, could surpass current models by unraveling intricate relationships buried in the datasets at the cost of a reduced interpretability due to the increased complexity of the classifier. At that point, deep learning models are often seen as “black boxes” as the internal mechanisms and decision-making processes become complex, making their interpretability challenging to humans.

To develop predictive biomarkers of VNS response and avoid unnecessary implantations, the analyses presented in this section should be replicated using pre-operative markers of vagal fiber engagement. In that context, the development of non-invasive optical techniques for stimulating the vagus nerve could provide information about the excitability of the nerve before implantation. In future research, a

comprehensive approach incorporating peripheral markers of effective nerve activation and markers assessing the effects of VNS at the central level (e.g., using fMRI, EEG, or pupillometry) could improve the response prediction. This could also help to unravel the potential co-acting mechanisms associated with therapeutic effectiveness and ensure (i) a correct activation of the vagus nerve and (ii) an appropriate level of activation at the central level of structures responsible for the antiseizure effects.

2.2 CENTRAL MARKERS OF THERAPEUTIC EFFICACY

A multimodal MRI approach was developed and highlighted structural and functional differences in the vagal afferent network between responders and non-responders to VNS.

2.2.1 LOCUS COERULEUS FEATURES

Previous research demonstrated the critical involvement of the LC in the antiseizure effects of VNS (84,86,98,103). The development of new imaging techniques allowed us to study the characteristics of this brainstem nucleus using specific MRI sequences that are not commonly used in clinical settings. ***Study 2*** constitutes a methodological investigation where structural and functional (phasic) characteristics of the LC (as assessed during a mismatch negativity task) were extracted in a cohort of healthy young and late middle-aged individuals using a UHF 7T MRI. Furthermore, aside from establishing an analysis pipeline that was used to explore LC features in patients with DRE and implanted with a VNS device (***Study 3***), it was shown in ***Study 2*** that potential age-related alteration in LC structural integrity may not be related to changes in its functional response.

In ***Study 3***, using a multimodal MRI approach based on 3T MRI data, a trend – that did not remain significant after correcting for multiple comparisons - toward a lower reactivity localized in the medial portion of the left LC was found in responders and partial responders compared to non-responders to VNS during an auditory oddball task. These findings aligned with previous EEG studies that found a higher P300 amplitude during an auditory oddball task in patients with a poorer response to VNS (98). Moreover, trends toward higher structural integrity - as assessed with the LC contrast - were found in the caudal portion of the right LC in patients showing a higher therapeutic efficacy with VNS. A trending relationship was also found between structural integrity in the medial portion of the LC (bilaterally) and therapy duration, independently of the VNS response. These results may reflect the modulatory effects of VNS on the LC-NE system and suggest potential variations in the structural and functional state of the vagal afferent network – and, more specifically, in the LC-NE system – across patients.

Knowing that a sufficient release of NE in the hippocampus could prevent the development of induced seizures in rats (86), structural characteristics of LC-hippocampus connections were extracted in ***Study 3*** and compared between responders/partial responders and non-responders. This analysis involved the use of high-gradient multi-shell diffusion MRI, along with single- (DTI) and a robust multi-compartment model (MF). The results suggested a significantly higher integrity of LC-hippocampus connections in patients exhibiting a more favorable response to VNS. While differences in DTI metrics demonstrated greater statistical discrimination, MF confirmed the interpretation of DTI metrics and provided additional insight by modeling the individual influence of crossing fascicles. In summary, ***Study 3*** highlighted interindividual variations in the structural and functional states of the LC-NE system across patients with DRE and implanted with a VNS device and introduced a novel methodology for extracting and analyzing LC features based on cutting-edge MRI analyses.

2.2.2 THALAMOCORTICAL TRACTS FEATURES

Activation of the thalamus has been reported in previous immunochemistry studies conducted in rats and imaging studies where PET and fMRI were used in humans (79,281–284). Moreover, it was suggested that thalamocortical tracts could be involved in the antiseizure effects of VNS, as their modulation with VNS could disrupt the synchronous and pathological activity of neurons that characterize the seizure activity (79,151,282–284). While studies using diffusion MRI to assess structural connectivity are limited in the field of DRE and VNS, a previous study used DTI to explore possible microstructural differences between patients. They found an increased FA in responders compared to non-responders in various tracts, including left thalamocortical, limbic, and association fibers. In ***Study 4***, a higher MD and RD were found in subsegments of the inferior and posterior thalamocortical tracts in non-responders compared to responders and partial responders, possibly reflecting a reduced density of axons or lower myelination (295–297). However, DTI presents several limitations. Indeed, this model cannot capture individual microstructural features of crossing fascicles, leading to poor specificity in interpreting DTI metrics.

High-gradient multi-shell diffusion MRI was used and allowed the use of multi-compartment models, including NODDI and MF, to refine the characterization of microstructural differences existing across patients. The lower NODDI-based NDI found in subsegments of thalamocortical tracts in non-responders – including the inferior and posterior thalamocortical tracts – suggested a reduced density of neurites compared to patients showing a higher therapeutic efficacy with VNS. Although only trends of significance were found in the same tracts using the MF-based wFVF metric, these findings suggest overall reduced integrity in thalamocortical projections in patients exhibiting a poor response to VNS. Therefore,

single-feature analyses of multi-compartment diffusion MRI models confirmed the interpretation of DTI metrics.

An SVM model was built based on diffusion metrics and reached a classification accuracy of 94.12% (sensitivity = 100%, specificity = 83.88%, AUC = 87.88%) when discriminating patients based on their response to VNS. During the feature selection, this model only selected DTI metrics for the classification, suggesting that DTI may be the most suitable model - to date - to support the clinical evaluation of responsiveness to VNS. Moreover, no clinical feature was selected for the classification, aligning with the findings of a prior study indicating that clinical features might not be useful for improving the prediction of VNS response (150).

The analyses conducted in this thesis focused on LC and thalamocortical connections, as these structures are known to be involved in the antiseizure effects of VNS (73,75–80,86,90,230,281–284,294). Regarding the vagal afferent network, the vagus nerve projects to the NTS, which in turn sends projections to different brain areas, including the LC and the thalamus. As our results suggested that lower integrity in the tracts arising from the LC and the thalamus was associated with a poorer response to VNS, one could investigate whether lower integrity systematically appears in both structures. This question could raise interest when exploring new titration strategies. Indeed, while classical VNS paradigms are thought to mediate brainstem nuclei, including NTS and the LC, it was suggested that microburst VNS can modulate the activity of the thalamus (334). While more research is needed to elucidate which network seeding from the thalamus could be specifically modulated with microburst VNS compared to classical VNS, a previous study that used high-frequency bursts of VNS measured evoked response in the parafascicular nucleus of the thalamus in primates (336). It was suggested that the parafascicular nucleus in turns, projects to subcortical regions - including the caudate nucleus, putamen, pallidum, and nucleus accumbens, the insula and the anterior cingulate cortex (337–342). Lower-density projections from the

parafascicular nucleus to the amygdala and the hippocampus have also been reported (343,344). While the LC itself projects to the parafascicular nucleus of the thalamus, it is worth noting that distinct stimulation paradigms could selectively engage these structures (334,345). Should one of the two subnetworks demonstrate superior integrity, a hypothesis could be formulated suggesting that selection between classical or microburst paradigms might optimize the recruitment of the structure showing the highest integrity and maximize the antiseizure effects. However, a preliminary study is needed to define the characteristics of a *"healthy network"* in terms of diffusion features for each subnetwork to help decide which structure could show the highest integrity. As patients with a poor response to VNS may show an overall altered brain circuitry, it is probable that lower integrity could be found systematically in subnetworks of the vagal afferent network in these patients. Although the microburst-specific recruitment of tracts has to be further investigated, a complementary analysis was conducted as part of this discussion to determine whether the integrity of the LC-hippocampus network was associated with the integrity of thalamocortical tracts in order to investigate if regional specificity of altered integrity in the vagal afferent network could exist. Therefore, diffusion metrics in thalamocortical tracts that showed differences between responders/partial responders and non-responders to VNS (investigated in ***Study 4***) were correlated to the same diffusion metrics in the corresponding – left or right – LC-hippocampus connections (investigated in ***Study 3***). For microstructural features in thalamocortical tracts that showed a significant relationship with therapeutic efficacy, approximately 40% were correlated with microstructural features in LC-hippocampus connections (**Supplementary Material S8.1**). Therefore, although poorer integrity in some thalamocortical tracts – including inferior thalamocortical tracts projecting to the insula or the temporal lobe and the posterior thalamocortical tracts projecting to the occipital lobe – seems to be related to poorer integrity in LC-hippocampus connections, not all tracts showed such an association. With a better understanding of the differential

modulation of subnetworks with microburst or classical VNS, further research could investigate the antiseizure effects when different stimulation paradigms are used and how these antiseizure effects correlate with the integrity of each system.

The continuous development of microstructural models allowing us to infer microstructural features with fewer assumptions and greater anatomical precision, coupled with the evolution of imaging systems that facilitate explorations in the microscopic realm and allow segmentation of structures with greater details, holds the potential to improve our understanding of structural differences existing among patients. These investigations will continue to refine our understanding of the biological factors associated with interindividual differences in response to VNS.

2.3 FINAL CONSIDERATIONS

It is essential to note that these findings require confirmation in a more extensive cohort of DRE patients. However, our samples of patients remain acceptable for a population of patients with DRE and implanted with a VNS device. Moreover, while extreme values in small datasets may skew the results toward larger effect sizes, all statistical models included covariates, and results were corrected for multiple comparisons to avoid erroneous inferences. Analyses conducted in ***Study 3*** and ***Study 4*** could benefit from UHF 7T MRI by improving resolution and sensitivity. Regarding the methodology presented in ***Study 3***, the LC delineation was realized manually by two independent raters, potentially introducing bias due to inter-rater variability. However, despite previous efforts to develop partially or fully automated LC segmentation to alleviate rater-related bias (141,231,240,276,346,347), the manual delineation of the LC is still considered the gold standard for creating LC masks. Moreover, partially, or fully automated techniques often require the use of a common space for

extracting LC masks. Given the clinical population of patients included in our studies, the coregistration of MRI images to a common space is challenging, particularly for individuals presenting congenital brain malformations and those who have undergone brain surgery. In the functional analyses of the LC conducted in ***Study 3***, respiratory and heart rate recordings could be used to regress out possible effects associated with physiological noise. Moreover, due to the proximity of the LC to the 4^{th} ventricle, extracting the BOLD signal in the 4^{th} ventricle and using it as a covariate for the statistical analyses could remove potential partial volume effects and improve the specificity of the analyses. In ***Study 3***, the phasic activity of the LC is explored, but future studies could evaluate whether the tonic activity of the LC differs between responders and non-responders to VNS. For example, exploration of the tonic LC activity could be explored using functional MRI during a perceptual rivalry task (e.g., Necker cube task) (348).

For the SVM models built in ***Study 1*** and ***Study 4***, an external cohort of patients could be used to validate the classifiers and evaluate the generalization properties of the models to new patients. Moreover, using nested cross-validation for tuning the hyperparameters could be useful for ***Study 1*** to avoid overfitting, as a small number of subjects were included in the study. However, nested cross-validation was used in ***Study 4***.

Based on the MRI analyses conducted in ***Study 3*** and ***Study 4***, it remains to be clarified if the differences observed in the vagal afferent network between patients reflect (i) an inherent inclination toward higher therapeutic efficacy with VNS, (ii) the detrimental effects of seizures in non-responders, as patients with a poor response to VNS may tend to experience seizures more frequently, or (iii) a higher modulatory effect of VNS on brain structures composing the vagal afferent network in patients exhibiting higher therapeutic efficacy. Moreover, one can not exclude that a placebo effect takes place after implantation of a VNS device. Future studies could investigate the placebo effect in VNS, by including another

group of freshly implanted VNS patients, in whom stimulation parameters are kept below the threshold of expected VNS-triggered effects.

Assessing the evolution of microstructural metrics over the course of the patient's treatment with VNS and comparing them with pre-implantation features could offer insights into the effective modulatory effect of the therapy on the vagal afferent network. Future research might consider incorporating a healthy cohort of subjects to compare the MRI markers with a baseline healthy state of the network. Moreover, adding a cohort of epileptic patients with the same seizure burden – quantifying seizure frequency, severity, and duration - as the patients included in our studies and implanted with a VNS device could also be useful to investigate the effect of VNS on diffusion metrics by removing potential detrimental effects of seizures on white matter microstructure, since it may affect the organization of the tracts. Investigations of the detrimental effects of seizures on diffusion MRI metrics in humans are limited. Implementation of such studies remains challenging as they need to include hospitalized patients able to undergo an MRI examination after having experienced a seizure. It was suggested that temporal changes occur in diffusion metrics following a seizure with a decreased MD in the hyperacute phase after a prolonged seizure or status epilepticus, possibly due to intracellular cytotoxic edema, a translocation of extracellular water to intracellular space leading to swelling and reduced interstitial space (306,349). Up to 5 days after the seizure – a period called the subacute peri-ictal phase, an increased MD has been reported and is possibly linked to vasogenic edema, a diffusion of plasma from the vessel to interstitial space that causes a fluid accumulation in the extracellular space (306,349,350). A further increase in MD has been reported chronically due to neuronal loss and gliosis, leading to an expansion of the interstitial water content (306). Therefore, while ruling out completely the chronic effect of seizures on white matter microstructure in the cohorts of patients included in ***Study 3*** and ***Study 4*** is unfeasible, the statistical analyses corrected for the duration of the epilepsy to remove potential chronic effects of seizures in patients

with a longer history of epilepsy. Moreover, an exclusion criterion excluded patients who had a seizure in the last 24h before the MRI examination to remove possible acute effects of seizures. Future studies, where seizures are induced in rats, could further our current understanding of the effect of different types of seizures on white matter microstructure. These studies could benefit from the use of ultra-high field MRI systems for animal imaging, ranging from 9.4 T to 21 T.

Additionally, some of the patients included in the analyses underwent brain surgery, and it has been suggested that diffusion MRI metrics can show dynamic changes following lobectomy. Indeed, a previous study evaluated the effect of anterior temporal lobe resection in patients with refractory temporal lobe epilepsy (351). They found that tracts at the resection, or nearby the resection, showed a reduced FA, increased MD, and increased RD, possibly due to a Wallerian degeneration occurring in the ipsilateral hemisphere following axonal transection (351). In the vicinity of the resected area, other studies found FA reduction occurring in the following year after the surgery (352–354). In other tracts, distant from the resection site, increased FA and AD were observed, a decreased RD to a lesser extent, and no change in MD. Most changes occur 3-4 months after surgery, but further changes can occur up to 12 months after the procedure. Finally, in that study, it was suggested that changes occur mainly ipsilaterally to the resection, with minimal effect on the contralateral hemisphere (351). In another study that explored changes in FA following anterior temporal lobectomy in mesial temporal lobe epilepsy patients who achieved seizure freedom at a two-year follow-up, different patterns of dynamic FA changes were found in distinct white matter tracts at different time points post-surgery (293). In opposition to Winston et al., four distinct patterns of FA changes were found in both ipsilateral and contralateral hemispheres, with tracts showing either (i) FA decreased after three months that remained relatively stable after – in the ipsilateral external capsule, cingulum, superior corona radiata, body of the corpus callosum, and inferior longitudinal fasciculus, (ii) FA decreased at three

months but increased later – in the ipsilateral superior cerebellar peduncle and contralateral corpus callosum, anterior corona radiata, external capsule and optic radiation, (iii) FA decreased at three months with further decreased after – in the ipsilateral cerebral peduncle, and contralateral middle cerebellar peduncle, or (iv) FA increased after surgery – in the ipsilateral posterior limb of the internal capsule, retrolenticular part of the internal capsule, and contralateral posterior corona radiata. Therefore, the results of these studies show that changes in diffusion metrics are complex and variable across different tracts. Some tracts may show a reduced integrity due to Wallerian degeneration, while other tracts may show an improved structural integrity resulting from neuroplasticity effects and neuronal remodeling - including axonal regeneration or improved myelination, possibly due to seizure control (293,351).

Based on these findings, while some patients included in our studies underwent brain surgery, not all of them had temporal lobe epilepsy. Following the surgical procedure, it is possible that some of them may have shown changes in structural integrity that are specific to the surgical procedure – frontal or temporal lobectomy in our cohort of patients - and, therefore, possibly impacted the investigated metrics. Although pre- and post-implantation data are needed to highlight microstructural changes in specific tracts in these patients, complementary analyses were conducted to evaluate a potential relationship between surgical procedures and possible abnormal diffusion metrics. The supplementary analysis suggests that the surgical procedures may not account for the outlier values detected in diffusion metrics in our cohort of patients. A detailed explanation can be found in **Supplementary Material S8.2**.

Incorporating MRI markers of the central effects of VNS and peripheral markers of effective nerve activation based on LMEPs could help to disentangle the contribution of causes behind non-response to VNS. In clinical practice, and for most of the studies conducted in the field, patients are categorized as *“responders”* or *“non-responders”*. This classification is

based on the seizures reported by the patients to the reference neurologist. Knowing the exact percentage of reduction in seizure frequency could greatly advance research by refining the categorization of patients, highlighting a possible beneficial role of VNS, and precisely tracking the evolution of epilepsy. Moreover, studies considering *seizure burden* instead of seizure frequency alone could deepen the characterization of the therapeutic efficacy of VNS by considering a spectrum of responses. For example, a more detailed classification of VNS outcomes exists with the McHugh classification which divides patients into five groups : (i) Class I are patients showing an 80-100% reduction in seizure frequency, including Class IA for patients showing improved ictal or postictal severity, or Class 1B for patients showing no improvement in ictal or postictal severity, (ii) Class II are patients showing a 50-79% reduction in seizure frequency, including Class IIA and Class IIB following the same criteria as previously defined, (iii) Class III for patients with a <50% reduction in seizure frequency, subdivided into Class IIIA and Class IIIB, (iv) Class IV for patients showing magnet benefit only, and (v) Class V for patients with no improvement (355). Encouraging patients to maintain a seizure diary or utilize an app for reporting their experienced seizures, together with the advancement of new systems able to record epileptic activity, could help to characterize the antiseizure effects of VNS more thoroughly and improve patient empowerment. However, it is important to acknowledge that these techniques also present challenges. Indeed, due to the severe conditions of some patients, keeping a seizure diary remains unrealistic as some patients may (i) not be conscious of the occurrence of a seizure, (ii) present a distorted perception of the seizure episode afterward (e.g., duration of a seizure or symptoms), or (iii) not be able to track the seizures due to a lack of motivation or a severe form of epilepsy leading to cognitive disabilities and limited self-reporting capacities. Regarding non-invasive devices to record non-invasively seizure activity, they may suffer from resolution problems or poor brain coverage, limiting the monitoring of the epileptic activity. Moreover, the cost and accessibility of these

devices can also constitute a barrier to using them. Finally, wearing such devices could be associated with stereotypes and stigmas, as they could serve as visible markers of illness.

CHAPTER 9. CONCLUSION

In this thesis, four studies were realized with the aim of optimizing VNS therapy for patients suffering from DRE. The analyses conducted in this thesis focused on refining the VNS treatment by introducing innovative electrophysiological and imaging techniques to explore variations in VNS response among individuals. Optimizing the therapy consists of developing (i) dosing biomarkers to determine the optimal VNS dose to be administered to maximize antiseizure effects and (ii) response biomarkers to extend the current understanding of the biological prerequisites necessary for observing therapeutic effects with VNS. While an in-depth discussion of the results obtained, limitations, and future prospects have been previously addressed, the primary findings are summarized in this conclusion.

In ***Study 1***, **a new titration technique that relies on a physiological indicator of fiber engagement was proposed in contrast to the method currently used, which is based on the subjective tolerance of the patients to the stimulation**. Our findings revealed that most clinically responsive patients are stimulated with an intensity between 1-fold and 2-fold of the intensity inducing LMEP saturation. In contrast, non-responders show a high inhomogeneity in the clinically used stimulation intensities. This suggests that assessing the current intensity inducing LMEPs saturation could help to determine in a personalized manner the optimal range of stimulation currents needed to maximize the likelihood of observing antiseizure effects. A classification model was built and highlighted **trending differences in recruitment characteristics of LMEPs between responders and non-responders to VNS, possibly suggesting higher excitability of the fibers in patients exhibiting more favorable therapeutic outcomes**. This classification model based on LMEPs features reached an accuracy of 80% (AUC = 82.1%).

While ***Study 2*** provided **a methodology for characterizing the LC structurally and functionally in a cohort of healthy subjects**, these techniques were used in ***Study 3***, where a cohort of DRE patients implanted with a VNS device was included. In this study, **a difference in structural and functional integrity of the LC-NE system was found between responders/partial responders and non-responders to VNS.** Indeed, a lower reactivity of the medial LC during an auditory oddball task was found in patients exhibiting higher therapeutic efficacy, suggesting that patients with a lower baseline activity of the nucleus could constitute good candidates for VNS compared to individuals with a less modulable network. Moreover, using high-gradient multi-shell diffusion MRI, our results suggested more robust LC-hippocampus connections in responders/partial responders compared to non-responders. Finally, **an effect of therapy duration on the structural integrity of the medial LC was found, possibly reflecting neuromodulatory effects of the therapy.**

In ***Study 4***, **higher microstructural integrity was found in subsegments of thalamocortical tracts in responders/partial responders to VNS compared to non-responders.** Based on microstructural features of thalamocortical tracts, a classification model was built and effectively differentiate patients based on their response to VNS with an accuracy of 94.12% (AUC = 87.88%). Notably, the inclusion of clinical covariates did not improve the classification of patients, emphasizing the robustness of diffusion MRI in comparison to clinical covariates to predict VNS response.

Finally, **we developed a device for remotely controlling the stimulation parameters of the Synergia Medical optoelectronic neurostimulator from the command room while the implant is in the MRI system.** This device holds exciting potential for exploring the central effects of acute VNS administration using fMRI. Moreover, it provides thrilling prospects for optimizing VNS therapy by tuning the stimulation parameters during fMRI acquisitions and selecting parameters that maximize the

activation of structures of the vagal afferent network involved in the antiseizure effects.

SUPPLEMENTARY MATERIALS

Supplementary Material S3.1: Recursive Feature Elimination (RFE) for the SVM model selection: summary table with the maximum accuracy of classification for models when different kernel (linear, polynomial, Radial Basis Function - RBF and sigmoid) functions are used, with the corresponding sensitivity, specificity, and the corresponding best-performing hyperparameters (C and γ). The model highlighted in bold is the final model used for the classification.

Kernel	Features	Maximum Accuracy	Maximum Sensitivity	Maximum Specificity	Best-performing Hyperparameters [C ; γ]
Linear Kernel	*All 6 features*	66.7 %	75 %	57.14 %	[2^{0} ; *N/A*]
	Top 5 features	66.7 %	75 %	57.14 %	[2^{0}, 2^{1}, 2^{2} ; *N/A*]
	Top 4 features	60 %	75 %	42.85 %	[2^{-3}, 2^{-2}, 2^{-1} ; *N/A*]
	Top 3 features	60 %	75 %	42.85 %	[2^{-3}, 2^{-2}, 2^{-1} ; *N/A*]
Polynomial Kernel	*All 6 features*	60 %	100 %	14.28 %	[2^{-3} ; 2^{-2}], [2^{0} ; 2^{-3}]
	Top 5 features	60 %	100 %	14.28 %	[2^{-5} ; 2^{-1}], [2^{-2} ; 2^{-2}], [2^{1} ; 2^{-3}]
	Top 4 features	53.3 %	87.5 %	14.28 %	[2^{-4} ; 2^{-1}], [2^{-3} ; 2^{-1}], [2^{-1} ; 2^{-2}], [2^{0} ; 2^{-2}], [2^{2} ; 2^{-3}]
	Top 3 features	60 %	100 %	14.28 %	[2^{-5} ; 2^{0}], [2^{-4} ; 2^{0}], [2^{-3} ; 2^{-1}], [2^{-2} ; 2^{-1}], [2^{-1} ; 2^{-1}] [2^{0} ; 2^{-2}], [2^{1} ; 2^{-2}], [2^{2} ; 2^{-2}]
Radial Basis Functions	*All 6 features*	53.3 %	75 %	28.57 %	[2^{1} ; 2^{-5}]
	Top 5 features	53.3 %	75 %	28.57 %	[2^{1} ; 2^{-5}]
	Top 4 features	53.3 %	75 %	28.57 %	[2^{1} ; 2^{-5}], [2^{1} ; 2^{-4}], [2^{2} ; 2^{-5}]
	Top 3 features	53.3 %	75 %	28.57 %	[2^{0} ; 2^{-3}], [2^{1} ; 2^{-4}], [2^{2} ; 2^{-5}]

Sigmoid	*All 6 features*	80 %	87.5 %	71.41 %	$[2^{0}; 2^{-2}]$, $[2^{2}; 2^{-2}]$
Kernel	*Top 5 features*	73.3 %	75 %	71.42 %	$[2^{0}; 2^{-1}]$
	Top 4 features	**80 %**	**75 %**	**85.71 %**	**$[2^{2}; 2^{0}]$**
	Top 3 features	73.3 %	75 %	71.42 %	$[2^{2}; 2^{-2}]$

Supplementary Material S4.1: Significant responses to the target sound. Significant activation foci for a statistical threshold of p < 0.05 FWE-corrected (p < 3.34e-8 uncorrected; t > 6.35), and a minimum cluster size of 20 voxels (38 clusters reported). R: Right, L: Left, TOP: Temporo-Occipital Part, AD: Anterior Division, PD: Posterior Division, SD: Superior Division. An extensive table without minimum cluster size and including 138 significant voxel clusters is available upon request to the corresponding author.

Brain region (Peak MNI coordinates)	**Cluster size**	**T_{49}**	**MNI coordinates (x, y, z) in mm**		
Insular Cortex L	59040	15.4465	-41	-4	11
Cerebellum (VI) R	34354	17.781	30	-55	-26
Middle Temporal Gyrus (TOP) R	18333	12.5287	63	-48	10
Cingulate Gyrus (AD) L	16879	17.86	-1	5	36
Insular Cortex R	12563	12.1277	42	5	-2
Thalamus L	1549	13.3082	-16	-18	5
Middle Temporal Gyrus (PD) R	972	10.6742	48	-25	-6
Cingulate Gyrus (PD) R	754	9.6633	6	-19	26
Thalamus R	541	10.0317	15	-14	7
Frontal Pole R	466	7.4437	39	41	22
Precuneus Cortex L	194	8.6936	-1	-44	59
Thalamus R	187	9.0946	15	-6	9
Middle Frontal Gyrus R	145	8.2982	38	-1	58
Middle Temporal Gyrus (PD) L	132	8.7711	-66	-29	-3
Precuneus Cortex L	96	7.8525	-9	-49	50
Planum Polare L	95	8.621	-40	-2	-18
Middle Temporal Gyrus (TOP) R	93	8.1126	46	-37	0
Middle Frontal Gyrus L	92	7.6677	-31	37	39
Frontal Pole L	91	7.4702	-28	54	22
Frontal Pole R	82	9.5149	25	41	-17
Cerebellum (VI) L	70	7.6427	-8	-74	-24
Caudate R	62	7.8333	14	15	4
Middle Temporal Gyrus (PD) L	58	7.5001	-50	-30	-6
Thalamus R	50	8.7706	4	-5	7
Frontal Orbital Cortex R	48	8.044	29	19	-13
Middle Temporal Gyrus (PD) L	47	7.1467	-59	-28	-4

Precuneus Cortex R	46	7.0337	7	-50	47
Lateral Occipital Cortex (SD) R	42	7.0278	35	-61	42
Cingulate Gyrus (PD) R	40	6.9469	13	-23	36
Caudate R	39	7.4336	12	6	9
Cerebellum (VIIIa) R	37	8.6327	9	-67	-49
Precuneus Cortex R	34	7.8746	8	-46	53
Superior Frontal Gyrus L	31	7.7228	-25	4	65
Cerebellum (I-IV) L	27	7.2685	-7	-46	-19
Frontal Pole L	27	6.6931	-35	50	22
Cuneal Cortex L	25	7.1918	0	-89	15
Precentral Gyrus L	23	7.2071	-52	1	34
Lingual Gyrus R	22	7.1215	14	-68	-5

Supplementary Material S5.1: Sagittal, coronal, and transverse views of the statistical maps corresponding to brain responses to the target stimuli during the auditory oddball task for all patients (X = 22, top figure) and only patients with a good (> 90% detection of target sounds) accuracy to the task (X = 18, bottom figure). In order to confirm typical brain responses to the oddball task, a 2nd-level analysis was conducted in the Montreal Neurological Institute (MNI) space (ICBM-MNI 152, version 2009c asymmetric). Individual 1st-level statistical map of target appearance was registered to the MNI space, and a random effects group analysis was conducted. Due to the small size of our sample, a lenient threshold p < 0.01 was used to report the general brain activations observed at the appearance of target sounds and ensure that the activations observed were not related to noise.

Whole-brain group-level analysis of fMRI data at a lenient statistical threshold (p < 0.01, uncorrected for multiple comparisons) revealed typical brain activations previously reported during an auditory oddball task, including the insular cortex, the anterior division of the cingulate gyrus, and the thalamus. A comprehensive table reporting the activation foci at the appearance of target sounds can be found in ***Supplementary Material S5.2****. A significant activation of the LC was not expected at the whole-brain group level, due to the small size of the nucleus and the limited sample size. Therefore, the LC activity was further analyzed in the space of the subject.*

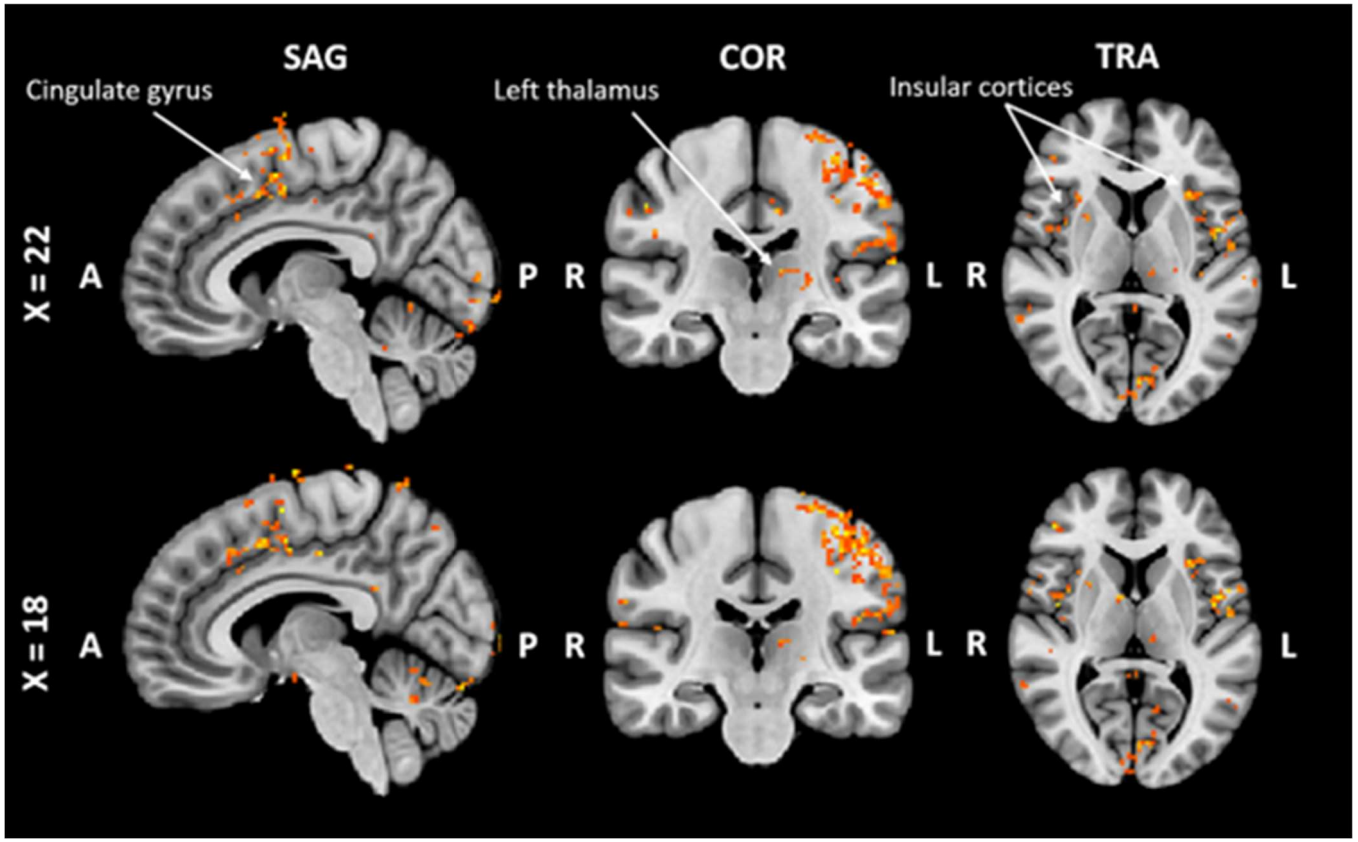
SAG
COR
TRA
Cingulate gyrus
Left thalamus
Insular cortices
X = 22
X = 18
A
P
R
L
R
L

Supplementary Material S5.2: Brain regions activated at the appearance of target sounds (second-level analysis, all patients included). Activation foci for p < 0.01. R: Right, L: Left, AD: Anterior Division, PD: Posterior Division.

Brain region (Peak MNI coordinates)	MNI coordinates (x, y, z)			t-value	p-value	Cluster size
R Supramarginal gyrus AD	68	-31	28	3.47965	0.002237	96
R Supramarginal gyrus PD	64	-43	24	5.160909	4.10E-05	152
R Precentral Gyrus	54	5	15	5.0936	4.80E-05	328
R Precentral Gyrus	58	9	1	3.871333	0.000883	96
R Supramarginal gyrus AD	51	-31	51	4.407302	0.000245	136
R Middle frontal gyrus	52	14	42	4.475682	0.000208	152
R Temporal pole	53	17	-9	3.931808	0.000765	96
R Insular cortex	37	6	6	4.20561	0.000397	376
R Middle frontal gyrus	42	33	34	3.618289	0.001612	136
R Middle frontal gyrus	40	3	62	3.988464	0.000668	120
R Superior frontal gyrus	25	1	55	6.848522	1.00E-06	440
R Temporal occipital fusiform	28	-63	-19	5.576286	1.60E-05	424
R Occipital fusiform gyrus	34	-69	-23	5.658057	1.30E-05	352
R Superior frontal gyrus	27	-1	63	4.253577	0.000354	160
R Cerebellum	20	-56	-20	5.302732	2.90E-05	680
R Precentral Gyrus	7	-2	62	5.979005	6.00E-06	784
R Superior frontal gyrus	10	12	66	4.502155	0.000196	112
R Lingual gyrus	14	-73	-13	4.872447	8.10E-05	144
Cingulate gyrus AD	0	-3	50	8.15703	0	3984
R Superior frontal gyrus	8	5	66	4.513535	0.00019	336
R Supracalcarine cortex	-2	-84	7	4.595208	0.000157	392
L Superior frontal gyrus	1	7	62	4.488734	0.000202	120
Precuneous cortex	0	-49	64	4.14519	0.000459	104
Left cingulate gyrus AD	-2	-2	33	4.895652	7.70E-05	112
R Lingual gyrus	-1	-88	-14	3.750914	0.001177	136

L Intracalcarine cortex	-9	-76	10	4.178679	0.000424	128
Left thalamus	-10	-21	9	4.382185	0.000261	112
L Temporal occipital fusiform	-23	-59	-18	4.734857	0.000112	840
L Precentral gyrus	-15	-13	75	3.68581	0.001374	104
L Precentral gyrus	-28	-8	58	6.184498	4.00E-06	2016
L Occipital fusiform gyrus	-16	-79	-22	5.315825	2.90E-05	224
L Cerebellum	-16	-75	-44	5.046857	5.40E-05	144
L Superior frontal gyrus	-17	-9	70	4.039196	0.000592	120
L Postcentral gyrus	-20	-35	74	4.457869	0.000217	104
L Postcentral gyrus	-36	-30	61	6.205268	4.00E-06	8232
L Occipital fusiform gyrus	-24	-79	-16	4.440164	0.000227	288
L Superior frontal gyrus	-25	-5	67	4.223297	0.000381	96
L Middle frontal gyrus	-31	3	67	4.435038	0.00023	136
L Cerebellum	-26	-85	-34	4.389474	0.000256	96
L Frontal operculum cortex	-37	21	6	4.839891	8.80E-05	224
L Cerebellum	-30	-55	-32	5.722091	1.10E-05	128
L Occipital fusiform gyrus	-33	-79	-20	4.873293	8.10E-05	120
L Precentral gyrus	-36	-7	69	4.713655	0.000118	280
L Middle frontal gyrus	-34	37	32	5.644079	1.30E-05	136
L Middle frontal gyrus	-37	35	24	4.634315	0.000143	96
L Superior parietal lobule	-38	-48	65	4.705645	0.00012	136
L Frontal operculum cortex	-47	10	-4	4.325704	0.000298	240
L Frontal orbital cortex	-37	25	-5	4.449174	0.000222	160
L Cerebellum	-37	-63	-25	4.053257	0.000572	136
L Occipital fusiform gyrus	-42	-69	-23	4.3321	0.000294	144
L Central opercular cortex	-49	0	6	6.906199	1.00E-06	216
L Parietal operculum cortex	-59	-27	15	4.538655	0.000179	888
L Cerebellum	-48	-67	-26	4.597201	0.000156	216
L Supramarginal gyrus, PD	-49	-42	25	4.884823	7.90E-05	112
L Inferior frontal gyrus, pars opercularis	-52	19	-5	5.02606	5.60E-05	232
L Angular gyrus	-52	-60	12	6.049971	5.00E-06	160

L Precentral gyrus	-51	6	11	4.332529	0.000293	128
L Temporal pole	-56	8	-1	5.201084	3.70E-05	96
L Supramarginal gyrus, PD	-61	-43	27	6.369423	3.00E-06	304
L Central opercular cortex	-60	-7	9	4.496726	0.000198	160
L Planum temporale	-59	-25	10	4.707882	0.00012	104

Supplementary Material S5.3: (A) Relationship between VNS response and LC activity. (B) Effect of therapy duration on LC activity (all patients included). (C) Relationship between VNS response and LC contrast. (D) Effect of therapy duration on the LC contrast. (E) Relationship between VNS response and diffusion metrics within the LC-hippocampus connections. (F) Effect of therapy duration and diffusion metrics. All statistical models correct for age, sex, ASM intake, benzodiazepine intake and epilepsy duration.

(A) LC activity ~		***Response***	***Age***	***Sex***	***ASM***	***Benzo***	***Epilepsy duration***
LEFT	Rostral	p = 0.42 t = -2.63	p = 0.69 t = -1.43	p = 0.66 t = 0.79	p = 0.73 t = -0.88	p = 0.14 t = 0.51	p = 0.71 t = 1.01
	Medial	**p = 0.01*** t = -2.63	p = 0.17 t = -1.43	p = 0.44 t = 0.79	p = 0.39 t = -0.88	p = 0.62 t = 0.51	p = 0.33 t = 1.01
	Caudal	p = 0.59 t = 0.55	p = 0.27 t = -0.14	p = 0.70 t = 0.38	p = 0.19 t = 1.38	p = 0.41 t = -0.84	p = 0.87 t = 0.16
RIGHT	Rostral	p = 0.52 t = 0.66	p = 0.70 t = 0.39	p = 0.65 t = -0.46	p = 0.10 t = 1.74	p = 0.41 t = -0.85	p = 0.45 t = 0.78
	Medial	p = 0.54 t = -0.62	p = 0.50 t = -0.69	p = 0.56 t = -0.60	p = 0.67 t = 0.44	p = 0.22 t = -1.29	p = 0.44 t = 0.78
	Caudal	p = 0.40 t = 0.87	p = 0.22 t = -1.28	p = 0.24 t = -1.21	p = 0.96 t = 0.05	p = 0.44 t = -0.79	p = 0.06 t = 2.00

(B) LC activity ~	***Therapy Duration***	***Age***	***Sex***	***ASM***	***Benzo***	***Epilepsy duration***

LEFT	Rostral	p = 0.07 t = -1.95	p = 0.23 t = 1.24	p = 0.45 t = -0.77	p = 0.84 t = -0.21	p = 0.24 t = 1.21	p = 0.65 t = -0.46
	Medial	p = 0.72 t = -0.36	p = 0.27 t = -1.13	p = 0.48 t = 0.73	p = 0.78 t = -0.28	p = 0.60 t = 0.53	p = 0.56 t = 1.30
	Caudal	p = 0.78 t = 0.28	p = 0.28 t = -1.11	p = 0.70 t = 0.38	p = 0.23 t = 1.23	p = 0.43 t = -0.81	p = 0.82 t = 0.23
RIGHT	Rostral	p = 0.20 t = 1.35	p = 0.93 t = -0.09	p = 0.73 t = -0.35	p = 0.16 t = 1.46	p = 0.52 t = -0.66	p = 0.34 t = 0.98
	Medial	p = 0.54 t = -0.62	p = 0.66 t = -0.45	p = 0.53 t = -0.64	p = 0.52 t = 0.65	p = 0.20 t = -1.34	p = 0.50 t = 0.68
	Caudal	p = 0.54 t = -0.61	p = 0.66 t = -0.45	p = 0.53 t = -0.64	p = 0.52 t = 0.66	p = 0.20 t = -1.34	p = 0.50 t = 0.68

(C) LC contrast ~		***Response***	***Age***	***Sex***	***ASM***	***Benzo***	***Epilepsy duration***
LEFT	Rostral	p = 0.84 t = 0.20	p = 0.58 t = 0.56	p = 0.55 t = -0.60	p = 0.91 t = 0.11	p = 0.26 t = 1.16	p = 0.60 t = -0.54
	Medial	p = 0.53 t = -0.64	p = 0.23 t = -1.24	p = 0.63 t = -0.49	p = 0.53 t = -0.64	p = 0.42 t = 0.83	p = 0.13 t = 1.57
	Caudal	p = 0.19 t = 1.37	p = 0.85 t = 0.19	p = 0.77 t = -0.30	p = 0.69 t = -0.41	p = 0.17 t = 1.45	p = 0.87 t = 0.16
RIGHT	Rostral	p = 0.21 t = 1.29	p = 0.29 t = 1.10	p = 0.43 t = -0.82	p = 0.79 t = 0.28	p = 0.54 t = 0.62	p = 0.17 t = -1.44
	Medial	p = 0.65 t = 0.46	p = 0.68 t = -0.42	p = 0.53 t = -0.65	p = 0.81 t = -0.24	p = 0.38 t = 0.89	p = 0.62 t = 0.51

	Caudal	**p = 0.03 *** t = 2.39	p = 0.61 t = 0.53	p = 0.79 t = -0.27	p = 0.79 t = 0.27	p = 0.27 t = 1.13	p = 0.64 t = -0.48

(D) LC contrast ~		***Therapy Duration***	***Age***	***Sex***	***ASMs***	***Benzo***	***Epilepsy duration***
LEFT	*Rostral*	p = 0.81 t = 0.25	p = 0.64 t = 0.47	p = 0.53 t = -0.63	p = 0.99 t = 0.007	p = 0.26 t = 1.18	p = 0.62 t = -0.49
	Medial	**p = 0.03*** t = 2.28	p = 0.08 t = -1.87	p = 0.83 t = -0.21	p = 0.32 t = -1.03	p = 0.16 t = 1.47	p = 0.09 t = 1.78
	Caudal	p = 0.29 t = 1.09	p = 0.86 t = -0.17	p = 0.63 t = -0.49	p = 0.33 t = -1.00	p = 0.14 t = 1.55	p = 0.66 t = 0.44
RIGHT	Rostral	p = 0.92 t = -0.09	p = 0.35 t = 0.96	p = 0.31 t = -1.07	p = 0.96 t = -0.04	p = 0.63 t = 0.48	O p = 0.26 t = -1.18
	Medial	**p = 0.04*** t = 2.26	p = 0.31 t = -1.05	p = 0.51 t = -0.67	p = 0.38 t = -0.90	p = 0.16 t = 1.46	p = 0.45 t = 0.77
	Caudal	p = 0.38 t = 0.89	p = 0.93 t = 0.09	p = 0.54 t = -0.62	p = 0.61 t = -0.51	p = 0.32 t = 1.03	p = 0.99 t = -0.01

(E) Diffusion metric ~		***Response***	***Age***	***Sex***	***ASMs***	***Benzo***	***Epilepsy duration***
LEFT	*wFVF*	**p = 0.02*** t = 2.61	**p = 9.18e-5*** t = 5.98	**p = 0.002*** t = -4.11	p = 0.48 t = 0.72	**p = 0.04*** t = -2.37	p = 0.05 t = -2.24
	FA	p = 0.83 t = 0.22	**p = 0.01*** t = 3.04	p = 0.11 t = -1.75	p = 0.56 t = 0.59	p = 0.31 t = -1.06	p = 0.09 t = -1.85
	MD	**p = 0.001*** t = -4.31	**p = 0.006*** t = -3.38	p = 0.82 t = -0.22	p = 0.07 t = -1.98	p = 0.06 t = 2.06	p = 0.07 t = 1.99

	AD	**p = 0.02*** t = -2.64	p = 0.54 t = -0.62	p = 0.29 t = -1.11	p = 0.29 t = 0.89	p = 0.39 t = 0.89	p = 0.62 t = 0.51
	RD	**p = 1.49e-5*** t = -7.33	**p = 1.67e-6*** t = -9.21	p = 0.07 t = 1.97	**p = 0.004*** t = -3.57	**p = 0.001*** t = 4.40	**p = 3e-4*** t = 5.07
RIGHT	*wFVF*	p = 0.10 t = 1.82	p = 0.06 t = 2.15	p = 0.97 t = 0.03	p = 0.44 t = 0.80	p = 0.59 t = -0.56	p = 0.31 t = -1.07
	FA	p = 0.79 t = 0.26	p = 0.3 t = 1.09	p = 0.96 t = 0.05	p = 0.85 t = 0.19	p = 0.67 t = -0.43	p = 0.28 t = -1.14
	MD	**p = 0.01*** t = -2.95	p = 0.2 t = -1.37	p = 0.29 t = -1.12	p = 0.13 t = -1.65	p = 0.93 t = 0.08	p = 0.65 t = 0.47
	AD	p = 0.07 t = -1.98	p = 0.65 t = -0.47	p = 0.38 t = -0.91	p = 0.24 t = -1.25	p = 0.91 t = 0.12	p = 0.85 t = -0.19
	RD	**p = 0.003*** t = -3.74	**p = 0.036*** t = -2.42	p = 0.26 t = -1.20	p = 0.09 t = -1.87	p = 0.99 t = 0.003	p = 0.21 t = 1.35

(F) Diffusion metric ~		***Therapy duration***	***Age***	***Sex***	***ASMs***	***Benzo***	***Epilepsy duration***
LEFT	wFVF	p = 0.17 t = -1.48	p = 4.3e-4 t = 4.93	p = 8.1e-3 t = -3.22	p = 0.74 t = 0.34	p = 0.06 t = -2.1	p = 0.10 t = -1.81
	FA	p = 0.70 t = -0.39	p = 0.01 t = 3.07	p = 0.11 t = -1.74	p = 0.57 t = 0.59	p = 0.30 t = -1.09	p = 0.09 t = -1.86
	MD	p = 0.32 t = 1.03	p = 0.09 t = -1.88	p = 0.59 t = -0.55	p = 0.39 t = -0.89	p = 0.21 t = 1.33	p = 0.29 t = 1.11
	AD	p = 0.51 t = 0.67	p = 0.79 t = -0.27	p = 0.25 t = -1.21	p = 0.56 t = -0.60	p = 0.49 t = 0.71	p = 0.78 t = 0.29

RIGHT	wFVF	p = 0.16 t = -1.51	p = 0.08 t = 1.95	p = 0.93 t = 0.09	p = 0.73 t = 0.35	p = 0.59 t = -0.55	p = 0.31 t = -1.08
	FA	p = 0.27 t = -1.17	p = 0.26 t = -1.17	p = 0.94 t = 0.08	p = 0.85 t = 0.19	p = 0.59 t = -0.55	p = 0.24 t = -1.25
	MD	p = 0.25 t = 1.22	p = 0.41 t = -0.86	p = 0.36 t = -0.95	p = 0.49 t = -0.71	p = 0.99 t = 8e-3	p = 0.69 t = 0.40
	AD	p = 0.65 t = 0.53	p = 0.83 t = -0.22	p = 0.42 t = -0.83	p = 0.54 t = 0.62	p = 0.98 t = 0.02	p = 0.89 t = -0.14

Supplementary Material S5.4: Tractography of left and right LC-hippocampus connections in all patients. Tractography of subject 16 was only conducted for the left LC-hippocampus connections, due to an amygdalohippocampectomy performed in the right hemisphere.

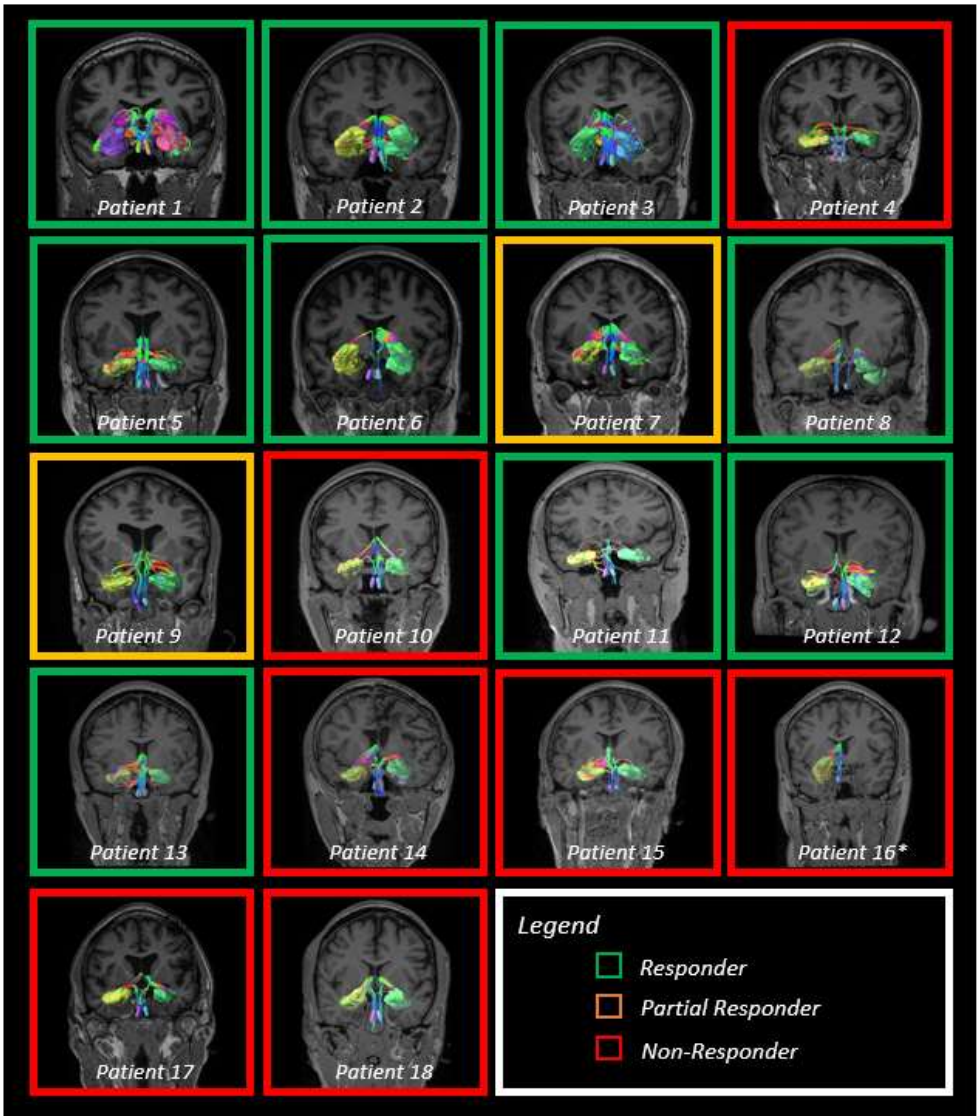

Supplementary Material S6.1: Linear models investigating the relationship between diffusion metrics and VNS response, correcting for age, sex, ASM intake, benzodiazepine intake, epilepsy duration, and VNS therapy duration. Models showing a significant relationship ($p_{FDR} < 0.05$) or a trend toward significance ($p < 0.05$) between diffusion metrics and VNS response are shown here (uncorrected p-values reported). Refer to text for FDR-corrected p-values of significant results.

Diffusion metric ~	***Response***	***Age***	***Sex***	***ASM***	***Benzo***	***Epilepsy duration***	***Duration VNS therapy***
DTI							
☆ MD Left I-I	p = 0.03 t = -2.43	p = 0.17 t = -1.48	p = 0.99 t = 0.002	p = 0.54 t = -0.63	p = 0.98 t = -0.02	p = 0.78 t = 0.28	p = 0.44 t = 0.80
★ MD Left I-T	p = 0.001 t = -4.44	p = 0.01 t = -3.05	p = 0.10 t = -1.82	p = 0.11 t = -1.72	p = 0.11 t = -1.76	p = 0.63 t = 0.49	p = 0.30 t = 1.10
☆ MD Left P-O	p = 0.03 t = -2.48	p = 0.04 t = -2.44	p = 0.08 t = -1.97	p = 0.11 t = -1.76	p = 0.27 t = -1.16	p = 0.09 t = 1.90	p = 0.10 t = 1.82
★ MD Left P-P	p = 0.01 t = -2.95	p = 0.06 t = -2.16	p = 0.22 t = -1.30	p = 0.14 t = -1.59	p = 0.64 t = -0.48	p = 0.19 t = 1.42	p = 0.45 t = 0.79
★ MD Right I-I	p = 0.007 t = -3.35	p = 0.20 t = -1.37	p = 0.96 t = -0.05	p = 0.47 t = -0.75	p = 0.47 t = -0.74	p = 0.83 t = -0.21	p = 0.69 t = 0.41
★ MD Right I-T	p = 0.002 t = -4.20	p = 0.04 t = -2.36	p = 0.33 t = -1.01	p = 0.13 t = -1.66	p = 0.23 t = -1.26	p = 0.51 t = 0.67	p = 0.77 t = 0.30
★ MD Right P-O	p = 0.004 t = -3.74	p = 0.04 t = -2.40	p = 0.08 t = -1.99	p = 0.08 t = -1.95	p = 0.10 t = -1.80	p = 0.24 t = 1.24	p = 0.23 t = 1.28
☆ MD Right P-P	p = 0.03 t = -2.58	p = 0.04 t = -2.35	p = 0.35 t = -0.98	p = 0.49 t = -0.72	p = 0.27 t = -1.17	p = 0.27 t = 1.18	p = 0.62 t = 0.51
☆ MD Right S	p = 0.04 t = -2.28	p = 0.39 t = -0.90	p = 0.75 t = -0.32	p = 0.59 t = 0.56	p = 0.30 t = -1.10	p = 0.98 t = 0.03	p = 0.32 t = 1.04

☆ RD Left I-I	p = 0.03 t = -2.49	p = 0.11 t = -1.78	p = 0.96 t = -0.04	p = 0.42 t = -0.84	p = 0.92 t = 0.10	p = 0.47 t = 0.75	p = 0.52 t = 0.67
☆ RD Left I-T	p = 0.02 t = -2.65	p = 0.14 t = -1.60	p = 0.49 t = -0.72	p = 0.43 t = -0.82	p = 0.19 t = -1.41	p = 0.90 t = 0.12	p = 0.85 t = 0.20
☆ RD Left P-P	p = 0.03 t = -2.43	p = 0.17 t = -1.47	p = 0.69 t = -0.41	p = 0.29 t = -1.12	p = 0.73 t = -0.35	p = 0.35 t = 0.97	p = 0.80 t = 0.26
★ RD Right I-I	p = 0.007 t = -3.38	p = 0.17 t = -1.47	p = 0.93 t = 0.09	p = 0.46 t = -0.76	p = 0.52 t = -0.66	p = 0.89 t = -0.14	p = 0.73 t = 0.35
★ RD Right I-T	p = 0.007 t = -3.39	p = 0.13 t = -1.64	p = 0.73 t = -0.34	p = 0.35 t = -0.98	p = 0.20 t = -1.37	p = 0.61 t = 0.52	p = 0.94 t = 0.07
★ RD Right P-O	p = 0.002 t = -4.04	p = 0.04 t = -2.39	p = 0.31 t = -1.06	p = 0.14 t = -1.60	p = 0.03 t = -2.54	p = 0.29 t = 1.11	p = 0.69 t = 0.40
☆ AD Left I-T	p = 0.04 t = -2.29	p = 0.09 t = -1.94	p = 0.15 t = -1.54	p = 0.24 t = -1.25	p = 0.80 t = -0.26	p = 0.56 t = 0.60	p = 0.23 t = 1.28
☆ AD Right I-I	p = 0.03 t = -2.62	p = 0.34 t = -0.99	p = 0.85 t = -0.20	p = 0.57 t = -0.59	p = 0.53 t = -0.65	p = 0.82 t = -0.23	p = 0.71 t = 0.38
☆ AD Right I-T	p = 0.02 t = -2.85	p = 0.07 t = -2.07	p = 0.18 t = -1.45	p = 0.11 t = -1.74	p = 0.77 t = -0.29	p = 0.63 t = 0.49	p = 0.63 t = 0.50
NODDI							
★ ICVF Left I-I	p = 0.02 t = 2.82	p = 0.08 t = 1.94	p = 0.71 t = -0.38	p = 0.32 t = 1.05	p = 0.98 t = 0.03	p = 0.95 t = -0.06	p = 0.53 t = -0.65
★ ICVF Left I-T	p = 0.005 t = 3.51	p = 0.04 t = 2.32	p = 0.64 t = 0.49	p = 0.15 t = 1.54	p = 0.20 t = 1.38	p = 0.91 t = 0.11	p = 0.53 t = -0.64
★ICVF Left P-O	p = 0.02 t = 2.69	p = 0.04 t = 2.32	p = 0.36 t = 0.95	p = 0.07 t = 2.02	p = 0.34 t = 1.00	p = 0.17 t = -1.47	p = 0.23 t = -1.28
★ ICVF Left P-P	p = 0.02 t = 2.59	p = 0.06 t = 2.13	p = 0.49 t = 0.71	p = 0.08 t = 1.98	p = 0.55 t = 0.62	p = 0.23 t = -1.29	p = 0.58 t = -0.58
★ ICVF Right I-I	p = 0.01 t = 2.87	p = 0.27 t = 1.16	p = 0.81 t = -0.24	p = 0.37 t = 0.94	p = 0.56 t = 0.60	p = 0.61 t = 0.52	p = 0.92 t = -0.10
★ ICVF Right I-T	p = 0.004 t = 3.70	p = 0.06 t = 2.11	p = 0.76 t = 0.31	p = 0.14 t = 1.60	p = 0.27 t = 1.18	p = 0.72 t = -0.37	p = 0.92 t = -0.10

★ ICVF Right P-O	p = 0.004 t = 3.68	p = 0.03 t = 2.46	p = 0.30 t = 1.10	p = 0.11 t = 1.73	p = 0.13 t = 1.64	p = 0.39 t = -0.89	p = 0.26 t = -1.20
MF							
☆ wFVF Left I-I	p = 0.04 t = 2.29	p = 0.14 t = 1.60	p = 0.33 t = -1.02	p = 0.44 t = 0.81	p = 0.61 t = -0.53	p = 0.79 t = -0.27	p = 0.69 t = -0.40
☆ wFVF Right I-I	p = 0.02 t = 2.69	p = 0.19 t = 1.39	p = 0.70 t = -0.39	p = 0.43 t = 0.82	p = 0.76 t = 0.32	p = 0.74 t = 0.34	p = 0.90 t = -0.13

I-I : Inferior thalamocortical tracts projecting to the insular cortex, I-T : Inferior thalamocortical tracts projecting to the temporal lobe, P-O : Posterior thalamocortical tracts projecting to the occipital lobe, P-P : Posterior thalamocortical tracts projecting to the parietal lobe, S : Superior thalamocortical tracts, MD : Mean Diffusivity, RD : Radial Diffusivity, AD : Axial Diffusivity, ICVF : Intracellular Volume Fraction, wFVF : weighted Fiber Volume Fraction. Filled stars represent results of the linear models that remained significant after False Discovery Rate (FDR) correction for multiple comparisons; Empty stars represent results of the linear models that were significant without correction only.

Supplementary Material S7.1: Measurement of the optical power losses with optical fibers and through skin for the optical wake-up of the implant.

Driving current LED (A)	Optical power LED only (mW)	Optical power LED + 15m bundle OPTICAL WAKE UP (mW)	Optical power LED + 15m bundle OPTICAL WAKE UP + 2mm skin (mW)	Optical power LED + 15m bundle OPTICAL WAKE UP + 3mm skin (mW)
0	0	0	0	0
0.025	41.5	7	1.7	0.1
0.05	69	13.5	2.3	0.3
0.075	99	14.4	2.7	0.6
0.1	131.5	17.	3.5	1.1
0.15	203.5	21.9	4	1.5
0.2	260	26.7	4.7	1.7
0.25	325	31.7	5.4	2.3
0.3	385	36.2	5.8	2.7
0.35	440	41.5	6.7	3
0.4	480	45.4	7.3	3.3
0.45	516.1	48.5	7.7	3.6
0.5	556.5	53	8.1	3.8
0.55	595.5	56.8	8.5	4
0.6	633.3	59.3	9	4.2
0.65	670.5	61.9	9.5	4.4
0.7	704.2	63.5	9.8	4.5
0.75	736	65.9	9.9	5.1
0.8	765.1	65.5	11.3	5
0.85	793.3	70.8	11.7	5.2
0.9	819.8	69.8	11.7	5.7
0.95	840	74.8	11.8	5.6
1	860.4	74.2	12.8	6.3

Supplementary Material S8.1: Correlation of microstructural features between tracts – thalamocortical tracts and LC-hippocampus connections. L(R)-LH: left (right) locus coeruleus – hippocampus tracts. L(R)-II: left (right) inferior thalamocortical tracts projecting to the insula. L(R)-IT: left (right) inferior thalamocortical tracts projecting to the temporal lobe. L(R)-PO: left (right) posterior thalamocortical tracts projecting to the occipital lobe. L(R)-PP: left (right) posterior thalamocortical tracts projecting to the parietal lobe. MD: mean diffusivity [s·mm^{-2}]. RD: radial diffusivity [s·mm^{-2}]. wFVF: weighted fiber volume fraction. Red: significant Spearman correlation between variables. Blue: non-significant Spearman correlation between variables.

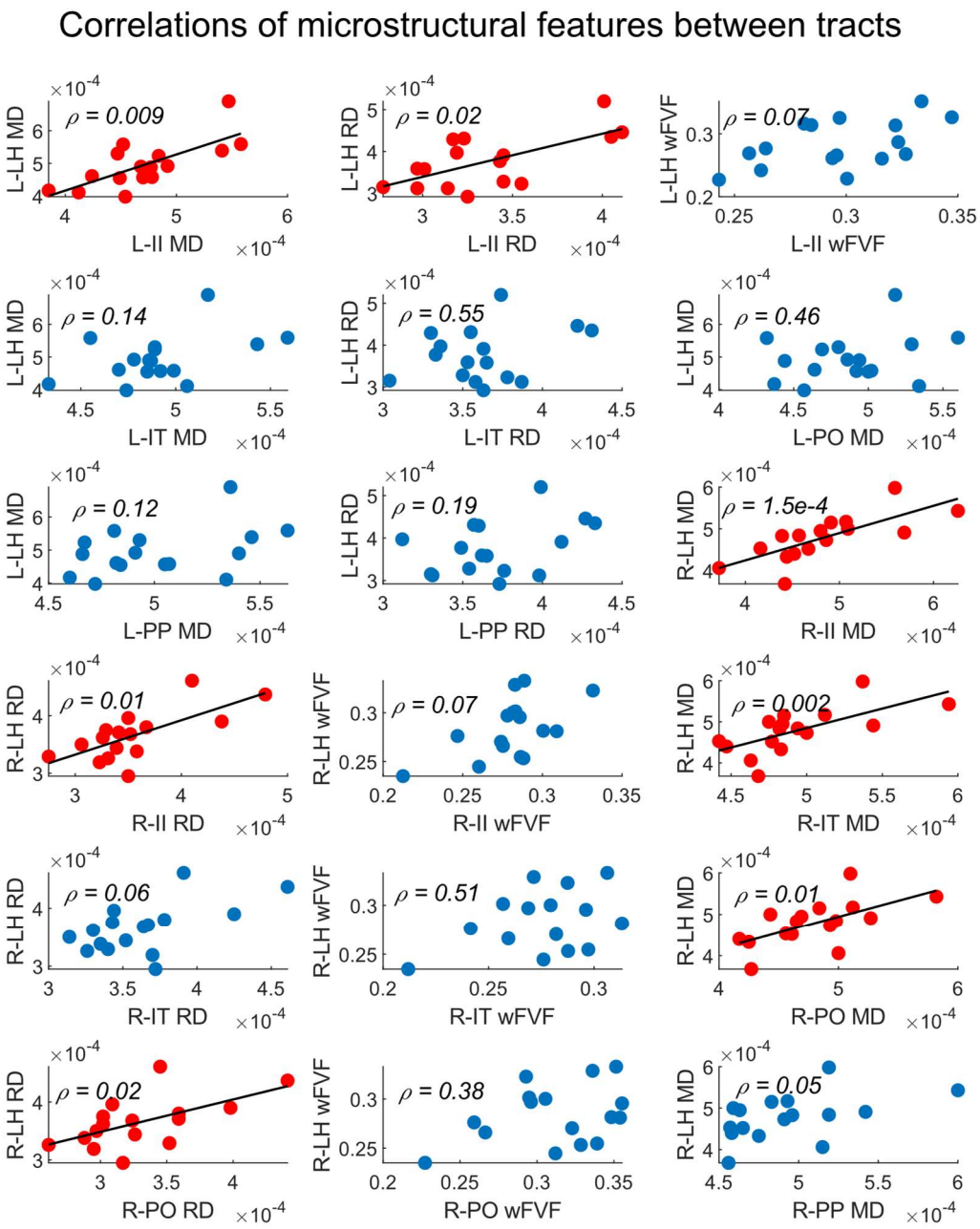
Correlations of microstructural features between tracts
L-LH MD
L-II MD
ρ = 0.009
L-LH RD
L-II RD
ρ = 0.02
L-LH wFVF
L-II wFVF
ρ = 0.07
L-IT MD
ρ = 0.14
L-IT RD
ρ = 0.55
L-PO MD
ρ = 0.46
L-PP MD
ρ = 0.12
L-PP RD
ρ = 0.19
R-LH MD
R-II MD
ρ = 1.5e-4
R-LH RD
R-II RD
ρ = 0.01
R-LH wFVF
R-II wFVF
ρ = 0.07
R-IT MD
ρ = 0.002
R-IT RD
ρ = 0.06
R-IT wFVF
ρ = 0.51
R-PO MD
ρ = 0.01
R-PO RD
ρ = 0.02
R-PO wFVF
ρ = 0.38
R-PP MD
ρ = 0.05

Supplementary Material S8.2: Investigation of a potential link between surgery and abnormal diffusion MRI values in thalamocortical tracts.

Figure S8.2A and **Figure S8.2B** show boxplots of DTI metrics and NODDI/MF metrics in all subsegments of the left and right thalamocortical tracts, respectively. Based on these boxplots, one patient who underwent brain surgery (mentioned as 'investigated case' - IC) shows outlier values (more than 1.5 interquartile ranges—IQR—above the upper quartile of 75% or below the lower quartile of 25%), for different diffusion metrics. As this patient may show abnormal diffusion metrics, further investigations were conducted to determine if the surgery could explain these values. The clinical description of this patient can be found in **Table S8.2A**.

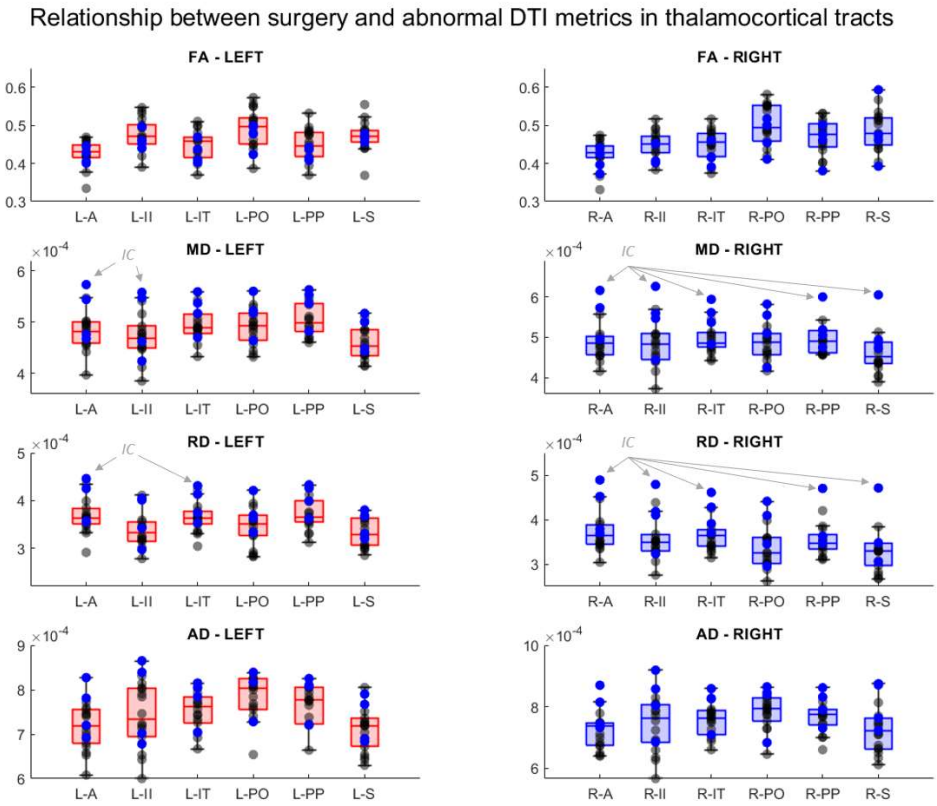

Figure S8.2A *– Evaluation of a potential relationship between surgery and abnormal DTI values. Boxplots of DTI values in subsegments of thalamocortical tracts for all patients included in* ***Study 4****. Red boxplot: metrics evaluated in the left subsegments of thalamocortical tracts. Blue boxplot: metrics evaluated in the right subsegments of thalamocortical tracts. Blue point: patients who had surgery (all localized in the right hemisphere). IC: Investigated Case – a patient who had surgery and showed several abnormal diffusion metrics values. A: Anterior thalamocortical tracts. II: Inferior thalamocortical tracts projecting to the insular cortex. IT: inferior thalamocortical tracts projecting to the temporal lobe. PO: Posterior thalamocortical tracts projecting to the occipital lobe.*

PP: Posterior thalamocortical tracts projecting to the parietal lobe. S: Superior thalamocortical tracts.

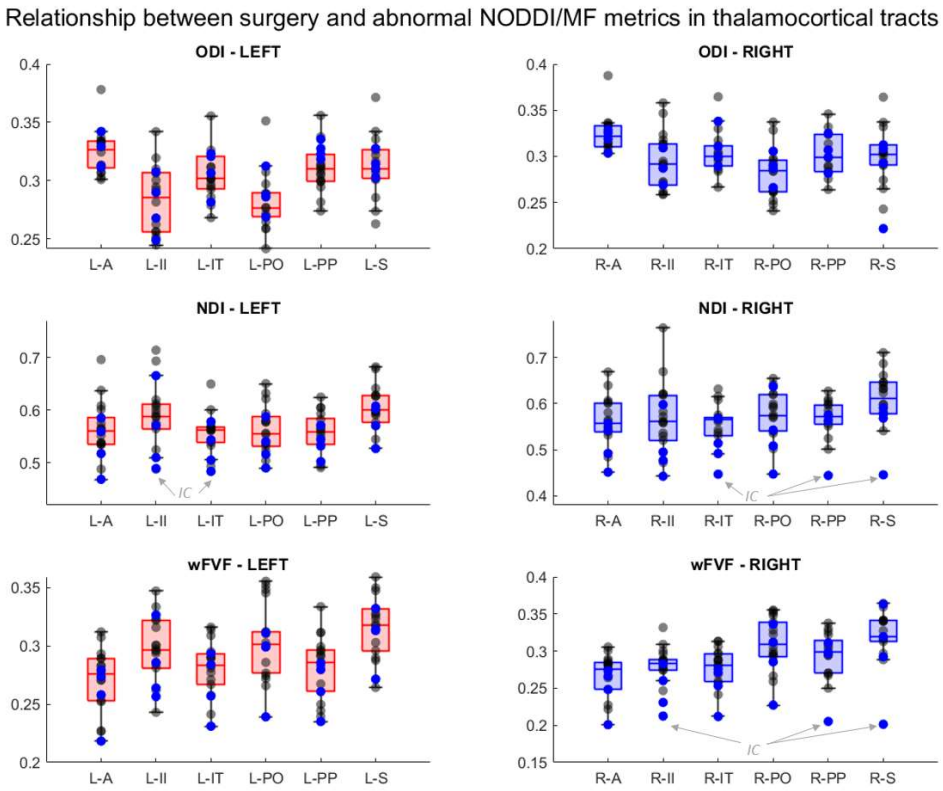

Figure S8.2B *- Evaluation of a potential relationship between surgery and abnormal NODDI/MF values. Boxplots of NODDI/MF values in subsegments of thalamocortical tracts for all patients included in* ***Study 4****. Red boxplots: metrics evaluated in the left subsegments of thalamocortical tracts. Blue boxplots: metrics evaluated in the right subsegments of thalamocortical tracts. Blue points: patients who had surgery (all localized in the right hemisphere). IC: Investigated Case – a patient who had surgery and showed several abnormal diffusion metrics. A: Anterior thalamocortical*

tracts. II: Inferior thalamocortical tracts projecting to the insular cortex. IT: inferior thalamocortical tracts projecting to the temporal lobe. PO: Posterior thalamocortical tracts projecting to the occipital lobe. PP: Posterior thalamocortical tracts projecting to the parietal lobe. S: Superior thalamocortical tracts.

Investigated case

Generalities	Male - 24 years old (at the time of the realization of ***Study 4***) – Right-handed – IQ: 48.
Epilepsy description	The patient has been diagnosed with epilepsy when he was 7 years old. The patient suffers from refractory epilepsy due to a right frontal dysplastic lesion. The epilepsy is evolving into Lennox-Gastaut syndrome. The patient presents generalized seizures (tonic-clonic seizures and atonic seizures) and occasionally focal seizures with a motor onset. Interictally, EEG findings revealed slow diffuse spikes with an anterior predominance and spikes or poly-spikes with a right prefrontal predominance.
Medical history: surgery, imaging findings, and VNS	A first comprehensive examination, including EEG recordings (19 electrodes: FP1, FP2, F3, F4, F7, F8, T3, T4, T5, T6, C3, C4, P3, P4, O1, O2, Fz, Cz, Pz), MRI (SIGNA 1.5 T, GE and ACHIEVA 3T, Philips), and PET acquisition (injection of fluorodeoxyglucose, Siemens HR+), was realized after having experienced a first episode resembling an epileptic seizure. No anomalies were found on the MRI: normal myelination, no gyration or migration disorder, no dysplasia, no mesial sclerosis, no cavernoma, no acquired cortical lesion, and no tumoral lesion. Spectroscopy revealed normal pics and the absence of lactate. The EEG examination revealed epileptiform activity in the right temporal region, which is increased during sleep. The PET examination revealed an asymmetry with hypometabolism in the right

hemisphere, more specifically, the right frontal and temporal regions. A hypometabolism was also found in the right thalamus.

The patient underwent a right frontal cortectomy (14 years before the realization of ***Study 4***).

Histological investigations of the resected area revealed reactional gliosis at the level of white matter (confirmed with the presence of glial fibrillary acidic protein – GFAP) and perivascular lesions (with hemosiderin deposits). Moreover, this analysis revealed cortical dysplasia with neurons present in the molecular layer and neuronal grouping (confirmed with the immunohistochemical examination of neuronal nuclear protein – NeuN).

One year after the surgery, the patient was implanted with a VNS device, as no effect was observed following the surgery. The patient did not show a positive effect with VNS.

A new presurgical evaluation was realized ten years after the first surgery due to the lack of response to VNS.

An MRI was realized and revealed bilateral hemorrhagic sequelae (more important on the left side than the right side) at the base of the frontal lobe and in the left temporal lobe. The right frontal cavity at the resected zone and a gliotic scar were highlighted and established as potentially epileptogenic factors. A PET scan (injection of fluorodeoxyglucose – Gemini TF64 – Philips system) revealed a right frontal hypometabolism outside of the resected zone, anteriorly to the cavity, and in the superior part of the right occipital cortex. Moreover, a metabolic asymmetry was found in the thalamus, with a hypometabolism mainly found on the right side (**Figure S8.2C**). An EEG source imaging analysis (Epilog®) was conducted and revealed a principal localization of the epileptogenic focus in the right frontal region, anteriorly and inferiorly on the edge of the resected zone and right anterior insula. A secondary cluster was detected on the

	right temporal lobe. Based on these findings, a right frontal disconnection, including the Supplementary Motor Area (SMA) and right inferior frontal gyrus BA 44 (2.5 years before the realization of ***Study 4***), was performed. At the same time, the VNS device was explanted, as the patient did not show a positive effect from VNS therapy (the patient has been implanted for 119 months in total).
Number of ASMs	At the time ***Study 4*** was realized, the patient was taking four ASMs daily: Depakine Chrono twice a day (500 mg/750 mg), Inovelon (800 mg, twice a day), Taloxa (900 mg, twice a day), and Topamax (125 mg, twice a day). The patient does not take benzodiazepines.

Table S8.2A*: Clinical history and description of the investigated case (patient showing outlier values for an array of diffusion MRI metrics).*

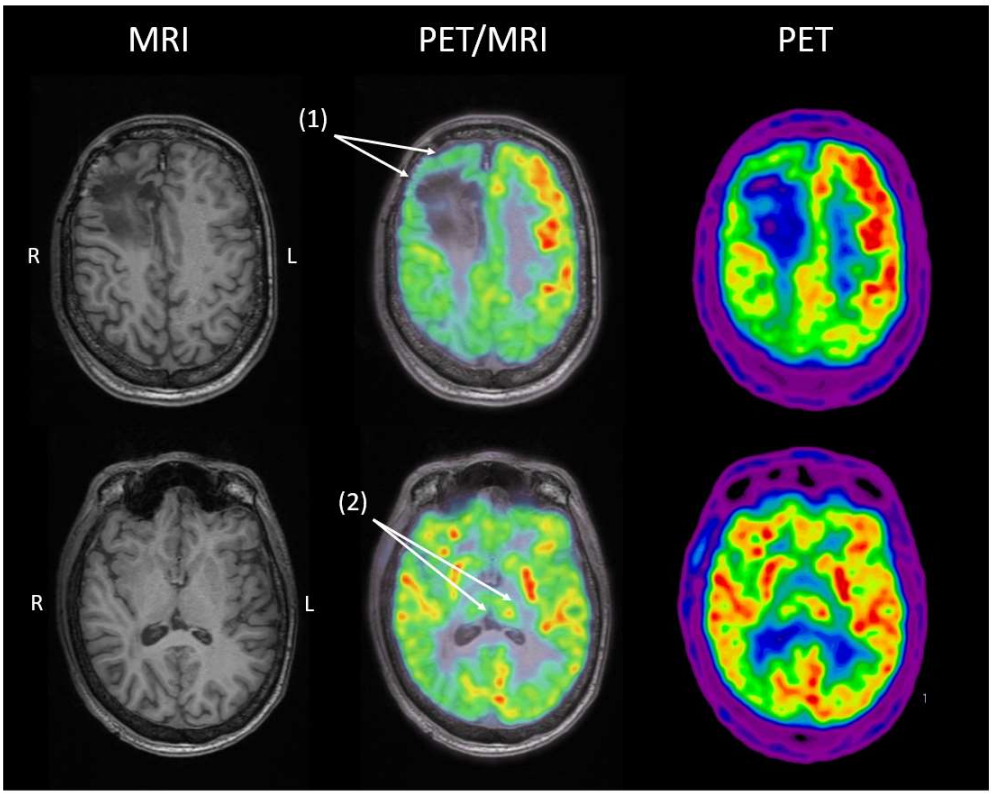

Figure S8.2C *– Results of the pre-operative PET examination (before second brain surgery). (1) Hypometabolism in the right frontal area anterior to the resected zone. (2) Hypometabolism in the right thalamus. R: right. L: left. Radiological convention for the orientation of the images.*

Segments of thalamocortical tracts with a mask corresponding to the resected region are shown in **Figure S8.3C**. The right anterior thalamocortical tracts are in the vicinity of the resected region and could have suffered from axonal transection.

Tractography of the left and right anterior thalamocortical tracts are respectively characterized by a number of tracts of 11 111 (left) - 18 020 (right), a mean length of 66.52 mm (left) - 35.45 mm (right), a volume of 33

012 mm^3 (left) - 22 245 mm^3 (right). While lower mean length and volume are found and were expected on the side of the surgical procedure, tractography of the right anterior thalamocortical tracts does not seem to be unusual outside of the resected area and was achieved without difficulty. It is important to consider that this patient underwent two surgeries, one at 10 years old and the other at 21 years old. Therefore, the patient may also have benefitted from high brain neuroplasticity as these interventions were realized at an early age. Moreover, the PET scan realized before the second surgery revealed a metabolic asymmetry at the expense of the right side in the thalamus. Moreover, the first PET examination realized before the first surgery already suggested a hypometabolism in the right thalamus. This proves that before the surgery, the thalamocortical network already presented pathological properties, excluding the idea that pathological characteristics of this network may have arisen from the surgical procedure itself. This discussion reinforces the results presented in *Study 4*, suggesting that a relatively good integrity of the thalamocortical network is needed to observe therapeutic efficacy with VNS.

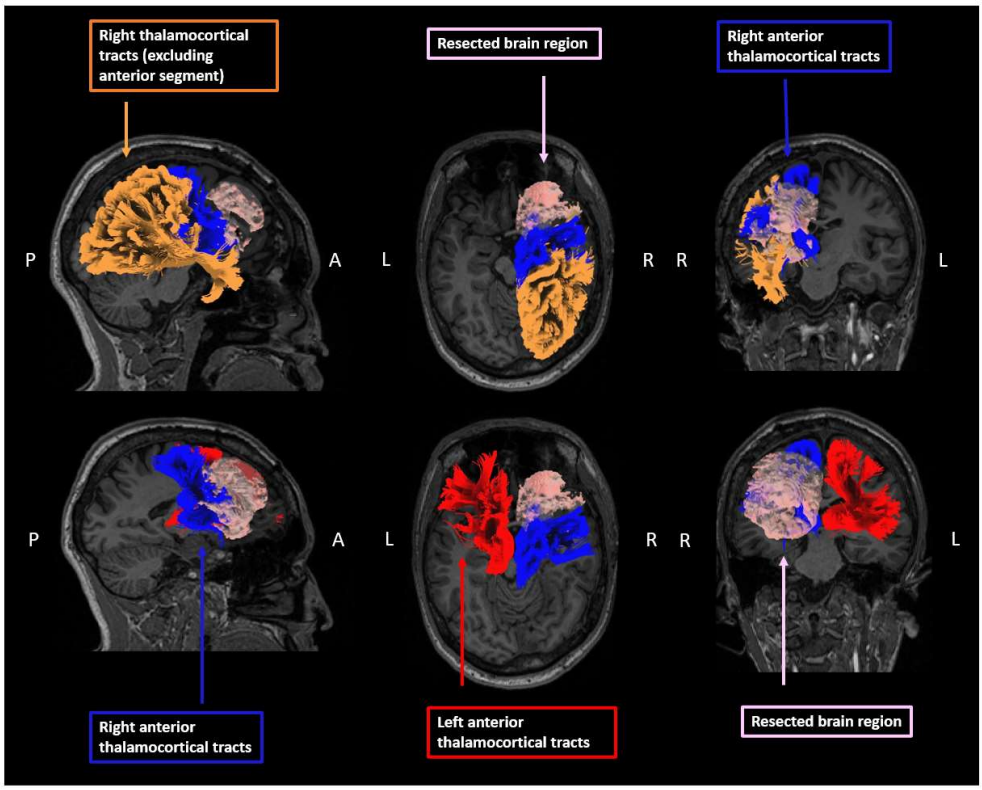

Figure S8.3C – Tractography of thalamocortical tracts in the investigated case (tractography realized in ***Study 4***). Orange: all subsegments of thalamocortical tracts (excluding the anterior portion). Blue: right anterior thalamocortical tracts. Pink: resected brain regions (following the second surgical procedure). Red: left anterior thalamocortical tracts. Neurological convention for the orientation of the images.

The investigated case shows a high MD in left and right thalamocortical tracts, left and right inferior thalamocortical tracts projecting to the insular cortex, right posterior parietal thalamocortical tracts, and right superior thalamocortical tracts compared to the rest of the

cohort of DRE patients. This patient also shows a higher RD in the left and right anterior thalamocortical tracts, right inferior thalamocortical tracts projecting to the insular cortex, left and right inferior thalamocortical tracts projecting to the temporal lobe, right posterior thalamocortical tracts projecting to the parietal lobe, and right superior thalamocortical tracts, compared to other patients. Finally, looking at the NODDI and MF metrics, this patient tends to show a lower NDI in the left inferior thalamocortical tracts projecting to the insular cortex, left and right inferior thalamocortical tracts projecting to the temporal lobe, right posterior thalamocortical tracts projecting to the parietal lobe, and right superior thalamocortical tracts.

Abnormal diffusion values seem to be more marked on the right side, corresponding to the surgery side. Nevertheless, discerning between the impacts of the surgical procedure and the inherent effects of seizures, potentially more prominent on the right side, presents a complex challenge. However, knowing that abnormal diffusion metrics are also found in the left side – the contralateral side of the surgery, and knowing that no change in MD and RD has been previously reported in the contralateral side of the surgery, this could show that the patient present overall lower integrity in thalamocortical tracts bilaterally, and may not be linked to the surgical procedure itself. In fact, we could expect improved integrity in the tracts that are not in the vicinity of the resected area – and, therefore, the contralateral side - as a marker of reduced seizure activity following the second surgical procedure. Finally, studies assessing the effects of surgical procedures on diffusion metrics reported reduced FA in the vicinity of the resected zone. No outlier FA values were found for the investigated case in any subsegments of thalamocortical tracts.

Taking together the clinical examinations presented above and the supplementary analysis of diffusion metrics, we do not expect the abnormal diffusion metrics to be specifically related to the surgical procedure in *Study 4*. Indeed, the intricate pathology in this patient may

explain the overall lower integrity of the thalamocortical tracts found, which may also explain the absence of therapeutic efficacy with VNS, as suggested by the results of *Study 4*.

PUBLICATIONS AND CONFERENCES

1. How is the norepinephrine system involved in the antiepileptic effects of vagus nerve stimulation ? **A. Berger**, S. Vespa, L. Dricot, M. Dumoulin, E. Iachim, P. Doguet, G. Vandewalle, R. El Tahry. *Frontiers in neuroscience 15:790943, 2021. doi: 10.3389/fnins.2021.790943.*

2. Vagus nerve stimulation-induced laryngeal motor evoked potentials for response prediction and intensity titration in drug-resistant epilepsy. **A. Berger**, E. Carapancea, S. Vespa, V. Danthine, P. Doguet, J. Delbeke, A. Nonclercq, R. El Tahry. *Clinical Neurophysiology 147, 2023. doi : 10.1016/j.clinph.2023.01.009.*

3. Structural and functional characterization of the locus coeruleus in young and late middle-aged individuals. **A. Berger**, E. Koshmanova, E. Beckers, R. Sharifpour, I. Paparella, I. Campbell, N. Mortazavi, F. Balda, Y.J. Yi, L. Lamalle, L. Dricot, C. Phillips, H. IL. Jacobs, P. Talwar, R. El Tahry, S. Sherif, G. Vandewalle. *Frontiers in neuroimaging 2:1207844, 2023. doi: 10.3389/fnimg.2023.1207844.*

4. Locus coeruleus activity while awake is associated with REM sleep quality in older individuals. E. Koshmanova, **A. Berger**, E. Beckers, I. Campbell, N. Mortazavi, R. Sharifpour, I. Paparella, F. Balda, C. Berthomier, C. Degueldre, E. Salmon, L. Lamalle, C. Bastin, M. Van Egroo, C. Phillips, P. Maquet, F. Collette, V. Muto, D. Chylinski, H. IL. Jacobs, P. Talwar, S. Sherif, G. Vandewalle. *JCI Insight, 2023. doi: 10.1172/jci.insight.172008.*

5. Light modulates task-dependent thalamo-cortical connectivity during an auditory attentional task. I. Paparella, I. Campbell, R. Sharifpour, E. Beckers, **A. Berger**, J.F. Balda Aizpurua, E. Koshmanova, N. Mortazavi, P. Talwar, C. Degueldre, L. Lamalle, S. Sherif, C. Phillips, P. Maquet, G. Vandewalle. *Communication Biology 6:945, 2023. doi : 10.1038/s42003-023-05337-5.*

6. MRI-assessed locus coeruleus integrity is linked to responsiveness to vagus nerve stimulation in patients with drug-resistant epilepsy. **A. Berger**, V. Danthine, S. Vespa, M. Dumoulin, L. Stumpp, E. Beckers, G. Duchêne, L. Dricot, G. Vandewalle, R. El Tahry. *14th European Epilepsy Congress*, Geneva, Switzerland, 9-13 July 2022, poster presentation.

7. Effect of vagus nerve stimulation therapy on MRI-assessed locus coeruleus integrity in patients with drug-resistant epilepsy. **A. Berger**, E. Beckers, V. Danthine, G. Duchêne, L. Dricot, G. Vandewalle. *35th International Epilepsy Congress*, Dublin, Ireland, 2-6 September 2023, poster presentation.

8. Impact of repeated short light exposures on sustained pupil responses in an fMRI environment. E. Beckers, I. Campbell, R. Sharifpour, I. Paparella, **A. Berger**, J. Fermin Balda Aizpurua, E. Koshmanova, N. Mortazavi, P. Talwar, S. Sherif, H. I.L. Jacobs, G. Vandewalle. *Journal of Sleep Research, 2023; e14085. doi : 10.1111/jsr.14085.*

9. Impact of light on task-evoked pupil responses during cognitive tasks. I. Campbell, E. Beckers, R. Sharifpour, **A. Berger**, I. Paparella, J. Fermin Balda Aizpurua, E. Koshmanova, N. Mortazavi, S. Sherif, G. Vandewalle. *Journal of Sleep Research*, 2023; e14101. *doi : 10.1111/jsr.14101*.

10. Functional response of the locus coeruleus and integrity of its connections with the hippocampus are associated with vagus nerve stimulation response in drug-resistant epilepsy. **A. Berger**, E. Beckers, V. Joris, G. Duchêne, V. Danthine, N. Delinte, B. Macq, L. Dricot, G. Vandewalle, R. El Tahry. *American Epilepsy Congress Annual Meeting*, Orlando, United States, 1-5 December 2023, poster presentation.

11. Locus coeruleus features are linked to vagus nerve stimulation response in drug-resistant epilepsy. **A. Berger**, E. Beckers, V. Joris, G. Duchêne, V. Danthine, N. Delinte, I. Cakiroglu, S. Sherif, E.I. Germany Morrison, A.T. Sánchez, B. Macq, L. Dricot, G. Vandewalle and R. El Tahry. *Frontiers in Neuroscience – Brain Imaging Methods, 2024;* 18:1296161. *doi: 10.3389/fnins.2024.1296161*

12. Regional response to light illuminance across the human hypothalamus. I Campbell, R. Sharifpour, J.F. Balda, E. Beckers, I. Paparella, **A. Berger**, E. Koshmanova, N. Mortazavi, F. Collette, S. Sherif, C. Phillips, L. Lamalle, G. Vandewalle. *eLife, 2024*. *doi : 10.7554/eLife.96576.2.sa4*.

13. Development of a method and tool for utilizing functional MRI to identify vagus nerve stimulation parameters that maximize therapeutic response to an optoelectronic neurostimulator. **A. Berger**, C. Léonard, A. Nieuwenhuys, S. Den Haene, J. Garnier, G. Vandewalle, R. El Tahry. *International Neuromodulation Society*, Vancouver, Canada, 11-16 May 2024, poster presentation.

14. Identifying responders to vagus nerve stimulation based on microstructural features of thalamocortical tracts in drug-resistant epilepsy. **A. Berger**, M. Cerra, V. Joris, V. Danthine, B. Macq, L. Dricot, G. Vandewalle, N. Delinte, R. El Tahry. Neurotherapeut*ics, in press (2024)*.

15. Exposure to light modulates the activity of the medial amygdala during emotional processing. I. Campbell, J.F. Balda, R. Sharifpour, I. Paparella, N. Mortazavi, E. Beckers, **A. Berger**, E. Koshmanova, J. Read, C. Phillips, F. Collette, S. Sherif, P. Talwar, M. Zubkov, L. Lamalle, G. Vandewalle. *Under review (2024)*.

16. Electroencephalogram synchronization measure as a predictive biomarker of vagus nerve stimulation response in refractory epilepsy: a retrospective study. V. Danthine, L. Cottin, **A. Berger**, E.I. Germany, G. Liberati, S. Ferrao Santos, J. Delbeke, A. Nonclercq, R. El Tahry. *PLOS One, 2024*; 19(6):e0304115. *doi : 10.1371/journal.pone.0304115*.

17. REM sleep quality is associated with balanced tonic activity of the locus coeruleus during wakefulness. N. Mortazavi, P. Talwar, E. Koshmanova, R. Sharifpour, E. Beckers, **A. Berger**, I. Campbell, I. Paparella, F. Balda, I. Dardour Hamzaoui, C. Berthomier, C. Bastin, C. Phillips, P. Maquet, F. Collette, M. Zubkov, L. Lamalle, G. Vandewalle. *Under review (2024)*.

BIBLIOGRAPHY

1. Kaculini CM, Tate-Looney AJ, Seifi A. The History of Epilepsy: From Ancient Mystery to Modern Misconception. Cureus. 2021 Mar 17;

2. Reynolds EH. Atlas: Epilepsy Care in the World. World Health Organization Press. Geneva: World Health Organization and International Bureau for Epilepsy (IBE) and International League Against Epilepsy, (ILAE); 2005.

3. Fiest KM, Sauro K.M., Wiebe S, Patten SB, Kwon CS, Dykeman J, et al. Prevalence and incidence of epilepsy. Neurology. 2017;88(3):296–303.

4. Brodie MJ, Barry SJE, Bamagous GA, Norrie JD, Kwan P. Patterns of treatment response in newly diagnosed epilepsy. Neurology. 2012;78(20):1548–54.

5. Fisher RS, Acevedo C, Arzimanoglou A, Bogacz A, Cross JH, Elger CE, et al. ILAE Official Report: A practical clinical definition of epilepsy. Epilepsia. 2014;55(4):475–82.

6. Fisher RS, van Emde Boas W, Blume W, Elger C, Genton P, Lee P, et al. Epileptic Seizures and Epilepsy: Definitions Proposed by the International League Against Epilepsy (ILAE) and the International Bureau for Epilepsy (IBE). Epilepsia. 2005;46(4):470–2.

7. Vera-Gonzalez A. Pathophysiological Mechanisms Underlying the Etiologies of Seizures and Epilepsy. In: J. Czuczwar S, editor. Exon Publications; 2022. p. 1–13. Available from: https://exonpublications.com/index.php/exon/issue/view/epilepsy

8. Egesa IJ, Newton CRJC, Kariuki SM. Evaluation of the International League Against Epilepsy 1981, 1989, and 2017 classifications of seizure semiology and etiology in a population-based cohort of children and adults with epilepsy. Epilepsia Open. 2022 Mar 29;7(1):98–109.

9. Falco-Walter JJ, Scheffer IE, Fisher RS. The new definition and classification of seizures and epilepsy. Epilepsy Res. 2018 Jan 1;139:73–9.

10. Walker MC. Hippocampal sclerosis: Causes and prevention. Semin Neurol. 2015 Jun 12;35(3):193–200.

11. El Achkar CM, Olson HE, Poduri A, Pearl PL. The Genetics of the Epilepsies. Curr Neurol Neurosci Rep. 2015 Jul 27;15(7).

12. Wang J, Lin ZJ, Liu L, Xu HQ, Shi YW, Yi YH, et al. Epilepsy-associated genes. Seizure. 2017 Jan 1;44:11–20.

13. Garg RK. HIV medicine HIV infection and seizures. Postgrad Med J. 1999;75(885):387–90.

14. Ngoungou EB, Bhalla D, Nzoghe A, Dardé ML, Preux PM. Toxoplasmosis and Epilepsy — Systematic Review and Meta Analysis. PLoS Negl Trop Dis. 2015;9(2).

15. Manole AM, Sirbu CA, Mititelu MR, Vasiliu O, Lorusso L, Sirbu OM, et al. State of the Art and Challenges in Epilepsy—A Narrative Review. J Pers Med. 2023 Apr 1;13(4).

16. Scheffer IE, Berkovic S, Capovilla G, Connolly MB, French J, Guilhoto L, et al. ILAE classification of the epilepsies: Position paper of the ILAE Commission for Classification and Terminology. Epilepsia. 2017 Apr 1;58(4):512–21.

17. Löscher W, Klein P. The Pharmacology and Clinical Efficacy of Antiseizure Medications: From Bromide Salts to Cenobamate and Beyond. CNS Drugs. 2021 Sep 1;35(9):935–63.

18. Berg AT, Shinnar S. Relapse following discontinuation of antiepileptic drugs: A meta-analysis. Neurology. 1994;44(4):601–8.

19. Spencer S, Huh L. Outcomes of epilepsy surgery in adults and children. Lancet Neurol. 2008 Jun;7(6):525–37.

20. Sheng J, Liu S, Qin H, Li B, Zhang X. Drug-Resistant Epilepsy and Surgery. Curr Neuropharmacol. 2017 Jun 30;16(1).

21. Hu WH, Zhang C, Zhang K, Meng FG, Chen N, Zhang JG. Selective amygdalohippocampectomy versus anterior temporal lobectomy in the management of mesial temporal lobe epilepsy: A meta-analysis of comparative studies A systematic review. J Neurosurg. 2013 Nov;119(5):1089–97.

22. Oxbury JM. Surgical treatment of epilepsy. In: Principles and Practice of Restorative Neurology. Elsevier; 1992. p. 177–88.

23. Abou-Khalil BW. When Should Corpus Callosotomy be Offered as Palliative Therapy? Epilepsy Curr. 2010 Jan 8;10(1):9–10.

24. Luat AF, Asano E, Kumar A, Chugani HT, Sood S. Corpus Callosotomy for Intractable Epilepsy Revisited: The Children's Hospital of Michigan Series. J Child Neurol. 2017 Jun 1;32(7):624–9.

25. Wong S, Mani R, Danish S. Comparison and Selection of Current Implantable Anti-Epileptic Devices. Neurotherapeutics. 2019 Apr 15;16(2):369–80.

26. Zangiabadi N, Ladino LDi, Sina F, Orozco-Hernández JP, Carter A, Téllez-Zenteno JF. Deep brain stimulation and drug-resistant epilepsy: A review of the literature. Front Neurol. 2019;10(JUN).

27. Frey J, Cagle J, Johnson KA, Wong JK, Hilliard JD, Butson CR, et al. Past, Present, and Future of Deep Brain Stimulation: Hardware, Software, Imaging, Physiology and Novel Approaches. Front Neurol. 2022 Mar 9;13.

28. Li MCH, Cook MJ. Deep brain stimulation for drug-resistant epilepsy. Epilepsia. 2018 Feb 1;59(2):273–90.

29. Kim SH, Lim SC, Kim J, Son BC, Lee KJ, Shon YM. Long-term follow-up of anterior thalamic deep brain stimulation in epilepsy: A 11-year, single center experience. Seizure. 2017 Nov 1;52:154–61.

30. Hartshorn A, Jobst B. Responsive brain stimulation in epilepsy. Vol. 9, Therapeutic Advances in Chronic Disease. SAGE Publications Ltd; 2018. p. 135–42.

31. Razavi B, Rao VR, Lin C, Bujarski KA, Patra SE, Burdette DE, et al. Real-world experience with direct brain-responsive neurostimulation for focal onset seizures. Epilepsia. 2020 Aug 1;61(8):1749–57.

32. Stone SSD, Teixeira CM, de Vito LM, Zaslavsky K, Josselyn SA, Lozano AM, et al. Stimulation of entorhinal cortex promotes adult neurogenesis and facilitates spatial memory. Journal of Neuroscience. 2011 Sep 21;31(38):13469–84.

33. Randall WC, Ardell JL, Becker DM, Randall W, Becker AM. Differential responses accompanying sequential stimulation and ablation of vagal branches to dog heart. The Americal Journal of Physiology [Internet]. 1985;1:133–40. Available from: www.physiology.org/journal/ajpheart

34. Spuck S, Nowak G, Renneberg A, Tronnier V, Sperner J. Right-sided vagus nerve stimulation in humans: An effective therapy? Epilepsy Res. 2008 Dec;82(2–3):232–4.

35. Giordano F, Zicca A, Barba C, Guerrini R, Genitori L. Vagus nerve stimulation: Surgical technique of implantation and revision and related morbidity. Epilepsia. 2017 Apr 1;58:85–90.

36. Pires do Prado HJ, Pinto LF, Bezerra DF, de Paola L, Arruda F, de Oliveira AJ, et al. Predictive factors for successful vagus nerve stimulation in patients with refractory epilepsy: real-life insights from a multicenter study. Front Neurosci [Internet]. 2023 Jul 27;17. Available from: https://www.frontiersin.org/articles/10.3389/fnins.2023.1210221/full

37. Sackeim HA, Rush AJ, George MS, Marangell LB, Husain MM, Nahas Z, et al. Vagus Nerve Stimulation (VNS™) for Treatment-Resistant Depression: Efficacy, Side Effects, and Predictors of Outcome. Neuropsychopharmacology [Internet]. 2001;25(5):713–28. Available from: www.acnp.org/citations/Npp

38. Thompson SL, O'Leary GH, Austelle CW, Gruber E, Kahn AT, Manett AJ, et al. A Review of Parameter Settings for Invasive and Non-invasive Vagus Nerve Stimulation (VNS) Applied in Neurological and Psychiatric Disorders. Front Neurosci. 2021 Jul 13;15.

39. Aalbers M, Vles J, Klinkenberg S, Hoogland G, Majoie M, Rijkers K. Animal models for vagus nerve stimulation in epilepsy. Exp Neurol. 2011 Aug;230(2):167–75.

40. Bonaz B, Sinniger V, Pellissier S. The vagus nerve in the neuro-immune axis: Implications in the pathology of the gastrointestinal tract. Front Immunol. 2017 Nov 2;8(NOV).

41. Vuckovic A, Tosato M, Struijk JJ. A comparative study of three techniques for diameter selective fiber activation in the vagal nerve: anodal block, depolarizing prepulses and slowly rising pulses. J Neural Eng. 2008 Sep 1;5(3):275–86.

42. Yoo PB, Lubock NB, Hincapie JG, Ruble SB, Hamann JJ, Grill WM. High-resolution measurement of electrically-evoked vagus nerve activity in the anesthetized dog. J Neural Eng. 2013 Apr;10(2).

43. Stakenborg N, Gomez-Pinilla PJ, Verlinden TJM, Wolthuis AM, D'Hoore A, Farré R, et al. Comparison between the cervical and abdominal vagus nerves in mice, pigs, and humans. Neurogastroenterology and Motility. 2020 Sep 1;32(9).

44. Groves DA, Brown VJ. Vagal nerve stimulation: A review of its applications and potential mechanisms that mediate its clinical effects. Vol. 29, Neuroscience and Biobehavioral Reviews. Elsevier Ltd; 2005. p. 493–500.

45. McCorry LK. Physiology of the Autonomic Nervous System. Am J Pharm Educ. 2007 Sep;71(4):78.

46. Terui N, Koizumi K. Responses of cardiac vagus and sympathetic nerves to excitation of somatic and visceral nerves. J Auton Nerv Syst. 1984 Apr;10(2):73–91.

47. Noller CM, Levine YA, Urakov TM, Aronson JP, Nash MS. Vagus Nerve Stimulation in Rodent Models: An Overview of Technical Considerations. Front Neurosci. 2019 Sep 4;13.

48. Ruffoli R, Giorgi FS, Pizzanelli C, Murri L, Paparelli A, Fornai F. The chemical neuroanatomy of vagus nerve stimulation. J Chem Neuroanat. 2011 Dec;42(4):288–96.

49. Woodbury DM, Woodbury JW. Effects of Vagal Stimulation on Experimentally Induced Seizures in Rats. Epilepsia. 1990 Jun;31(s2):S7–19.

50. Krahl SE, Senanayake SS, Handforth A. Destruction of peripheral C-fibers does not alter subsequent vagus nerve stimulation-induced seizure suppression in rats. Epilepsia. 2001;42(5):586–9.

51. McAllen RM, Shafton AD, Bratton BO, Trevaks D, Furness JB. Calibration of thresholds for functional engagement of vagal A, B and C fiber groups in vivo . Bioelectron Med (Lond). 2018 Jan;1(1):21–7.

52. Smets H, Stumpp L, Julémont N, Cury J, Debelle A, Innocenti B, et al. Analysing vagus nerve spontaneous activity using finite element modelling. J Neural Eng. 2021 Feb 15;

53. Chang YC, Cracchiolo M, Ahmed U, Mughrabi I, Gabalski A, Daytz A, et al. Quantitative estimation of nerve fiber engagement by vagus nerve stimulation using physiological markers. Brain Stimul. 2020 Nov 1;13(6):1617–30.

54. Koo B, Ham SD, Sood S, Tarver B. Human Vagus Nerve Electrophysiology. Journal of Clinical Neurophysiology. 2001 Sep;18(5):429–33.

55. Fornai F, Ruffoli R, Giorgi FS, Paparelli A. The role of locus coeruleus in the antiepileptic activity induced by vagus nerve stimulation. European Journal of Neuroscience. 2011 Jun;33(12):2169–78.

56. Keren NI, Lozar CT, Harris KC, Morgan PS, Eckert MA. In vivo mapping of the human locus coeruleus. Neuroimage. 2009 Oct;47(4):1261–7.

57. Aston-Jones G, Ennis M, Pieribone VA, Nickell WT, Shipley MT. The Brain Nucleus Locus Coeruleus: Restricted Afferent Control of a Broad Efferent Network. Science (1979). 1986 Nov 7;234(4777):734–7.

58. Loughlin SE, Foote SL, Fallon JH. Locus coeruleus projections to cortex: Topography, morphology and collateralization. Brain Res Bull. 1982 Jul;9(1–6):287–94.

59. Berridge CW, Waterhouse BD. The locus coeruleus–noradrenergic system: modulation of behavioral state and state-dependent cognitive processes. Brain Res Rev. 2003 Apr;42(1):33–84.

60. Waterhouse BD, Woodward DJ. Interaction of norepinephrine with cerebrocortical activity evoked by stimulation of somatosensory afferent pathways in the rat. Exp Neurol. 1980 Jan;67(1):11–34.

61. Aston-Jones G, Cohen JD. An Integrative Theory of Locus Coeruleus-Norepinephrine Function: Adaptive Gain and Optimal Performance. Annu Rev Neurosci. 2005 Jul 21;28(1):403–50.

62. Aston-Jones G, Shipley MT, Chouvet G, Ennis M, van Bockstaele E, Pieribone V, et al. Afferent regulation of locus coeruleus neurons: anatomy, physiology and pharmacology. In 1991. p. 47–75.

63. Luppi PH, Aston-Jones G, Akaoka H, Chouvet G, Jouvet M. Afferent projections to the rat locus coeruleus demonstrated by retrograde and anterograde tracing with cholera-toxin B subunit and Phaseolus vulgaris leucoagglutinin. Neuroscience. 1995 Mar;65(1):119–60.

64. Ennis M, Aston-Jones G. GABA-mediated inhibition of locus coeruleus from the dorsomedial rostral medulla. The Journal of Neuroscience. 1989 Aug 1;9(8):2973–81.

65. Ennis M, Aston-Jones G, Shiekhattar R. Activation of locus coeruleus neurons by nucleus paragigantocellularis or noxious sensory stimulation is mediated by

intracoerulear excitatory amino acid neurotransmission. Brain Res. 1992 Dec;598(1–2):185–95.

66. Fanselow EE, Reid AP, Nicolelis MAL. Reduction of Pentylenetetrazole-Induced Seizure Activity in Awake Rats by Seizure-Triggered Trigeminal Nerve Stimulation. The Journal of Neuroscience. 2000 Nov 1;20(21):8160–8.

67. DeGiorgio CM, Shewmon DA, Whitehurst T. Trigeminal nerve stimulation for epilepsy. Neurology. 2003 Aug 12;61(3):421–2.

68. Luo PF, Wang BR, Peng ZZ, Li JS. Morphological characteristics and terminating patterns of masseteric neurons of the mesencephalic trigeminal nucleus in the rat: An intracellular horseradish peroxidase labeling study. J Comp Neurol. 1991 Jan 8;303(2):286–99.

69. Allen G V., Barbrick B, Esser MJ. Trigeminal-parabrachial connections: possible pathway for nociception-induced cardiovascular reflex responses. Brain Res. 1996 Apr;715(1–2):125–35.

70. Schrader LM, Cook IA, Miller PR, Maremont ER, DeGiorgio CM. Trigeminal nerve stimulation in major depressive disorder: First proof of concept in an open pilot trial. Epilepsy & Behavior. 2011 Nov;22(3):475–8.

71. Jiao J, Jensen W, Harreby KR, Lykholt LE. The Effect of Spinal Cord Stimulation on Epileptic Seizures Suppression. Biomedical Engineering / Biomedizinische Technik. 2013 Jan 7;

72. Song Z, Ansah OB, Meyerson BA, Pertovaara A, Linderoth B. Exploration of supraspinal mechanisms in effects of spinal cord stimulation: Role of the locus coeruleus. Neuroscience. 2013 Dec;253:426–34.

73. Krahl SE, Clark KB, Smith DC, Browning RA. Locus Coeruleus Lesions Suppress the Seizure-Attenuating Effects of Vagus Nerve Stimulation. Epilepsia. 1998 Jul;39(7):709–14.

74. Castel-Branco MM, Alves GL, Figueiredo IV, Falcao AC, Caramona MM. The maximal electroshock seizure (MES) model in the preclinical assessment of potential new antiepileptic drugs. Methods Find Exp Clin Pharmacol. 2009;31(2):101.

75. Groves DA, Bowman EM, Brown VJ. Recordings from the rat locus coeruleus during acute vagal nerve stimulation in the anaesthetised rat. Neurosci Lett. 2005 May;379(3):174–9.

76. Dorr AE, Debonnel G. Effect of Vagus Nerve Stimulation on Serotonergic and Noradrenergic Transmission. Journal of Pharmacology and Experimental Therapeutics. 2006 Aug;318(2):890–8.

77. Manta S, Dong J, Debonnel G, Blier P. Enhancement of the function of rat serotonin and norepinephrine neurons by sustained vagus nerve stimulation. J Psychiatry Neurosci. 2009 Jul;34(4):272–80.

78. Shen H, Fuchino Y, Miyamoto D, Nomura H, Matsuki N. Vagus nerve stimulation enhances perforant path-CA3 synaptic transmission via the activation of β-adrenergic receptors and the locus coeruleus. Int J Neuropsychopharmacol. 2012 May 17;15(04):523–30.

79. Naritoku DK, Terry WJ, Helfert RH. Regional induction of fos immunoreactivity in the brain by anticonvulsant stimulation of the vagus nerve. Epilepsy Res. 1995 Sep;22(1):53–62.

80. Cunningham JT, Mifflin SW, Gould GG, Frazer A. Induction of c-Fos and ΔFosB Immunoreactivity in Rat Brain by Vagal Nerve Stimulation. Neuropsychopharmacology. 2008 Jul 24;33(8):1884–95.

81. Bagdy G, Kecskemeti V, Riba P, Jakus R. Serotonin and epilepsy. J Neurochem. 2007 Feb;100(4):857–73.

82. Baraban JM, Aghajanian GK. Suppression of firing activity of 5-HT neurons in the dorsal raphe by alpha-adrenoceptor antagonists. Neuropharmacology. 1980 Apr;19(4):355–63.

83. Elliott RE, Morsi A, Tanweer O, Grobelny B, Geller E, Carlson C, et al. Efficacy of vagus nerve stimulation over time: Review of 65 consecutive patients with treatment-resistant epilepsy treated with VNS >10years. Epilepsy & Behavior. 2011 Mar;20(3):478–83.

84. Roosevelt RW, Smith DC, Clough RW, Jensen RA, Browning RA. Increased extracellular concentrations of norepinephrine in cortex and hippocampus following vagus nerve stimulation in the rat. Brain Res. 2006 Nov;1119(1):124–32.

85. Follesa P, Biggio F, Gorini G, Caria S, Talani G, Dazzi L, et al. Vagus nerve stimulation increases norepinephrine concentration and the gene expression of BDNF and bFGF in the rat brain. Brain Res. 2007 Nov;1179:28–34.

86. Raedt R, Clinckers R, Mollet L, Vonck K, El Tahry R, Wyckhuys T, et al. Increased hippocampal noradrenaline is a biomarker for efficacy of vagus nerve stimulation in a limbic seizure model. J Neurochem. 2011 May;117(3):461–9.

87. Manta S, El Mansari M, Debonnel G, Blier P. Electrophysiological and neurochemical effects of long-term vagus nerve stimulation on the rat monoaminergic systems. International Journal of Neuropsychopharmacology. 2013 Mar 1;16(2):459–70.

88. Collins L, Boddington L, Steffan PJ, McCormick D. Vagus nerve stimulation induces widespread cortical and behavioral activation. Current Biology. 2021 May;31(10):2088-2098.e3.

89. Curet O, de Montigny C. Electrophysiological characterization of adrenoceptors in the rat dorsal hippocampus. I. Receptors mediating the effect of microiontophoretically applied norepinephrine. Brain Res. 1988 Dec;475(1):35–46.

90. Hulsey DR, Riley JR, Loerwald KW, Rennaker RL, Kilgard MP, Hays SA. Parametric characterization of neural activity in the locus coeruleus in response to vagus nerve stimulation. Exp Neurol. 2017 Mar;289:21–30.

91. Castoro MA, Yoo PB, Hincapie JG, Hamann JJ, Ruble SB, Wolf PD, et al. Excitation properties of the right cervical vagus nerve in adult dogs. Exp Neurol. 2011 Jan;227(1):62–8.

92. Agnew WF, McCreery DB, Yuen TGH, Bullara LA. Histologic and physiologic evaluation of electrically stimulated peripheral nerve: Considerations for the selection of parameters. Ann Biomed Eng. 1989 Jan;17(1):39–60.

93. Mridha Z, de Gee JW, Shi Y, Alkashgari R, Williams J, Suminski A, et al. Graded recruitment of pupil-linked neuromodulation by parametric stimulation of the vagus nerve. Nat Commun. 2021 Mar 9;12(1):1539.

94. Revesz D, Tjernstrom M, Ben-Menachem E, Thorlin T. Effects of vagus nerve stimulation on rat hippocampal progenitor proliferation. Exp Neurol. 2008 Dec;214(2):259–65.

95. Kulkarni VA, Jha S, Vaidya VA. Depletion of norepinephrine decreases the proliferation, but does not influence the survival and differentiation, of granule cell progenitors in the adult rat hippocampus. European Journal of Neuroscience. 2002 Nov;16(10):2008–12.

96. Malberg JE, Eisch AJ, Nestler EJ, Duman RS. Chronic Antidepressant Treatment Increases Neurogenesis in Adult Rat Hippocampus. The Journal of Neuroscience. 2000 Dec 15;20(24):9104–10.

97. Laxer KD, Sourkes TL, Fang TY, Young SN, Gauthier SG, Missala K. Monoamine metabolites in the CSF of epileptic patients. Neurology. 1979 Aug 1;29(8):1157–1157.

98. De Taeye L, Vonck K, van Bochove M, Boon P, Van Roost D, Mollet L, et al. The P3 Event-Related Potential is a Biomarker for the Efficacy of Vagus Nerve Stimulation in Patients with Epilepsy. Neurotherapeutics. 2014 Jul 8;11(3):612–22.

99. Hammond EJ, Uthman BM, Reid SA, Wilder BJ. Electrophysiologic Studies of Cervical Vagus Nerve Stimulation in Humans: II. Evoked Potentials. Epilepsia. 1992 Nov;33(6):1021–8.

100. Brazdil M, Chadim P, Daniel P, Kuba R, Rektor I, Novak Z, et al. Effect of vagal nerve stimulation on auditory and visual event-related potentials. Eur J Neurol. 2001 Sep 18;8(5):457–61.

101. Nieuwenhuis S, Aston-Jones G, Cohen JD. Decision making, the P3, and the locus coeruleus--norepinephrine system. Psychol Bull. 2005;131(4):510–32.

102. Wostyn S, Staljanssens W, De Taeye L, Strobbe G, Gadeyne S, Van Roost D, et al. EEG Derived Brain Activity Reflects Treatment Response from Vagus Nerve Stimulation in Patients with Epilepsy. Int J Neural Syst. 2017 Jun 10;27(04):1650048.

103. Hödl S, Carrette S, Meurs A, Carrette E, Mertens A, Gadeyne S, et al. Neurophysiological investigations of drug resistant epilepsy patients treated with vagus nerve stimulation to differentiate responders from non-responders. Eur J Neurol. 2020 Jul 19;27(7):1178–89.

104. Joshi S, Li Y, Kalwani RM, Gold JI. Relationships between Pupil Diameter and Neuronal Activity in the Locus Coeruleus, Colliculi, and Cingulate Cortex. Neuron. 2016 Jan;89(1):221–34.

105. Murphy PR, O'Connell RG, O'Sullivan M, Robertson IH, Balsters JH. Pupil diameter covaries with BOLD activity in human locus coeruleus. Hum Brain Mapp. 2014 Aug 7;35(8):4140–54.

106. Desbeaumes Jodoin V, Lespérance P, Nguyen DK, Fournier-Gosselin MP, Richer F. Effects of vagus nerve stimulation on pupillary function. International Journal of Psychophysiology. 2015 Dec;98(3):455–9.

107. Chmielewski WX, Mückschel M, Ziemssen T, Beste C. The norepinephrine system affects specific neurophysiological subprocesses in the modulation of inhibitory control by working memory demands. Hum Brain Mapp. 2017 Jan 13;38(1):68–81.

108. Chamberlain SR, Müller U, Blackwell AD, Clark L, Robbins TW, Sahakian BJ. Neurochemical Modulation of Response Inhibition and Probabilistic Learning in Humans. Science (1979). 2006 Feb 10;311(5762):861–3.

109. Robinson ESJ, Eagle DM, Mar AC, Bari A, Banerjee G, Jiang X, et al. Similar Effects of the Selective Noradrenaline Reuptake Inhibitor Atomoxetine on Three Distinct Forms of Impulsivity in the Rat. Neuropsychopharmacology. 2008 Apr 18;33(5):1028–37.

110. Schevernels H, van Bochove ME, De Taeye L, Bombeke K, Vonck K, Van Roost D, et al. The effect of vagus nerve stimulation on response inhibition. Epilepsy & Behavior. 2016 Nov;64:171–9.

111. Bekker EM, Kenemans JL, Hoeksma MR, Talsma D, Verbaten MN. The pure electrophysiology of stopping. International Journal of Psychophysiology. 2005 Feb;55(2):191–8.

112. Lansbergen MM, Böcker KBE, Bekker EM, Kenemans JL. Neural correlates of stopping and self-reported impulsivity. Clinical Neurophysiology. 2007 Sep;118(9):2089–103.

113. Wessel JR, Aron AR. It's not too late: The onset of the frontocentral P3 indexes successful response inhibition in the stop-signal paradigm. Psychophysiology. 2015 Apr;52(4):472–80.

114. van Bochove ME, De Taeye L, Raedt R, Vonck K, Meurs A, Boon P, et al. Reduced distractor interference during vagus nerve stimulation. International Journal of Psychophysiology. 2018 Jun;128:93–9.

115. Aston-Jones G, Bloom F. Activity of norepinephrine-containing locus coeruleus neurons in behaving rats anticipates fluctuations in the sleep-waking cycle. The Journal of Neuroscience. 1981 Aug 1;1(8):876–86.

116. Siegel JM. REM sleep: A biological and psychological paradox. Sleep Med Rev. 2011 Jun;15(3):139–42.

117. Rizzo P, Beelke M, De Carli F, Canovaro P, Nobili L, Robert A, et al. Chronic Vagus Nerve Stimulation Improves Alertness and Reduces Rapid Eye Movement Sleep in Patients Affected by Refractory Epilepsy. Sleep. 2003 Aug;26(5):607–11.

118. Yang JD, Elphick M, Sharpley AL, Cowen PJ. Effects of carbamazepine on sleep in healthy volunteers. Biol Psychiatry. 1989 Jul;26(3):324–8.

119. Drake ME, Pakalnis A, Bogner JE, Andrews JM. Outpatient Sleep Recording during Antiepileptic Drug Monotherapy. Clinical Electroencephalography. 1990 Jul 27;21(3):170–3.

120. Hallböök T, Lundgren J, Köhler S, Blennow G, Strömblad LG, Rosén I. Beneficial effects on sleep of vagus nerve stimulation in children with therapy resistant epilepsy. European Journal of Paediatric Neurology. 2005 Nov;9(6):399–407.

121. Shaffer F, Ginsberg JP. An Overview of Heart Rate Variability Metrics and Norms. Front Public Health. 2017 Sep 28;5.

122. Malik M, Bigger JT, Camm AJ, Kleiger RE, Malliani A, Moss AJ, et al. Heart rate variability: Standards of measurement, physiological interpretation, and clinical use. Eur Heart J. 1996 Mar 1;17(3):354–81.

123. Fang X, Liu HY, Wang ZY, Yang Z, Cheng TY, Hu CH, et al. Preoperative Heart Rate Variability During Sleep Predicts Vagus Nerve Stimulation Outcome Better in Patients With Drug-Resistant Epilepsy. Front Neurol. 2021 Jul 7;12.

124. Ding JJ, Liu P, Rebernig H, Suller-Marti A, Parrent AG, Burneo JG, et al. Vagus nerve stimulation does not alter brainstem nuclei morphology in patients with refractory epilepsy. Epilepsy & Behavior. 2021 May;118:107940.

125. Yap JYY, Keatch C, Lambert E, Woods W, Stoddart PR, Kameneva T. Critical Review of Transcutaneous Vagus Nerve Stimulation: Challenges for Translation to Clinical Practice. Front Neurosci. 2020 Apr 28;14.

126. Frangos E, Ellrich J, Komisaruk BR. Non-invasive Access to the Vagus Nerve Central Projections via Electrical Stimulation of the External Ear: fMRI Evidence in Humans. Brain Stimul. 2015 May;8(3):624–36.

127. Bauer S, Baier H, Baumgartner C, Bohlmann K, Fauser S, Graf W, et al. Transcutaneous Vagus Nerve Stimulation (tVNS) for Treatment of Drug-Resistant Epilepsy: A Randomized, Double-Blind Clinical Trial (cMPsE02). Brain Stimul. 2016 May;9(3):356–63.

128. Sharon O, Fahoum F, Nir Y. Transcutaneous Vagus Nerve Stimulation in Humans Induces Pupil Dilation and Attenuates Alpha Oscillations. The Journal of Neuroscience. 2021 Jan 13;41(2):320–30.

129. Warren CM, Tona KD, Ouwerkerk L, van Paridon J, Poletiek F, van Steenbergen H, et al. The neuromodulatory and hormonal effects of transcutaneous vagus nerve stimulation as evidenced by salivary alpha amylase, salivary cortisol, pupil diameter, and the P3 event-related potential. Brain Stimul. 2019 May;12(3):635–42.

130. Keute M, Demirezen M, Graf A, Mueller NG, Zaehle T. No modulation of pupil size and event-related pupil response by transcutaneous auricular vagus nerve stimulation (taVNS). Sci Rep. 2019 Aug 7;9(1):11452.

131. Ehlert U, Erni K, Hebisch G, Nater U. Salivary α-Amylase Levels after Yohimbine Challenge in Healthy Men. J Clin Endocrinol Metab. 2006 Dec 1;91(12):5130–3.

132. Warren CM, van den Brink RL, Nieuwenhuis S, Bosch JA. Norepinephrine transporter blocker atomoxetine increases salivary alpha amylase. Psychoneuroendocrinology. 2017 Apr;78:233–6.

133. Hill SA, Taylor MJ, Harmer CJ, Cowen PJ. Acute Reboxetine Administration Increases Plasma and Salivary Cortisol. Journal of Psychopharmacology. 2003 Sep 1;17(3):273–5.

134. Berger A. Quantifying microstructural brain anomalies in patients with Alzheimer's disease via diffusion Magnetic Resonance Imaging [Internet]. 2019. Available from: http://hdl.handle.net/2078.1/thesis:25156

135. Kamiya K, Hori M, Aoki S. NODDI in clinical research. Vol. 346, Journal of Neuroscience Methods. Elsevier B.V.; 2020.

136. Jelescu IO, Veraart J, Fieremans E, Novikov DS. Degeneracy in model parameter estimation for multi-compartmental diffusion in neuronal tissue. NMR Biomed. 2016 Jan 29;29(1):33–47.

137. Rensonnet G, Scherrer B, Girard G, Jankovski A, Warfield SK, Macq B, et al. Towards microstructure fingerprinting: Estimation of tissue properties from a dictionary of Monte Carlo diffusion MRI simulations. Neuroimage. 2019 Jan 1;184:964–80.

138. Sara SJ. The locus coeruleus and noradrenergic modulation of cognition. Vol. 10, Nature Reviews Neuroscience. 2009. p. 211–23.

139. Jacobs HIL, Becker JA, Kwong K, Engels-Domínguez N, Prokopiou PC, Papp K V., et al. In vivo and neuropathology data support locus coeruleus integrity as indicator of Alzheimer's disease pathology and cognitive decline. Sci Transl Med. 2021 Sep 22;13(612).

140. Braak H, Tredici K Del, Rüb U, De Vos RAI, Jansen Steur ENH, Braak E. Staging of brain pathology related to sporadic Parkinson's disease. Vol. 24, Neurobiology of Aging. 2003.

141. García-Lorenzo D, Longo-Dos Santos C, Ewenczyk C, Leu-Semenescu S, Gallea C, Quattrocchi G, et al. The coeruleus/subcoeruleus complex in rapid eye movement sleep behaviour disorders in Parkinson's disease. Brain. 2013;136(7):2120–9.

142. Van Someren J, Altena E, Astill-Schutte R, Benjamins J, Blanken T, Bruijel J, et al. Brain mechanisms of insomnia: new perspectives on causes and consequences. Physiol Rev. 2020;

143. Morris LS, McCall JG, Charney DS, Murrough JW. The role of the locus coeruleus in the generation of pathological anxiety. Brain Neurosci Adv. 2020 Jan;4:239821282093032.

144. Guinea-Izquierdo A, Giménez M, Martínez-Zalacaín I, del Cerro I, Canal-Noguer P, Blasco G, et al. Lower Locus Coeruleus MRI intensity in patients with late-life major depression. PeerJ. 2021 Feb 16;9.

145. Mäki-Marttunen V, Andreassen OA, Espeseth T. The role of norepinephrine in the pathophysiology of schizophrenia. Neurosci Biobehav Rev. 2020 Nov 1;118:298–314.

146. Galgani A, Lombardo F, Latta D Della, Martini N, Bonuccelli U, Fornai F, et al. Locus Coeruleus Magnetic Resonance Imaging in Neurological Diseases. Current Neurology and Neuroscience Report [Internet]. 2021;21(2). Available from: https://doi.org/10.1007/s11910-020-01087-7

147. Watanabe T, Tan Z, Wang X, Martinez-Hernandez A, Frahm J. Magnetic resonance imaging of noradrenergic neurons. Brain Struct Funct. 2019;

148. Betts MJ, Cardenas-Blanco A, Kanowski M, Spottke A, Teipel SJ, Kilimann I, et al. Locus coeruleus MRI contrast is reduced in Alzheimer's disease dementia and correlates with CSF Aβ levels. Alzheimer's and Dementia: Diagnosis, Assessment and Disease Monitoring. 2019 Dec 1;11:281–5.

149. Hansen N. Locus Coeruleus Malfunction Is Linked to Psychopathology in Prodromal Dementia With Lewy Bodies. Front Aging Neurosci. 2021 Mar 1;13.

150. Mithani K, Mikhail M, Morgan BR, Wong S, Weil AG, Deschenes S, et al. Connectomic Profiling Identifies Responders to Vagus Nerve Stimulation. Ann Neurol. 2019 Nov 1;86(5):743–53.

151. Ibrahim GM, Sharma P, Hyslop A, Guillen MR, Morgan BR, Wong S, et al. Presurgical thalamocortical connectivity is associated with response to vagus nerve stimulation in children with intractable epilepsy. Neuroimage Clin. 2017;16:634–42.

152. Yu R, Park HJ, Cho H, Ko A, Pae C, Oh MK, et al. Interregional metabolic connectivity of 2-deoxy-2[18 F]fluoro-D-glucose positron emission tomography in vagus nerve stimulation for pediatric patients with epilepsy: A retrospective cross-sectional study. Epilepsia. 2018 Dec 1;59(12):2249–59.

153. Krahl S. Vagus nerve stimulation for epilepsy: A review of the peripheral mechanisms. Surg Neurol Int. 2012;3(2):47.

154. El Tahry R, Mollet L, Raedt R, Delbeke J, De Herdt V, Wyckhuys T, et al. Repeated assessment of larynx compound muscle action potentials using a self-sizing cuff electrode around the vagus nerve in experimental rats. J Neurosci Methods. 2011 Jun;198(2):287–93.

155. Vespa S, Stumpp L, Bouckaert C, Delbeke J, Smets H, Cury J, et al. Vagus Nerve Stimulation-Induced Laryngeal Motor Evoked Potentials: A Possible Biomarker of Effective Nerve Activation. Front Neurosci. 2019 Aug 27;13.

156. Bouckaert C, Raedt R, Larsen LE, El Tahry R, Gadeyne S, Carrette E, et al. Laryngeal Muscle-Evoked Potential Recording as an Indicator of Vagal Nerve Fiber Activation. Neuromodulation: Technology at the Neural Interface. 2022 Apr;25(3):461–70.

157. Grimonprez A, Raedt R, De Taeye L, Larsen LE, Delbeke J, Boon P, et al. A Preclinical Study of Laryngeal Motor-Evoked Potentials as a Marker Vagus Nerve Activation. Int J Neural Syst. 2015 Dec 20;25(08):1550034.

158. Rijkers K, Aalbers M, Hoogland G, van Winden L, Vles J, Steinbusch H, et al. Acute seizure-suppressing effect of vagus nerve stimulation in the amygdala kindled rat. Brain Res. 2010 Mar;1319:155–63.

159. Boyd IA, Kalu KU. Scaling factor relating conduction velocity and diameter for myelinated afferent nerve fibres in the cat hind limb. J Physiol. 1979 Apr 1;289(1):277–97.

160. Ardesch JJ, Sikken JR, Veltink PH, van der Aa HE, Hageman G, Buschman HPJ. Vagus nerve stimulation for epilepsy activates the vocal folds maximally at therapeutic levels. Epilepsy Res. 2010 May;89(2–3):227–31.

161. Kamani D, Potenza AS, Cernea CR, Kamani Y V., Randolph GW. The nonrecurrent laryngeal nerve: Anatomic and electrophysiologic algorithm for reliable identification. Laryngoscope. 2015 Feb;125(2):503–8.

162. Kayyali H, Abdelmoity S, Bansal L, Kaufman C, Smith K, Fecske E, et al. The Efficacy and Safety of Rapid Cycling Vagus Nerve Stimulation in Children With Intractable Epilepsy. Pediatr Neurol. 2020 Aug;109:35–8.

163. DeGiorgio C, Heck C, Bunch S, Britton J, Green P, Lancman M, et al. Vagus nerve stimulation for epilepsy: Randomized comparison of three stimulation paradigms. Neurology. 2005 Jul 26;65(2):317–9.

164. Heck C, Helmers SL, DeGiorgio CM. Vagus nerve stimulation therapy, epilepsy, and device parameters: Scientific basis and recommendations for use. Neurology. 2002 Sep 24;59(Issue 6, Supplement 4):S31–7.

165. Yamamoto T. Vagus Nerve Stimulation Therapy: Indications, Programing, and Outcomes. Neurol Med Chir (Tokyo). 2015;55(5):407–15.

166. Devanne H, Lavoie BA, Capaday C. Input-output properties and gain changes in the human corticospinal pathway. Exp Brain Res. 1997 Apr 16;114(2):329–38.

167. Hill PD. Kernel estimation of a distribution function. Commun Stat Theory Methods. 1985 Jan 27;14(3):605–20.

168. Pedregosa F, Varoquaux G, Gramfort A, Michel V, Thirion B, Grisel O, et al. Scikit-learn: Machine Learning in Python. Journal of Machine Learning Research [Internet]. 2011;12:2825–30. Available from: http://scikit-learn.sourceforge.net.

169. Loerwald KW, Borland MS, Rennaker RL, Hays SA, Kilgard MP. The interaction of pulse width and current intensity on the extent of cortical plasticity evoked by vagus nerve stimulation. Brain Stimul. 2018 Mar;11(2):271–7.

170. Fahoum F, Boffini M, Kann L, Faini S, Gordon C, Tzadok M, et al. VNS parameters for clinical response in Epilepsy. Brain Stimul. 2022 May;15(3):814–21.

171. Morrison RA, Hulsey DR, Adcock KS, Rennaker RL, Kilgard MP, Hays SA. Vagus nerve stimulation intensity influences motor cortex plasticity. Brain Stimul. 2019 Mar;12(2):256–62.

172. Morrison RA, Danaphongse TT, Abe ST, Stevens ME, Ezhil V, Seyedahmadi A, et al. High intensity VNS disrupts VNS-mediated plasticity in motor cortex. Brain Res. 2021 Apr;1756:147332.

173. Morrison RA, Danaphongse TT, Pruitt DT, Adcock KS, Mathew JK, Abe ST, et al. A limited range of vagus nerve stimulation intensities produce motor cortex reorganization when delivered during training. Behavioural Brain Research. 2020 Aug;391:112705.

174. Pruitt DT, Danaphongse TT, Lutchman M, Patel N, Reddy P, Wang V, et al. Optimizing Dosing of Vagus Nerve Stimulation for Stroke Recovery. Transl Stroke Res. 2021 Feb 25;12(1):65–71.

175. Souza RR, Robertson NM, McIntyre CK, Rennaker RL, Hays SA, Kilgard MP. Vagus nerve stimulation enhances fear extinction as an inverted-U function of stimulation intensity. Exp Neurol. 2021 Jul;341:113718.

176. Liu KY, Acosta-Cabronero J, Cardenas-Blanco A, Loane C, Berry AJ, Betts MJ, et al. In vivo visualization of age-related differences in the locus coeruleus. Neurobiol Aging. 2019 Feb 1;74:101–11.

177. Shibata E, Sasaki M, Tohyama K, Kanbara Y, Otsuka K, Ehara S, et al. Age-related Changes in Locus Ceruleus on Neuromelanin Magnetic Resonance Imaging at 3 Tesla. Vol. 5, Magn Reson Med Sci. 2006.

178. Prokopiou PC, Engels-Domínguez N, Papp K V., Scott MR, Schultz AP, Schneider C, et al. Lower novelty-related locus coeruleus function is associated with Aβ-related cognitive decline in clinically healthy individuals. Nat Commun. 2022 Dec 1;13(1).

179. Juckel G, Karch S, Kawohl W, Kirsch V, Jäger L, Leicht G, et al. Age effects on the P300 potential and the corresponding fMRI BOLD-signal. Neuroimage. 2012 May 1;60(4):2027–34.

180. van Dinteren R, Arns M, Jongsma MLA, Kessels RPC. P300 development across the lifespan: A systematic review and meta-analysis. PLoS One. 2014 Feb 13;9(2).

181. Coblentz JM, Mattis S, Zingesser LH, Kasoff SS, Wisniewski HM, Katzman R. Presenile Dementia Clinical Aspects and Evaluation of Cerebrospinal Fluid Dynamics. Arch Neurol [Internet]. 1973;29(5):299–308. Available from: http://archneur.jamanetwork.com/

182. Folstein MF, Folstein SE, Mchugh PR. "Mini-mental state": A practical method for grading the cognitive state of patients for the clinician. J Psychiatr Res. 1975;12(3):189–98.

183. Beck AT, Steer RA, Carbin MC. Psychometric properties of the Beck Depression Inventory: Twenty-five years of evaluation. Clin Psychol Rev. 1988;8:77–100.

184. Beck AT, Brown G, Epstein N, Steer RA. An Inventory for Measuring Clinical Anxiety: Psychometric Properties. J Consult Clin Psychol. 1988;56(6):893–7.

185. Buysse DJ, Reynolds Ill CF, Monk TH, Berman SR, Kupfer DJ. The Pittsburgh Sleep Quality Index: A New Instrument for Psychiatric Practice and Research. Psychiatry Res. 1988;28:193–5.

186. Osorio-Forero A, Cherrad N, Banterle L, Fernandez LMJ, Lüthi A. When the Locus Coeruleus Speaks Up in Sleep: Recent Insights, Emerging Perspectives. Int J Mol Sci. 2022 May 1;23(9).

187. Gonzalez MMC, Aston-Jones G. Circadian Regulation of Arousal: Role of the Noradrenergic Locus Coeruleus System and Light Exposure. Sleep [Internet]. 2006;29(10):1327–36. Available from: https://academic.oup.com/sleep/article/29/10/1327/2709214

188. Mathôt S, Schreij D, Theeuwes J. OpenSesame: An open-source, graphical experiment builder for the social sciences. Behav Res Methods. 2012 Jun;44(2):314–24.

189. Marques JP, Gruetter R. New Developments and Applications of the MP2RAGE Sequence - Focusing the Contrast and High Spatial Resolution R1 Mapping. PLoS One. 2013 Jul 16;8(7).

190. O'Brien KR, Kober T, Hagmann P, Maeder P, Marques J, Lazeyras F, et al. Robust T1-weighted structural brain imaging and morphometry at 7T using MP2RAGE. PLoS One. 2014 Jun 16;9(6).

191. Avants BB, Tustison NJ, Song G, Cook PA, Klein A, Gee JC. A reproducible evaluation of ANTs similarity metric performance in brain image registration. Neuroimage. 2011 Feb 1;54(3):2033–44.

192. Iglesias JE, Liu CY, Thompson PM, Tu Z. Robust brain extraction across datasets and comparison with publicly available methods. IEEE Trans Med Imaging. 2011 Sep;30(9):1617–34.

193. Yushkevich PA, Gao Y, Gerig G. ITK-SNAP: an interactive tool for semi-automatic segmentation of multi-modality biomedical images [Internet]. 2016. Available from: http://itksnap.org

194. Kasper L, Bollmann S, Diaconescu AO, Hutton C, Heinzle J, Iglesias S, et al. The PhysIO Toolbox for Modeling Physiological Noise in fMRI Data. J Neurosci Methods. 2017 Jan 30;276:56–72.

195. Desikan RS, Ségonne F, Fischl B, Quinn BT, Dickerson BC, Blacker D, et al. An automated labeling system for subdividing the human cerebral cortex on MRI scans into gyral based regions of interest. Neuroimage. 2006 Jul 1;31(3):968–80.

196. Duff EP, Cunnington R, Egan GF. REX: Response exploration for neuroimaging datasets. Neuroinformatics. 2007 Dec;5(4):223–34.

197. Faul F, Erdfelder E, Buchner A, Lang AG. Statistical power analyses using G*Power 3.1: Tests for correlation and regression analyses. Behav Res Methods. 2009;41(4):1149–60.

198. Linden DE, Prvulovic D, Formisano E, Völlinger M., Zanella FE, Goebel R, et al. The functional neuroanatomy of target detection: an fMRI study of visual and auditory oddball tasks. Cerebral Cortex. 1999;9(8):815–23.

199. Kiehl KA, Laurens KR, Duty TL, Forster BB, Liddle PF. An Event-Related fMRI Study of Visual and Auditory Oddball Tasks. J Psychophysiol. 2001;221–40.

200. Kiehl KA, Laurens KR, Duty TL, Forster BB, Liddle PF. Neural sources involved in auditory target detection and novelty processing: An event-related fMRI study. Psychophysiology. 2001;38(1):133–42.

201. Menon V, Ford JM, Lim K.O., Glover GH, Pfefferbaum A. Combined event-related fMRI and EEG evidence for temporal–parietal cortex activation during target detection. Neuroreport. 1997;8:3029–37.

202. Brázdil M, Dobšík M, Mikl M, Hluštík P, Daniel P, Pažourková M, et al. Combined event-related fMRI and intracerebral ERP study of an auditory oddball task. Neuroimage. 2005 May 15;26(1):285–93.

203. Fedorow H, Halliday GM, Rickert CH, Gerlach M, Riederer P, Double KL. Evidence for specific phases in the development of human neuromelanin. Neurobiol Aging. 2006 Mar;27(3):506–12.

204. Zucca FA, Bellei C, Giannelli S, Terreni MR, Gallorini M, Rizzio E, et al. Neuromelanin and iron in human locus coeruleus and substantia nigra during aging: Consequences for neuronal vulnerability. J Neural Transm. 2006 Jun;113(6):757–67.

205. Keren NI, Taheri S, Vazey EM, Morgan PS, Granholm ACE, Aston-Jones GS, et al. Histologic validation of locus coeruleus MRI contrast in post-mortem tissue. Neuroimage. 2015 Jun 1;113:235–45.

206. Betts MJ, Cardenas-Blanco A, Kanowski M, Jessen F, Düzel E. In vivo MRI assessment of the human locus coeruleus along its rostrocaudal extent in young and older adults. Neuroimage. 2017 Dec 1;163:150–9.

207. Priovoulos N, van Boxel SCJ, Jacobs HIL, Poser BA, Uludag K, Verhey FRJ, et al. Unraveling the contributions to the neuromelanin-MRI contrast. Brain Struct Funct. 2020 Dec 1;225(9):2757–74.

208. Clewett D V., Lee TH, Greening S, Ponzio A, Margalit E, Mather M. Neuromelanin marks the spot: identifying a locus coeruleus biomarker of cognitive reserve in healthy aging. Neurobiol Aging. 2016 Jan 1;37:117–26.

209. Theofilas P, Ehrenberg AJ, Dunlop S, Di Lorenzo Alho AT, Nguy A, Leite REP, et al. Locus coeruleus volume and cell population changes during Alzheimer's disease progression: A stereological study in human postmortem brains with potential implication for early-stage biomarker discovery. Alzheimer's and Dementia. 2017 Mar 1;13(3):236–46.

210. Braak H, Del Tredici K. The pathological process underlying Alzheimer's disease in individuals under thirty. Acta Neuropathol. 2011 Feb;121(2):171–81.

211. Braak H, Thal DR, Ghebremedhin E, Tredici K Del. Stages of the Pathologic Process in Alzheimer Disease: Age Categories From 1 to 100 Years. J Neuropathol Exp Neurol [Internet]. 2011;70(11):960–9. Available from: https://academic.oup.com/jnen/article/70/11/960/2917408

212. Krebs RM, Park HRP, Bombeke K, Boehler CN. Modulation of locus coeruleus activity by novel oddball stimuli. Brain Imaging Behav. 2018 Apr 1;12(2):577–84.

213. Sterpenich V, D'Argembeau A, Desseilles M, Balteau E, Albouy G, Vandewalle G, et al. The locus ceruleus is involved in the successful retrieval of emotional memories in humans. Journal of Neuroscience. 2006;26(28):7416–23.

214. Lee TH, Kim SH, Katz B, Mather M. The Decline in Intrinsic Connectivity Between the Salience Network and Locus Coeruleus in Older Adults: Implications for Distractibility. Front Aging Neurosci. 2020 Jan 31;12.

215. Bouret S, Sara SJ. Network reset: A simplified overarching theory of locus coeruleus noradrenaline function. Trends Neurosci. 2005;28(11):574–82.

216. Jacobs HIL, Priovoulos N, Poser BA, Pagen LHG, Ivanov D, Verhey FRJ, et al. Dynamic behavior of the locus coeruleus during arousal-related memory processing in a multi-modal 7T fMRI paradigm. Elife. 2020 Jun 1;9:1–30.

217. Poe GR, Foote S, Eschenko O, Johansen JP, Bouret S, Aston-Jones G, et al. Locus coeruleus: a new look at the blue spot. Vol. 21, Nature Reviews Neuroscience. Nature Research; 2020. p. 644–59.

218. Mason ST, Fibiger HC. Regional topography within noradrenergic locus coeruleus as revealed by retrograde transport of horseradish peroxidase. J Comp Neurol. 1979;187(4):703–24.

219. Loughlin SE, Foora SL, Grzanna R. Efferent projections of nucleus locus coeruleus: Morphologic subpopulations have different efferent targets. Neuroscience. 1986;18(2):307–19.

220. Simpson KL, Altman DW, Wang L, Kirifides ML, C-s Lin R, Waterhouse BD. Lateralization and Functional Organization of the Locus Coeruleus Projection to the Trigeminal Somatosensory Pathway in Rat. J Comp Neurol. 1997;385:135–47.

221. Reuter-Lorenz PA, Park DC. Human neuroscience and the aging mind: A new look at old problems. Journals of Gerontology - Series B Psychological Sciences and Social Sciences. 2010;65 B(4):405–15.

222. Jacobs HIL, Müller-Ehrenberg L, Priovoulos N, Roebroeck A. Curvilinear locus coeruleus functional connectivity trajectories over the adult lifespan: a 7T MRI study. Neurobiol Aging. 2018 Sep 1;69:167–76.

223. Kety SS. The possible role of the adrenergic systems of the cortex in learning. Res Publ Assoc Res Nerv Ment Dis. 1972;50:376–89.

224. Sara SJ. Noradrenergic Modulation of Selective Attention: Its Role in Memory Retrieval. Annals of the New York Academy of Science. 1985;444:178–93.

225. Sara SJ, Segal M. Plasticity of sensory responses of locus coeruleus neurons in the behaving rat: implications for cognition. Prog Brain Res. 1991;88:571–85.

226. Aghajanian GK. Tolerance of locus coeruleus neurones to morphine and suppression of withdrawal response by clonidine. Nature. 1978;276(5684):186–8.

227. del Cerro I, Martínez-Zalacaín I, Guinea-Izquierdo A, Gascón-Bayarri J, Viñas-Diez V, Urretavizcaya M, et al. Locus coeruleus connectivity alterations in late-life major depressive disorder during a visual oddball task. Neuroimage Clin. 2020 Jan 1;28.

228. Szot P, Franklin A, Miguelez C, Wang Y, Vidaurrazaga I, Ugedo L, et al. Depressive-like behavior observed with a minimal loss of locus coeruleus (LC) neurons following administration of 6-hydroxydopamine is associated with electrophysiological changes and reversed with precursors of norepinephrine. Neuropharmacology. 2016 Feb 1;101:76–86.

229. Yamamoto KI, Shinba T, Yoshii M. Psychiatric symptoms of noradrenergic dysfunction: A pathophysiological view. Psychiatry Clin Neurosci. 2014 Jan;68(1):1–20.

230. Berger A, Vespa S, Dricot L, Dumoulin M, Iachim E, Doguet P, et al. How Is the Norepinephrine System Involved in the Antiepileptic Effects of Vagus Nerve Stimulation? Front Neurosci. 2021 Dec 2;15.

231. Giorgi FS, Lombardo F, Galgani A, Hlavata H, Della Latta D, Martini N, et al. Locus Coeruleus magnetic resonance imaging in cognitively intact elderly subjects. Brain Imaging Behav. 2022 Jun 1;16(3):1077–87.

232. Dahl MJ, Mather M, Düzel S, Bodammer NC, Lindenberger U, Kühn S, et al. Rostral locus coeruleus integrity is associated with better memory performance in older adults. Nat Hum Behav. 2019 Nov 1;3(11):1203–14.

233. Chen X, Huddleston DE, Langley J, Ahn S, Barnum CJ, Factor SA, et al. Simultaneous imaging of locus coeruleus and substantia nigra with a quantitative neuromelanin MRI approach. Magn Reson Imaging. 2014;32(10):1301–6.

234. Nakane T, Nihashi T, Kawai H, Naganawa S. Visualization of Neuromelanin in the Substantia Nigra and Locus Ceruleus at 1.5T Using a 3D-gradient Echo Sequence with Magnetization Transfer Contrast. Magn Reson Med Sci. 2008;7(4):205–10.

235. Schwarz ST, Xing Y, Tomar P, Bajaj N, Auer DP. In Vivo assessment of brainstem depigmentation in Parkinson disease: Potential as a severity marker for multicenter studies. Radiology. 2017 Jun 1;283(3):789–98.

236. Sasaki M, Shibata E, Tohyama K, Takahashi J, Otsuka K, Tsuchiya K, et al. Neuromelanin magnetic resonance imaging of locus ceruleus and substantia nigra in Parkinson's disease.

237. Priovoulos N, Jacobs HIL, Ivanov D, Uludağ K, Verhey FRJ, Poser BA. High-resolution in vivo imaging of human locus coeruleus by magnetization transfer MRI at 3T and 7T. Neuroimage. 2018 Mar 1;168:427–36.

238. Wang S, Wu T, Cai Y, Yu Y, Chen X, Wang L. Neuromelanin magnetic resonance imaging of substantia nigra and locus coeruleus in Parkinson's disease with freezing of gait. Front Aging Neurosci. 2023 Feb 2;15.

239. Griffis JC, Allendorfer JB, Szaflarski JP. Voxel-based Gaussian naïve Bayes classification of ischemic stroke lesions in individual T1-weighted MRI scans. J Neurosci Methods. 2016 Jan 15;257:97–108.

240. Ariz M, Abad RC, Castellanos G, Martinez M, Munoz-Barrutia A, Fernandez-Seara MA, et al. Dynamic atlas-based segmentation and quantification of neuromelanin-rich brainstem structures in Parkinson disease. IEEE Trans Med Imaging. 2019 Mar 1;38(3):813–23.

241. Yi YJ, Lüsebrink F, Ludwig M, Maaß A, Ziegler G, Yakupov R, et al. It is the locus coeruleus! Or… is it?: a proposition for analyses and reporting standards for structural and functional magnetic resonance imaging of the noradrenergic locus coeruleus. Neurobiol Aging. 2023 Sep;129:137–48.

242. Tona KD, Keuken MC, de Rover M, Lakke E, Forstmann BU, Nieuwenhuis S, et al. In vivo visualization of the locus coeruleus in humans: quantifying the test–retest reliability. Brain Struct Funct. 2017 Dec 1;222(9):4203–17.

243. Murphy PR, Robertson IH, Balsters JH, O'connell RG. Pupillometry and P3 index the locus coeruleus-noradrenergic arousal function in humans. Psychophysiology. 2011;48(11):1532–43.

244. Berger A, Koshmanova E, Beckers E, Sharifpour R, Paparella I, Campbell I, et al. Structural and functional characterization of the locus coeruleus in young and late middle-aged individuals. Frontiers in Neuroimaging. 2023 Jun 21;2.

245. Yushkevich PA, Piven J, Hazlett HC, Smith RG, Ho S, Gee JC, et al. User-guided 3D active contour segmentation of anatomical structures: Significantly improved efficiency and reliability. Neuroimage. 2006 Jul 1;31(3):1116–28.

246. Shibata E, Sasaki M, Tohyama K, Otsuka K, Sakai A. Reduced signal of locus ceruleus in depression in quantitative neuromelanin magnetic resonance imaging. Neuroreport. 2007 Mar;18(5):415–8.

247. Liu KY, Kievit RA, Tsvetanov KA, Betts MJ, Düzel E, Rowe JB, et al. Noradrenergic-dependent functions are associated with age-related locus coeruleus signal intensity differences. Nat Commun. 2020 Apr 6;11(1):1712.

248. Doppler CEJ, Kinnerup MB, Brune C, Farrher E, Betts M, Fedorova TD, et al. Regional locus coeruleus degeneration is uncoupled from noradrenergic terminal loss in Parkinson's disease. Brain. 2021 Oct 22;144(9):2732–44.

249. Calarco N, Cassidy CM, Selby B, Hawco C, Voineskos AN, Diniz BS, et al. Associations between locus coeruleus integrity and diagnosis, age, and cognitive performance in older adults with and without late-life depression: An exploratory study. Neuroimage Clin. 2022;36:103182.

250. Bell TR, Elman JA, Beck A, Fennema-Notestine C, Gustavson DE, Hagler DJ, et al. Rostral-middle locus coeruleus integrity and subjective cognitive decline in early old age. Journal of the International Neuropsychological Society. 2023 Oct 16;29(8):763–74.

251. Pickel VM, Segal M, Bloom FE. A radioautographic study of the efferent pathways of the nucleus locus coeruleus. Journal of Comparative Neurology. 1974 May 9;155(1):15–41.

252. Satoh K, Tohyama M, Yamamoto K, Sakumoto T, Shimizu N. Noradrenaline innervation of the spinal cord studied by the horseradish peroxidase method combined with monoamine oxidase staining. Exp Brain Res. 1977 Nov;30–30(2–3).

253. Garyfallidis E, Brett M, Amirbekian B, Rokem A, van der Walt S, Descoteaux M, et al. Dipy, a library for the analysis of diffusion MRI data. Front Neuroinform. 2014 Feb 21;8(FEB).

254. Veraart J, Novikov DS, Christiaens D, Ades-aron B, Sijbers J, Fieremans E. Denoising of diffusion MRI using random matrix theory. Neuroimage. 2016 Nov 15;142:394–406.

255. Andersson JLR, Sotiropoulos SN. An integrated approach to correction for off-resonance effects and subject movement in diffusion MR imaging. Neuroimage. 2016 Jan 15;125:1063–78.

256. Delinte N, Gosse C, Dricot L, Dessain Q, Simon M, Macq B, et al. Microstructural alterations in the white matter of children with dyslexia assessed by multi-fascicle diffusion compartment imaging. In: Proc Intl Soc Mag Reson Med. John Wiley and Sons Inc.; 2021.

257. Yeh FC, Wedeen VJ, Tseng WYI. Generalized q-sampling imaging. IEEE Trans Med Imaging. 2010 Sep;29(9):1626–35.

258. Stewart SA. The effects of benzodiazepines on cognition. J Clin Psychiatry. 2005;66 Suppl 2:9–13.

259. Xu C, Lin H, Xu J, Zhang X, Hao G, Liu QQ, et al. Long-term outcomes and prognosis factors of vagus nerve stimulation in patients with refractory epilepsy. Acta Epileptologica. 2022 Dec 1;4(1).

260. Marien MR, Colpaert FC, Rosenquist AC. Noradrenergic mechanisms in neurodegenerative diseases: A theory. Brain Res Rev. 2004;45(1):38–78.

261. Reyes BAS, Van Bockstaele EJ. Divergent Projections of Catecholaminergic Neurons in the Nucleus of the Solitary Tract to Limbic Forebrain and Medullary Autonomic Brain Regions. Brain Res. 2006;1117(1):69–79.

262. Ennis M, Aston-Jones G. Activation of Locus Coeruleus from Nucleus New Excitatory Amino Acid Pathway in Brain. The Journal of Neuroscience. 1988;8(10):3644–57.

263. Marzo A, Totah NK, Neves RM, Logothetis NK, Eschenko O. Unilateral electrical stimulation of rat locus coeruleus elicits bilateral response of norepinephrine neurons and sustained activation of medial prefrontal cortex. J Neurophysiol [Internet]. 2014;111:2570–88. Available from: www.jn.org

264. Mccrea RA, Baker R. Anatomical Connections of the Nucleus Prepositus of the Cat. J Comp Neurol. 1985;237(377):407.

265. Van Bockstaele EJ, Pieribone VA, Astonjones G. Diverse Merents Converge on the Nucleus Paragigantocelldark i n the Rat Ventrolateral Medulla: Retrograde and Anterograde Tracing Studies. J Comp Neurol. 1989;290:561–84.

266. Schwarz LA, Luo L. Organization of the locus coeruleus-norepinephrine system. Current Biology. 2015;25(21):R1051–6.

267. Beck D, de Lange AM, Maximov II, Richard G, Andreassen OA, Nordvik JE, et al. White matter microstructure across the adult lifespan: A mixed longitudinal and cross-sectional study using advanced diffusion models and brain-age prediction. Neuroimage. 2021 Jan 1;224.

268. Porat S, Sibilia F, Yoon J, Shi Y, Dahl MJ, Werkle-Bergner M, et al. Age differences in diffusivity in the locus coeruleus and its ascending noradrenergic tract. Neuroimage. 2022 May 1;251.

269. Hansen N. The Longevity of Hippocampus-Dependent Memory Is Orchestrated by the Locus Coeruleus-Noradrenergic System. Neural Plast. 2017;2017.

270. Bowden DM, German DC, Douglas Poynter W. An autoradiographic, semistereotaxic mapping of major projections from locus coeruleus and adjacent nuclei in Macaca mulatta. Brain Res. 1978 Apr;145(2):257–76.

271. Saunders RC, Rosene DL, Van Hoesen GW. Comparison of the efferents of the amygdala and the hippocampal formation in the rhesus monkey: II. Reciprocal and non-reciprocal connections. Journal of Comparative Neurology. 1988 May 8;271(2):185–207.

272. Canteras NS, Swanson LW. Projections of the ventral subiculum to the amygdala, septum, and hypothalamus: A PHAL anterograde tract-tracing study in the rat. Journal of Comparative Neurology. 1992 Oct 8;324(2):180–94.

273. McDonald AJ. Cortical pathways to the mammalian amygdala. Prog Neurobiol. 1998 Jun;55(3):257–332.

274. Pitakänen A, Pikkarainen M, Nurminen N, Ylinen A. Reciprocal Connections between the Amygdala and the Hippocampal Formation, Perirhinal Cortex, and Postrhinal Cortex in Rat: A Review. Ann N Y Acad Sci. 2000 Jun 25;911(1):369–91.

275. Meisner OC, Nair A, Chang SWC. Amygdala connectivity and implications for social cognition and disorders. In 2022. p. 381–403.

276. Langley J, Huddleston DE, Liu CJ, Hu X. Reproducibility of locus coeruleus and substantia nigra imaging with neuromelanin sensitive MRI. Magnetic Resonance Materials in Physics, Biology and Medicine. 2017 Apr 29;30(2):121–5.

277. Wengler K, He X, Abi-Dargham A, Horga G. Reproducibility assessment of neuromelanin-sensitive magnetic resonance imaging protocols for region-of-interest and voxelwise analyses. Neuroimage. 2020 Mar;208:116457.

278. van der Pluijm M, Cassidy C, Zandstra M, Wallert E, de Bruin K, Booij J, et al. Reliability and Reproducibility of Neuromelanin-Sensitive Imaging of the Substantia Nigra: A Comparison of Three Different Sequences. Journal of Magnetic Resonance Imaging. 2021 Mar 9;53(3):712–21.

279. Krahl SE, Clark KB. Vagus nerve stimulation for epilepsy: A review of central mechanisms. Surg Neurol Int. 2012 Oct 1;3(SUPPL4).

280. Sarlo GL, Holton KF. Brain concentrations of glutamate and GABA in human epilepsy: A review. Seizure. 2021 Oct 1;91:213–27.

281. Henry TR, Bakay RAE, Pennell PB, Epstein CM, Votaw JR. Brain Blood-flow Alterations Induced by Therapeutic Vagus Nerve Stimulation in Partial Epilepsy: II. Prolonged Effects at High and Low Levels of Stimulation. Epilepsia. 2004 Sep 24;45(9):1064–70.

282. Henry TR, Votaw JR, Pennell PB, Epstein CM, Bakay RAE, Faber TL, et al. Acute blood flow changes and efficacy of vagus nerve stimulation in partial epilepsy. Neurology. 1999 Apr 1;52(6):1166–1166.

283. Henry TR, Bakay RAE, Votaw JR, Pennell PB, Epstein CM, Faber TL, et al. Brain Blood Flow Alterations Induced by Therapeutic Vagus Nerve Stimulation in Partial Epilepsy: I. Acute Effects at High and Low Levels of Stimulation. Epilepsia. 1998 Sep 3;39(9):983–90.

284. Liu WC. BOLD fMRI activation induced by vagus nerve stimulation in seizure patients. J Neurol Neurosurg Psychiatry. 2003 Jun 1;74(6):811–3.

285. Rensonnet G. In vivo diffusion magnetic resonance imaging of the white matter microstructure from dictionaries generated by Monte Carlo simulations: development and validation. 2019.

286. Kayyali H, Abdelmoity S, Bansal L, Kaufman C, Smith K, Fecske E, et al. The Efficacy and Safety of Rapid Cycling Vagus Nerve Stimulation in Children With Intractable Epilepsy. Pediatr Neurol. 2020 Aug 1;109:35–8.

287. Dessain Q, Mathieu S, Delinte N. Hyedryn/elikopy: v0.3 - Bug fixes (v0.3). Zenodo. [Internet]. 2024 [cited 2024 Jan 16]. Available from: https://zenodo.org/records/10514466

288. Fick RHJ, Wassermann D, Deriche R. The Dmipy Toolbox: Diffusion MRI Multi-Compartment Modeling and Microstructure Recovery Made Easy. Front Neuroinform. 2019 Oct 15;13.

289. Jeurissen B, Tournier JD, Dhollander T, Connelly A, Sijbers J. Multi-tissue constrained spherical deconvolution for improved analysis of multi-shell diffusion MRI data. Neuroimage. 2014 Dec 1;103:411–26.

290. George K, M Das J. Neuroanatomy, Thalamocortical Radiations. 2023.

291. Yeh WC, Jiang Y, Tan SY, Yeh CY. A New Support Vector Machine Based on Convolution Product. Complexity. 2021 Jun 11;2021:1–19.

292. Winston GP, Vos SB, Caldairou B, Hong SJ, Czech M, Wood TC, et al. Microstructural imaging in temporal lobe epilepsy: Diffusion imaging changes relate to reduced neurite density. Neuroimage Clin. 2020 Jan 1;26.

293. Li W, An D, Tong X, Liu W, Xiao F, Ren J, et al. Different patterns of white matter changes after successful surgery of mesial temporal lobe epilepsy. Neuroimage Clin. 2019;21:101631.

294. Foutz TJ, Wong M. Brain stimulation treatments in epilepsy: Basic mechanisms and clinical advances. Vol. 45, Biomedical Journal. Elsevier B.V.; 2022. p. 27–37.

295. Winklewski PJ, Sabisz A, Naumczyk P, Jodzio K, Szurowska E, Szarmach A. Understanding the Physiopathology Behind Axial and Radial Diffusivity Changes—What Do We Know? Front Neurol. 2018 Feb 27;9.

296. Aung WY, Mar S, Benzinger TL. Diffusion tensor MRI as a biomarker in axonal and myelin damage. Imaging Med. 2013 Oct;5(5):427–40.

297. Solowij N, Zalesky A, Lorenzetti V, Yücel M. Chronic Cannabis Use and Axonal Fiber Connectivity. In: Handbook of Cannabis and Related Pathologies. Elsevier; 2017. p. 391–400.

298. Fu X, Shrestha S, Sun M, Wu Q, Luo Y, Zhang X, et al. Microstructural White Matter Alterations in Mild Cognitive Impairment and Alzheimer's Disease: Study Based on Neurite Orientation Dispersion and Density Imaging (NODDI). Clin Neuroradiol. 2020 Sep 1;30(3):569–79.

299. Kamagata K, Hatano T, Okuzumi A, Motoi Y, Abe O, Shimoji K, et al. Neurite orientation dispersion and density imaging in the substantia nigra in idiopathic Parkinson disease. Eur Radiol. 2016 Aug 1;26(8):2567–77.

300. Nazeri A, Mulsant BH, Rajji TK, Levesque ML, Pipitone J, Stefanik L, et al. Gray Matter Neuritic Microstructure Deficits in Schizophrenia and Bipolar Disorder. Biol Psychiatry. 2017 Nov 15;82(10):726–36.

301. Narayanan JT, Watts R, Haddad N, Labar DR, Li PM, Filippi CG. Cerebral activation during vagus nerve stimulation: A functional MR study. Epilepsia. 2002 Dec 1;43(12):1509–14.

302. Muthiah N, Mallela AN, Vodovotz L, Sharma N, Akwayena E, Pan E, et al. Development of a clinical model to predict vagus nerve stimulation response in pediatric patients with drug-resistant epilepsy. J Neurosurg Pediatr. 2023 Feb 1;1–8.

303. Ma J, Wang Z, Cheng T, Hu Y, Qin X, Wang W, et al. A prediction model integrating synchronization biomarkers and clinical features to identify responders to vagus nerve stimulation among pediatric patients with drug-resistant epilepsy. CNS Neurosci Ther. 2022 Nov 27;28(11):1838–48.

304. Kostov KH, Kostov H, Larsson PG, Henning O, Eckmann CAC, Lossius MI, et al. Norwegian population-based study of long-term effects, safety, and predictors of response of vagus nerve stimulation treatment in drug-resistant epilepsy: The NORPulse study. Epilepsia. 2022 Feb 21;63(2):414–25.

305. Lee DA, Ko J, Kim HC, Shin KJ, Park BS, Kim IH, et al. Identifying juvenile myoclonic epilepsy via diffusion tensor imaging using machine learning analysis. Journal of Clinical Neuroscience. 2021 Sep 1;91:327–33.

306. Concha L, Kim H, Bernasconi A, Bernhardt BC, Bernasconi N. Spatial patterns of water diffusion along white matter tracts in temporal lobe epilepsy. Neurology. 2012 Jul 31;79(5):455–62.

307. Drees C, Afra P, Verner R, Kaye L, Keith A, Jiang M, et al. Feasibility study of microburst VNS therapy in drug-resistant focal and generalized epilepsy. Brain Stimul. 2024 Mar;17(2):382–91.

308. Szaflarski JP, Allendorfer JB, Begnaud J, Ranuzzi G, Shamshiri E, Verner R. Optimized microburst VNS elicits fMRI responses beyond thalamic-specific response from standard VNS. Ann Clin Transl Neurol. 2024 May 26;11(5):1135–47.

309. Doguet P, Nieuwenhuys A, Botquin Y, Garnier J. Active implantable stimulating device for on-demand stimulation of a vagus nerve [Internet]. EP3930828B1, 2022 [cited 2023 Oct 3]. Available from: https://worldwide.espacenet.com/patent/search/family/070554060/publication/EP3930828B1?q=EP%203930828%20B1

310. Fetzer S, Dibué M, Nagel AM, Trollmann R. A systematic review of magnetic resonance imaging in patients with an implanted vagus nerve stimulation system. Neuroradiology. 2021 Sep 12;63(9):1407–17.

311. Lomarev M, Denslow S, Nahas Z, Chae JH, George MS, Bohning DE. Vagus nerve stimulation (VNS) synchronized BOLD fMRI suggests that VNS in depressed adults has frequency/dose dependent effects. J Psychiatr Res. 2002 Jul;36(4):219–27.

312. Sucholeiki R, Alsaadi TM, Morris GL, Ulmer JL, Biswal B, Mueller WM. fMRI in patients implanted with a vagal nerve stimulator. Seizure. 2002;11(3):157–62.

313. Maniker A, Liu WC, Marks D, Moser K, Kalnin A. Positioning of vagal nerve stimulators: technical note. Surg Neurol. 2000 Feb;53(2):178–81.

314. Benbadis SR, Nyhenhuis J, Tatum IV WO, Murtagh FR, Gieron M, Vale FL. MRI of the brain is safe in patients implanted with the vagus nerve stimulator. Seizure. 2001 Oct;10(7):512–5.

315. Basser PJ, Roth BJ. Stimulation of a myelinated nerve axon by electromagnetic induction. Med Biol Eng Comput. 1991 May;29(3):261–8.

316. Kawaji H, Yamamoto T, Fujimoto A, Uchida D, Ichikawa N, Yamazoe T, et al. Additional seizure reduction by replacement with Vagus Nerve Stimulation Model 106 (AspireSR). Neurosci Lett. 2020 Jan;716:134636.

317. Tzadok M, Harush A, Nissenkorn A, Zauberman Y, Feldman Z, Ben-zeev B. Clinical outcomes of closed-loop vagal nerve stimulation in patients with refractory epilepsy. Seizure. 2019 Oct;71:140–4.

318. Hamilton P, Soryal I, Dhahri P, Wimalachandra W, Leat A, Hughes D, et al. Clinical outcomes of VNS therapy with AspireSR® (including cardiac-based seizure detection) at a large complex epilepsy and surgery centre. Seizure. 2018 May;58:120–6.

319. Danthine V, Cottin L, Germany Morrison EI, Delbeke J, Liberati G, Nonclercq A, et al. A Longitudinal Vagus Nerve Stimulation Study: Effects on Laryngeal Motor Evoked Potentials and EEG Synchronization. American Epilepsy Society ; 2023 Dec 3.

320. Gil-López F, Boget T, Manzanares I, Donaire A, Conde-Blanco E, Baillés E, et al. External trigeminal nerve stimulation for drug resistant epilepsy: A randomized controlled trial. Brain Stimul. 2020 Sep;13(5):1245–53.

321. Vespa S, Stumpp L, Liberati G, Delbeke J, Nonclercq A, Mouraux A, et al. Characterization of vagus nerve stimulation-induced pupillary responses in epileptic patients. Brain Stimul. 2022 Nov 1;15(6):1498–507.

322. Mollet L, Grimonprez A, Raedt R, Delbeke J, El Tahry R, De Herdt V, et al. Intensity-dependent modulatory effects of vagus nerve stimulation on cortical excitability. Acta Neurol Scand. 2013 Dec;128(6):391–6.

323. Zagon A, Kemeny AA. Slow Hyperpolarization in Cortical Neurons: A Possible Mechanism Behind Vagus Nerve Simulation Therapy for Refractory Epilepsy? Epilepsia. 2000 Nov 2;41(11):1382–9.

324. Cavada C, Goldman-Rakic PS. Posterior parietal cortex in rhesus monkey: II. Evidence for segregated corticocortical networks linking sensory and limbic areas with the frontal lobe. Journal of Comparative Neurology. 1989 Sep 22;287(4):422–45.

325. Fanardjian VV, Papoyan EV. Patterns of inputs to the parietal cortex efferent neurons from the motor cortex and cerebellum in the cat. Neuroscience. 1997 Feb;77(4):965–74.

326. Simson P, Weiss J. Alpha-2 receptor blockade increases responsiveness of locus coeruleus neurons to excitatory stimulation. The Journal of Neuroscience. 1987 Jun 1;7(6):1732–40.

327. Fernández-Pastor B, Meana JJ. In vivo tonic modulation of the noradrenaline release in the rat cortex by locus coeruleus somatodendritic α2-adrenoceptors. Eur J Pharmacol. 2002 May;442(3):225–9.

328. Aghajanian GK, Vandermaelen CP, Andrade R. Intracellular studies on the role of calcium in regulating the activity and reactivity of locus coeruleus neurons in vivo. Brain Res. 1983 Aug;273(2):237–43.

329. Aghajanian GK, VanderMaelen CP. Alpha 2-Adrenoceptor-Mediated Hyperpolarization of Locus Coeruleus Neurons: Intracellular Studies in Vivo. Science (1979). 1982 Mar 12;215(4538):1394–6.

330. Baral S, Hosseini H, More K, Fabrin TMC, Braun J, Prigge M. Spike-Dependent Dynamic Partitioning of the Locus Coeruleus Network through Noradrenergic Volume Release in a Simulation of the Nucleus Core. Brain Sci. 2022 Jun 1;12(6):728.

331. Szaflarski JP, Allendorfer JB, Begnaud J, Ranuzzi G, Shamshiri E, Verner R. Optimized microburst VNS elicits fMRI responses beyond thalamic-specific response from standard VNS. Ann Clin Transl Neurol. 2024 May 26;11(5):1135–47.

332. Farrand A, Jacquemet V, Verner R, Owens M, Beaumont E. Vagus nerve stimulation parameters evoke differential neuronal responses in the locus coeruleus. Physiol Rep. 2023 Mar 10;11(5).

333. Mu Q, Bohning DE, Nahas Z, Walker J, Anderson B, Johnson KA, et al. Acute vagus nerve stimulation using different pulse widths produces varying brain effects. Biol Psychiatry. 2004 Apr;55(8):816–25.

334. Verner R, Szaflarski JP, Allendorfer JB, Vonck K, Giannicola G. Modulation of the thalamus by microburst vagus nerve stimulation: a feasibility study protocol. Front Neurol. 2023 Jun 13;14.

335. Sclocco R, Garcia RG, Kettner NW, Isenburg K, Fisher HP, Hubbard CS, et al. The influence of respiration on brainstem and cardiovagal response to auricular vagus nerve stimulation: A multimodal ultrahigh-field (7T) fMRI study. Brain Stimul. 2019 Jul;12(4):911–21.

336. Ito SI, Craig AD. Vagal-Evoked Activity in the Parafascicular Nucleus of the Primate Thalamus. J Neurophysiol. 2005 Oct;94(4):2976–82.

337. Macchi G, Bentivoglio M, Molinari M, Minciacchi D. The thalamo-caudate versus thalamo-cortical projections as studied in the cat with fluorescent retrograde double labeling. Exp Brain Res. 1984 Mar;54(2).

338. Berendse HW, Groenewegen HJ. Restricted cortical termination fields of the midline and intralaminar thalamic nuclei in the rat. Neuroscience. 1991 Jan;42(1):73–102.

339. Krettek JE, Price JL. The cortical projections of the mediodorsal nucleus and adjacent thalamic nuclei in the rat. Journal of Comparative Neurology. 1977 Jan 15;171(2):157–91.

340. Jayaraman A. Organization of thalamic projections in the nucleus accumbens and the caudate nucleus in cats and its relation with hippocampal and other subcortical afferents. Journal of Comparative Neurology. 1985 Jan 15;231(3):396–420.

341. Van der Werf YD, Witter MP, Groenewegen HJ. The intralaminar and midline nuclei of the thalamus. Anatomical and functional evidence for participation in processes of arousal and awareness. Brain Res Rev. 2002 Sep;39(2–3):107–40.

342. Eckert U, Metzger CD, Buchmann JE, Kaufmann J, Osoba A, Li M, et al. Preferential networks of the mediodorsal nucleus and centromedian–parafascicular complex of the thalamus—A DTI tractography study. Hum Brain Mapp. 2012 Nov 20;33(11):2627–37.

343. Çavdar S, Onat FY, Çakmak YÖ, Yananli HR, Gülçebi M, Aker R. The pathways connecting the hippocampal formation, the thalamic reuniens nucleus and the thalamic reticular nucleus in the rat. J Anat. 2008 Mar;212(3):249–56.

344. Ottersen OP, Ben-Ari Y. Afferent connections to the amygdaloid complex of the rat and cat. I. Projections from the thalamus. Journal of Comparative Neurology. 1979 Sep 15;187(2):401–24.

345. Ao Y, Yang B, Zhang C, Wu B, Zhang X, Xing D, et al. Locus Coeruleus to Paraventricular Thalamus Projections Facilitate Emergence From Isoflurane Anesthesia in Mice. Front Pharmacol. 2021 Apr 27;12.

346. Wolters AF, Heijmans M, Priovoulos N, Jacobs HIL, Postma AA, Temel Y, et al. Neuromelanin related ultra-high field signal intensity of the locus coeruleus differs between Parkinson's disease and controls. Neuroimage Clin. 2023;39:103479.

347. Olivieri P, Lagarde J, Lehericy S, Valabrègue R, Michel A, Macé P, et al. Early alteration of the locus coeruleus in phenotypic variants of Alzheimer's disease. Ann Clin Transl Neurol. 2019 Jul 23;6(7):1345–51.

348. Einhäuser W, Stout J, Koch C, Carter O. Pupil dilation reflects perceptual selection and predicts subsequent stability in perceptual rivalry. Proceedings of the National Academy of Sciences. 2008 Feb 5;105(5):1704–9.

349. Huang TH, Lai MC, Chen YS, Huang CW. Brain Imaging in Epilepsy-Focus on Diffusion-Weighted Imaging. Diagnostics. 2022 Oct 27;12(11):2602.

350. Scott RC, King MD, Gadian DG, Neville BGR, Connelly A. Prolonged Febrile Seizures Are Associated with Hippocampal Vasogenic Edema and Developmental Changes. Epilepsia. 2006 Sep 13;47(9):1493–8.

351. Winston GP, Stretton J, Sidhu MK, Symms MR, Duncan JS. Progressive white matter changes following anterior temporal lobe resection for epilepsy. Neuroimage Clin. 2014;4:190–200.

352. McDonald CR, Hagler DJ, Girard HM, Pung C, Ahmadi ME, Holland D, et al. Changes in fiber tract integrity and visual fields after anterior temporal lobectomy. Neurology. 2010 Nov 2;75(18):1631–8.

353. Concha L, Beaulieu C, Wheatley BM, Gross DW. Bilateral White Matter Diffusion Changes Persist after Epilepsy Surgery. Epilepsia. 2007 May 13;48(5):931–40.

354. Liu M, Gross DW, Wheatley BM, Concha L, Beaulieu C. The acute phase of Wallerian degeneration: Longitudinal diffusion tensor imaging of the fornix following temporal lobe surgery. Neuroimage. 2013 Jul;74:128–39.

355. McHugh JC, Singh HW, Phillips J, Murphy K, Doherty CP, Delanty N. Outcome Measurement after Vagal Nerve Stimulation Therapy: Proposal of a New Classification. Epilepsia. 2007 Feb 2;48(2):375–8.